



University of Kentucky
UKnowledge

University of Kentucky Doctoral Dissertations

Graduate School

2009

LONG-PERIOD GROUND MOTIONS IN THE UPPER MISSISSIPPI EMBAYMENT FROM FINITE-FAULT, FINITE-DIFFERENCE SIMULATIONS

Kenneth A. Macpherson
University of Kentucky, macpherson@yahoo.com

[Right click to open a feedback form in a new tab to let us know how this document benefits you.](#)

Recommended Citation

Macpherson, Kenneth A., "LONG-PERIOD GROUND MOTIONS IN THE UPPER MISSISSIPPI EMBAYMENT FROM FINITE-FAULT, FINITE-DIFFERENCE SIMULATIONS" (2009). *University of Kentucky Doctoral Dissertations*. 746.
https://uknowledge.uky.edu/gradschool_diss/746

This Dissertation is brought to you for free and open access by the Graduate School at UKnowledge. It has been accepted for inclusion in University of Kentucky Doctoral Dissertations by an authorized administrator of UKnowledge. For more information, please contact UKnowledge@lsv.uky.edu.

ABSTRACT OF DISSERTATION

Kenneth A. Macpherson

The Graduate School
University of Kentucky
2009

LONG-PERIOD GROUND MOTIONS IN THE UPPER MISSISSIPPI
EMBAYMENT FROM FINITE-FAULT, FINITE-DIFFERENCE SIMULATIONS

ABSTRACT OF DISSERTATION

A dissertation submitted in partial
fulfillment of the requirements for
the degree of Doctor of Philosophy
in the College of Arts and Sciences
at the University of Kentucky

By
Kenneth A. Macpherson
Lexington, Kentucky

Director: Dr. Edward W. Woolery, Professor of Geophysics
Lexington, Kentucky 2009

Copyright© Kenneth A. Macpherson 2009

ABSTRACT OF DISSERTATION

LONG-PERIOD GROUND MOTIONS IN THE UPPER MISSISSIPPI EMBAYMENT FROM FINITE-FAULT, FINITE-DIFFERENCE SIMULATIONS

A 3D velocity model and 3D wave propagation code have been employed to simulate long-period ground motions in the upper Mississippi embayment. This region is exposed to seismic hazard in the form of large earthquakes in the New Madrid seismic zone and observational data are sparse, making simulation a valuable tool for predicting the effects of large events. These simulations were undertaken in order to estimate ground-motion characteristics and to investigate the influence of the 3D embayment structure and finite-fault mechanics. There are three primary fault zones in the New Madrid seismic zone, each of which was likely associated with one of the three main shocks of the 1811-1812 earthquake sequence. For this study, three simulations have been conducted on each major segment, evaluating the effects of different epicentral locations and rupture directions on ground motions. The full wave field up to a frequency of 0.5 Hz was computed on a $200 \times 200 \times 50 \text{ km}^3$ volume, and up to a frequency of 1.0 Hz on a $100 \times 100 \times 50 \text{ km}^3$ volume, using a staggered-grid finite-difference code. Peak horizontal velocity, bracketed durations, and pseudospectral accelerations were calculated at the free surface. Animations showing the evolution of peak horizontal velocity through time at the free surface were also generated. The New Madrid seismic zone simulations indicate that for the considered bandwidth, finite-fault mechanics such as fault proximity, directivity effect, and slip distribution exert the most control on ground motions. The 3D geologic structure of the upper Mississippi embayment also influences ground motion, with indications that the bedrock surface acts as a wave guide, trapping waves in shallow, low-velocity parts of the embayment.

KEYWORDS: seismology, earthquakes, strong motion, simulation, finite-difference

Author's signature: Kenneth A. Macpherson

Date: June 29, 2009

LONG-PERIOD GROUND MOTIONS IN THE UPPER MISSISSIPPI
EMBAYMENT FROM FINITE-FAULT, FINITE-DIFFERENCE SIMULATIONS

By
Kenneth A. Macpherson

Director of Dissertation: Edward W. Woolery

Director of Graduate Studies: Dhananjay Ravat

Date: June 29, 2009

DISSERTATION

Kenneth A. Macpherson

The Graduate School
University of Kentucky
2009

LONG-PERIOD GROUND MOTIONS IN THE UPPER MISSISSIPPI
EMBAYMENT FROM FINITE-FAULT, FINITE-DIFFERENCE SIMULATIONS

DISSERTATION

A dissertation submitted in partial
fulfillment of the requirements for
the degree of Doctor of Philosophy
in the College of Arts and Sciences
at the University of Kentucky

By
Kenneth A. Macpherson
Lexington, Kentucky

Director: Dr. Edward W. Woolery, Professor of Geophysics
Lexington, Kentucky 2009

Copyright© Kenneth A. Macpherson 2009

ACKNOWLEDGMENTS

I would like to thank the Department of Earth and Environmental Sciences for allowing me the opportunity to study seismology and mathematics at the University of Kentucky. My four years at the University have been among the best of my life to this point.

Thank you to Dr. Edward Woolery for agreeing to guide me through the last four years and also for very enjoyable geophysics classes that hooked me on the discipline in the first place. Dr. Zhenming Wang has been extremely supportive throughout, being generous with his time over the course of years and even administering a seismology class for just two students. Dr. Qiang Ye has significantly contributed to my training, both as a committee member and through his excellent numerical analysis classes. I would like to thank Dr. Kieran O'Hara for being such a valuable member of my committee. He has been very generous with his time and offered much insight that improved the work. Classes taught by Dr. William Thomas, Dr. Sung H. Kang, and Dr. Michael Jabbour were extremely helpful and informative. These professors were also very generous with their time outside of class. Dr. Michael Kalinski was the outside examiner at my defense and I thank him for his time and contribution to the discussion. Thank you very much to Dr. Dhananjay Ravat for hooding me.

Throughout the course of my time at the University of Kentucky I have been fortunate to receive funding from a variety of sources. I thank the Department of Earth and Environmental Sciences, the Graduate School at the University of Kentucky, The Algebra³ program, and the Seismological Society of America for generous support.

I would like to thank my fellow graduate students at the Department of Earth and Environmental Sciences. The environment at the Department is warm, friendly, and supportive, and this is due in large part to the students. Writing a dissertation

would have been a much more difficult task without the moral support provided by friends in the Department.

Amy Murphy has been my companion through the course of dissertation work. Surprisingly, despite having witnessed many trials and tribulations that I, and indirectly she has been subjected to, she still has plans to pursue a doctorate. In a just world, she would receive credit towards her own studies for being able to put up with me for the last four years! She has been consistently supportive and having her by my side has been an invaluable source of comfort. She was always able to boost my spirits when things were difficult or when doubts crept in. Thank you. I love you.

Finally, I want to thank my family. Thank you for your support, both material and spiritual, over the years. My Mum and Dad believed in me when even I did not. I could never thank you enough.

To my family.

“All models are wrong, but some of them are useful.”
–George Edward Pelham Box

“It is important to point out that the mathematical formulation of the physicists
often crude experience leads in an uncanny number of cases to an amazingly
accurate description of a large class of phenomena.”
–Eugene Wigner

TABLE OF CONTENTS

Acknowledgments	iii
Table of Contents	v
List of Figures	vii
List of Tables	x
Chapter 1 Introduction	1
1.1 Seismotectonic Setting	2
1.2 Project Objective	5
1.3 Modeling Procedure	7
Chapter 2 A Velocity Model for the Upper Mississippi Embayment	11
2.1 Major Geological Boundaries	11
2.2 Method of Velocity Model Construction	19
2.3 Validation	20
Chapter 3 Simulation Methods	36
3.1 The 3D Viscoelastic Finite-Difference Code	36
3.2 Model Validation	39
3.3 Ground-Motion Parameters	42
3.4 Source Modeling	47
Chapter 4 Results and Discussion	60
4.1 Output	60
4.2 Conclusions	63
4.3 Alternate Scenarios	66
4.4 Recommendations	69
Computer Codes	148
Code for Writing Velocity Model Files	148
Code for Writing Bardwell Source File	157
Code for Calculating PHV	160
Code for Calculating Bracketed Durations	162
Code for Calculating PSA	164
Code for Writing Snapshot Files	168
SAC Macro for Preprocessing	171
Code for Writing Source Files	172
Code for Writing Reelfoot Fault Source Files	180
Animations	190

References	191
Vita	197

LIST OF FIGURES

1.1 Study area	9
1.2 The modeling process	10
2.1 Generalized geologic cross section	23
2.2 V_s^{30} data	24
2.3 Structure contour map of Paleozoic unconformity.	25
2.4 Sites with post-Paleozoic layer velocities	26
2.5 Post-Paleozoic shear-wave velocity modeling	27
2.6 Structure-contour map of the Precambrian unconformity	28
2.7 Structure-contour map of the top of the rift pillow	29
2.8 Velocity model for the middle crust	30
2.9 Isopach map of the anomalous crustal layer	31
2.10 Velocity model for the anomalous crust	32
2.11 Velocity profile at a point in the center of the 0.5-Hz region.	33
2.12 Velocity profile at a point in the center of the 1.0-Hz region.	34
2.13 Velocity model validation	35
3.1 Bardwell focal mechanism and strong-motion station WIKY	54
3.2 Observed and simulated Bardwell accelerograms	55
3.3 An SDOF system	56
3.4 The k^{-2} slip distribution on the Cottonwood Grove fault.	57
3.5 Rise time on the Cottonwood Grove fault	58
3.6 Rupture front arrival time on the Cottonwood Grove fault	59
4.1 PHV, Cottonwood Grove fault, hypocenter to the south	77
4.2 Bracketed duration, Cottonwood Grove fault, hypocenter to the south	78
4.3 PSA with T=1.0 s, Cottonwood Grove fault, hypocenter to the south	79
4.4 PSA with T=3.0 s, Cottonwood Grove fault, hypocenter to the south	80
4.5 PSA with T=5.0 s, Cottonwood Grove fault, hypocenter to the south	81
4.6 PHV, Cottonwood Grove fault, hypocenter to the north	82
4.7 Bracketed duration, Cottonwood Grove fault, hypocenter to the north	83
4.8 PSA with T=1.0 s, Cottonwood Grove fault, hypocenter to the north	84
4.9 PSA with T=3.0 s, Cottonwood Grove fault, hypocenter to the north	85
4.10 PSA with T=5.0 s, Cottonwood Grove fault, hypocenter to the north	86
4.11 PHV, Cottonwood Grove fault, hypocenter mid-fault	87
4.12 Bracketed duration, Cottonwood Grove fault, hypocenter mid-fault	88
4.13 PSA with T=1.0 s, Cottonwood Grove fault, hypocenter mid-fault	89
4.14 PSA with T=3.0 s, Cottonwood Grove fault, hypocenter mid-fault	90
4.15 PSA with T=5.0 s, Cottonwood Grove fault, hypocenter mid-fault	91
4.16 PHV, Reelfoot thrust, hypocenter to the south	92
4.17 Bracketed duration, Reelfoot thrust, hypocenter to the south	93

4.18	PSA with T=1.0 s, Reelfoot thrust, hypocenter to the south	94
4.19	PSA with T=3.0 s, Reelfoot thrust, hypocenter to the south	95
4.20	PSA with T=5.0 s, Reelfoot thrust, hypocenter to the south	96
4.21	PHV, Reelfoot thrust, hypocenter to the north	97
4.22	Bracketed duration, Reelfoot thrust, hypocenter to the north	98
4.23	PSA with T=1.0 s, Reelfoot thrust, hypocenter to the north	99
4.24	PSA with T=3.0 s, Reelfoot thrust, hypocenter to the north	100
4.25	PSA with T=5.0 s, Reelfoot thrust, hypocenter to the north	101
4.26	PHV, Reelfoot thrust, hypocenter mid-fault	102
4.27	Bracketed duration, Reelfoot thrust, hypocenter mid-fault	103
4.28	PSA with T=1.0 s, Reelfoot thrust, hypocenter mid-fault	104
4.29	PSA with T=3.0 s, Reelfoot thrust, hypocenter mid-fault	105
4.30	PSA with T=5.0 s, Reelfoot thrust, hypocenter mid-fault	106
4.31	PHV, North fault, hypocenter to the south	107
4.32	Bracketed duration, North fault, hypocenter to the south	108
4.33	PSA with T=1.0 s, North fault, hypocenter to the south	109
4.34	PSA with T=3.0 s, North fault, hypocenter to the south	110
4.35	PSA with T=5.0 s, North fault, hypocenter to the south	111
4.36	PHV, North fault, hypocenter to the north	112
4.37	Bracketed duration, North fault, hypocenter to the north	113
4.38	PSA with T=1.0 s, North fault, hypocenter to the north	114
4.39	PSA with T=3.0 s, North fault, hypocenter to the north	115
4.40	PSA with T=5.0 s, North fault, hypocenter to the north	116
4.41	PHV, North fault, hypocenter mid-fault	117
4.42	Bracketed duration, North fault, hypocenter mid-fault	118
4.43	PSA with T=1.0 s, North fault, hypocenter mid-fault	119
4.44	PSA with T=3.0 s, North fault, hypocenter mid-fault	120
4.45	PSA with T=5.0 s, North fault, hypocenter mid-fault	121
4.46	PGA from the May 12, 2008, $M_w = 7.9$ Sichuan, China earthquake.	122
4.47	Time series near Paducah, Ky.	123
4.48	Time series near Paducah, Ky.	124
4.49	3D/1D amplification map, Cottonwood Grove fault	125
4.50	3D/1D amplification map, Reelfoot thrust	126
4.51	3D/1D amplification map, New Madrid North fault	127
4.52	Study area for alternate scenarios	128
4.53	Depth of $V_s = 2000\text{m/s}$ layer	129
4.54	PHV, Cottonwood Grove fault, hypocenter to the south	130
4.55	Bracketed duration, Cottonwood Grove fault, hypocenter to the south	131
4.56	PHV, Cottonwood Grove fault, hypocenter to the north	132
4.57	Bracketed duration, Cottonwood Grove fault, hypocenter to the north	133
4.58	PHV, Cottonwood Grove fault, hypocenter mid-fault	134
4.59	Bracketed duration, Cottonwood Grove fault, hypocenter mid-fault	135
4.60	PHV, Reelfoot thrust, hypocenter to the south	136
4.61	Bracketed duration, Reelfoot thrust, hypocenter to the south	137
4.62	PHV, Reelfoot thrust, hypocenter to the north	138

4.63	Bracketed duration, Reelfoot thrust, hypocenter to the north	139
4.64	PHV, Reelfoot thrust, hypocenter mid-fault	140
4.65	Bracketed duration, Reelfoot thrust, hypocenter mid-fault	141
4.66	PHV, North fault, hypocenter to the south	142
4.67	Bracketed duration, North fault, hypocenter to the south	143
4.68	PHV, North fault, hypocenter to the north	144
4.69	Bracketed duration, North fault, hypocenter to the north	145
4.70	PHV, North fault, hypocenter mid-fault	146
4.71	Bracketed duration, North fault, hypocenter mid-fault	147

LIST OF TABLES

2.1	Major Geological Boundaries	22
3.1	Bardwell Simulation Parameters	53
4.1	Cottonwood Grove Simulation Parameters	71
4.2	Reelfoot Simulation Parameters	72
4.3	North Fault Simulation Parameters	73
4.4	Cottonwood Grove Simulation Parameters	74
4.5	Reelfoot Fault Simulation Parameters	75
4.6	North Fault Simulation Parameters	76

Chapter 1 Introduction

Seismic hazards affect human populations by causing death, injury, and property damage [Kramer \(1996\)](#). The toll of significant seismic events can be staggering in both human and economic terms. A recent example is the May 12, Sichuan, China, earthquake, which killed an estimated 70,000 people and injured 374,000, with another 18,000 missing and presumed dead ([USGS, 2008](#)). The economic cost of this event is estimated at 86 billion US dollars. Such events have occurred repeatedly throughout human history, and humans will continue to be exposed to such hazards as long as they live in seismically active regions. A large ($7.0 \leq M_w < 8.0$) earthquake occurs an average of once per month somewhere on the globe and an average of 11,500 people per year have been killed by earthquakes over the last hundred years ([Stein and Wyession, 2005](#)).

Although most earthquakes occur on active plate margins, large intraplate earthquakes also occur. The 26 January, Bhuj, India, earthquake killed over 20,000 people and devastated the cities of Bhuj and Anjar in the province of Gujarat ([Antolik and Dreger, 2003](#)). The epicenter of this $M_w = 7.6$ earthquake was located some 400 km from the nearest plate boundary in central Pakistan. The event occurred on a blind thrust fault within a failed rift where strain may be concentrated in a region with an otherwise low strain rate. The fact that the Bhuj event occurred in the nominally stable continental interior and seems to be associated with a failed rift invites comparison with the central United States, another intraplate area where large seismic events are known to have occurred.

During the winter of 1811-1812, a sequence of three large earthquakes struck the central United States. The largest of these events is thought to exceed the size of any Western continental earthquake ([Johnston and Schweig, 1996](#)). Although there are no instrumental recordings of these events, magnitude estimates based on observed intensities indicate that all three main shocks of the 1811-1812 earthquake sequence were between $M_w = 7.0$ and $M_w = 8.0$ ([Bakun and Hopper, 2004](#)). Paleoliquefaction studies indicate that large events have occurred previously in the region in the 10th century and the 15th century ([Tuttle et al., 2002](#)). These studies contain significant ranges of uncertainty, but suggest a mean recurrence rate of one large event every 500 years.

In addition to these large events, at least 23 damaging earthquakes with epicentral intensities in excess of modified Mercalli intensity VI have occurred in the central

Mississippi valley since the first historically recorded large event of 1811 (Nuttli, 1982). This makes the central Mississippi valley the most active seismic area in the central United States, most seismicity being associated with the Wabash Valley fault system or the New Madrid seismic zone (Nuttli, 1982).

The high rates of seismicity and relatively short recurrence interval of large events suggested by paleoliquefaction data indicate a substantial seismic hazard in the central United States. In the winter of 1811-1812, risk was low, purely as a function of the sparsity of the population and lack of significant infrastructure. Although some towns such as the riverboat town of New Madrid, Mo. were devastated, overall casualties were light (Johnston and Schweig, 1996). If an earthquake of the scale of the 1811-1812 event were to occur today however, large loss of life and catastrophic damage to infrastructure could be expected. In order to mitigate the risk associated with the seismic hazard in the eastern United States, estimates of the level of ground shaking are required in order to inform public policy and decision making (Cramer, 2001). Such parameters are difficult to predict, however, because of the lack of instrumental recordings of large ($M_w \geq 7.0$) events in the region. Because of this lack of ground-motion data in the central United States, we are left with simulation as the most effective way of quantifying the seismic hazard posed by large earthquakes in the region. Numerical methods and high-speed digital computers make it possible to analyze the response of the regional geology to a large earthquake in the central Mississippi valley in order to evaluate the consequent strong motion and the potential impact on humans and infrastructure.

1.1 Seismotectonic Setting

A plot of modern microseismicity in the eastern United States delineates the active faults in the New Madrid seismic zone (Fig. 1.1). Each of the three arms was likely the source of one of the main shocks of the 1811-1812 earthquake sequence (Johnston and Schweig, 1996). Such earthquake triples on intersecting fault segments are a distinct feature of large intraplate events and differentiate them from large events at plate margins that typically occur on simple, well-developed, through-going faults (Johnston and Schweig, 1996). The faults of the New Madrid seismic zone appear to be associated with the Reelfoot rift, a failed rift that was active in late Proterozoic through early Cambrian times (Johnston and Schweig, 1996). Rifting was initiated in the Precambrian, when the area underwent epeirogenic uplift associated with the emplacement of anomalous mantle material at the crustal base (Ervin and McGinnis,

1975). This uplift, which may have been on the order of several kilometers, produced an axial rift or graben, the faults of which have remained active into modern times (Ervin and McGinnis, 1975). The rift is deeply buried and difficult to study, but aeromagnetic investigations indicate that it is 70 km wide by 200 km long. Information about rift geometry and seismogenic zones may also be inferred by analogy to exposed rifts such as the east African rift. Studies of exposed rifts indicate that the axial zone of a rift is the most unstable part in the long term, and this fits observation of the New Madrid seismic zone, where much of the current seismicity is coincident with the inferred axis of the rift (McKeown and Pakiser, 1982).

Seismogenic Faults

The seismogenic faults associated with the Reelfoot rift can be divided into three major segments, or arms (Fig. 1.1). The Blythville fault zone is the southern, northeast-striking segment and is most likely the source of the December main shock of the 1811-1812 triple (Johnston and Schweig, 1996). It is likely that the Blythville fault zone is an extension of the Cottonwood Grove fault, and hereafter the southern axial fault zone is referred to as the Cottonwood Grove fault. The fault dips steeply and the sense of faulting is right-lateral, strike-slip (Shumway, 2008). Modern microseismicity on this fault is concentrated at depths between 4 and 14 km (Chiu et al., 1992).

The Reelfoot fault is the northwest-striking central segment that was most likely responsible for the February shock of the 1811-1812 triple (Johnston and Schweig, 1996). The fault was the subject of an investigation by Chiu et al. (1992) using a portable seismic network to image the fault via microseismicity. The study located more than 700 events in the New Madrid seismic zone, with magnitudes up to m_{bLg} 4.6. The precise hypocentral locations from this data set were used to delineate the active faults in the New Madrid seismic zone, with particular attention paid to the central region, and provide good control on the geometry of the Reelfoot fault (Chiu et al., 1992). The Reelfoot fault is a northwest-striking thrust fault that dips to the southwest. The dip of the fault changes along strike, with an average dip of 31° north of the intersection with the axial Cottonwood Grove fault, and an average dip of 48° for the southern segment of the fault. The majority of hypocenters are located at depths between 4 and 15 km. This is the only seismogenic fault in the New Madrid seismic zone that has a surface expression in the form of the Reelfoot scarp (Johnston and Schweig, 1996). The source zone most likely responsible for

the January main shock is the New Madrid North fault, a northeast-striking fault (Johnston and Schweig, 1996). The January main shock is the least well understood of the three main shocks because of the lack of modified Mercalli intensity data for this event (Shumway, 2008). This, and the fact that the background seismicity is less clearly defined for the North fault (see Fig. 1.1), has led to debate about the location of the fault. Trends of seismicity have been identified running from just east of New Madrid, Mo. to just west of Paducah, Ky. as well as possibly extending south of Charleston, Mo. to Bardwell, Ky. (Shumway, 2008). The present study places the New Madrid North fault on the more northerly alignment of seismicity, as this is suggested by Johnston and Schweig (1996) as the most likely location of the January main shock. The sense of faulting is right-lateral, strike-slip (Shumway, 2008). The modern-day microseismicity associated with this fault is concentrated at depths between 4 and 14 km, the fault plane appearing to dip at approximately 90° (Chiu et al., 1992).

Strain Rates

Although the faults associated with the Reelfoot rift constitute zones of weakness on which slip may occur, it is difficult to account for sufficient strain in the stable craton that would cause events of the magnitude of the 1811-1812 sequence. For example, the San Andreas fault in the western United States has strain rates of 1 to 3 cm per year, whereas some of the less conservative estimates of deformation on faults in the central United States give strain rates on the order of 1 to 2 mm per year (McKeown and Pakiser, 1982). High-accuracy GPS studies have shown some near-field motions to be as high as 2.7 ± 1.6 mm/year, but these rates do not apply on a regional scale (Smalley Jr et al., 2005). In order for large earthquakes to occur in such an environment, there must be some mechanism by which stress is concentrated on the faults of the New Madrid seismic zone. Pleistocene glacial unloading has been suggested as a mechanism to explain the geologically sudden onset of seismicity, indicated by small fault offsets in reflection studies, in the Holocene (Grollimund and Zoback, 2001). Numerical modeling indicates that lithospheric bending in response to glacial unloading is likely to result in failure and seismicity. Another proposed mechanism for stress concentration is the pull of a sinking rift pillow, the anomalous mantle material emplaced during the formation of the Reelfoot rift, inducing stress in the upper crust (Pollitz et al., 2001). In this model, crustal weakening as a result of Pleistocene deglaciation removes support for the dense rift pillow, which then sinks, exerting a pull and subsequent stress on the upper crust.

The Mississippi Embayment

Complicating the seismic hazard in the region is the presence of the Mississippi embayment, a southwest-plunging synclinal trough filled with thick sequences of unconsolidated to poorly-consolidated sediments known to amplify seismic waves (Street et al., 2001). It formed as a result of subsidence beginning in the late Cretaceous and continuing into the Holocene (McKeown and Pakiser, 1982). During the late Cretaceous, the Mississippi valley tectonically “drifted” over the Bermuda hotspot, forming a north-trending thermally induced arch (Van Arsdale and TenBrink, 2000). After erosion of over 2 km of Paleozoic material, the area moved away from the hotspot, causing cooling and subsidence and the formation of the Mississippi embayment trough. Subsidence has continued through the Holocene, and may still have been occurring as recently as 6,000 BP (McKeown and Pakiser, 1982). The thick sequences of alluvium that fill the Mississippi embayment were deposited during Pleistocene and Holocene times. These sequences of unconsolidated sediment, that are as much as 1,000 m thick in the Mississippi embayment, can affect strong ground motion by amplifying waves as they propagate toward the surface (Street et al., 1995) (Wang, 1998) (Kawase and Aki, 1989).

1.2 Project Objective

The broad objective of this project is to estimate the intensity of shaking that structures at the surface of the Mississippi embayment are likely to undergo in the event of a large ($M_w \geq 7.0$) earthquake in the New Madrid seismic zone by simulating long-period ground motions. Specifically, this project attempts to answer the following questions:

- What is the maximum velocity and duration of shaking likely to occur in the Mississippi embayment in response to a large New Madrid seismic zone earthquake?
- What is the influence of the 3D geologic structure of the Mississippi embayment on ground motions?
- What affect does finite-fault mechanics have on ground motions?

In order to answer these questions, the simulations use the criteria discussed below.

Simulations in 3D

Simulations must be conducted in three dimensions in order to realistically capture the complexity of the wave field and its interaction with geologic structures. This is particularly important to capture basin effects, the effect of the 3D geometry of sedimentary basins on wave propagation and subsequent ground motion. Long-period surface waves generated by the interaction of body waves with basin edges can significantly affect ground motions at sites in a sedimentary basin (Street et al., 2004). Waves that have been “trapped” or focused by the curvature of the basin may cause longer durations and more intense shaking than what would be predicted by a site-specific, one-dimensional ground-motion analysis (Kramer, 1996). The worst damage belt associated with the 1995 Kobe, Japan, earthquake, which killed over 6,500 people and destroyed 170,000 buildings, was most likely a result of Rayleigh waves diffracted by interaction with the basin edge (Kawase, 1996). The 3D geometry of both the Precambrian unconformity and the Paleozoic unconformity has the potential to induce basin effects.

Another way that the 3D geologic structure is likely to affect ground motion is through resonance. Resonance can induce amplification and lengthen the duration of shaking in sedimentary basins when surface waves generated at basin edges propagate back and forth within soft basin sediments (Bard and Bouchon, 1985). Resonance is usually most pronounced near basin centers and tapers to zero at basin edges. The 3D basin geometry should be modeled realistically in order to capture this phenomenon.

A Substantial Volume of Simulation

The simulations should be conducted on as large a volume as is computationally feasible. This is important so that New Madrid source zones and critical geologic structures such as embayment boundaries can be fit into the same domain of computation. Of course, the larger the surface area on which simulations are conducted, the more regional information is gained from the simulation.

It is also important that the volume be significantly deep in order to capture all of the major impedance boundaries in the region. Impedance boundaries can be important controls on ground motion, as they will change the frequency content of propagating waves in two ways. If the waves are crossing a boundary into low-velocity material, long-period motions will be amplified and short-period motions will be de-amplified (Kramer, 1996). Higher frequencies will tend to be amplified at sites with higher-velocity materials. In order to capture all of the major impedance boundaries

likely to influence ground motion, the volume of computation extends vertically from the surface to a depth of 50 km. This depth includes the Mohorovic discontinuity, so that the volume extends into the upper mantle.

The areas chosen for simulation are shown by the squares in Figure 1.1. The larger area is 200 km² and the smaller is 100 km². These areas were chosen because they cover a significant portion of the upper embayment, include the major fault zones of the New Madrid seismic zone, and incorporate parts of the embayment boundary. Conducting simulations on such large volumes restricts the frequency content that may be calculated, however. For the larger volume, synthetic time series may be calculated up to a frequency of 0.5 Hz. Frequencies of up to 1.0 Hz are calculated for the smaller region. This restriction is imposed by the numerical scheme used for the simulations, which requires a denser grid to model higher frequencies. If simulations are to be conducted on a large volume, the grid must be kept sufficiently coarse to allow computation. The long-period nature of the synthetics that are calculated for this study are a regular feature of large-scale ground-motion simulations, however (Saikia et al., 2006)(Olsen, 2000). The numerical restrictions on frequency content and shear wave velocity are discussed more fully in chapter 2.

Finite Sources

Large earthquake sources are inherently finite. For example, the 2008 Sichuan earthquake was the result of a rupture length in excess of 200 km (Xiaojun et al., 2008). It is unrealistic to model such a rupture as a point source, and such a representation is likely to miss important finite-fault controls on ground motion such as directivity effects and the spatial distribution of slip. Also, clearly there is much more area that is near-fault than can be captured by a point-source simulation.

1.3 Modeling Procedure

In order to achieve the project objectives stated in section 1.2, the modeling procedure displayed in Figure 1.3 was implemented. This procedure consists of the construction of two mathematical models of natural phenomena for input into a numerical wave propagation code. The first is a velocity model for the volume on which simulations are to be conducted. This velocity model should contain all elastic parameters necessary for the calculation of the wave field, as well as a realistic representation of the geometry of impedance boundaries. The construction of a velocity model for the upper Mississippi embayment is the subject of chapter 2.

The second set of inputs is source-time functions. These are numerical representations of plausible New Madrid seismic zone earthquakes. They consist of all source parameters needed for the simulation, including fault geometry, seismic moment, rise time, and rupture time. The construction of these functions is discussed in section 3.4.

These two sets of data are the input for the wave propagation code. This code simulates the wave field in 3D by solving wave equations at discrete time steps on a high-speed computer. The specifics of the code and the numerical technique may be found in section 3.1. The code writes output in the form of three-component seismograms at hypothetical receivers that may be placed anywhere within the domain of computation. The model is validated by simulating historical events and comparing synthetic data to recorded data. If the comparison is satisfactory, then output can be processed into meaningful ground-motion parameters. Processing techniques are described in section 3.3. This processed output is interpreted, and conclusions about the seismic hazard in the upper Mississippi embayment are drawn. Processed output is shown and conclusions are discussed in chapter 4.

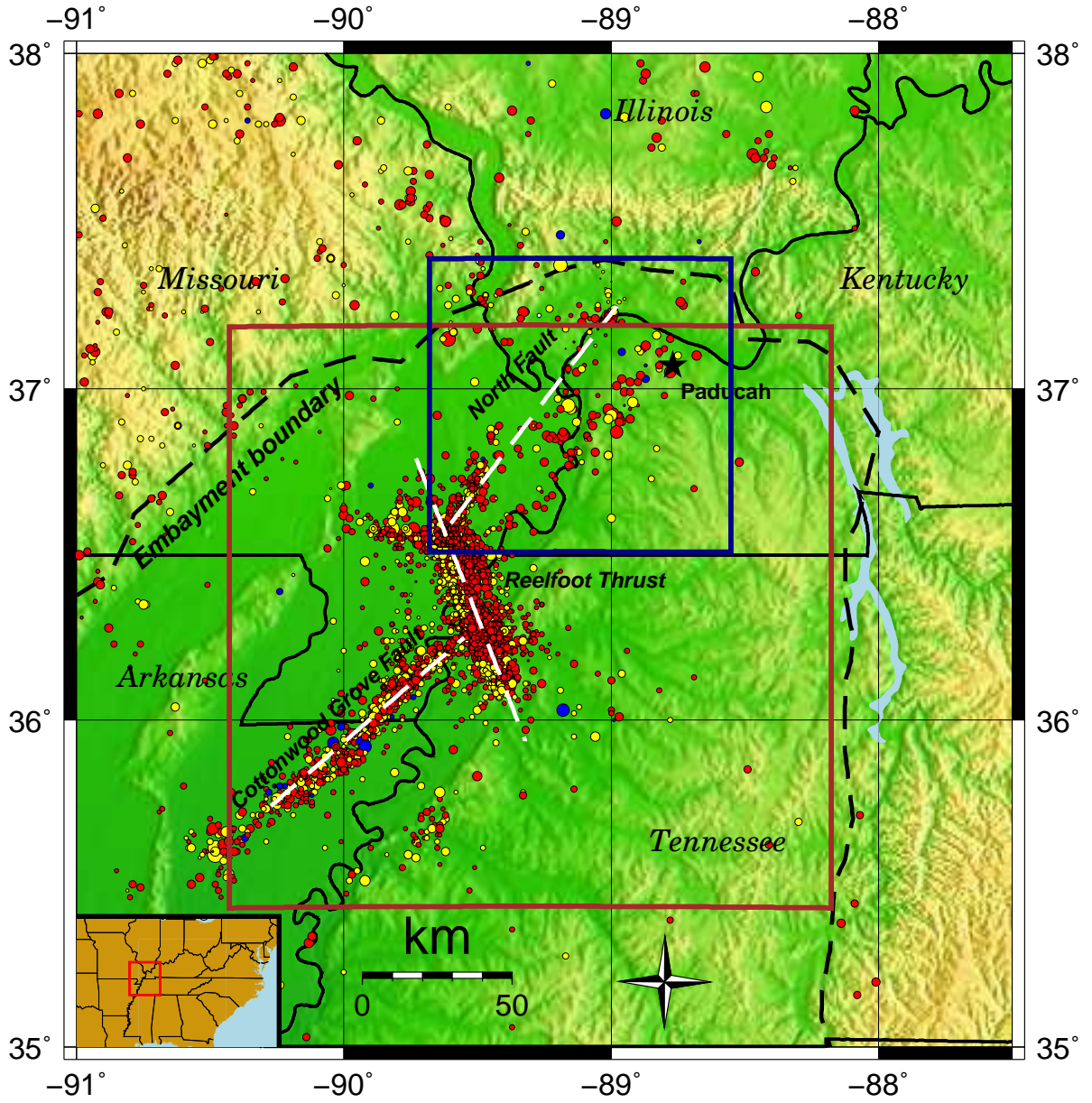


Figure 1.1: Study area showing fault traces and background seismicity since 1974. Red, yellow, and blue data points represent focal mechanisms of increasing depth.

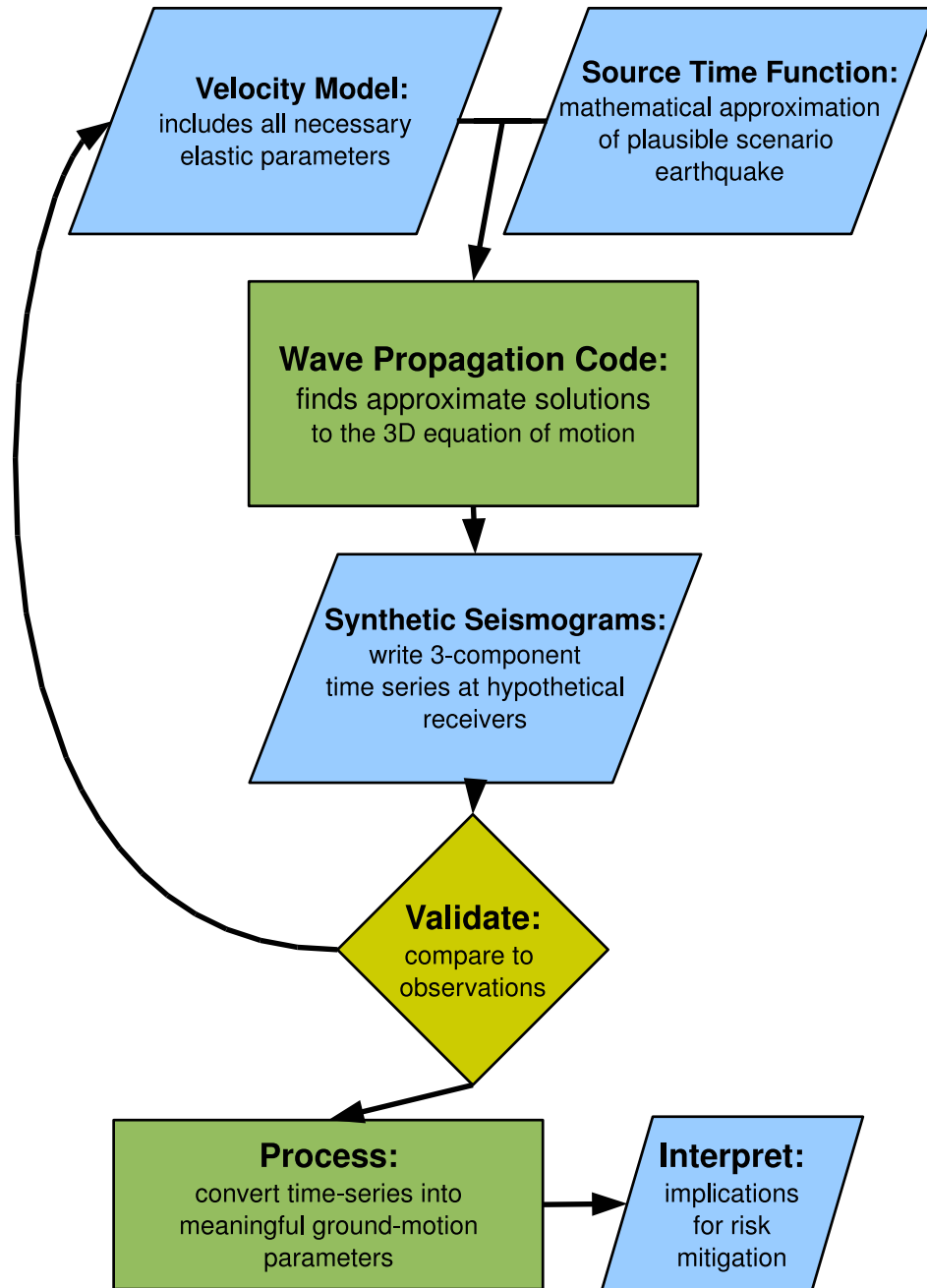


Figure 1.2: Flow chart showing the overall modeling process.

Chapter 2 A Velocity Model for the Upper Mississippi Embayment

A critical step in conducting a regional-scale ground-motion simulation is the construction of a basin wide velocity model. Without a good velocity model, even the best numerical basin response simulations will not work well (Kagawa et al., 2004). Therefore, a combination of theoretical relations and available data has been used in order to develop a physical model within the constraints of the given time and data.

The region between longitude 90.35°W to 88.18°W and latitude 37.23°N to 35.39°N is a roughly $200 \times 200 \times 50 \text{ km}^3$ volume. Although the construction of a detailed and highly accurate velocity model for such a large volume is impractical at this time, several data sources are here used to construct an idealized first-order velocity model. Though general in nature, this model is sufficient for the calculation of long-period wave propagation and the examination of the effect of basin geometry on low-frequency ground motion. Descriptions of the basin features considered and the data used to model them are given below.

2.1 Major Geological Boundaries

The major geological boundaries in the northern Mississippi embayment are important features of the velocity model because they represent impedance boundaries across which the amplitudes of propagating waves will vary (Shearer, 1999). Also, because these boundaries are between geologic formations with similar elastic parameters, they delineate a series of layers that may be used to form the basis of the velocity model. The layers that are considered in the velocity model and the geological boundaries separating them are listed in Table 2.1.

Data sets compiled by Csontos (2007) provide good constraint on the elevation of the boundaries listed in Table 2.1. These data were used by Csontos (2007) to produce detailed 3D structure-contour maps of the major geological boundaries in the Reelfoot rift region. Similar maps were developed in this study for the region of interest using slightly different techniques to interpolate the surfaces. These maps form the basis of the velocity model, as any point in the volume of interest may be assigned elastic parameters based on the layer in which it resides. Data are maintained and manipulated in GRASS 6.2, a freely available, open-source geographic information system (GIS). Detailed descriptions of each layer defined in the embayment velocity model follow below. A cross section along the axis of the embayment showing the

major impedance boundaries and geological layers used in the velocity model is shown in Figure 2.1.

V_s^{30} Data

Poorly consolidated, low-velocity near-surface sediments are expected to affect amplitude and frequency content of ground motions at sites in the upper Mississippi embayment (Street et al., 1997). In particular, V_s^{30} , the average shear wave velocity of the upper 30 m of sediment, is used as a standard indicator of seismic site conditions (Street et al., 2001)(Wald and Allen, 2007). The University of Kentucky maintains a database of some 519 V_s^{30} measurements that have been collected since the early 1990s (Vance, 2006). These data were imported into GRASS 6.2 and interpolated with the `v.surf.rst` command, which uses a regularized spline with tension, in order to produce a V_s^{30} map of the region (see Fig. 2.2). Note that some of the velocity values are less than 200 m/s.

Although it would be desirable to include these data in the velocity model, computational limitations preclude using such low shear-wave velocities for 3D wave-propagation simulations. Consider the spatial sampling criteria of the fourth-order finite-difference scheme given by

$$h < \frac{V_{s \min}}{5.6 \cdot \text{freq}_{\max}} \quad (2.1)$$

where h is the spatial grid spacing, $V_{s \min}$ is the minimum shear-wave velocity modeled, and freq_{\max} is the maximum frequency modeled (Moczo et al., 2004). If $V_{s \min} = 200$ m/s, then equation (2.1) yields $h \approx 36$ m maximum grid spacing for simulations up to 1.0 Hz. For the $100 \times 100 \times 50$ km³ volume for which 1.0 Hz synthetics are calculated, and using three times coarser spacing for the region deeper than 10,000 m, this would mean 2.460879947×10^9 grid points. The digital arrays that result from such a vast finite-difference grid will not compile even using a four-processor node on the University of Kentucky’s high -performance network. Although this problem could be overcome by using the network to its full potential via the message passing interface, there are further problems, as wave propagation may become nonlinear at shear-wave velocities less than 500 m/s (Liu, personal communication). For these computational reasons, the minimum shear-wave velocity of the embayment sediments was set to 600 m/s. A similar strategy was employed by Saikia et al. (2006) in their 3D simulation studies in the embayment.

Post-Paleozoic Layer

The Paleozoic unconformity forms a southwest-plunging trough in the study area that is filled with up to a 1,000 m of late Cretaceous and Cenozoic sediments (Van Arsdale and TenBrink, 2000). The unconformity constitutes a major impedance boundary, in which poorly consolidated low-velocity sediments lie directly atop the Paleozoic carbonate rock. It is not uncommon for shear-wave velocities to differ by a factor 6 between the post-Paleozoic sediments and the underlying bedrock (Street et al., 1997) (Street et al., 2001). These sharp velocity contrasts have been shown by one-dimensional simulation studies to induce amplification, particularly near basin edges. In addition, the curved, parabolic shape of the unconformity surface has the potential to act as a wave guide, trapping body waves in the alluvium and increasing ground-motion amplitudes and durations in response to earthquakes in the New Madrid seismic zone (Kramer, 1996).

Csontos (2007) compiled Paleozoic unconformity elevation data from published refraction and reflection seismic lines and petroleum exploration wells. This data set is composed of over 3,000 points, providing excellent control on the elevation of the surface. For this study, the data were imported into GRASS GIS, where they were converted from elevation to depth by using a digital elevation model of the region from the global 30 arc-second topographic data. A structure contour map of the surface was then derived by using GRASS's `v.surf.rst` command to interpolate the depth using a regularized spline with tension. The resulting map and the data points used for the interpolation are shown in Figure 2.3

The surface of the Paleozoic unconformity and the free surface together form the boundary of the post-Paleozoic layer of the velocity model. The material in this layer must be assigned velocities and other elastic parameters in order to make it useful for input into the numerical model. Because of the geological complexity of the upper Mississippi embayment and the relatively large region under consideration, there is likely to be significant lateral heterogeneity within each layer defined in the current velocity model. Although the model may be updated as additional data sets become available, for the present study, each layer is assumed to be laterally homogeneous and isotropic. This simplifying assumption is reasonable because the goal of the study is the quantification of long-period ground motion, which is primarily controlled by basin geometry, impedance boundaries, and finite-fault mechanics. Thus, elastic parameters will vary vertically but not laterally within each layer. Also, velocity inversions are avoided for numerical reasons.

Data from the University of Kentucky’s shear-wave database were used as a basis for assigning shear-wave velocities to material in the post-Paleozoic layer. Seismic surveys have been conducted by University of Kentucky researchers at 66 sites throughout the Jackson Purchase region of western Kentucky (see Fig. 2.4) (Vance, 2006). At each of these sites, data were recorded for depth to boundaries and average layer velocities. In order to generalize these data into a working model, the average layer shear-wave velocity at each site was related to the median depth of the layer. This resulted in 231 velocity-depth pairs that were imported into the open-source statistics package R for analysis. An expression for shear-wave velocity as a function of depth for the post-Paleozoic layer was extracted from these data via a nonlinear least-squares fit using R’s `nls()` command. The `nls()` command does not provide an r^2 as a measure of data fit, so one was calculated manually using

$$r^2 = \frac{RSS}{TSS} \quad (2.2)$$

where RSS is the residual sum of squares and TSS is the mean adjusted total sum of squares. For this model, equation 2.2 yields $r^2 \approx .75$. A plot of the data and regression line are shown in Figure 2.5. The expression for V_s as a function of depth for the post-Paleozoic sediments in the study area is given by

$$V_s(z) = 151.1844 \cdot z^{-.3188} \quad (2.3)$$

where z is depth in meters (positive down) and when $V_s(z) \geq 600$ m/s. For the numerical reasons discussed above, V_s is set to 600 m/s when equation 2.3 is < 600 m/s.

To be useful for numerical simulations, the velocity model must contain additional elastic parameters. The finite-difference model used in this study requires P -wave and S -wave velocities (V_p and V_s , respectively), densities (ρ), and quality factors for both P -wave (Q_p) and S -wave (Q_s). Once an initial parameter has been assigned, such as V_s for the post-Paleozoic layer, expressions are needed to assign the remaining parameters. Brocher (2005) used data from borehole logs, seismic profiles, hand sample measurements, and tomographic studies to develop empirical relationships between V_p , V_s , and ρ . These expressions are given by

$$V_p(V_s) = 0.9409 + 2.0947V_s - 0.8206V_s^2 + 0.2683V_s^3 - 0.0251V_s^4 \quad (2.4)$$

$$\rho(V_p) = 1.6612V_p - 0.4721V_p^2 + 0.0671V_p^3 - 0.0043V_p^4 + 0.000106V_p^5 \quad (2.5)$$

where V_p and V_s are in km/s and ρ is in g/cm³ (Brocher, 2005). For the post-Paleozoic sediments, once V_s is found via equation 2.3, then V_p and ρ are calculated from equation 2.4 and equation 2.5, respectively.

Wang et al. (1994) developed an expression for Q_s in poorly consolidated upper Mississippi embayment sediments. Assuming homogeneous layers with constant V_s and Q_s , they used a pulse-broadening technique to analyse 20 *SH*-wave refraction profiles. This analysis yielded the following equation applicable to the study area:

$$Q_s(V_s) = 0.08V_s + 6.99 \quad (2.6)$$

Q_p is then modeled simply as

$$Q_p(Q_s) = 1.5Q_s \quad (2.7)$$

which is a common strategy when a more specific relationship is unavailable (Olsen, 2000).

Note that all elastic parameters are essentially monotonically increasing functions of depth. For any point determined to reside in the post-Paleozoic layer, V_s is assigned via equation 2.3, which depends on depth, and the remaining elastic parameters are functions of velocity.

Upper Crust

The upper crustal layer of the velocity model is bounded above by the Paleozoic unconformity and below by the Precambrian unconformity. Good control on the elevation of the Precambrian surface is provided by the Csontos (2007) data set, which contains over 3,000 points obtained from well logs and seismic reflection data. A structure-contour map was again developed by interpolation using `v.surf.rst` after converting elevation to depth. The data points contained in the study area, as well as the structure-contour map, are shown in Figure 2.6. Note the surface topography that is suspected to induce wave-guide effects, in particular if the velocity model is employed for higher-frequency studies in the future (Saikia et al., 2006). The upper Intrarift basin described by Dart and Swolfs (1998) is a prominent feature in the study area, as well as an additional intrarift basin near Paducah, Ky.

Between the surfaces of the Paleozoic unconformity and Precambrian unconformity lie the Devonian and Mississippian dolomites, cherty limestones, shales, and siltstones of what is referred to here as the upper crustal layer (McBride et al., 2003). The *P*-wave velocity of such “stiff” sedimentary rock may be modeled via the Faust

(1951) equation, which relates V_p to depth and age of the deposit. Faust (1951) derived this empirical relation by sorting averaged shale and sandstone velocities from 500 well surveys by depth and age. He found that V_p increases with depth, and that the rate of increase increases with age. The equation describing this situation is given by

$$V_p = k(da)^{\frac{1}{6}} \quad (2.8)$$

where a is age in years, d is depth in meters, and k is a constant (Faust, 1951). This equation was found to not model carbonates as effectively as it models sandstones and shales, but is used to model V_p in the Paleozoic rock of the upper crustal layer because of the paucity of observed data for these deposits. Equation 2.8 has been used extensively to construct velocity models for use in ground-motion simulations (Magistrale et al., 2000) (Magistrale et al., 1996). It forms the basis of the southern California reference three-dimensional velocity model that has been used for ground-motion simulation studies (Olsen, 2000). For the southern California model, the Faust equation (equation 2.8) was calibrated for the region by comparing it to available velocity data from oil well sonic logs and seismic surveys (Magistrale et al., 2000). In order to calibrate k to the upper Mississippi embayment region, the Faust equation was compared to known Paleozoic depth and velocities at two sites: one in the northeastern part of the study area at strong-motion station VSAP, and one in the southwestern part in Arkansas. The top of the Paleozoic bedrock at site VSAP is at approximately 100 m depth where the shear-wave velocity was determined by split-spoon samples and cross-hole measurements to be 2592 m/s (Street et al., 1997). This value was used to estimate V_p via equation 2.4 and then compared to the Faust equation with $d = 100$ m:

$$43,950 = k(100 \cdot a)^{\frac{1}{6}} \quad (2.9)$$

Because the Paleozoic layer is considered to be homogeneous, with no internal stratigraphic horizons, a constant Devonian/Mississippian age of 350 million years was used. Using this age in equation 2.9, we find that $k \approx 76.84$. In order to check this value in a different part of the embayment, a similar comparison of the Faust equation was made to data recorded at a site in eastern Arkansas in an SH -wave seismic survey. This site is near the Embayment boundary, and has a bedrock depth of 23 m and $V_s = 1,743$ m/s $\Rightarrow V_p = 32,880$ m/s (Street et al., 2001). Inserting these values into the Faust equation yielded $k \approx 73.45$, a similar value to the one derived

at VSAP. Using the average of these two k values, we have the the following version of the Faust equation for the upper crustal layer of the upper Mississippi embayment:

$$V_p(z) = 56.68(3.5 \times 10^8 z)^{\frac{1}{6}} \quad (2.10)$$

where z is the depth in meters.

Once V_p was assigned via equation 2.8, V_s was calculated via Brocher's regression fit, an empirical relation given by

$$V_s(V_p) = 0.7858 - 1.2344V_p + 0.7949V_p^2 - 0.1238V_p^3 + 0.0064V_p^4 \quad (2.11)$$

where the velocities are in kilometers per second (Brocher, 2005). Density was calculated via equation 2.5. The attenuation relationships used for the post-Paleozoic layer are not applicable to deeper layers. Because of a lack of specific expressions for Q in deep embayment sediments, the following relationship, which describes Q_s as a function of V_s for California, was used:

$$Q_s = \begin{cases} 0.06V_s, & \text{when } V_s \leq 1000 \\ 0.14V_s, & \text{when } 100 < V_s < 2000 \\ 0.06V_s, & \text{when } V_s \geq 2000 \end{cases} \quad (2.12)$$

given by Liu and Archuleta (2006). Q_p was found via equation 2.7.

Middle Crust

The crystalline basement of the middle crustal layer is bounded above by the Precambrian unconformity and below by the anomalous mantle material of the fossil rift pillow. A contour map of the top of the rift pillow was generated by Hildenbrand (1985) via the inversion of magnetic and gravity data. Csontos (2007) digitized the contours in order to develop a raster map of the surface. His digitized data were imported into GRASS and interpolated using `v.surf.rst`. The resulting structure contour map is shown in Figure 2.7.

Samples from deep drill holes indicate that the middle crustal layer is composed primarily of Precambrian granite, porphyritic granite, and dioritic gneiss (Dart and Swolfs, 1998). The Faust equation is not applicable to crystalline rock, so the HAMBURG velocity model was used as the basis for assigning V_p in the middle crust. This model was derived by Herrmann and Ammon (1997) by using a wave form modeling technique. The HAMBURG values between a depth of 5 and 35.5 km were selected

as falling within the range of the middle crustal layer. These data were imported into R where `nls()` yielded the following equation for V_p :

$$V_p(z) = 4176.0 \cdot z^{.04504} \quad (2.13)$$

where z is the depth in meters. The data points and equation 2.13 are plotted in Figure 2.8. Once V_p was assigned to a point in the middle crustal layer, then the other four elastic parameters were assigned using equations 2.5, 2.11, and 2.12.

Anomalous Crustal Layer

A fossil rift pillow, an intrusion composed of dense mafic rock, forms the anomalous crustal layer above the Mohorovicic discontinuity (Csontos, 2007). This layer reaches its thickest extent near the center of the study area where Paleozoic rifting has induced the most crustal thinning along the axis of the Reelfoot rift (Hildenbrand, 1985).

Csontos (2007) digitized the contours representing the thickness of anomalous crust published by Hildenbrand (1985). These data were imported into GRASS GIS, where the depth to the Moho was calculated by adding the thickness of the anomalous crust to the surface generated for the top of the rift pillow. The data were then contoured using `v.surf.rst` in order to produce a structure contour map of the Moho. The data points and map are shown in Figure 2.9. This surface and the top of the rift pillow form the bottom and top, respectively, of the anomalous crustal layer.

The HAMBURG earth model was used as the basis for assigning elastic parameters. Only five values of the HAMBURG data have depths corresponding to the anomalous crustal layers. Using `nls()` yields the following equation for V_p :

$$V_p(z) = 61.0036 \cdot z^{.4514} \quad (2.14)$$

where z is the depth in meters. The data points and regression equation are shown in Figure 2.10. Because of the large amount of relief in the surface representing the top of the anomalous crust, however, this expression tends to become too “slow” for shallower regions. Therefore the lower bound of V_p for this layer was set at 7,000 km per second. This results in a reasonably high velocity for such a dense layer and still incorporates a velocity gradient for deeper regions. This is important because a crust-mantle velocity gradient has been found to be necessary to improve fit in waveform modeling studies (Herrmann and Ammon, 1997). As before, once V_p has been assigned via equation 2.14, then the other four elastic parameters were assigned using equations 2.5, 2.11, and 2.12.

Mantle

The velocity model was constructed to a depth of 50 km, a depth that takes it well into the mantle. Although [Saikia et al. \(2006\)](#) found that the inclusion of the Moho discontinuity had a minimal impact on 2D simulations, this major impedance boundary was included in order to investigate its affect on 3D wave propagation. The upper Mantle is modeled as a constant velocity layer, with the average layer velocity of $V_p = 8,250$ m/s presented by [Catchings \(1999\)](#) used as a starting point. The other elastic parameters were assigned as usual using equations [2.5](#), [2.11](#), and [2.12](#).

2.2 Method of Velocity Model Construction

The challenging aspect of constructing the velocity model was the need to write text files for the $200 \times 200 \times 50$ km³ volume, using the criteria discussed in the sections above, in a format suitable for input into the finite-difference wave propagation code. The code reads velocity files in ASCII format through a nested loop of the form:

```
for 1 to 50/DZ
  for 1 to 100/DY
    for 1 to 100/DX
      read data
    end
  end
end
```

where DX, DY, and DZ are the grid spacing in kilometers in the longitudinal, latitudinal, and vertical directions, respectively. In order to preserve much of the topographic structure of the major geological boundaries, the velocity model should have at most half a kilometer horizontal resolution. This is particularly important for the shallower, lower-velocity layers, where the geometry of the Paleozoic and Precambrian unconformities are expected to affect wave propagation. Since these resolutions require millions of grid points, automation is required for the writing of velocity files.

Automation was achieved by means of an Octave script (see the Appendix for source code). Octave is a free, open-source numerical package that is very similar to the commercial software MATLABTM. It was chosen for this application because of its ability to smoothly interact with the GRASS GIS. As discussed above, the data defining the major geological boundaries in the model are maintained in GRASS. The data were projected using the universal transverse Mercator (UTM) coordinate

system, Zone 16 North. This coordinate system was chosen so that the meters of the eastings and northings would correspond to the meters of the x and y , respectively, of the finite-difference model's Cartesian coordinate system. This assumes, incorrectly, that the UTM system is Euclidean, but the error over the course of 200 km is minimal. The structure-contour maps developed from interpolation were stored in a raster format and may be exported as a `*.mat` file that is readable by Octave/MATLABTM using the command `r.out.mat`. The resolution of the raster, set with `g.region` and infinitely variable, determined the resolution of the velocity model.

When the m-file containing the Octave script was run, it loaded the `*.mat` files representing the surface of each of the major geological boundaries. The script determined the resolution and extent of the volume from data contained in these files. It then looped over the three dimensions of the volume and at each point determined in which layer the point resided. Elastic parameters were assigned to the point as discussed above. Finally, the data were printed to an ASCII file suitable for input into the finite-difference code. In order to minimize the size of these files, the Octave script divides the volume into two regions that may have different resolutions. This allows higher-velocity deep layers to be modeled at a lower resolution.

Velocity profiles constructed from the velocity model are shown in Figures 2.11 and 2.12. The first is through the center of the 0.5-Hz region and the second is from the center of the 1.0-Hz region. Note that the impedance boundaries imposed by the major geological boundaries are clearly visible.

2.3 Validation

The equations used in the construction of the velocity model are empirical, and some of them, such as Brocher's regression equation (equation 2.11), were derived from data at continental margins. Although some of these expressions may not be ideal for use in the continental interior, the model described above was expected to provide an approximation of conditions in the upper Mississippi embayment sufficient to investigate the effects of basin geometry and impedance boundaries on ground motion. The timing of first arrivals was not expected to be correct in the simulations because of the hypothetical nature of the velocity model, but what was crucial to this study was the impact of 3D structures and finite-fault mechanics on ground motions. The detailed representation of the major impedance boundaries in the velocity model should render the model adequate for these investigations.

In order to gain some confidence in the accuracy of the velocity model, the model was compared to the crustal model developed by [Catchings \(1999\)](#). Catchings compiled a 2D velocity profile between Memphis, Tn. and St. Louis, Mo. using seismic-refraction and gravity data. A part of this profile is across the Reelfoot rift and the average layer velocities for this section are plotted along with a vertical profile of the center of the velocity model developed in this study in [Figure 2.13](#). There is generally good agreement between the two models even though [equation 2.11](#) appears to overestimate V_s . This is particularly evident in the mantle and this may be a result of the equation being more applicable to continental margins.

Table 2.1: Major geological boundaries and layers used in the velocity model. Layers are listed in order of increasing depth

Boundary	Layer	Type of Material
Paleozoic unconformity	post-Paleozoic	poorly consolidated sediments
Precambrian unconformity	upper crust	Paleozoic carbonates and shales
rift pillow	middle crust	crystalline basement
Mohorovicic discontinuity	anomalous crust	emplaced mantle material
	mantle	high-velocity mantle material

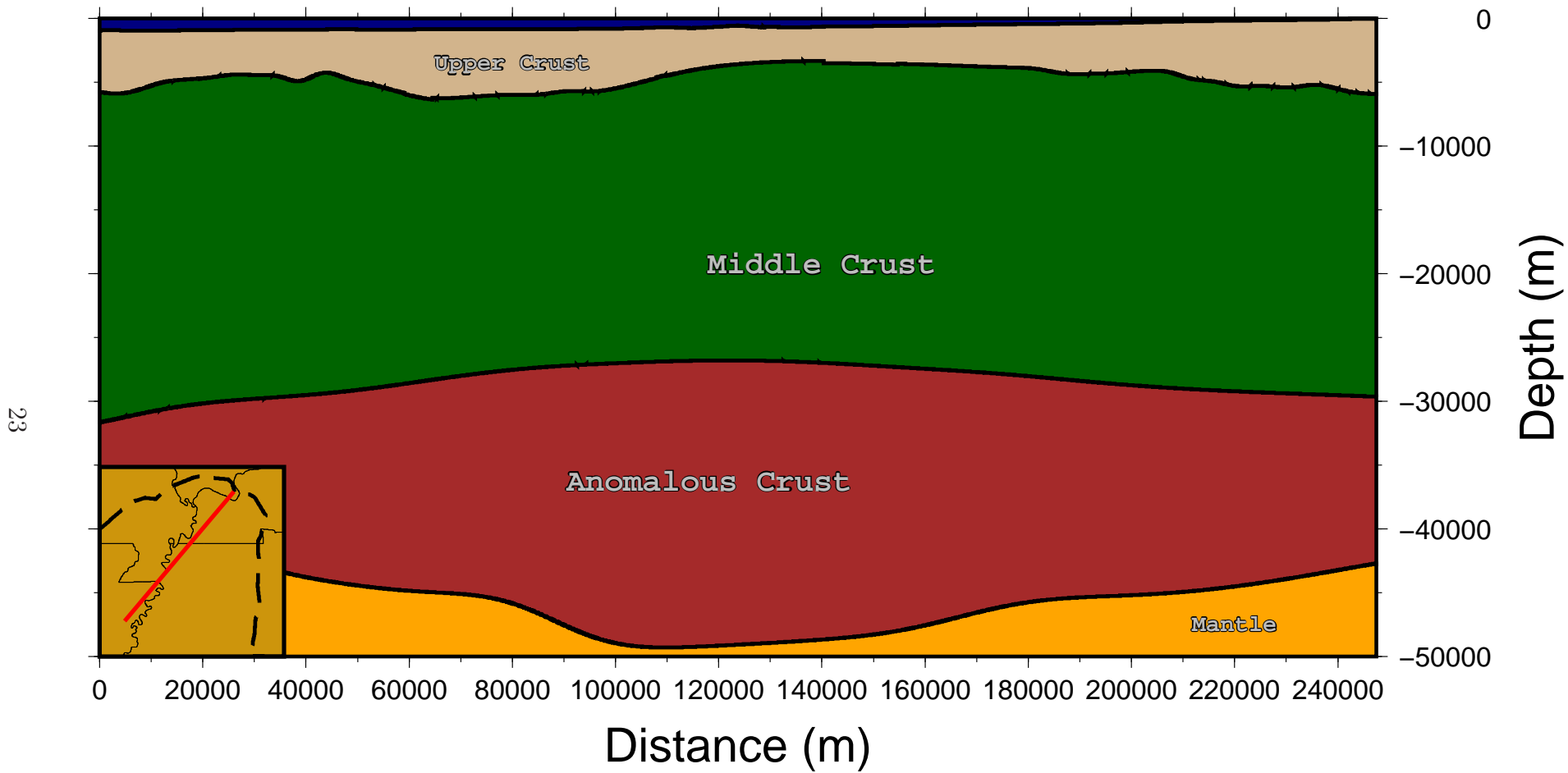


Figure 2.1: Cross section of generalized geologic model for the upper Mississippi embayment.

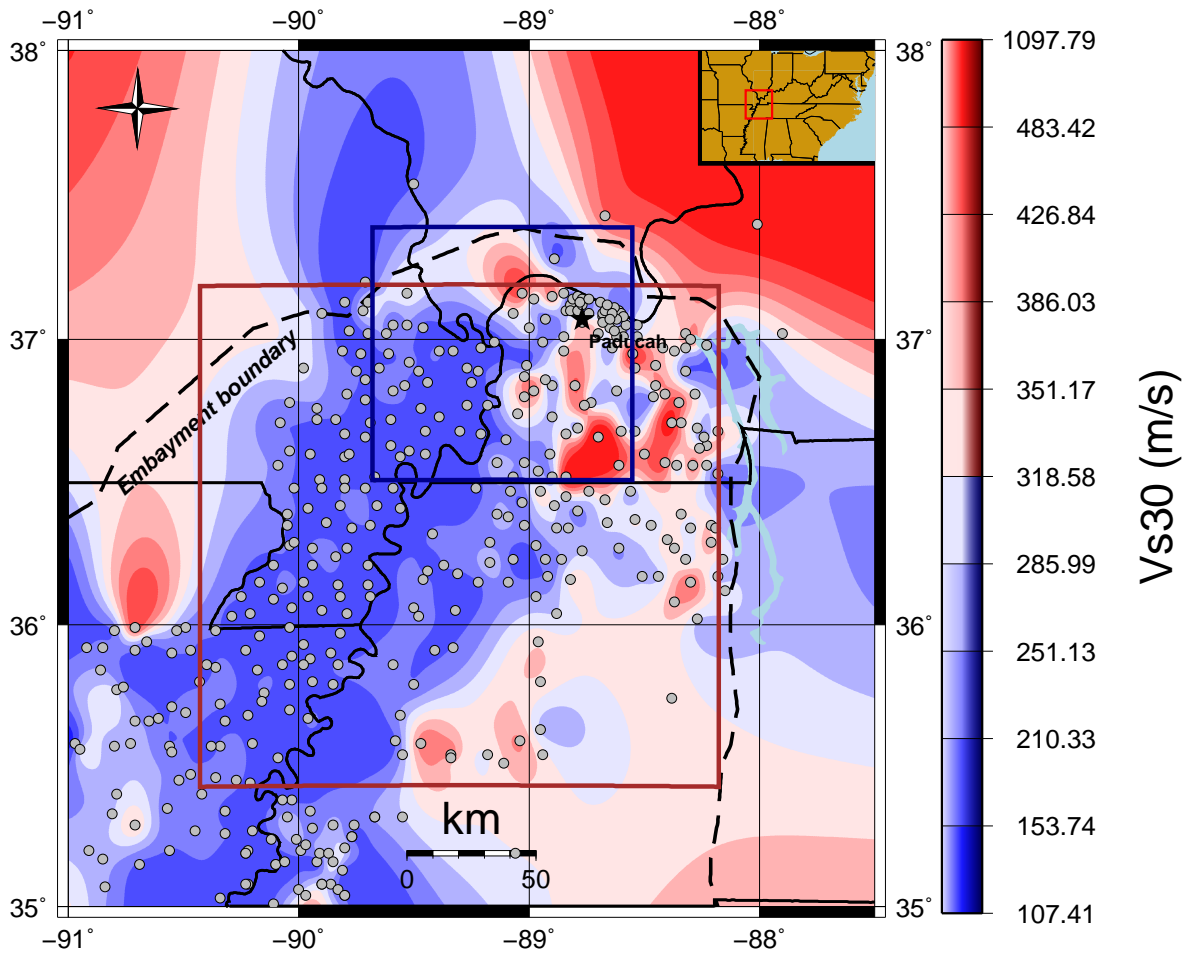


Figure 2.2: Sites with V_s^{30} data in the study area and interpolated velocity map.

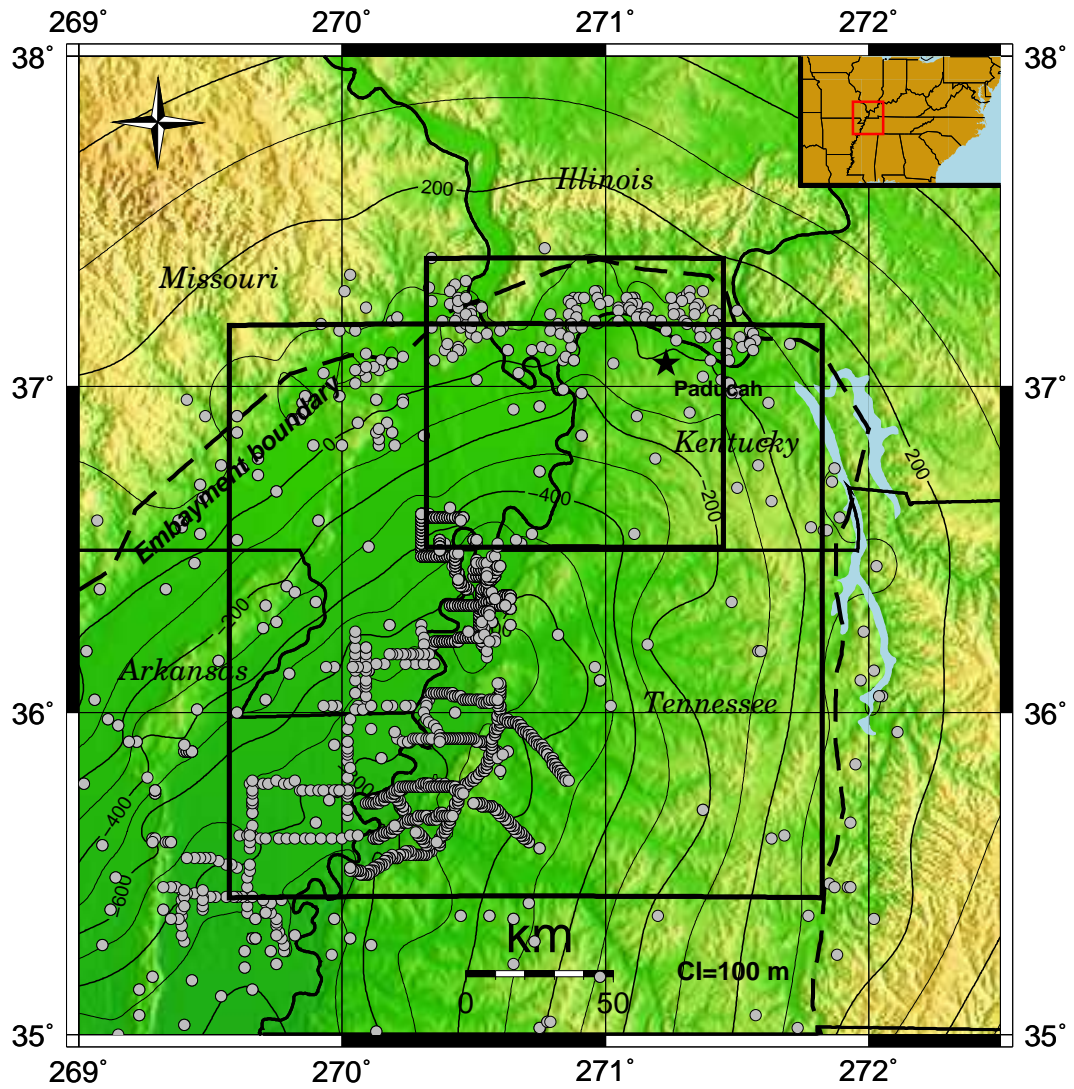


Figure 2.3: Structure-contour map of Paleozoic unconformity. Contour labels are in meters. Data points used to constrain the surface are shown as gray circles.

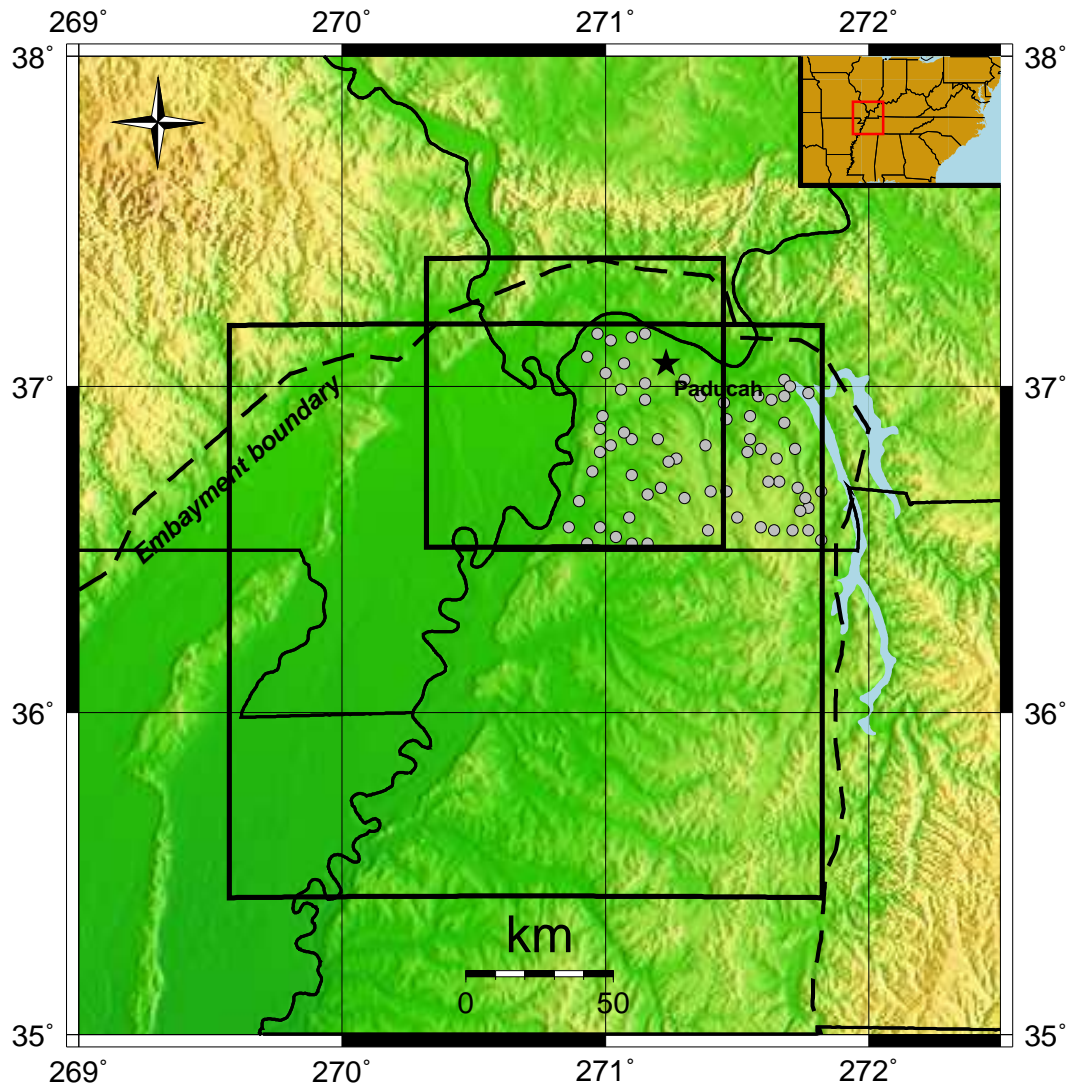


Figure 2.4: Locations of sites with post-Paleozoic layer depth and average layer velocity data.

Post-Paleozoic S-Wave Velocities in the Northern Embayment

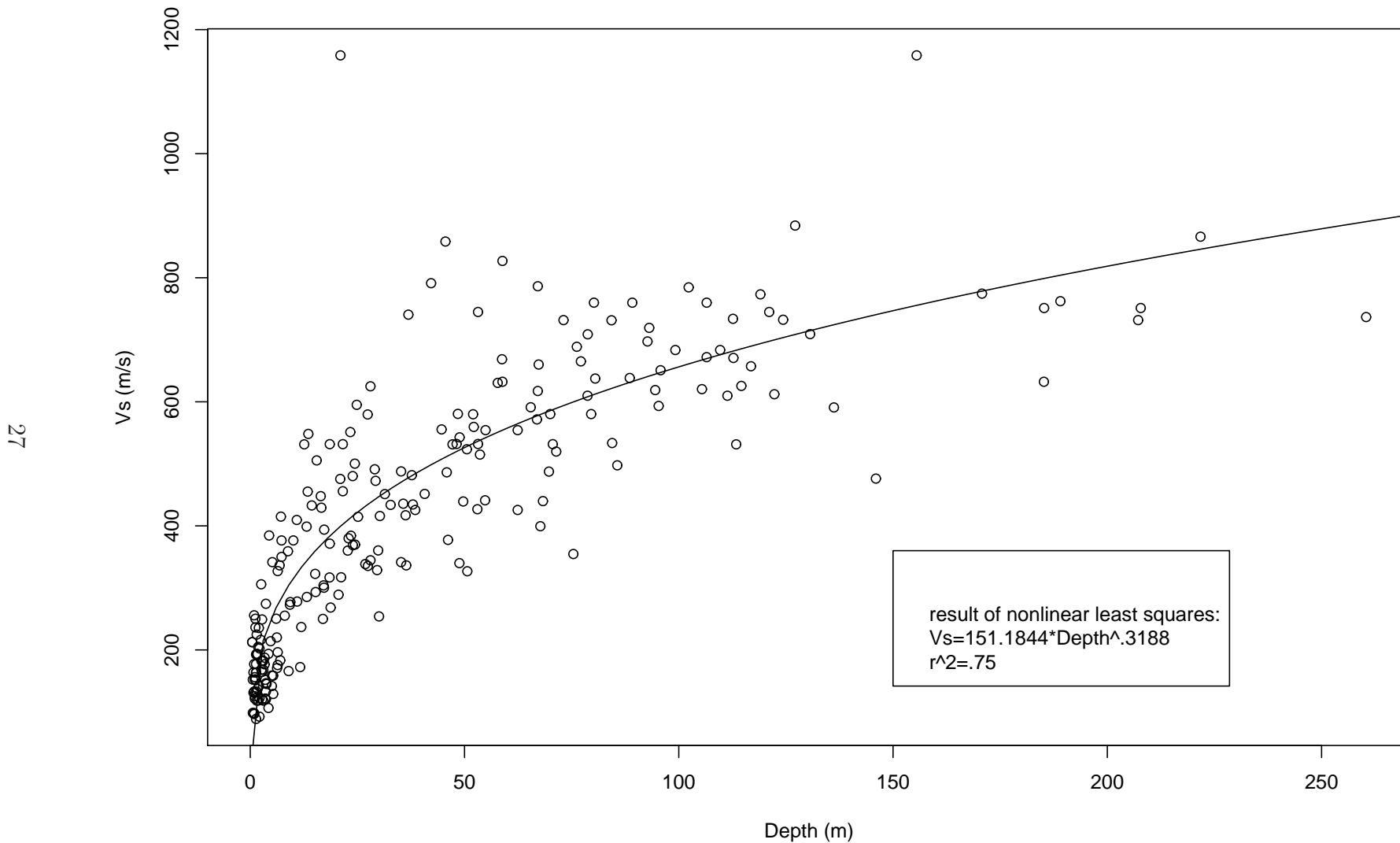


Figure 2.5: Data points and regression line used to model post-Paleozoic shear-wave velocities

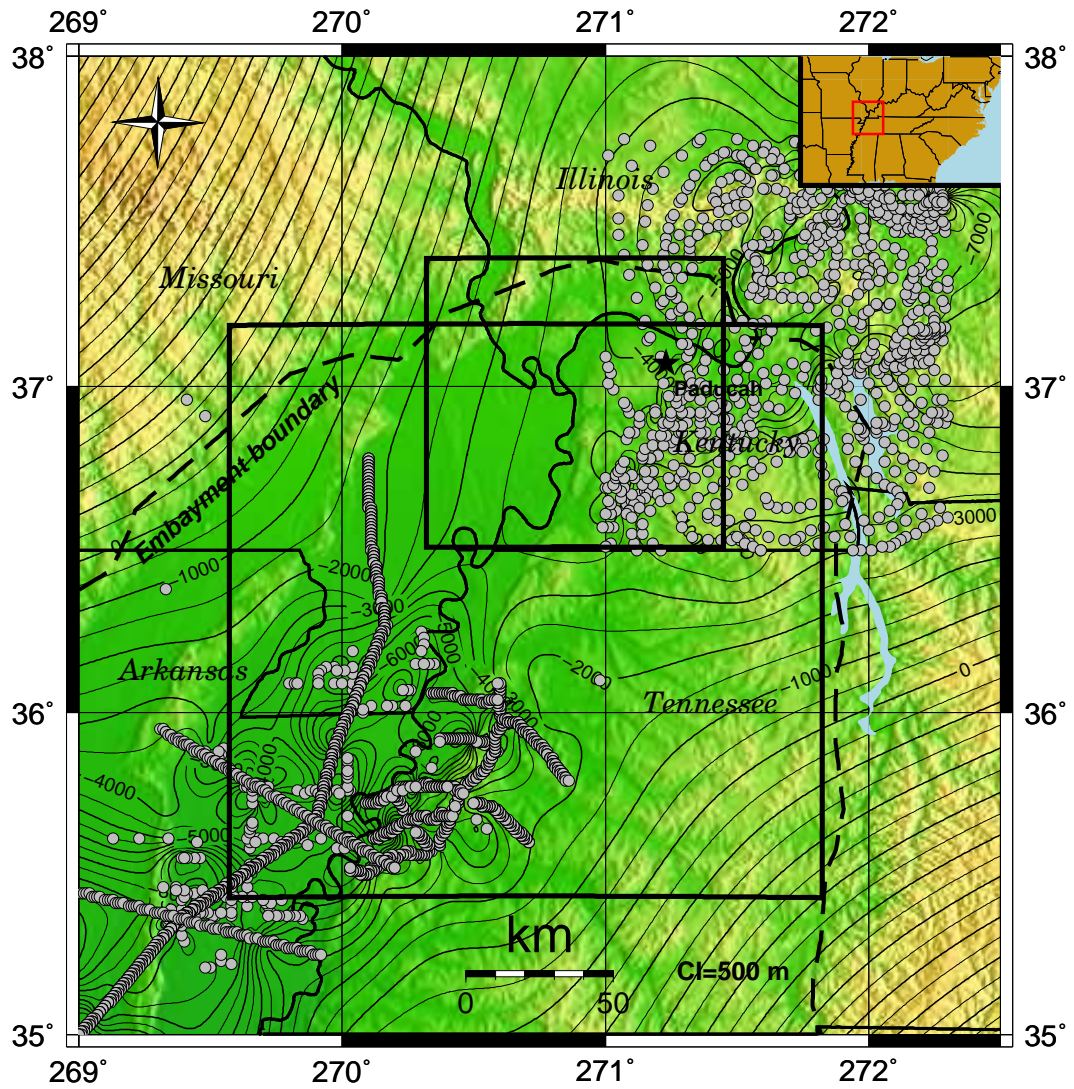


Figure 2.6: Structure-contour map of the Precambrian unconformity. Contour labels are in meters. Data points used to constrain the surface are shown as gray circles.

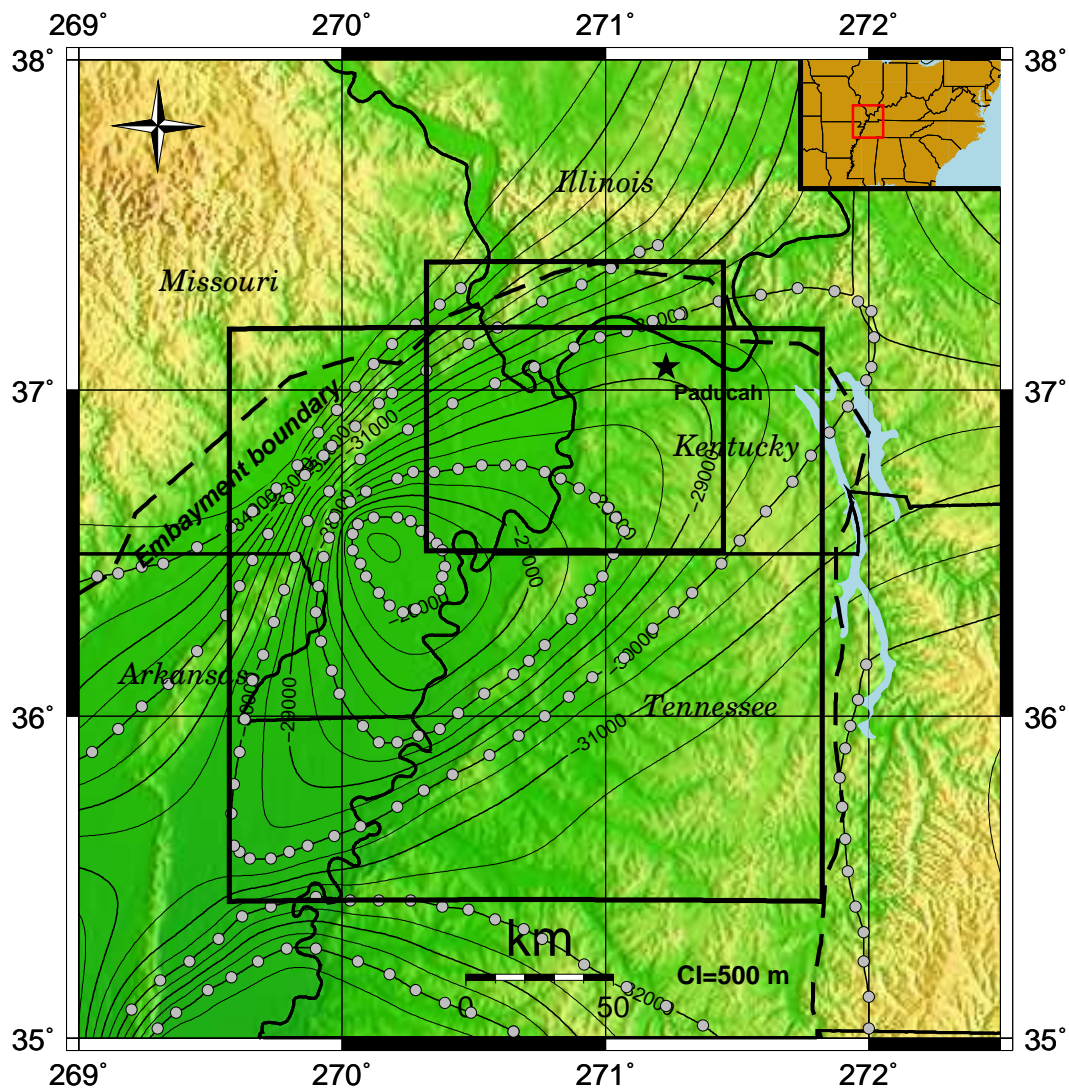


Figure 2.7: Structure-contour map of the top of the rift pillow. Contour labels are in meters. Data points used to constrain the surface are shown as gray.

P-Wave Velocities in the Middle Crust

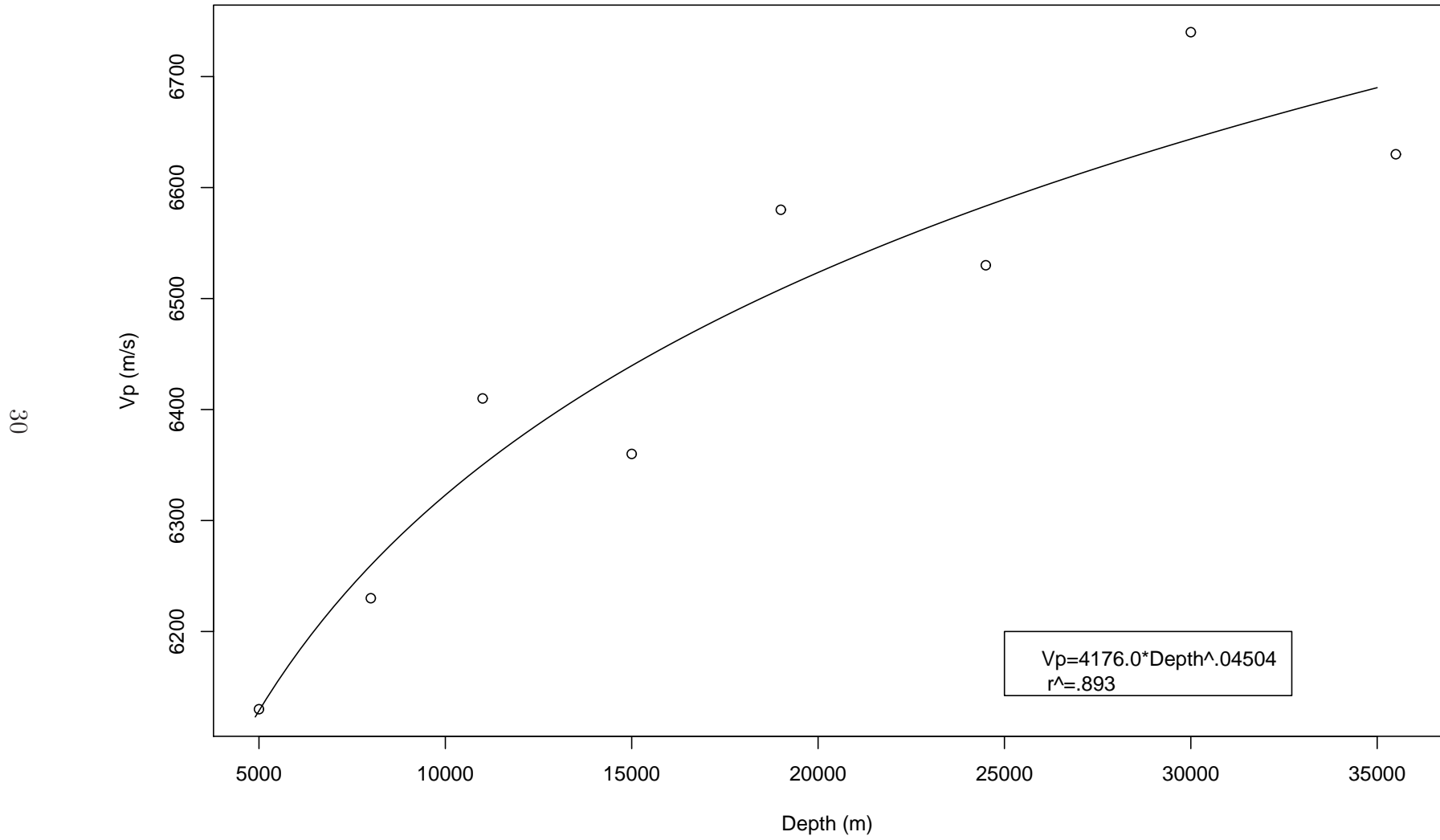


Figure 2.8: Data points from the HAMBURG earth model and regression equation for middle crust V_p .

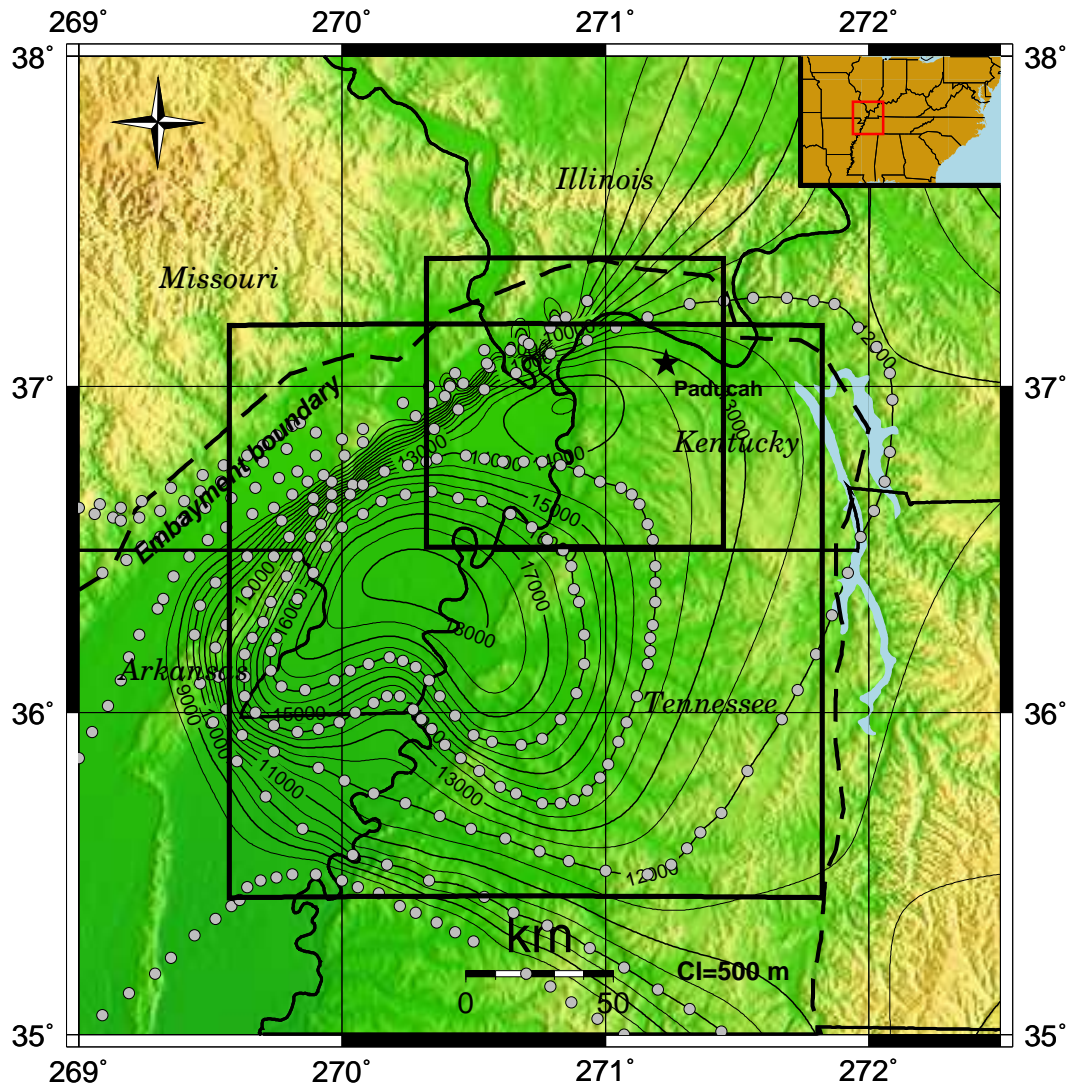


Figure 2.9: Isopach map of the anomalous crustal layer. Contour labels are in meters. Data points used to constrain the surface are shown as gray circles.

P-Wave Velocities in the Anomalous Crust

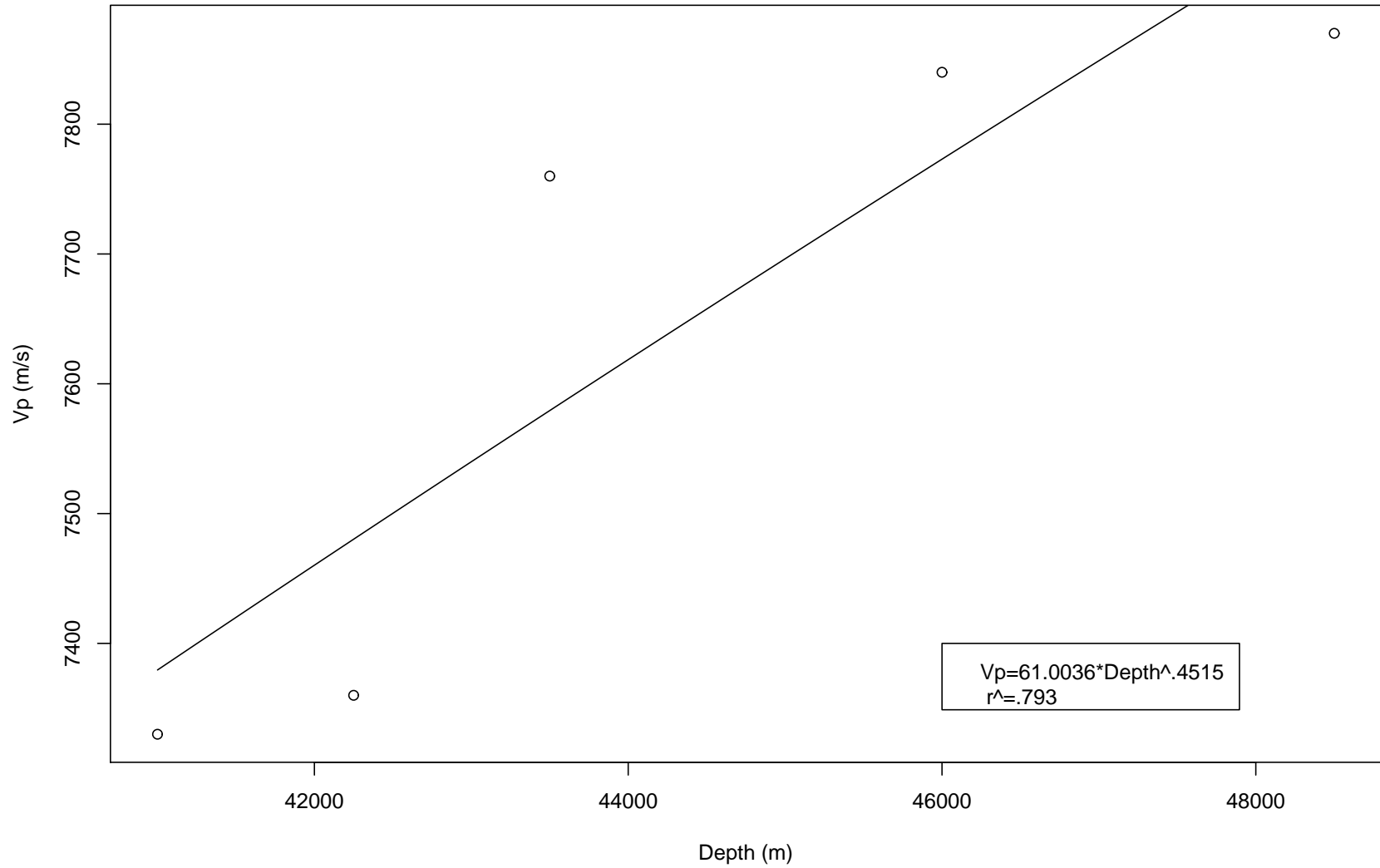


Figure 2.10: Data points from the HAMBURG earth model and regression equation for the anomalous crust V_p .

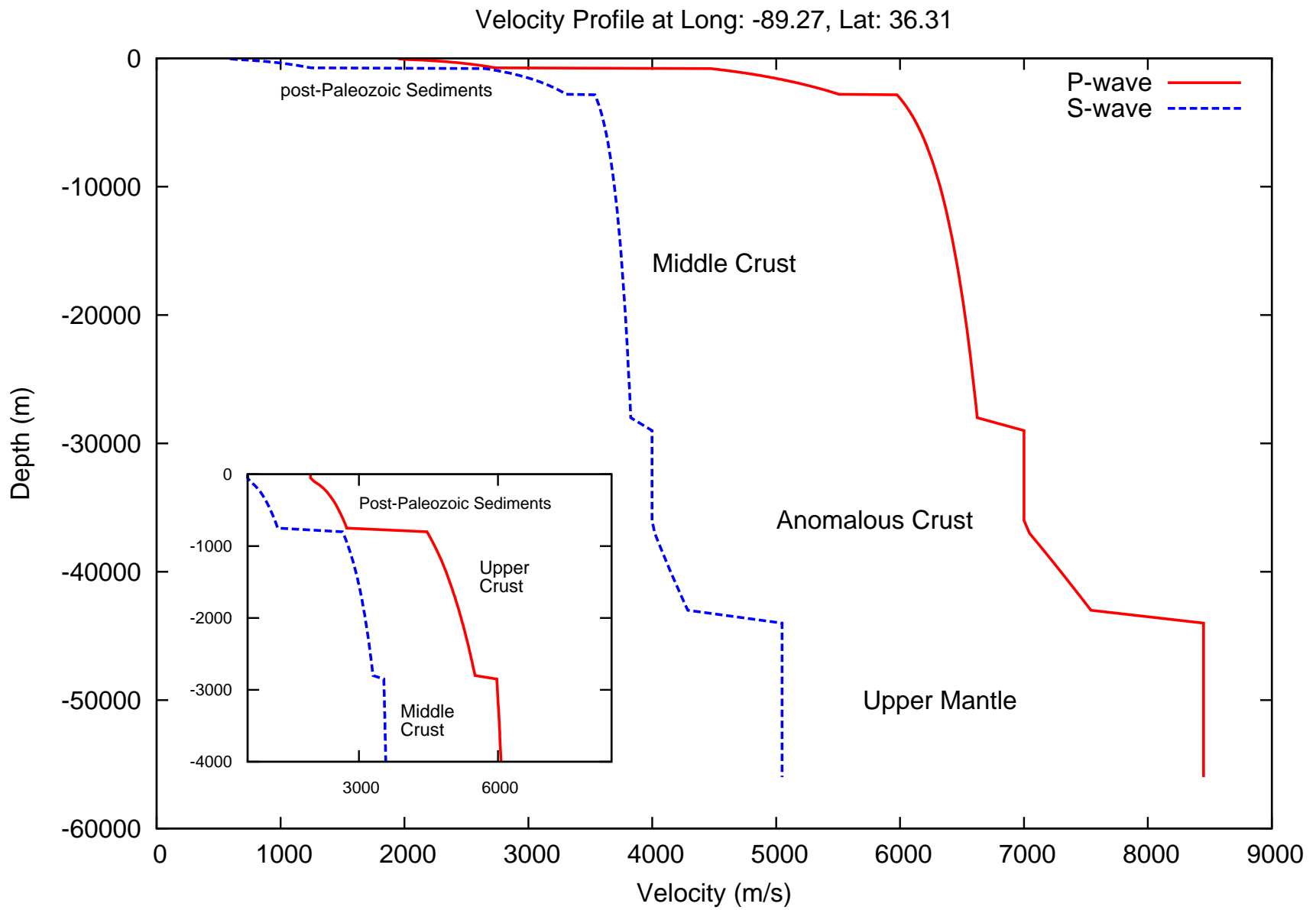


Figure 2.11: Velocity profile at a point in the center of the 0.5-Hz region.

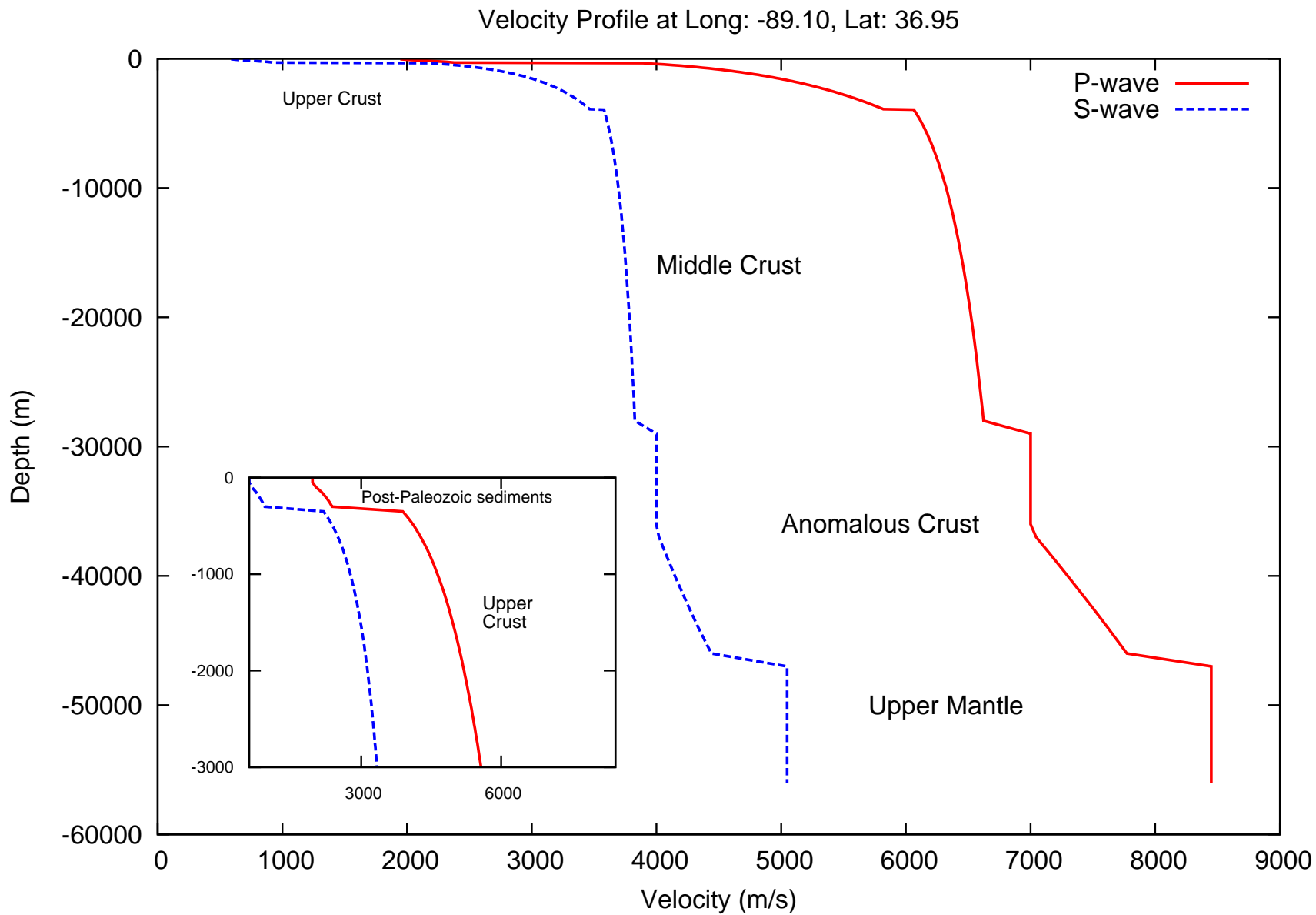


Figure 2.12: Velocity profile at a point in the center of the 1.0-Hz region.

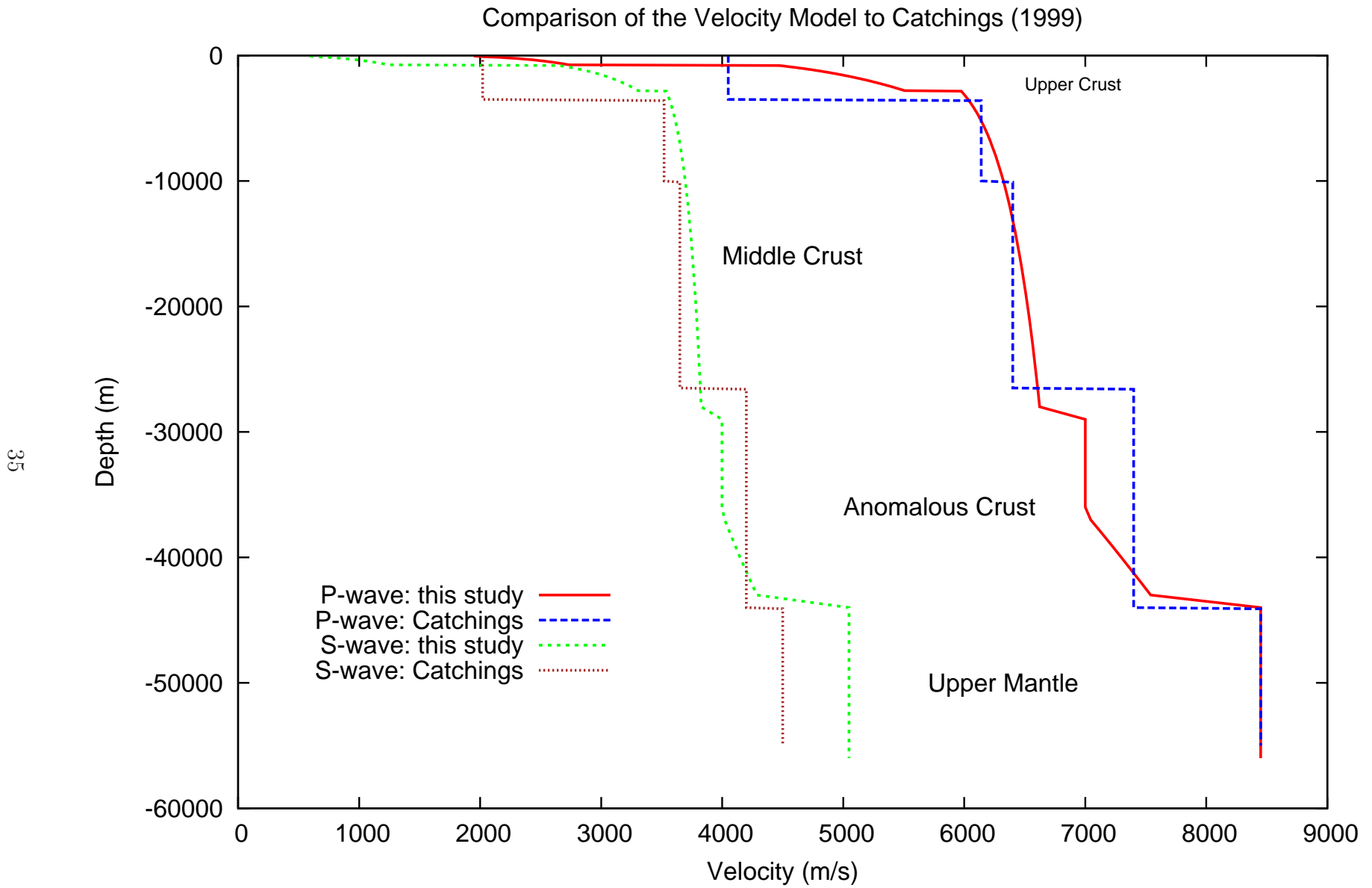


Figure 2.13: A typical profile of the velocity model compared to ? averaged values for the Reelfoot rift.

Chapter 3 Simulation Methods

Numerical methods provide seismologists with powerful, general tools for solving an array of problems that would be impossible to solve analytically. One such problem is the modeling of seismic wave propagation in complex, heterogeneous media. There are no analytical solutions of the elastic wave equation for most subsurface models, particularly those of sufficient complexity to be of interest to seismologists or engineers. Thus approximation approximation is necessary (Kelly et al., 1976). The mathematical tools for constructing such approximations are usually in the form of finite difference-methods, finite-element methods (Toshinawa and Ohmachi, 1992), spectral-element methods (Komatitsch and Vilotte, 1998), the boundary integral equation method (Bouchon and Coutant, 1994), or a hybrid scheme that is some combination of methods (Ma et al., 2004). For the proposed study, the finite-difference method was chosen because of its robust representation in the literature (e.g. (Alterman and Karal, 1968) (Kelly et al., 1976) (Virieux, 1984) (Virieux, 1986) (Levander, 1988) (Graves, 1996) (Pitarka, 1999)) and its history of effectiveness in simulating wave propagation in three dimensions (e.g. (Frankel and Stephenson, 2000)).

3.1 The 3D Viscoelastic Finite-Difference Code

The equation of motion governing seismic wave propagation in a three dimensional, isotropic elastic medium is given by:

$$\rho \frac{\partial^2 u_i}{\partial t^2} = \partial_j \tau_{ij} + f_i \quad (3.1)$$

where ρ is density, u_i is displacement, t is time, τ is stress, f_i is the source function (neglecting the gravity term), and $i, j \in \{x, y, z\}$ (Shearer, 1999). Equation 3.1 may be solved by expressing τ as a function of displacement. This is accomplished via the linear stress-strain relationship:

$$\tau_{ij} = \lambda \delta_{ij} \partial_k u_k + \mu (\partial u_j + \partial u_i) \quad (3.2)$$

where λ and μ are Lamé's parameters. Equations 3.1) and 3.2 are a coupled set of second-order differential equations describing displacement and stress. These equations can be expressed as a set of first-order equations by differentiating Equation 3.1

with respect to time and replacing $\partial_t u_i$ with v_i to obtain:

$$\frac{\partial v_i}{\partial t} = \frac{1}{\rho}(\partial_j \tau_{ij} + f_i) \quad (3.3)$$

which are expressions for velocity, and:

$$\begin{aligned} \frac{\partial \tau_{ii}}{\partial t} &= (\lambda + 2\mu)\partial_i v_i + \lambda(\partial_j v_j + \partial_k v_k) \\ \frac{\partial \tau_{ij}}{\partial t} &= \mu(\partial_j v_i + \partial_i v_j) \end{aligned} \quad (3.4)$$

which are expressions for stress where $i, j, k \in \{x, y, z\}$. This results in a total of three equations for velocity and six equations for stress to completely describe wave propagation in a three-dimensional medium (Graves, 1996).

Because of the complexity of earth's subsurface, analytical solutions of the system of equations developed above are not possible for realistic geological models (Moczo et al., 2004). Solutions may be approximated by applying the finite-difference method, however. This method replaces the continuous differential equations (equations 3.3–3.4) with a system of algebraic equations on a discrete grid. The domain of computation is discretized into a finite-difference grid where continuous derivatives are approximated by difference equations stored in computer memory. In the case of the hyperbolic equations discussed above, the discretization is both temporal and spatial, as equations at each grid point are solved at particular times.

A common strategy when developing a finite-difference scheme to approximate equations 3.3 and 3.4 is to apply a staggered-grid. In this scheme, the equations for velocity are separated from the equations for stress by one-half grid point in time and one-half grid point in space. This differencing over twice smaller grid spacing has the effect of reducing the leading error term by a factor of 4 as compared to a conventional grid (Moczo et al., 2004). The discrete form of equation 3.3 on a velocity-stress staggered grid is given by:

$$\begin{aligned} v_{xi+1/2,j,k}^{n+1/2} &= v_{xi+1/2,j,k}^{n-1/2} + [\Delta t \bar{b}_x (D_x \tau_{xx} \\ &\quad + D_y \tau_{xy} + D_z \tau_{xz} + f_x)]_{i+1/2,j,k}^n \\ v_{yi,j+1/2,k}^{n+1/2} &= v_{yi,j+1/2,k}^{n-1/2} + [\Delta t \bar{b}_y (D_x \tau_{xy} \\ &\quad + D_y \tau_{yy} + D_z \tau_{yz} + f_y)]_{i,j+1/2,k}^n \\ v_{zi,j,k+1/2}^{n+1/2} &= v_{zi,j,k+1/2}^{n-1/2} + [\Delta t \bar{b}_z (D_x \tau_{xz} \\ &\quad + D_y \tau_{yz} + D_z \tau_{zz} + f_z)]_{i,j,k+1/2}^n \end{aligned} \quad (3.5)$$

where \bar{b} is the buoyancy (reciprocal of density), n is the time index, Δt is the time step, D_i is the fourth-order center-difference operator given by, e.g. ,

$$D_x v_x|_{i,j,k} = \frac{1}{h} c_0 [v_{xi+1/2,j,k} - v_{xi-1/2,j,k}] - c_1 [v_{xi+3/2,j,k} - v_{xi-3/2,j,k}] \quad (3.6)$$

where h is the grid spacing. Typically, in this type of scheme the buoyancy will also have its own spatial difference operators. The discrete form of equation 3.4 is given by:

$$\begin{aligned} \tau_{xxi,j,k}^{n+1} &= \tau_{xxi,j,k}^n + \Delta t [(\lambda + 2\mu) D_x v_x \\ &\quad + \lambda (D_y v_y + D_z v_z)]|_{i,j,k}^{n+1/2} \\ \tau_{yyi,j,k}^{n+1} &= \tau_{yyi,j,k}^n + \Delta t [(\lambda + 2\mu) D_y v_y \\ &\quad + \lambda (D_x v_x + D_z v_z)]|_{i,j,k}^{n+1/2} \\ \tau_{zzj,k}^{n+1} &= \tau_{zzj,k}^n + \Delta t [(\lambda + 2\mu) D_z v_z \\ &\quad + \lambda (D_x v_x + D_y v_y)]|_{i,j,k}^{n+1/2} \\ \tau_{xyi+1/2,j+1/2,k}^{n+1} &= \tau_{xyi+1/2,j+1/2,k}^n + \Delta t [\bar{\mu}_{xy}^H (D_y v_z \\ &\quad + D_x v_y)]|_{i+1/2,j+1/2,k}^{n+1/2} \\ \tau_{xzi+1/2,j,k+1/2}^{n+1} &= \tau_{xzi+1/2,j,k+1/2}^n + \Delta t [\bar{\mu}_{xz}^H (D_z v_x \\ &\quad + D_x v_x)]|_{i+1/2,j,k+1/2}^{n+1/2} \\ \tau_{yzi,j+1/2,k+1/2}^{n+1} &= \tau_{yzi,j+1/2,k+1/2}^n + \Delta t [\bar{\mu}_{yz}^H (D_x v_y \\ &\quad + D_y v_z)]|_{i,j+1/2,k+1/2}^{n+1/2} \end{aligned} \quad (3.7)$$

where the rigidity is approximated by its own finite-difference operator. This scheme is second-order accurate in time and fourth-order accurate in space. Also, note that the scheme is implicit, with velocity at time $n + 1/2$ being calculated from velocities at time $n - 1/2$ and stresses at time n , and stresses at time $n + 1$ being calculated from velocities at time $n + 1/2$ and stresses at time n .

The code used in this study was developed by [Liu and Archuleta \(2002\)](#) and uses a velocity-stress staggered-grid finite-difference numerical scheme similar to that described above. The full wave field is calculated in a heterogeneous, isotropic, viscoelastic volume ([Harmsen et al., 2008](#)). The free-surface boundary condition is modeled as the flat top of the “box” and this presents no difficulty because of the absence of significant relief in the upper Mississippi embayment. Artificial boundary conditions, a consequence of having to truncate the domain laterally, are modeled using the perfectly matched layer so as to prevent spurious reflections from contam-

inating the solution within the domain of computation (Liu and Archuleta, 2006). The finite-difference grid is divided into two regions, the deeper having three times coarser grid spacing than the shallower. This is very memory efficient, as deeper layers with larger shear-wave velocities do not require as fine a grid spacing as shallower, low-velocity layers. This is apparent upon inspection of equation 2.1, the spatial sampling criteria. The depth of the interface between the regions with different grid spacing is determined automatically by the code and is the shallowest depth at which all shear-wave velocities are at least three times greater than the models minimum shear-wave velocity (Harmsen et al., 2008). So for this study, the interface was at the shallowest depth for which $V_s \geq 3 \cdot 600 \text{ m/s} = 1,800 \text{ m/s}$ which is typically 1,000 m deep.

Hardware

The University of Kentucky’s Center for Computational Sciences operates a high-performance Linux cluster which was used for this project. As of November 2008, UK’s facility was ranked 494 on the Top500TM Supercomputers list (Top500, 2008). This system consists of an IBM Bladecenter HS21 Linux Cluster with 340 nodes connected via Infiniband. Each node is composed of four Intel XeonTM64-bit 3.0-gigahertz processors for a total of 1,360 processor cores.

A proprietary Intel compiler was used to compile the FORTRAN 77 finite-difference code. Because the code does not make use of the Message Passing Interface (MPI), it was not possible to employ the high-performance cluster to its full potential. Even though the simulations could only be run on a single node utilizing four processors, this hardware still provided performance superior to any available desktop workstations. Runs producing time series of 120 seconds were completed on the order of a few hours, even without the use of MPI.

3.2 Model Validation

In order to evaluate the effectiveness of the finite-difference code at modeling the ground-motion parameters of interest, synthetic seismograms were compared with recordings of events in the study area. In this way a degree of confidence in the modeling results could be gained. Ideally, computed synthetics would be compared with recorded events that are similar in magnitude and fault geometry to the events to be modeled. Unfortunately, there are no such recordings of large events in the study area. Of course, this is one of the reasons that simulating such events is so

important. The Kentucky Strong-Motion Network has made numerous recordings of microearthquakes in the region, however. More than 200 recordings of such events had been made as of 2006 (Wang and Woolery, 2006). One of these small earthquakes was simulated using the finite-difference code and velocity model described above and compared to a recorded time-series in an effort to validate the effectiveness of the model.

The 6 June, 2003, Bardwell, Ky., earthquake was chosen for simulation because there were high-quality recordings of the event and because the source mechanism has been thoroughly studied (Horton et al., 2005). The event occurred in western Kentucky (Fig. 3.1) at 12:29 UTC and caused minor damage to structures in Bardwell; some residents reported difficulty standing. The event was recorded by thirteen stations in the regional seismic network, and five temporary broadband seismographs were deployed to study the aftershock sequence. These data provide good constraint on fault geometry, depth, and focal mechanism. The Bardwell source and simulation parameters are shown in Table 3.1.

Although this study is primarily constrained to long-period ground-motions (frequency ≤ 1.0 Hz), the small dimensions of the Bardwell source are likely to produce accelerograms with predominantly high-frequency content. For this reason, a minimum grid spacing of $\Delta x = 36.36$ m was used for the Bardwell simulations so that synthetics could be accurately calculated up to 3.0 Hz. This fine grid spacing imposed a severe restriction on the extent of the volume that could be included in the simulation. Fortunately, strong-motion station WIKY is located within 13 km of the Bardwell source. This allowed for 3.0-Hz synthetics to be calculated on a $14 \text{ km} \times 18 \text{ km} \times 50 \text{ km}$ (50 km deep) volume containing the source and the receiver. The Bardwell source was modeled by randomly placing point sources in a disk with a radius of 440 m and width of 200 m so that the disk center was located at the centroid of the source. The total seismic moment was distributed evenly among the point sources. In order to simulate asperities in the fault plane, fault parameters were allowed to vary randomly within an envelope of 20° . No attempt was made to model rupture propagation because it was unlikely that a pronounced directivity effect would be apparent from such a small source. The rise time and rupture time of each point source was pseudo-randomized within a global rise time of 0.4 s. The simulation parameters are listed in Table 3.1. The Octave script for producing the source file is found in the Appendix.

In order to compare the recorded and simulated data, filters were applied so that time-series with similar frequency content were being compared. Strong-motion

station WIKY recorded a broadband accelerogram for the Bardwell event. This record was converted to the Seismic Analysis Code (SAC) format for processing. The mean was removed, the units converted to cm/s^2 , and the instrument response removed. Finally, a low-pass Butterworth filter with a 3.0-Hz corner frequency was applied so as to match the frequency content of the synthetics.

The finite-difference code outputs velocity records with units of m/s . The simulated Bardwell record was differentiated using SAC's DIF command to obtain an accelerogram and converted to cm/s^2 . Because spurious high-frequency signals typically contaminate finite-difference synthetic seismograms due to grid dispersion, a low-pass filter was also applied to the simulated record. The horizontal components of the processed simulated and recorded accelerograms are shown in Figure 3.2.

Figure 3.2 shows that there was generally good agreement between the observed and simulated peak amplitudes. The peak horizontal acceleration (PHA) was calculated for the observed and synthetic time-series for purposes of comparison. PHA is the vector sum of the horizontal components of acceleration,

$$\text{PHA} = \max_t \sqrt{a_x^2(t) + a_y^2(t)}$$

where a_x and a_y are the horizontal components of acceleration (cm/s^2) and t is time in seconds. The Bardwell PHA is $\text{PHA}_o = 8.3070 \text{ cm/s}^2$ and $\text{PHA}_s = 9.4651 \text{ cm/s}^2$ for observed and simulated PHA, respectively. Because

$$\frac{\text{PHA}_o}{\text{PHA}_s} = 0.8776,$$

the model was approximately 88 percent effective in simulating peak ground accelerations. The model did a less satisfactory job of predicting the duration of shaking, another important ground-motion parameter. As can be seen in Figure 3.2, the simulated record appears to be more highly attenuating, with amplitudes decreasing much more rapidly than in the observed record. This is perhaps because very low-velocity near-surface sediments that were not included in the velocity model acted as a wave guide in the recorded accelerogram. Also, arrivals from waves generated at basin edges may be absent in the synthetic seismogram because the small domain of computation does not include embayment boundaries.

The simulation of the Bardwell earthquake indicates that the model does an adequate job of predicting peak ground-motion amplitudes. Estimates of duration of shaking made from the model are likely to underestimate actual durations, however.

3.3 Ground-Motion Parameters

The finite-difference code described above produces one three-component synthetic seismogram per simulated receiver placed within the domain of computation. The three components are in the x , y , and z directions corresponding to the Cartesian coordinates of the finite-difference grid, with z being vertical. The output is velocity and has units of m/s. Because we were interested in strong ground motion, all receivers for the simulations described below were placed at the free-surface.

These three-component velocity time-series may be thought of as “raw” data, and care was taken to apply processing steps that would produce parameters that convey information about the seismic hazard in the upper Mississippi embayment while losing only an acceptable amount of information from the inevitable smoothing effect that is the result of processing. Because earthquake-induced ground motion is such a complex phenomenon, no one ground-motion parameter is sufficient for describing it. Several parameters were chosen to quantify the simulated ground motions at the surface, and processing steps to compute them are described in detail below. In all cases, the raw data velocity time-series were preprocessed in the SAC environment before calculating the ground-motion parameter of interest. Also, vertical-component data were discarded because vertical amplitudes are typically smaller than horizontal components and engineered structures are less susceptible to damage from vertical motions ([Kramer, 1996](#)).

Data Preprocessing

Before any of the ground-motion parameters discussed below could be calculated, the output from the finite-difference code had to be preprocessed in order to apply filters and convert the data to the appropriate units. In order to provide good coverage of the free-surface in the domain of computation, hypothetical receivers were placed on a grid with 6 km spacing for the large 0.5-Hz volume and 3 km spacing for the smaller 1.0-Hz volume. This resulted in 961 and 900 stations for the large and small volumes, respectively. Therefore, for each simulation run, the output from the finite-difference code consisted of either $3 \times 900 = 2,700$ or $3 \times 961 = 2,883$ time-series files. Processing so many files presented a challenge and required automation through the use of an SAC macro.

The macro read 600 of the data files at a time for processing. A variety of tasks could be performed using the macro, including lowpass filtering via a Butterworth filter in order to remove spurious high-frequency signal introduced by grid dispersion.

The macro could also apply a numerical integration or numerical differentiation algorithm to convert to displacement or acceleration, respectively. The acceleration data could be converted to units of g in order to calculate pseudospectral accelerations. The data could also be trimmed if there was little information at the end of the time-series in order to expedite subsequent processing steps. The SAC macro can be found in the Appendix.

For all simulations described below, the data were low-pass filtered using a Butterworth filter with a corner frequency of 0.5 Hz for the large volume and 1.0 Hz for the smaller volume. The data were left as velocity in m/s for the peak ground-motion calculation, as this removed the step of conversion to acceleration and because velocities are more sensitive than accelerations to low-to mid-frequency signal (Kramer, 1996). The data were converted to acceleration in g's for both the bracketed duration and pseudospectral acceleration calculations. The macro was convenient to use and could process the 2,883 files from a simulation in approximately 2 minutes.

The application of the low-pass filter reduced the amplitudes in the time-series and this had to be kept in mind when interpreting results. As a rule of thumb, peak amplitudes are reduced by a factor of $\sqrt{2}$ (Harmsen et al., 2008). The phenomena is not so well behaved, however, that the time-series could be corrected by a simple scaling.

Peak Horizontal Velocity

Although peak horizontal acceleration is perhaps the most common peak ground-motion amplitude parameter, peak horizontal velocity (PHV) was chosen for this study for two reasons. Leaving the seismograms in velocity format removed an additional processing step of differentiating the time-series. Also, the long-period synthetic computed by the finite-difference code should be better characterized by velocity than by acceleration, which is more sensitive to higher-frequency signal (Kramer, 1996).

PHV is calculated by taking the vector sum of the maximum horizontal components of velocity, i.e.,

$$\text{PHV} = \max_t \sqrt{V_x^2(t) + V_y^2(t)} \quad (3.8)$$

where V_x and V_y are the horizontal components of velocity (m/s) and t is time (s) (Harmsen et al., 2008). The direction of the PHV is unlikely to coincide with the direction of either component. Also, the PHV occurs at different receivers at different

times as the maximum amplitude is found for the duration of the times-series.

Because some 1,922 time-series were used for each PHV calculation, it was necessary to automate the process through the use of an Octave script. The script wrote a file containing the coordinates and PHV for each receiver that was suitable for plotting using the Generic Mapping Tools (GMT) so that PHV maps could be created for the entire free-surface (Wessel and Smith, 1998). The script may be found in the Appendix.

Bracketed Duration

In addition to ground-motion amplitudes, the duration of shaking can significantly influence the amount of damage caused by an earthquake. Ground motions with moderate amplitudes and long duration may be more damaging than high-amplitude motions with shorter durations (Kramer, 1996). Because the earthquakes simulated in this study were large in magnitude and had spatially large faults, some points in the study area would be likely to experience long durations, particularly for scenarios that rupture in strictly one direction.

In order to quantify the duration of shaking predicted by the simulations, the technique of bracketed durations was employed. The bracketed duration is the length of time between the first and last exceedances of a threshold amplitude (Kramer, 1996). The threshold amplitude is usually an acceleration of 0.005 g, and this threshold was adopted even though it necessitated the conversion of the synthetic seismograms to acceleration. Again, the large number of receivers prompted automation via a Octave script, the output of which is suitable for plotting in GMT to provide maps of duration at the surface (see the Appendix).

Pseudospectral Acceleration

The PHV discussed above indicates the maximum ground-motion amplitudes that are likely to occur at points on the free-surface in the study area, but equally important from an engineering perspective in the response of simple structures to such motion. A measure of such response is given by the response spectrum, the maximum response of a single-degree-of-freedom (SDOF) system to a particular input ground motion (Kramer, 1996). The response spectrum is a function of the percent damping and natural frequency of the SDOF system and may be expressed as spectral acceleration, spectral velocity, or spectral displacement.

A common SDOF system is one in which a rigid mass m is connected in series

to a dashpot with a viscous damping c , a spring of stiffness k , and exposed to base acceleration $\alpha(t)$ (see Fig. 3.3) (Kramer, 1996). The equation of motion describing the response of the system shown in Figure 3.3 is given by:

$$\ddot{u} + 2\beta\omega\dot{u} + \omega^2u = -\alpha(t) \quad (3.9)$$

where x is displacement, β is the percent damping, α is acceleration as a function of time, and a dot denotes a derivative with respect to time (Nigam and Jennings, 1969). Nigam and Jennings (1969) developed an analytical solution for this equation by assuming that $\alpha(t)$ may be approximated by linear segments. This is ideal for situations when the base acceleration, $\alpha(t)$, is in the form of a digital seismogram with equal time intervals, as is the case with the output from the finite-difference code. The solution is of the form:

$$\begin{bmatrix} u_{i+1} \\ \dot{u}_{i+1} \end{bmatrix} = \begin{bmatrix} a_{11} & a_{12} \\ a_{21} & a_{22} \end{bmatrix} \begin{bmatrix} u_i \\ \dot{u}_i \end{bmatrix} + \begin{bmatrix} b_{11} & b_{12} \\ b_{21} & b_{22} \end{bmatrix} \begin{bmatrix} \alpha_i \\ \alpha_{i+1} \end{bmatrix} \quad (3.10)$$

where the a_{ij} s and b_{ij} s are functions of ω and β and $i \in \{1, 2, \dots, N\}$ where N is the length of the acceleration record. These equations make very convenient stencils for numerical integration if expressed as:

$$\begin{aligned} u_{i+1} &= a_{11}u_i + a_{12}\dot{u}_i + b_{11}\alpha_i + b_{12}\alpha_{i+1} \\ \dot{u}_{i+1} &= a_{21}u_i + a_{22}\dot{u}_i + b_{21}\alpha_i + b_{22}\alpha_{i+1} \end{aligned} \quad (3.11)$$

forming explicit operators that calculate spectral displacement and spectral velocity by sweeping through the acceleration time series. Once u and \dot{u} have been calculated by equation 3.11, the absolute acceleration of the mass at time t_i is calculated via:

$$\ddot{z}_i = -(2\beta\omega\dot{u}_i + \omega^2u_i). \quad (3.12)$$

Finally, the response spectra of the SDOF system is constructed by finding the maximums of the spectral displacement, spectral velocity, and spectral acceleration.

An Octave script was written to implement the numerical scheme in equation 3.11. First, the velocity time-series is processed to acceleration by differentiation. Then, using the initial conditions:

$$\begin{aligned} u_i &= 0 \\ \dot{u}_i &= 0 \end{aligned} \quad (3.13)$$

the acceleration record of each horizontal component is swept by equations 3.11 and 3.12. The response spectra are then computed by finding the maximum values of u_i , \dot{u}_i , and \ddot{z}_i for all i . The pseudospectral acceleration of each component is found by

$$\text{PSA}_j = \omega^2 \cdot \text{SA}_j = \omega^2 \cdot \max_{i=1,N}(\ddot{z}_i, j)$$

where N is the length of the input acceleration record and the subscript j indicates that the PSA may be for the x or y component. PSA at each station is defined as the geometric mean of the PSA of each component, i.e.,

$$\text{PSA} = \sqrt{\text{PSA}_x \cdot \text{PSA}_y}.$$

The octave code may be found in the Appendix.

3D/1D Ratios

As discussed above, a major goal of this study is to evaluate the extent to which strong motion is affected by the 3D geologic structure of the embayment. A measure of this effect is provided by the ratio of 3D to 1D PHV, i. e.,

$$\text{Amp} = \frac{\text{PHV}_{3D}}{\text{PHV}_{1D}} \quad (3.14)$$

where PHV_{3D} and PHV_{1D} are the 3D and 1D PHV, respectively (Olsen, 2000). This number may be thought of as the amplification induced by the 3D structure. For values of $\text{Amp} > 1$, the 3D structure has an amplifying effect, whereas for $0 < \text{Amp} < 1$, the structure has a deamplifying effect.

In order to obtain amplification values, PHV_{1D} must be calculated by conducting finite-difference simulations on a 1D velocity model. All aspects of the calculations are identical to those for obtaining PHV_{3D} with the exception of the velocity model. The velocity model employed is a 1D layered-earth model taken from a profile from the center of the 3D velocity model. This keeps all parameters such as source, receiver placement, and grid spacing constant between the 3D and 1D simulations so that all differences between the two may be attributed to the velocity model.

Snapshots and Animations

Although not a true ground-motion parameter, temporal snapshots are useful for observing how the wave field changes with time at the free-surface. This may help inform the interpretation of the PHV and PSA maps, which are not functions of time.

For this purpose, the seismograms at each station were sampled at regular intervals and files were generated that were suitable for mapping. To further enhance the usability of such information, the snapshot maps are combined to create animations in MPG format. The Octave code for sampling the seismograms and producing snapshots is in the Appendix.

3.4 Source Modeling

A realistic source model is required for strong-motion synthesis, particularly for moderate to large earthquakes and for near-fault areas (Gallovic and Brokesova, 2004). An earthquake of a particular moment may produce a range of ground motions because of variability in slip distribution, rise time, rupture velocity, and location of the hypocenter (Harmsen et al., 2008). Therefore, it is important to calculate these quantities in as realistic a fashion as possible based on empirical relations in the literature.

Because the wave propagation calculation is performed on a discrete grid, the finite-difference code reads in a source file with a list of point sources. The source is implemented by injecting high-frequency energy into the wave equation solutions at the point sources (Harmsen et al., 2008). For each point source, a list of parameters must be provided, including the coordinates of the source, strike, dip, rake, sub-source rise time, sub-source moment, and rupture time. In order to adequately approximate the large finite faults considered in this study, a source file with several thousand points is generated. The process of writing such a file has been automated by the use of an Octave script (see the Appendix). The methods used to calculate each of the source parameters are described below.

Fault Discretization

When approximating a continuous surface such as a fault plane with a set of points, the more points used, the more accurate the representation. This fact must be balanced against the computational burden of writing a file with many points. Because the algorithm used to compute the slip model uses a Fourier transform (see below), the discretization must be a power of 2 and must be equal in the strike and dip directions. For this reason, a discretization in strike and dip direction of $2^7 = 128$ points was chosen, resulting in $128^2 = 16,384$ points or sub-sources. This number of points results in a manageable file size that can be produced on a desktop computer

in a few seconds while still providing adequate resolution, with the along-strike grid spacing of the longest fault (North fault) being 700 m.

The geometry of the fault plane is assumed to be rectangular, the top and bottom of the rectangle being defined by the user. Fault widths are calculated simply from the user-determined top and bottom of the fault. The termini of the rectangle are defined by the user in UTM's based on the areal extent of the background seismicity shown in Figure 1.1. Once the extent of the fault plane has been defined by the user, the coordinates are transformed into a Cartesian system and the fault plane is discretized. The strike of the fault is based on the azimuth of the fault trace and the dip and rake are entered by the user. The values of strike, dip, and rake are allowed to randomly vary within a user-prescribed envelope (usually 5°) in order to simulate some "roughness" in the fault plane. If the fault plane is dipping, then the rectangle is tilted at the appropriate angle to simulate the dip of the finite fault.

There is considerable variation in the estimates of the moment magnitude to be expected from a large New Madrid earthquake (Johnston and Schweig, 1996) (Cramer, 2001) (Tuttle et al., 2002) (Saikia et al., 2006). Rather than specify the magnitude explicitly, the moment magnitude was calculated based on the fault area. In this way, the magnitude was related to the modern observed seismicity shown in Figure 1.1. Wells and Coppersmith (1994) compiled source parameters from 421 historical earthquakes in order to develop empirical relationships among fault geometry, average displacement, and moment magnitude. We used their expressions to calculate moment magnitude as a function of fault area:

$$\mathbf{M}_w = \begin{cases} 3.98 + 1.02 \cdot \log(A), & \text{for strike-slip earthquakes} \\ 4.33 + 0.90 \cdot \log(A), & \text{for reverse fault earthquakes} \end{cases} \quad (3.15)$$

where A is the fault area in km^2 (Wells and Coppersmith, 1994). Once the moment magnitude was determined, the seismic moment was calculated via the well-known expression:

$$M_0 = 10^{\frac{3}{2}\mathbf{M}_w+9.1} \quad (3.16)$$

where M_0 is in N-m. Now, M_0 is the total energy released for the entire finite fault. This energy must be partitioned among the 16,384 sub-sources in a realistic fashion such that the sum of the sub-source moments is equal to M_0 , the target moment. How this is accomplished and how the sub-source moment relates to the slip distribution is described below.

Slip Model

An investigation of slip models of historical earthquakes indicated that the spatial distribution of slip is an important parameter of the earthquake source (Somerville et al., 1999). Observations based on long-period strong-motion data provide simplified, deterministic source descriptions whereas shorter-period ground motions are stochastic (Somerville et al., 1999). For this study, both deterministic and stochastic models were investigated. These included a random moment distribution, a pseudo-Gaussian distribution that concentrated slip at the center of the fault, and also the composite source model (Zeng et al., 1994). The composite source model produced unreasonably high PHV, probably as a result of sub-source overlap, which is a feature of the method. Both the random and pseudo-Gaussian methods produced PHV with reasonable amplitudes. These methods were not used, however, as they have no real physical basis. The k^{-2} slip distribution was used, as it produces reasonable amplitudes, has a firm physical basis, and is well documented in the literature.

The k^{-2} slip spectrum was derived by Herrero and Bernard (1994) in order to model a self-similar rupture process that accounts for the ω^2 spectral law of seismic body-wave radiation. This slip distribution has been used to model both historical earthquakes and to simulate hypothetical events. Hartzell et al. (2005) used the k^{-2} distribution to model the 1994 Northridge earthquake. They compared the fit of three different slip distributions to the Northridge observed data and found that the k^{-2} model performed as well as the Von Karman distributions. The k^{-2} slip model has also been used to simulate hypothetical events using finite-difference methods, so it was an obvious choice for the present study (Harmsen et al., 2008).

For a rectangular fault of length L and width W , the spatial 2D Fourier spectrum of the slip distribution is given by:

$$D(k_x, k_z) = \frac{\Delta\bar{u}LW}{\sqrt{1 + \left(\left(\frac{k_x L}{K}\right)^2 + \left(\frac{k_z W}{K}\right)^2\right)}} e^{i\phi(k_x, k_z)} \quad (3.17)$$

where K is a dimensionless constant that controls the corner wave numbers, $\Delta\bar{u}$ is the mean slip, and ϕ is the slip spectrum (Galovic and Brokesova, 2004). In equation 3.17, k_x and k_z are the along-strike and down-dip wave numbers, respectively. The fault correlation lengths are given by L/K and W/K and the corner wave numbers are given by their reciprocals. Above these corner wave numbers, the slip spectrum decays asymptotically as a function of k^{-2} .

Herrero and Bernard (1994) considered ϕ to be random at any wave number outside the circle

$$k_x^2 + k_z^2 \leq \frac{1}{L^2} + \frac{1}{W^2}.$$

Within this circle, small wave numbers are chosen in order to concentrate slip near the center of the rectangular fault. This essentially places a large asperity, or region of slip at least twice the mean slip, near the center of the fault (Somerville et al., 1999). Gallovic and Brokesova (2004) pointed out that the deterministic part of this scheme may not be realistic, as many inversion studies indicate the presence of asperities at random locations on the fault plane. In order to employ a k^{-2} slip distribution that places asperities more realistically, Gallovic and Brokesova (2004) introduced what they called a hybrid slip generator. This technique produces asperities by placing blocks of constant slip on the fault plane before transformation to the wave number domain and application of equation 3.17 with random phase. Noise is added to the deterministic part of the distribution by the application of equation 3.17.

Slip distribution files were written for the simulations below using the FORTRAN code written by Gallovic and Brokesova (2004). This code allows the user to specify the mean slip and the number of asperities on the fault. Wells and Coppersmith (1994) equations were used to choose an appropriate mean slip for each fault. These are regression equations relating mean slip to moment magnitude:

$$\log(\Delta\bar{u}) = \begin{cases} -6.32 + 0.90 \cdot \log(\mathbf{M}_w), & \text{for strike-slip earthquakes} \\ -4.80 + 0.69 \cdot \log(\mathbf{M}_w), & \text{for reverse fault earthquakes} \end{cases} \quad (3.18)$$

where \mathbf{M}_w is the moment magnitude and $\Delta\bar{u}$ is the mean slip in meters. Two asperities per fault were used as this is consistent with the average number of asperities per fault (2.6) found by Somerville et al. (1999) in their investigation of historical earthquakes. Because of the relatively small number of scenarios considered in the present study, the character of the slip distribution was not changed between scenarios. This strategy essentially removed a variable between simulations and made it easier to observe the effect of structure on ground motions. The only change in slip model from fault to fault is the change in length and the subsequent change in mean slip based on \mathbf{M}_w . A plot of the hybrid k^{-2} slip distribution for the Cottonwood Grove fault is shown in Figure 3.4.

Because the finite-difference code requires input in seismic moment, once the slip distribution has been developed, it must be converted to moment in N-m. In general, moment is related to slip by:

$$M_0 = \mu A \bar{u} \quad (3.19)$$

where A is the ruptured area, μ is the rigidity of the material, and \bar{u} is the slip (Shearer, 1999). This equation is used to calculate the moment at each sub-source by using a 1D velocity model to estimate μ . Because $V_s = \sqrt{\mu/\rho}$, where ρ is the material density, a discrete form of equation 3.19 for each sub-source becomes:

$$M_{0,i} = \rho_i V_{s,i}^2 \Delta u_i A_i \quad (3.20)$$

for $i = 1, \dots, N$, where $V_{s,i}$ is the shear-wave velocity at the sub-source, A_i is the area of the sub-source, ρ_i is the material density at the sub-source, Δu_i is the slip at the sub-source, and N is the number of sub-sources. Once the moment has been calculated via equation 3.20, then $\sum_{i=1}^N M_{0,i}$ is compared to the target moment, calculated by equations 3.15 and 3.16. For all three slip models, $\sum_{i=1}^N M_{0,i}$ was within a few percentages of the target moment. The moment distribution was adjusted slightly by adding or subtracting a constant amount of moment to areas with nonzero slip in order to ensure that the correct target moment was reached.

Rise Time

Even at a point source, slip does not occur instantaneously, but is best modeled as a ramp function that is active for a certain duration, or rise time (Stein and Wysession, 2005). The rise time of each sub-source is calculated as a function of moment, following the method of Harmsen et al. (2008). If the sub-source moment is $M_{0,i}$, then the sub-source rise time is given by:

$$T_{r,i} = \begin{cases} T_{r0} + [M_{0,i}/\max(M_0)]\Delta, & \text{for } z \geq 5\text{km} \\ \max(T_{r0} + \Delta[(5 - z)/5], T_{r,i}(\text{for } z \geq 5\text{km})), & \text{for } z < 5\text{km} \end{cases} \quad (3.21)$$

for $i = 1, 2, \dots, N$, where N is the number of sub-sources (Harmsen et al., 2008). In equation 3.21, z is depth in km and T_{r0} is the shortest assumed rise time. For $M_w \geq 7$, which includes all hypothetical earthquakes in this study, T_{r0} is 2 s. Also, $\max(M_0)$ is the largest sub-source moment and Δ is a spread parameter, the suggested range of which is $0.8 \text{ s} < \Delta < 1.0 \text{ s}$. For the simulations below, Δ is set at 0.9 s.

For depths greater than 5 km, equation 3.21 increases rise time linearly with the seismic moment. Shallow sub-sources are assigned above average rise times. A plot of the rise time for the Cottonwood Grove slip model is shown in Figure 3.5.

Rupture Time

In order to capture the directivity effect in the ground-motion simulations, fault rupture must propagate in a realistic fashion. A common strategy in ground-motion simulations is to use a constant rupture velocity (e.g., [Saikia et al. \(2006\)](#)). This can lead to overly high ground motions in the direction of rupture associated with supershear occurring on shallow, low-velocity parts of the fault, however ([Harmsen et al., 2008](#)). For this reason, in the simulations below, the rupture propagates at 80 percent of the shear-wave velocity ([Stein and Wysession, 2005](#)).

The rupture time of each sub-source is calculated in the Octave script as a function of the distance from the hypocenter and a simplified 1D shear-wave velocity model. The user defines the hypocenter, which may be placed anywhere within the fault plane, and then the rupture time, t_{rup} , is computed via:

$$t_{rup} = \frac{\Delta_{hyp}}{0.8 \cdot V_s(z)} \quad (3.22)$$

where Δ_{hyp} is the distance from the hypocenter to the sub-source in m and $V_s(z)$ is the shear-wave velocity in m/s at depth z . A plot of the rupture front arrival time on the Cottonwood Grove fault with the hypocenter at the southern terminus of the fault is shown in [Figure 3.6](#). Note the lag in arrival time in shallow, low-velocity parts of the fault plane.

Table 3.1: Source and simulation parameters for the 6 June, 2003, Bardwell, Ky., earthquake.

centroid: -89.010° , 36.875° , depth=2400 km
fault geometry: circular, radius=440 m
$M_w = 4.0$
$M_0 = 1.3(\pm 0.5) \times 10^{15}$ N-m
$\phi = 90^\circ$
$\delta = 89^\circ$
$\lambda = -165^\circ$
volume of computation: $14 \times 18 \times 50$ km ³
fault geometry: disk, radius=440 m, width=200 m
global rise time=0.4 s
minimum grid spacing: 36.36 m
maximum frequency modeled: 3.0 Hz
time step: 0.00417 s
Number of point sources: 789

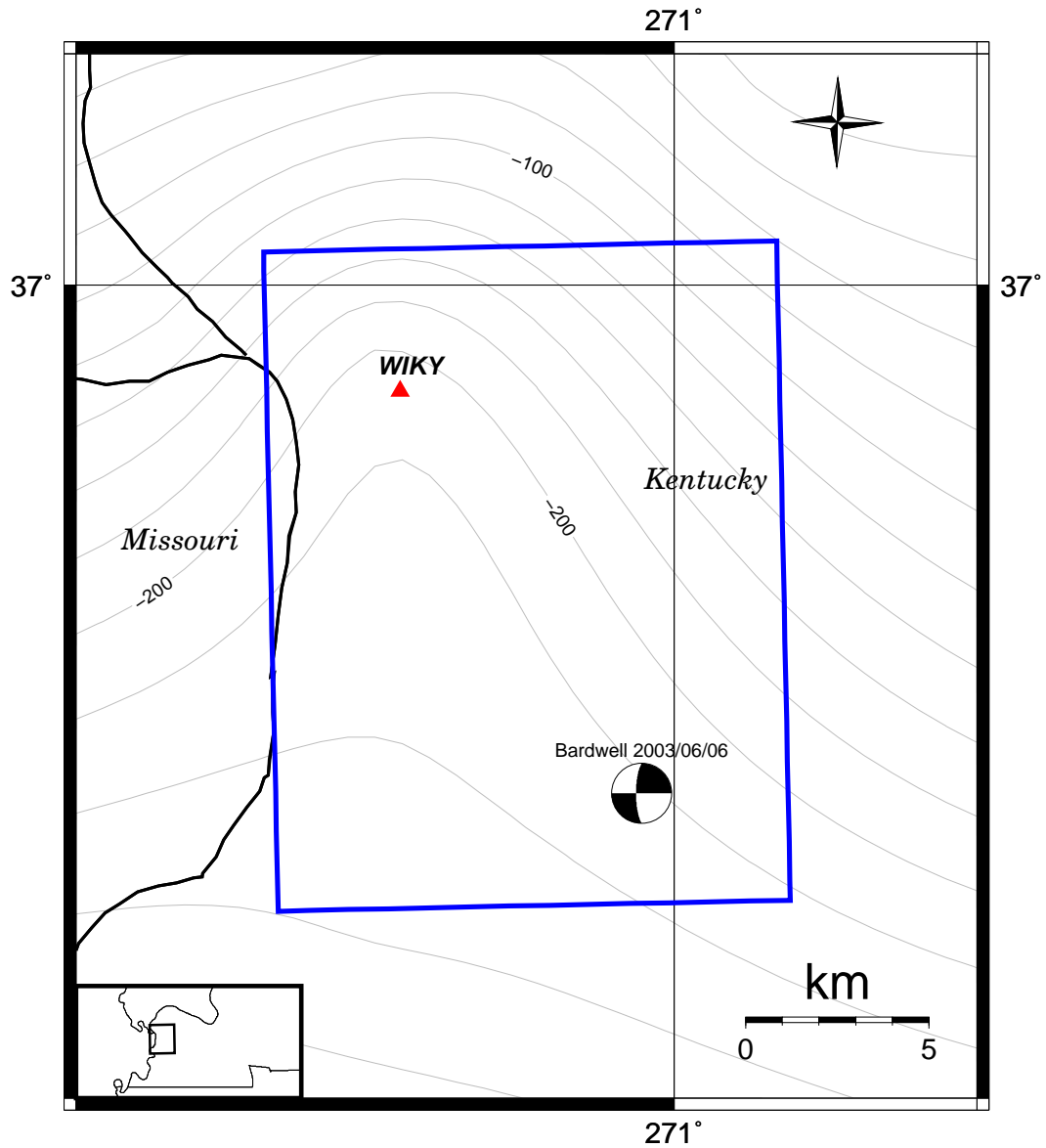


Figure 3.1: Bardwell focal mechanism and strong-motion station WIKY. Area of simulation is outlined by the blue rectangle. Contour lines are depth to Paleozoic bedrock in meters.

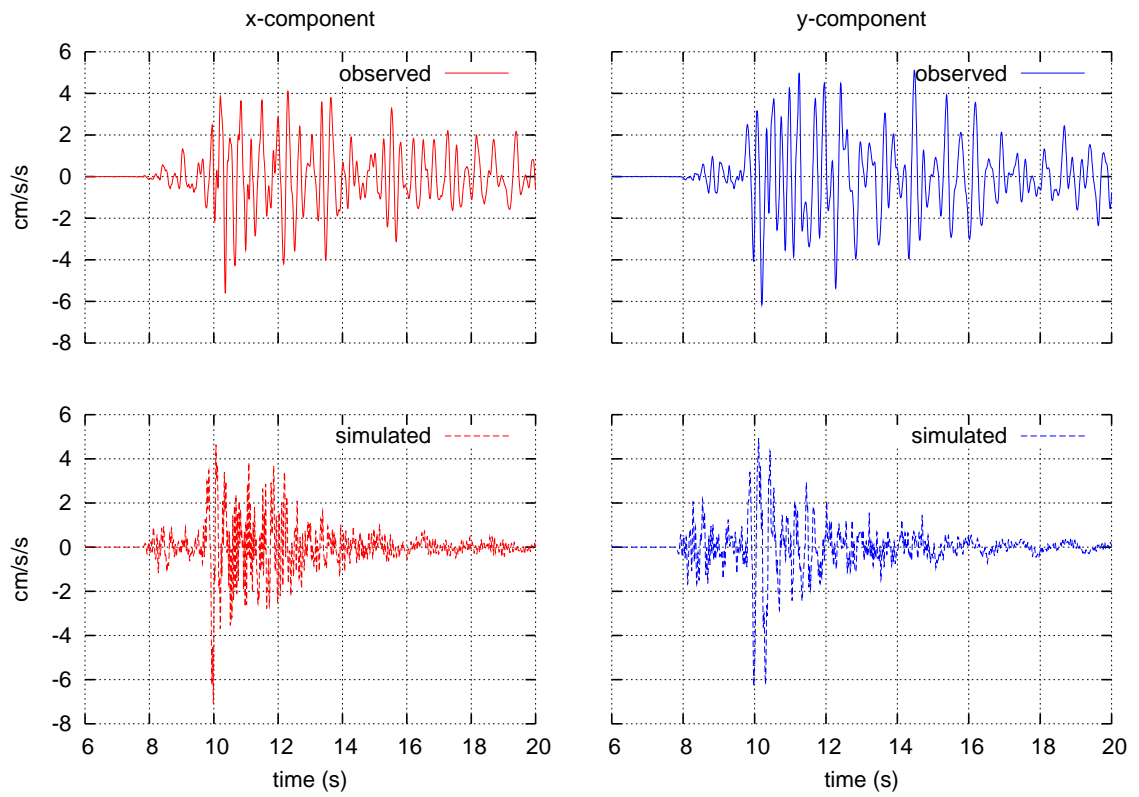


Figure 3.2: Observed and simulated Bardwell accelerograms at strong-motion station WIKY. Only the horizontal components are shown.

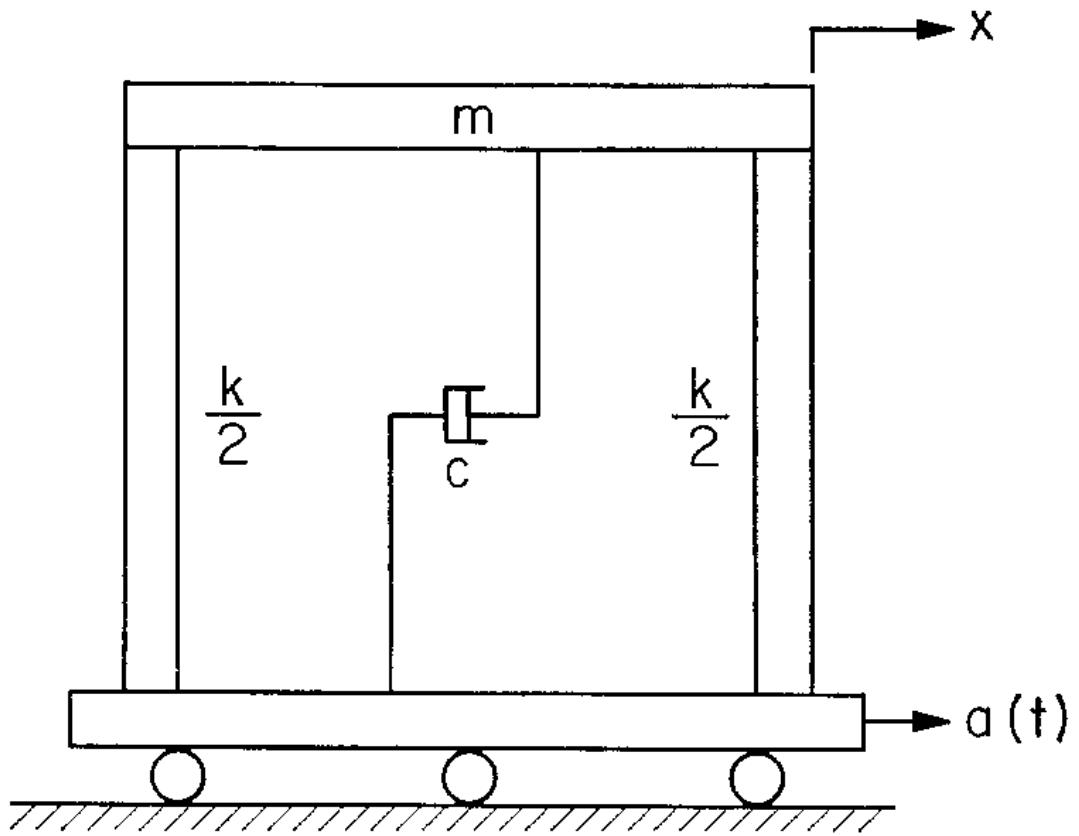


Figure 3.3: A single-degree-of-freedom system. From [Nigam and Jennings \(1969\)](#).

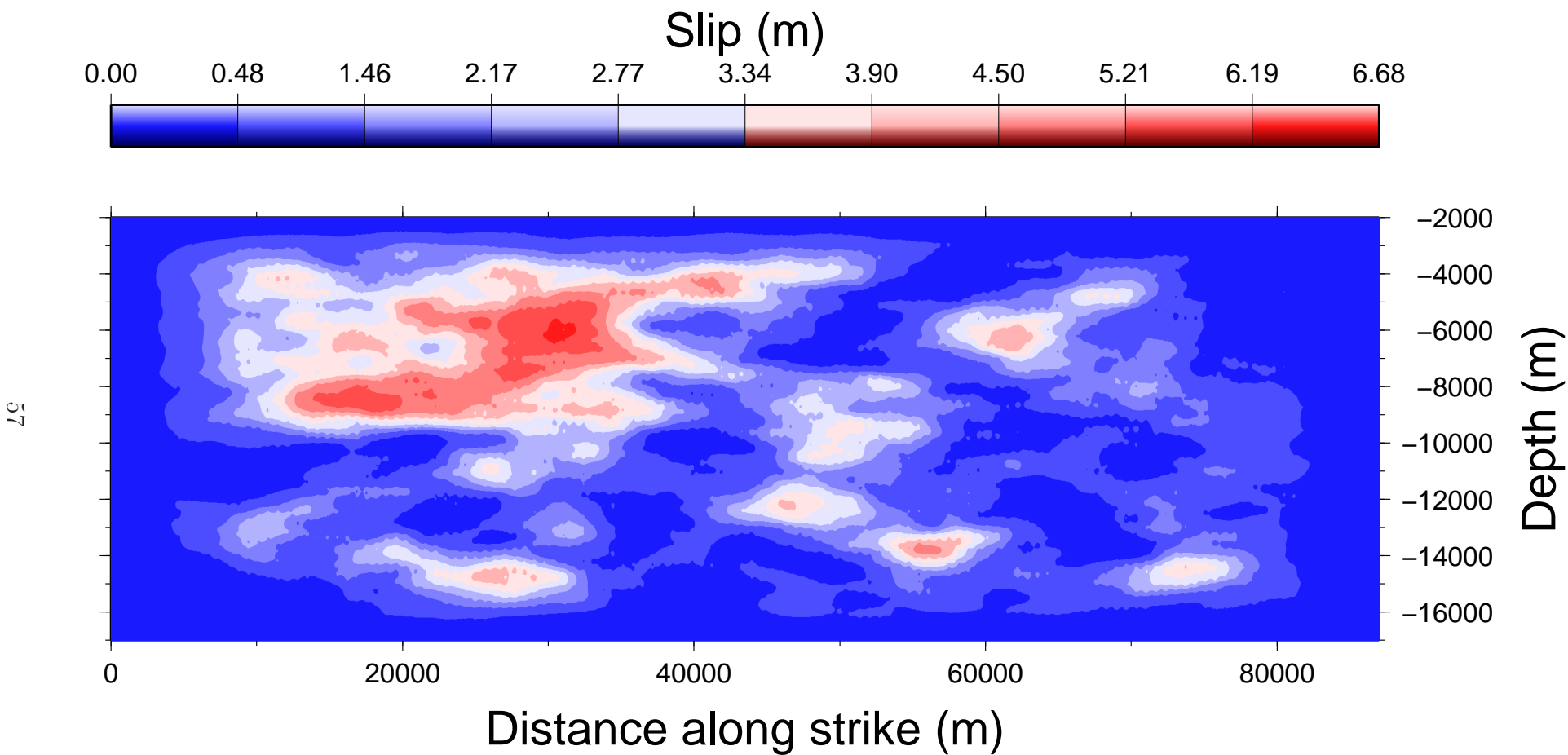


Figure 3.4: The k^{-2} slip distribution on the Cottonwood Grove fault.

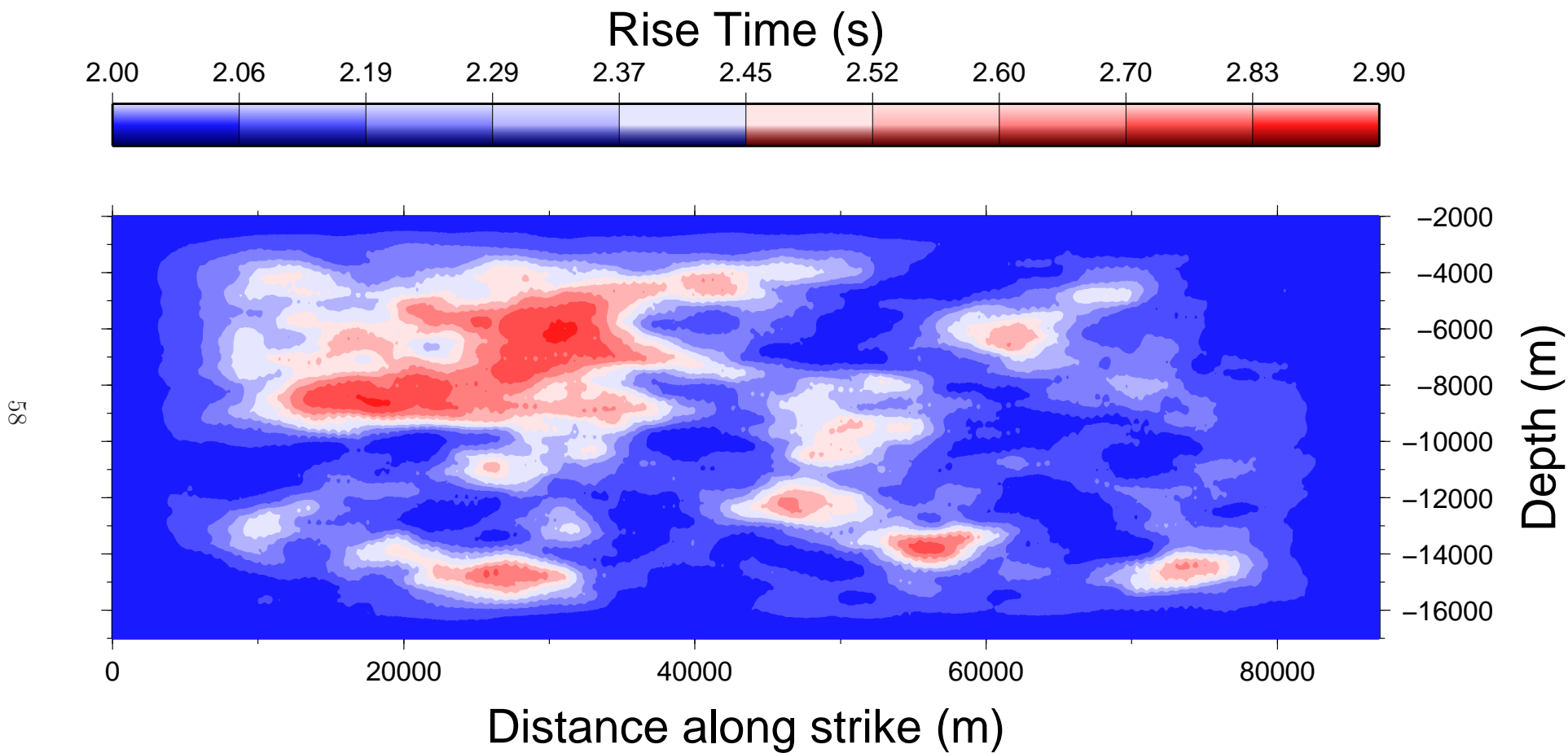


Figure 3.5: Rise time, calculated as a function of moment, on the Cottonwood Grove fault.

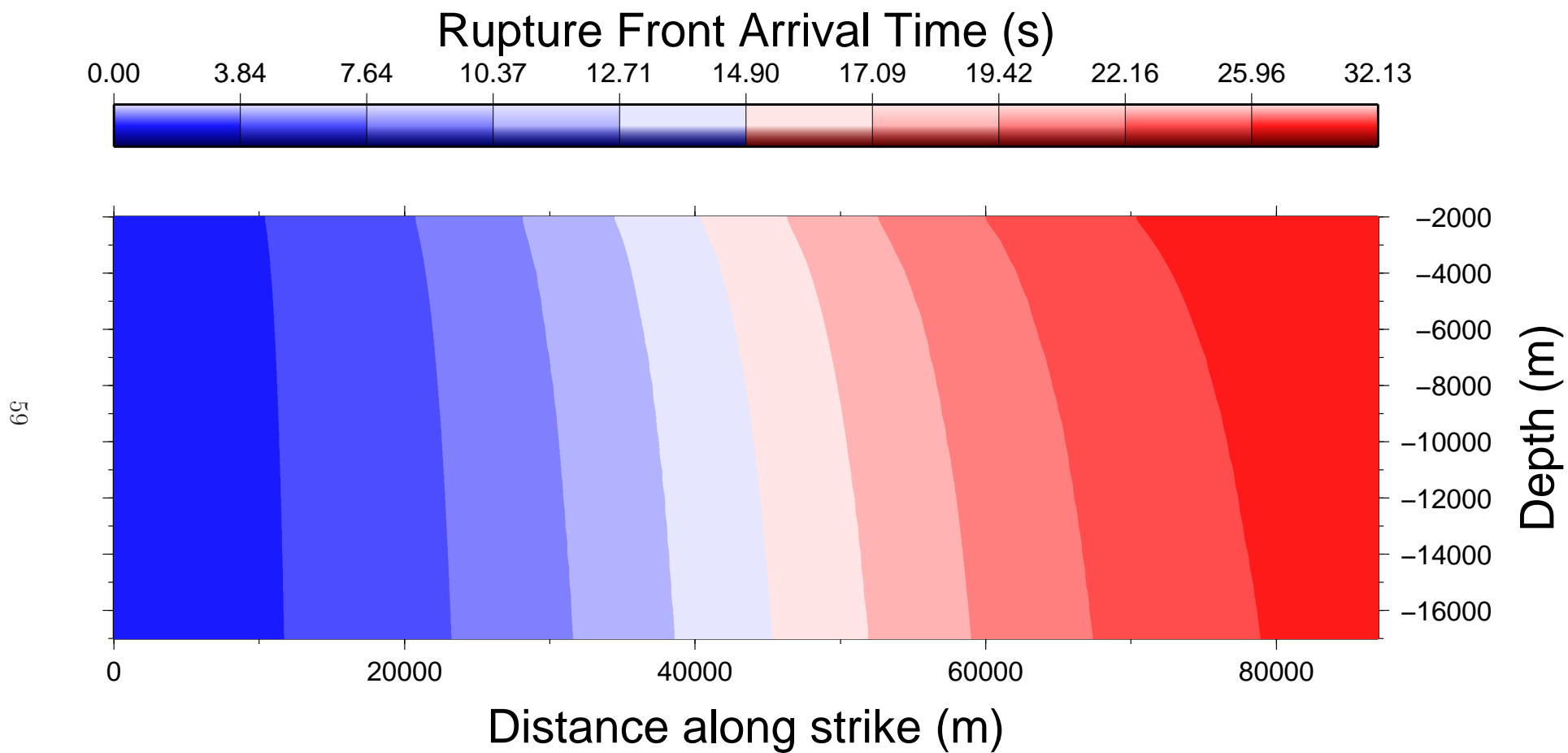


Figure 3.6: Rupture front arrival time on the Cottonwood Grove fault with hypocenter at the southern end of the fault.

Chapter 4 Results and Discussion

4.1 Output

The processed output from the finite-difference simulations is found at the end of this chapter in the form of ground-motion parameter maps of the free surface (Figs. 4.1–4.45). Also, animations showing how the PHV changes with time at the free surface are shown in the Appendix. Nine simulations were conducted, three simulations for each of the three major fault segments in the New Madrid seismic zone shown in Figure 1.1. For each fault segment, simulations were made with the hypocenter at the southern terminus of the fault and the rupture propagating to the north, and with the hypocenter at the northern terminus and the rupture propagating to the south; a bilateral fault was simulated by placing the hypocenter at the midpoint of the fault. All fault parameters, with the exception of the position of the hypocenter, were unchanged for each of the three simulations on a particular fault segment.

After processing the data from each run in order to compute the ground-motion parameter of interest, the parameter was plotted on a map of the study area using GMT. In order to produce the map, the ground-motion parameter was interpolated between the grid of hypothetical receivers using a variable tension spline via GMT's `surface` command. This allowed a large amount of information to be displayed graphically in a way that was easy to interpret.

Cottonwood Grove Fault

The Cottonwood Grove fault correlates to the southern arm of the New Madrid seismic zone as outlined by modern seismicity (Fig. 1.1). The length of the simulated rupture is based on the extent of modern observed seismicity. The width of the fault is modeled as 15 km with the top of the fault at a depth of 2 km. This width and depth is from Saikia et al. (2006) and is consistent with Chiu et al. (1992) as discussed in section 1.1. All other fault parameters used in the simulations are shown in Table 4.1.

Near-fault PHV values for the Cottonwood Grove fault with a northward propagating rupture are as high as 1.2 m/s. The area with the highest PHV is probably associated with the large, relatively shallow asperity that can be seen in the slip model (see Fig. 3.4). A clear directivity effect can be observed in the velocity and acceleration maps and is most pronounced in the animation. A notable feature in

the bracketed duration map (Fig. 4.2) is the area of longest duration not correlating with the area of highest PHV. Rather, the longest durations seem to be near the center of the embayment, suggesting that resonance associated with a particular depth to bedrock may be lengthening the duration of shaking. PSA maps indicate that structures with a 3.0-s period would be particularly vulnerable in this scenario, with accelerations reaching over 1.0 g for this period (see Fig. 4.4). Also, with a 5.0-s period, a large oval region of relatively high accelerations can be observed near the basin center, again suggesting resonance (see Fig. 4.5).

For the southward-propagating Cottonwood Grove scenario, all ground-motion parameters are smaller in magnitude than in the previous scenario. This seems to be a result of the proximity of the southern terminus of the fault to the boundary of the domain of computation. A large amount of the energy released by the rupture simply travels “out” of the domain of computation.

As expected, the PHV associated with the bilateral rupture is less than for the simple rupture propagating to the north (Fig. 4.11). That fact that it is higher than that for the southward-propagating rupture is probably a result of energy loss out of the domain of computation, as discussed above. The largest PHV values again appear to be associated with the the southern part of the fault, which contains the largest asperity. The duration map shows the longest duration to be near the basin center and away from the area with the largest PHV. The highest PSA values for this scenario are for 3-s periods. The bilateral rupture exhibits an obvious directivity effect, particularly to the north, as well as a secondary directivity effect orthogonal to the fault trace emanating from the epicenter (Fig. 4.11).

Reelfoot Thrust Fault

The extent of the Reelfoot thrust fault is outlined by the seismicity in Figure 1.1. As discussed in section 1.1, the dip varies along strike between 31° and 48°, but for convenience, an average dip of $(31 + 48)/2 = 39.5^\circ$ was used for the simulations below so that the source could be modeled as a rectangle. This averaging of dip is unlikely to significantly affect ground motions, and in fact, some researchers have modeled this fault as vertically dipping for convenience (Saikia et al., 2006). The vertical width of the fault in this study was 15 km and the top of the fault was at a depth of 2 km, as in Saikia et al. (2006). The width and depth herein is consistent with the observations made by Chiu et al. (1992), discussed in section 1.1. All other fault and simulation parameters are in Table 4.2.

The northward-propagating Reelfoot scenario shows a clear directivity effect and

the largest values of PHV are associated with the part of the fault with the largest slip (Fig. 4.16). The bracketed duration map shows a north–south-trending ellipse of long duration (Fig. 4.17). The longest durations are at the extreme northern edge of the domain of computation and appear to be a result of the basin edge effect. The animation of this scenario clearly shows persistently high velocities in this area as the shallow past-Paleozoic sediments appear to act as a wave guide. Both PHV and PSA values are higher for this scenario than for the Cottonwood Grove scenarios discussed above, consistent with the tendency of dip-slip faults to produce higher ground motions than strike-slip faults (Kramer, 1996).

For the southward-propagating scenario, PHV values are higher than those in the previous scenario, but durations are shorter (Figs. 4.16–4.17). This may be because the direction of propagation is away from the embayment boundary so that there is no wave guide effect. This scenario has the smallest magnitude but the highest PHV values of all the scenarios, including the higher frequency North fault scenarios. This indicates that, all else being equal, thrust-fault earthquakes may be much more damaging than an earthquake on a strike-slip fault in the region. As another indication of this, PSA with 3-s periods for this event approach 1.5 g (Fig. 4.24).

The bilateral rupture on the Reelfoot thrust fault shows very high PHV associated with fault asperities (Fig. 4.26). Long durations are exhibited in the southern, deep part of the embayment (Fig. 4.27). Once again, PSA's with periods of 3 s have the highest magnitudes, with a linear area of high magnitude to the south and sub-parallel to the strike of the fault. The bilateral rupture exhibits a secondary directivity effect orthogonal to the fault trace emanating from the epicenter (Fig. 4.26).

New Madrid North Fault

The New Madrid North fault is delineated by modern-day microseismicity (see Fig. 1.1). The width of the fault was modeled as 15 km and the top of the fault at a depth of 2 km. This is consistent with Chiu et al. (1992), Saikia and Somerville (1997), and Saikia et al. (2006) as discussed in section 1.1. As discussed above, one of the goals of this study is to investigate the effect of a large event on the north fault on Paducah, Ky. Because the North fault, Paducah, and a significant area of the embayment boundary are relatively close to each other, these features could be included in a smaller domain of computation in order to compute synthetics with a higher frequency content (1.0 Hz). All other simulation and fault parameters for the North fault are found in Table 4.3.

In the northward-propagating scenario, the directivity effect is again visible (Fig.

4.31). Although maximum PHV is not as high as in the Reelfoot thrust scenarios, there are still velocities as high as 1.44 m/s, with Paducah experiencing 0.5 m/s. Bracketed durations are the longest of all the scenarios and show a distinct asymmetry, indicating a high degree of influence from the embayment structure (Fig. 4.32). Paducah experiences accelerations in excess of 0.05 g for between 12 and 15 s. Structures in and around Paducah with a natural frequency of 3 s would be particularly vulnerable, experiencing accelerations between 0.5 g and 0.7 g (Fig. 4.33). In the PSA map with 5-s period for this scenario (Fig. 4.35), there is an area of anomalously high acceleration to the west that may be a result of numerical instability in the absorbing boundary region or may be resonance associated with a particular depth to bedrock. The fact that it is not present in other maps from the same simulation run argues against it being a numerical artifact.

Maximum PHV values for the southward-propagating scenario are lower than for the previous scenarios, possibly because the rupture does not propagate toward the embayment boundary. Bracketed durations are very short, and would probably be longer to the south of the domain of computation due to the directivity effect. Values for PHV and PSA at Paducah for this event are very low relative to the previous scenario, highlighting the importance of the directivity effect.

The bilateral rupture scenario exhibits higher values of PHV than the previous scenario and again places Paducah in an area of high velocity, although the highest values of PHV are along the southern half of the fault (Fig. 4.41). Time-series for a receiver within 3 km of Paducah show that the city is likely to experience higher amplitudes in response to northward-propagating simple rupture (Fig. 4.47) compared to a bilateral rupture (Fig. 4.48).

Despite the higher PHV being found to the south in this scenario, the longest durations are found to the northeast and are probably a result of the basin edge effect. The highest values of PSA are to the south for 3- and 5-s periods, but to the north for the 1-s period. The bilateral rupture exhibits a secondary directivity effect orthogonal to the fault trace emanating from the epicenter (Fig. 4.41).

4.2 Conclusions

The simulations described above indicate that at the frequencies considered, the following are the most salient features affecting strong ground motion in the upper Mississippi embayment:

1. fault proximity

2. directivity effect
3. asperity distribution
4. 3D geologic structure

Each of these features is discussed in detail below.

Faulty Proximity

Although it is not surprising that the highest-magnitude ground motions are near the fault trace, the simulations above show that PHV drops very quickly with increasing distance from the fault if the distance is orthogonal to strike. For example, in Figure 4.31 the area of maximum PHV is centered on the fault trace and falls off quickly with distance from the fault, roughly following:

$$\text{PHV}(d) = 1.4942 \times .9263^d \quad (4.1)$$

where d is distance from the fault trace orthogonal to the strike of the fault. Equation 4.1 indicates that, even for the large ($M_w \approx 7.17$) event simulated in Figure 4.31, areas 20 km from the fault trace experience velocities of 0.3 m/s and areas 50 km away experience 0.03 m/s.

Although in a different tectonic setting than the intraplate events simulated here, the $M_w = 7.9$ Sichuan, China, earthquake of May 12, 2008, provides a real-world example of the importance of fault proximity to ground motion. The hypocenter was located 80 km west-northwest of Chengdu, China, on the northeast-striking Longmenshan thrust fault (USGS, 2008). The length of rupture was more than 260 km, affecting a broad swath of central China. Figure 4.46 shows a plot of the peak ground acceleration (PGA) for this event. Note that the peak PGA (0.65 g) is very near-fault and that PGA values drop quickly with increasing distance from the fault trace in a similar fashion to what is observed in the simulations discussed above.

Directivity Effect

The phenomenon that provides perhaps the most dramatic effect on strong motion is the directivity effect. This can be seen by comparing Figure 4.31 with Figure 4.36. It should be stressed that the only difference between these two simulations is the location of the hypocenter and the direction of rupture propagation, yet Paducah, Ky., experiences dramatically different PHV and duration of shaking. In Figure

4.36, Paducah experiences $PHV \leq 0.065$ despite being within 35 kilometers of the hypocenter. In Figure 4.31, however, where the rupture propagates toward Paducah, the city experiences PHV of up to 0.47 m/s, with durations of as long as 15 s.

Also apparent in the simulations is the way in which directivity can trigger a basin edge effect. In all the scenarios, higher PHV and longer durations are visible where the direction of rupture is to the north, toward the basin edge, when compared to southward-propagating ruptures. Basin edge effects are further discussed below.

The distribution of PGA from the Sichuan earthquake exhibits a clear directivity effect, with higher accelerations occurring in the directions of rupture. The hypocenter of this event was near the southwestern terminus of the ruptured area and the propagation was to the northeast. A comparison of the northeast-propagating Sichuan event (Fig. 4.46) to the northeast-propagating Cottonwood Grove scenario (Fig. 4.1) shows a similar directivity pattern.

Asperity Distribution

In all the simulations shown below, the maximum values of PHV are located at the part of the fault with the greatest slip, associated with the large asperity visible in Figure 3.4. This is to be expected as this is the region of highest energy release and it is a relatively shallow asperity. It does, however, highlight the importance of the slip distribution to strong ground motion, and because of the highly variable nature of earthquake slip distributions, indicates the uncertainty inherent in deterministic earthquake models.

3D Geologic Structure

The effect of the 3D structure on ground motion is indicated by the asymmetry that may be observed in the ground-motion parameter maps below (e.g., Fig. 4.31). This effect may be quantified by the use of equation 3.14. Amplification maps from simulations of ruptures on the three major faults with hypocenters to the south are shown in Figures 4.49–4.51. These maps indicate that for the majority of the volume, the 3D structure has a deamplifying effect on the PHV. The exception is the northern parts of the region, where a combination of directivity and basin edge effects seems to be inducing amplification.

The deamplifying nature of the 3D embayment structure in the study area is consistent with results obtained by Saikia et al. (2006). They compared 3D to 1D synthetics generated in finite-difference simulations and concluded that the represen-

tation of impedance boundaries in the sediment rather than the 3D geometry of the structure is more of a control on ground motions.

Despite the deamplifying nature of the 3D structure, it does seem to have a significant influence on duration of shaking, as indicated by the bracketed duration maps below. In Figures 4.2, 4.12, 4.22, and 4.27, the areas of longest duration all seem to be associated with the deeper, central part of the basin. Also, Figures 4.17, 4.32, and 4.42 all show areas of high duration that appear to be induced by the basin edge effect.

The basin edge effect is perhaps the most salient structurally induced effect in the ground-motion maps below. It appears to increase PHV as the directivity effects interact with the basin boundary in Figures 4.16 and 4.31. The effect is seen most clearly in Figure 4.49, where PHV is amplified by a factor of 3.5 at the boundary. This is a result of shallow, low-velocity sediments lying directly on the Precambrian bedrock (Street et al., 2001). Also, the animation of the northward-propagating rupture in the Reelfoot thrust shows a wave guide effect as waves propagate into the increasingly shallower sediment to the north.

4.3 Alternate Scenarios

The simulations discussed above were undertaken assuming that the active faults in the New Madrid seismic zone are delineated by the modern background seismicity. The location and lateral extent of the finite sources used in the simulations were approximated by lines through the areas with the greatest concentrations of seismicity. Although this is a reasonable strategy, another method would be to model finite faults that are similar to those that were responsible for the 1811-1812 earthquake triple. Every earthquake is unique, but simulated finite sources can be given a degree of realism by modeling faults that have produced large earthquakes in the past.

The fault traces used below are most like the “S1” scenario of Johnston and Schweig (1996), those other preferred scenario. The fault traces were digitized from Johnston and Schweig (1996) and are shown in Figure 4.52. The North fault and Cottonwood Grove fault are composed of linear segments whereas the Reelfoot fault is composed of three linear segments with variable strike. The finite sources were constructed as described in section 3.4 with the exception of the Reelfoot fault parameters. Writing source files for the Reelfoot fault was more complicated in these scenarios because the fault trace is no longer a simple linear segment. The code for writing source files was modified to account for this, as well as for the dipping nature

of the Reelfoot fault. The code is similar to that used in the previous simulations except that now the fault trace is defined in a piecewise manner. The strike of each point depends upon the segment on which it lies. Also, the discretization is done in rows of increasing depth, so that each row may be laterally shifted to account for the dip of the fault plane. The code is in the Appendix. All fault parameters are listed in Tables 4.4–4.6.

Synthetics up to a frequency of 0.5 Hz were calculated for these scenarios in a $200 \text{ km} \times 200 \text{ km} \times 50 \text{ km}$ volume. This volume is in a slightly different location than the one described above, so as to keep all three faults away from the volume boundaries and to incorporate a significant part of the Mississippi embayment boundary.

The velocity model for these simulations was constructed as described in chapter 2. A contour map showing the depth to the layer with a shear wave velocity of 2000 m/s is shown in Figure 4.53 for reference. The areas with greatest depth to this layer are along the embayment axis, consistent with the synclinal nature of the basin. Profiles of the velocity model are found in chapter 2.

Results and Discussion for Alternate Scenarios

The output from the alternate scenario simulations can be found in Figures 4.54–4.71 and in the Appendix. Plots of peak horizontal velocity (PHV) and bracketed duration are shown, as well as animations of the evolution of horizontal velocity at the free surface. Nine scenarios were simulated, three for each of the three “S1” major fault segments of Johnston and Schweig (1996). For each fault segment, a simulation was made with the hypocenter at the ends of the faults and with a bilateral rupture with the hypocenter located mid-fault. The same slip model was retained for each of the three simulations for a particular fault segment. The velocity model and volume of simulation was the same for all nine scenarios.

The largest ground motion amplitudes and longest durations resulted from ruptures along the Cottonwood Grove fault (Figs. 4.54–4.58). The length of the Cottonwood grove fault digitized from Johnston and Schweig (1996) is significantly larger than both the North fault and the Reelfoot fault. Consequently, the energy released from ruptures on the Cottonwood Grove fault is 1.8 times that of the Reelfoot fault and 2.3 times that of the North fault, resulting in the high ground motions. The bracketed duration for the rupture with the hypocenter at the south is 17 seconds longer than the longest duration from the Reelfoot fault or North fault simulations. The longer duration in the southern hypocenter may be a result of the rupture propagating in the direction in which the basin is shallowing, causing waves enhanced by

the directivity effect to be trapped in the increasingly thin post-Paleozoic sediments. This is in contrast to the values of PHV in the south-propagating rupture that are lower by nearly half; therefore, this is interpreted this as a result of the rupture propagating towards the deepest portion of the basin.

For the bilateral rupture, values of PHV and durations were similar to those for the northward-propagating rupture. In this scenario, the effect of slip distribution is most apparent, with the large asperity being located on the southern half of the fault plane in the region of highest PHV (Fig. 3.4). This scenario also exhibits a secondary directivity effect, emanating from the hypocenter and perpendicular to strike.

Patterns of ground motion from the Reelfoot fault scenarios differed from the strike-slip scenarios as a result of the mechanics of the thrust fault (Figs. 4.60–4.65). Values of PHV and durations were less localized around the fault trace. This is because the fault dips to the southwest and because the variations in strike tend to disperse the directivity effect; therefore, this results in a larger area with $\text{PHV} \geq 0.4$ m/s compared with the Cottonwood Grove scenarios. As expected, areas of highest PHV and longest duration are on the hanging wall of the reverse fault. The rupture with the hypocenter to the south probably produces a lower PHV than the other two Reelfoot scenarios because of the change in fault strike, thus disrupting the directivity effect soon after the rupture front passes the area of largest slip. In all three Reelfoot scenarios, the longest durations are found near the northern end of the fault trace where the basin is the shallowest. Also exhibited in all three Reelfoot scenarios is the degree to which PHV is controlled by the asperity distribution in the slip model, with the highest values of PHV (e.g., $\text{PHV} \approx 2.4$ m/s in the bilateral rupture) being close to the fault segment with the highest slip.

The digitized fault areas of 1,859.78 km², 1,321.7 km², and 1,071.21 km² for the Cottonwood Grove, Reelfoot, and North faults, respectively, result in the energy release from the North fault scenarios being 43 percent of the Cottonwood Grove scenarios and 79% of the the Reelfoot scenarios. Consequently, North fault ruptures result in the lowest PHV values (maximum 1.6 m/s) and the shortest durations (as short as 15 s) of all of the scenarios (see Figs. 4.66–4.70). PHV as high as 1.6 m/s are observed in the south end fault rupture, and is interpreted as a result of the interaction of the directivity and the basin edge. Unexpectedly, the longest durations from the North fault rupture were associated with the southward-propagating scenario, the scenario with the smallest PHV. This is likely caused by the short durations in the north-propagating rupture and proximity of the source to the absorbing boundary.

In all three North fault scenarios, the highest values of PHV, and longest durations are in the vicinity of the large asperity on the southern half of the fault plane.

Conclusions for Alternate Scenarios

Additional simulations using fault traces digitized from [Johnston and Schweig \(1996\)](#) exhibit similar characteristics to the simulations discussed in [Sec. 4.1](#) in that the long-period ground motions considered are most strongly controlled by finite-fault mechanics. The directivity effect is obvious in all nine scenarios, as well as the spatial correlation between regions of high PHV with portions of the fault containing asperities. There is also evidence of the effect of 3D geological structure on ground motions in the form of longer durations near basin edges in the Cottonwood Grove and Reelfoot scenarios, and perhaps increased durations as a result of resonance in the North fault scenarios.

4.4 Recommendations

Few large-scale, full wave-field ground-motion simulations have been conducted for the upper Mississippi embayment. Although [Saikia et al. \(2006\)](#) and this study have provided preliminary long-period results using a simplified velocity model, more work is needed to expand the frequency content of simulations, simulate the wave-field on a larger region, and refine the velocity model.

Limits were imposed on the frequency content and extent of the domain of computation by [equation 2.1](#), the spatial sampling criteria. This is an inherent feature of the explicit finite-difference scheme and may only be overcome by employing more computing resources. At the University of Kentucky, such resources are available in the form of supercomputing facilities. Although the simulations above were conducted on a single node of this network (four processors), 1,360 processors are actually available. Applying these resources to ground-motion simulations would allow for higher frequencies to be modeled on a larger volume.

In order to utilize the University of Kentucky's supercomputer to its full potential, calculations must be partitioned and distributed to the processing nodes using the Message Passing Interface (MPI). [Minkoff \(2002\)](#) developed a spatially parallel 3D finite-difference scheme on a staggered-grid for the simulation of wave propagation that exhibited scaled speed-ups of up to 94 percent over non-parallel algorithms. Applying such a technique to the upper Mississippi embayment would provide simulations on an unprecedented scale and frequency content. The drawback to this method

would be the difficulty of implementing MPI, which requires significant programming expertise.

Another method used to achieve higher frequency content in ground-motion simulations is to combine 3D and 1D synthetics. In this method, 3D synthetics are computed using a finite-difference technique on a 3D velocity structure up to a frequency of 1.0 to 2.0 Hz. High-frequency synthetics are computed on a 1D velocity structure using a less computationally intensive linear equivalent model, such as **SHAKE**. The broadband synthetics are computed by combining the 3D and 1D synthetics through the use of a matched-filter technique (Liu and Archuleta, 2006). This method could be easily implemented in the study area by combining 1D simulations with the 3D synthetics computed in this study.

The velocity model described in chapter 2 was compiled largely from general empirical relations. Only the very near-surface, post-Paleozoic layer has elastic parameters derived from direct observation. Although this level of accuracy is appropriate for long-period simulations, where the mechanics of the finite-fault is the greatest control of peak ground motions, the velocity model will need to be improved as simulations acquire a more realistic frequency content. Data should be added to the velocity model from additional near-surface seismic surveys and from data inversion from the regional seismic network. One of the most promising techniques for deriving basin-wide 3D velocities is the *S*-to-*P* converted wave method employed by Chen et al. (1996). This method can estimate sediment shear-wave velocity if the *P*-wave velocity and sediment thickness below a receiver is known. These parameters may be directly measured using seismic refraction surveys and well-log data. Shear-wave velocity can then be calculated by measuring the travel-time difference between the direct *S*-wave and the *S_p*-wave, the *S*-wave converted to *P* at the Paleozoic unconformity. This technique is currently being used to derive a basin-wide 3D velocity model of the upper Mississippi embayment (Liu, personal communication).

Simulations of ground motion in the upper Mississippi embayment will continue to improve. Velocity models of the region will become more realistic as data are gathered from both controlled-source experiments and passive observations of seismicity. Simulations will become more robust as additional computing power becomes available and as numerical techniques become more efficient. It is hoped that these models will help seismologists and engineers gain insight into the seismic hazard in the eastern United States, and that such insights will help planners mitigate the risk in the region.

Copyright© Kenneth A. Macpherson, 2009.

Table 4.1: Source and Simulation parameters for the Cottonwood Grove fault

Northern most point=	-89.37°, 36.37°
Southern most point=	-90.27°, 35.73°
Hypocenter _{south} (x, y, z) =	-90.27°, 35.73°, 9000 meters
Hypocenter _{north} (x, y, z) =	-89.37°, 36.37°, 9000 meters
Hypocenter _{mid} (x, y, z) =	-89.91°, 35.99°, 9000 meters
Length of the main fault =	86549.3 meters
Width of main fault =	15,000 meters
Area of Main fault =	1,298.24 km ²
Total number of sub-events=	16,384
Number of points along the length of the fault=	128
Number of points along the width of the fault=	128
M_w =	7.15562
Maximum Slip =	6.68067 meters
Average Slip =	1.31837 meters
Sum of sub-event moments =	6.81449×10^{19} N-m
Target Moment =	6.81449×10^{19} N-m
Accuracy before adjustment =	0.995247 %
Strike =	52.3053°
Dip =	90°
Rake =	180°
Envelope in which parameters vary =	5°
Start Time =	0.0 seconds
Volume of computation:	$200 \times 200 \times 50$ km ³
Minimum grid spacing:	218.18 meters
Minimum number of nodes per wavelength:	6.14
Maximum frequency modeled:	0.5 Hz
Time step:	0.0203 seconds

Table 4.2: Source and simulation parameters for the Reelfoot thrust fault

Northern most point= $-89.58^\circ, 36.59^\circ$
 Southern most point= $-89.30^\circ, 36.16^\circ$
 Hypocenter_{south} $(x, y, z) = -89.30^\circ, 36.16^\circ, 9000$ meters
 Hypocenter_{north} $(x, y, z) = -89.58^\circ, 36.59^\circ, 9000$ meters
 Hypocenter_{mid} $(x, y, z) = -89.43^\circ, 36.42^\circ, 9000$ meters
 Length of the main fault = 75,631.3 meters
 Width of main fault =15,000 meters
 Area of Main fault = 1,134.47 km²
 Total number of sub-events= 16,384
 Number of points along the length of the fault= 128
 Number of points along the width of the fault= 128
 $M_w = 7.07931$
 Maximum Slip = 6.14539 meters
 Average Slip = 1.215 meters
 Sum of sub-event moments = 5.23565×10^{19} N-m
 Target Moment = 5.23565×10^{19} N-m
 Accuracy before adjustment = 1.04319 %
 Strike = 338.449°
 Dip = 39.5°
 Rake = 90°
 Envelope in which parameters vary = 5°
 Start Time =0.0 seconds
 Volume of computation: $200 \times 200 \times 50$ km³
 Minimum grid spacing: 218.18 meters
 Minimum number of nodes per wavelength: 6.14
 Maximum frequency modeled: 0.5 Hz
 Time step: 0.0203 seconds

Table 4.3: Source and simulation parameters for the North fault

Northern most point= $-89.27^\circ, 37.01^\circ$
 Southern most point= $-89.62^\circ, 36.55^\circ$
 Hypocenter_{south} $(x, y, z) = -89.62^\circ, 36.55^\circ, 9000$ meters
 Hypocenter_{north} $(x, y, z) = -89.27^\circ, 37.01^\circ, 9000$ meters
 Hypocenter_{mid} $(x, y, z) = -89.45^\circ, 36.78^\circ, 9000$ meters
 Length of the main fault =91,084 meters
 Width of main fault =15,000 meters
 Area of Main fault = 1,366.26 km²
 Total number of sub-events= 16,384
 Number of points along the length of the fault= 128
 Number of points along the width of the fault= 128
 $M_w = 7.17824$
 Maximum Slip = 6.9692 meters
 Average Slip = 1.38 meters
 Sum of sub-event moments = 7.36828×10^{19} N-m
 Target Moment = 7.36828×10^{19} N-m
 Accuracy before adjustment = 1.01393 %
 Strike = 37.3762°
 Dip = 90°
 Rake = 180°
 Envelope in which parameters vary = 5°
 Start Time =0.0 seconds
 Volume of computation: $100 \times 100 \times 50$ km³
 Minimum grid spacing: 109.09 meters
 Minimum number of nodes per wavelength: 5.54
 Maximum frequency modeled: 1.0 Hz
 Time step: 0.0112 seconds

Table 4.4: Source and simulation parameters for the Cottonwood Grove fault

Northern most point=	-89.48°, 36.30°
Southern most point=	-90.38°, 35.55°
Hypocenter _{south} (x, y, z) =	-90.38°, 35.55°, 9000 meters
Hypocenter _{north} (x, y, z) =	-89.48°, 36.30°, 9000 meters
Hypocenter _{mid} (x, y, z) =	-89.93°, 35.92°, 9000 meters
Length of the main fault =	116,236 meters
Width of main fault =	16,000 meters
Area of Main fault =	1,859.78 km ²
Total number of sub-events=	16,384
Number of points along the length of the fault=	128
Number of points along the width of the fault=	128
M_w =	7.31485
Maximum Slip =	9.27048 meters
Average Slip =	1.8335 meters
Sum of sub-event moments =	1.18108×10^{20} N-m
Target Moment =	1.18108×10^{20} N-m
Accuracy before adjustment =	1.12125 %
Strike =	45.4085°
Dip =	90°
Rake =	180°
Envelope in which parameters vary =	5°
Start Time =	0.0 seconds
Volume of computation:	$200 \times 200 \times 50$ km ³
Minimum grid spacing:	218.18 meters
Minimum number of nodes per wavelength:	6.14
Maximum frequency modeled:	0.5 Hz
Time step:	0.0203 seconds

Table 4.5: Source and simulation parameters for the Reelfoot fault

Northern most point= $-88.97^\circ, 37.24^\circ$
 Southern most point= $-89.59^\circ, 36.59^\circ$
 Hypocenter_{south} $(x, y, z) = -89.59^\circ, 36.59^\circ, 9000$ meters
 Hypocenter_{north} $(x, y, z) = -88.97^\circ, 37.24^\circ, 9000$ meters
 Hypocenter_{mid} $(x, y, z) = -89.29^\circ, 36.92^\circ, 9000$ meters
 Length of the main fault =57,933.5 meters
 Width of main fault =22,814 meters
 Area of Main fault = 1,321.7 km²
 Total number of sub-events= 16,384
 Number of points along the length of the fault= 128
 Number of points along the width of the fault= 128
 $M_w = 7.13902$
 Maximum Slip = 6.66151 meters
 Average Slip = 1.3355 meters
 Sum of sub-event moments = 6.43469×10^{19} N-m
 Target Moment = 6.4369×10^{19} N-m
 Accuracy before adjustment = 1.09966 %
 Strike = 332.736° (average)
 Dip = 39.5°
 Rake = 90°
 Envelope in which parameters vary = 5°
 Start Time =0.0 seconds
 Volume of computation: $200 \times 200 \times 50$ km³
 Minimum grid spacing: 218.18 meters
 Minimum number of nodes per wavelength: 6.14
 Maximum frequency modeled: 0.5 Hz
 Time step: 0.0203 seconds

Table 4.6: Source and simulation parameters for the North fault

Northern most point= $-88.97^\circ, 37.24^\circ$
 Southern most point= $-89.59^\circ, 36.59^\circ$
 Hypocenter_{south} $(x, y, z) = -89.59^\circ, 36.59^\circ, 9000$ meters
 Hypocenter_{north} $(x, y, z) = -88.97^\circ, 37.24^\circ, 9000$ meters
 Hypocenter_{mid} $(x, y, z) = -89.29^\circ, 36.92^\circ, 9000$ meters
 Length of the main fault =59,511.4 meters
 Width of main fault =18,000 meters
 Area of Main fault = 1,071.21 km²
 Total number of sub-events= 16,384
 Number of points along the length of the fault= 128
 Number of points along the width of the fault= 128
 $M_w = 7.07047$
 Maximum Slip = 5.93803 meters
 Average Slip = 1.17465 meters
 Sum of sub-event moments = 5.07815×10^{19} N-m
 Target Moment = 5.07815×10^{19} N-m
 Accuracy before adjustment = 0.983213 %
 Strike = 33.0721°
 Dip = 90°
 Rake = 180°
 Envelope in which parameters vary = 5°
 Start Time =0.0 seconds
 Volume of computation: $200 \times 200 \times 50$ km³
 Minimum grid spacing: 218.18 meters
 Minimum number of nodes per wavelength: 6.14
 Maximum frequency modeled: 0.5 Hz
 Time step: 0.0203 seconds

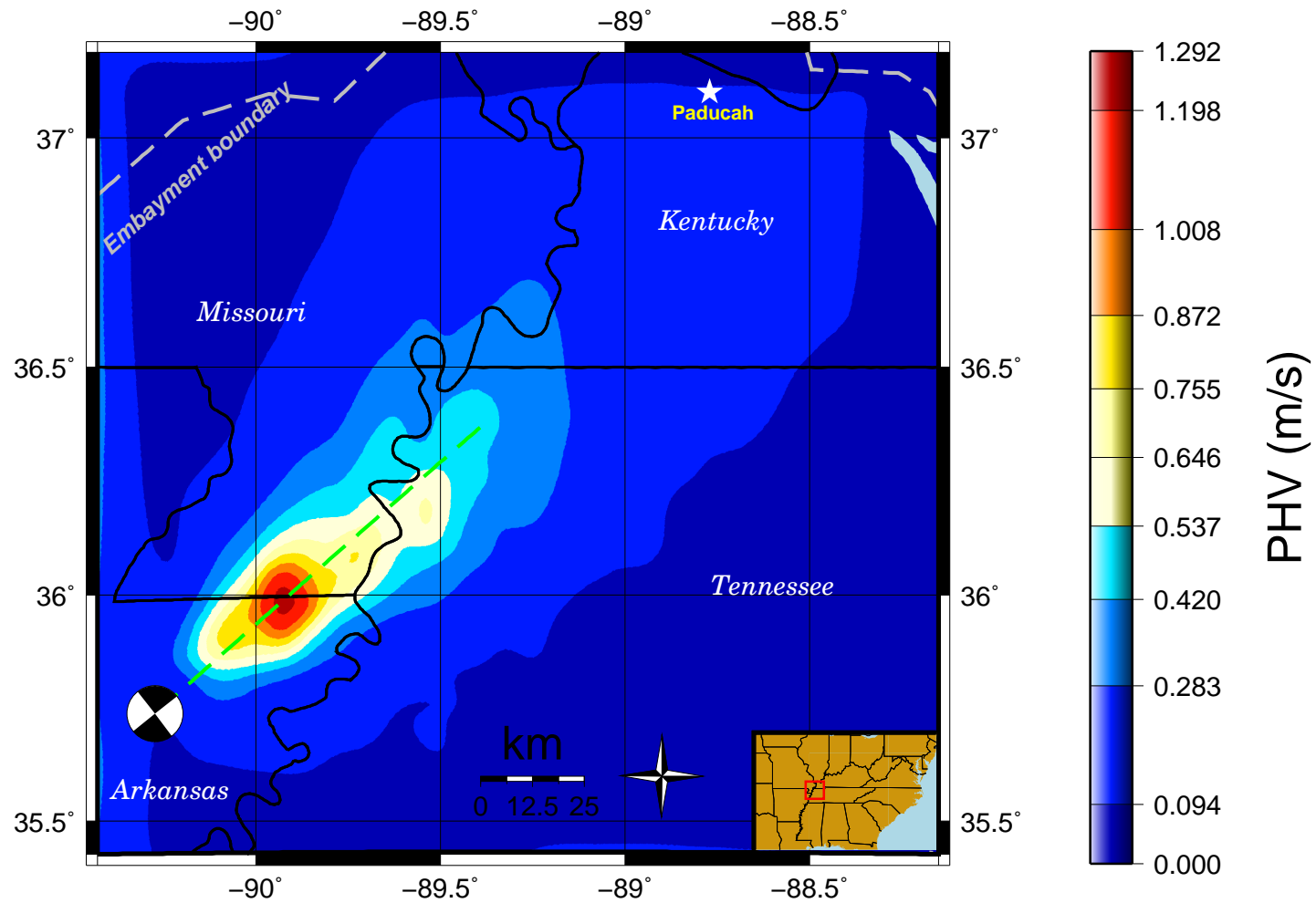


Figure 4.1: PHV from rupture on the strike-slip Cottonwood Grove fault. Focal mechanism is shown at the hypocenter.

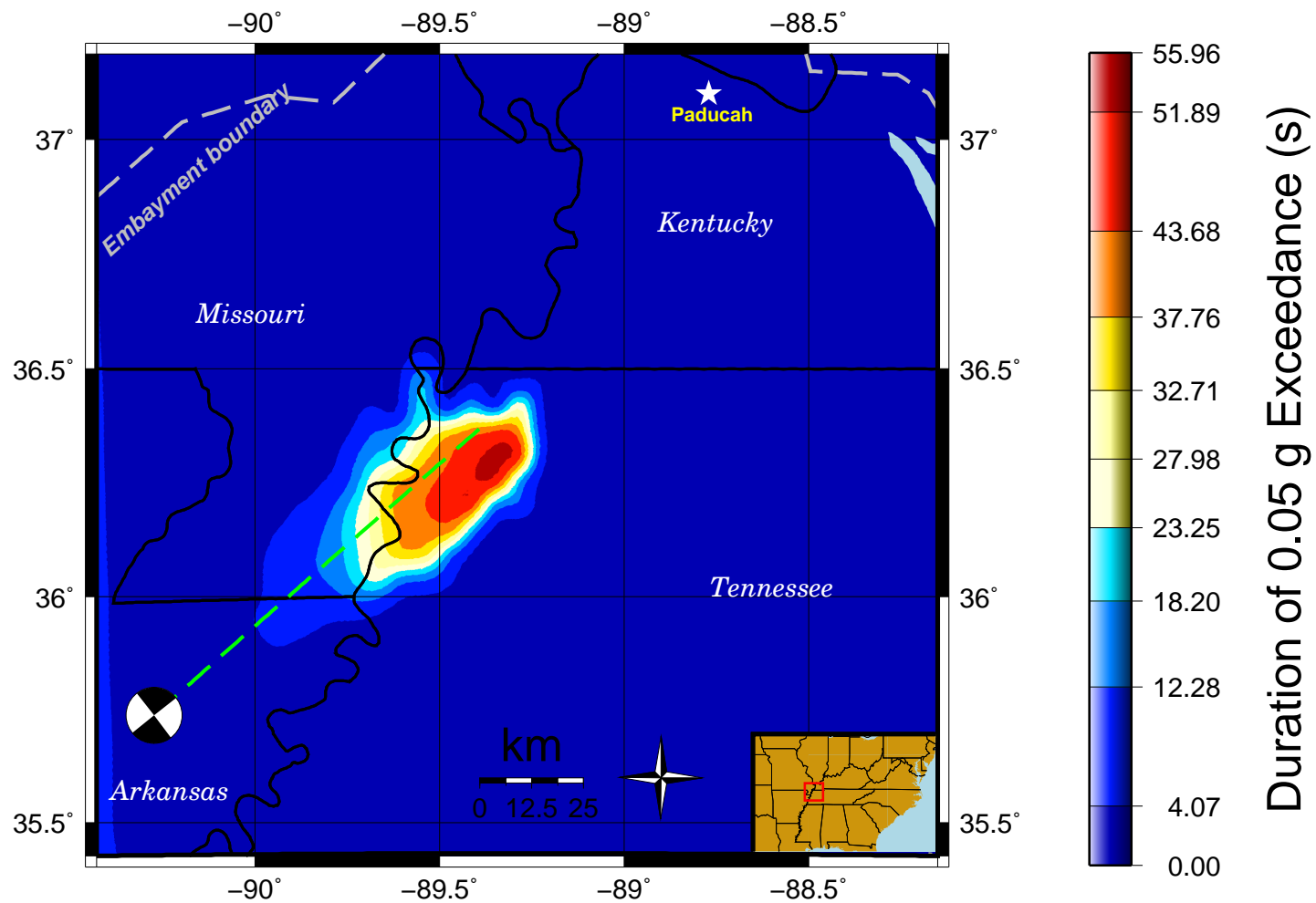


Figure 4.2: Bracketed Duration from rupture on the strike-slip Cottonwood Grove Fault. Focal mechanism is shown at the hypocenter.

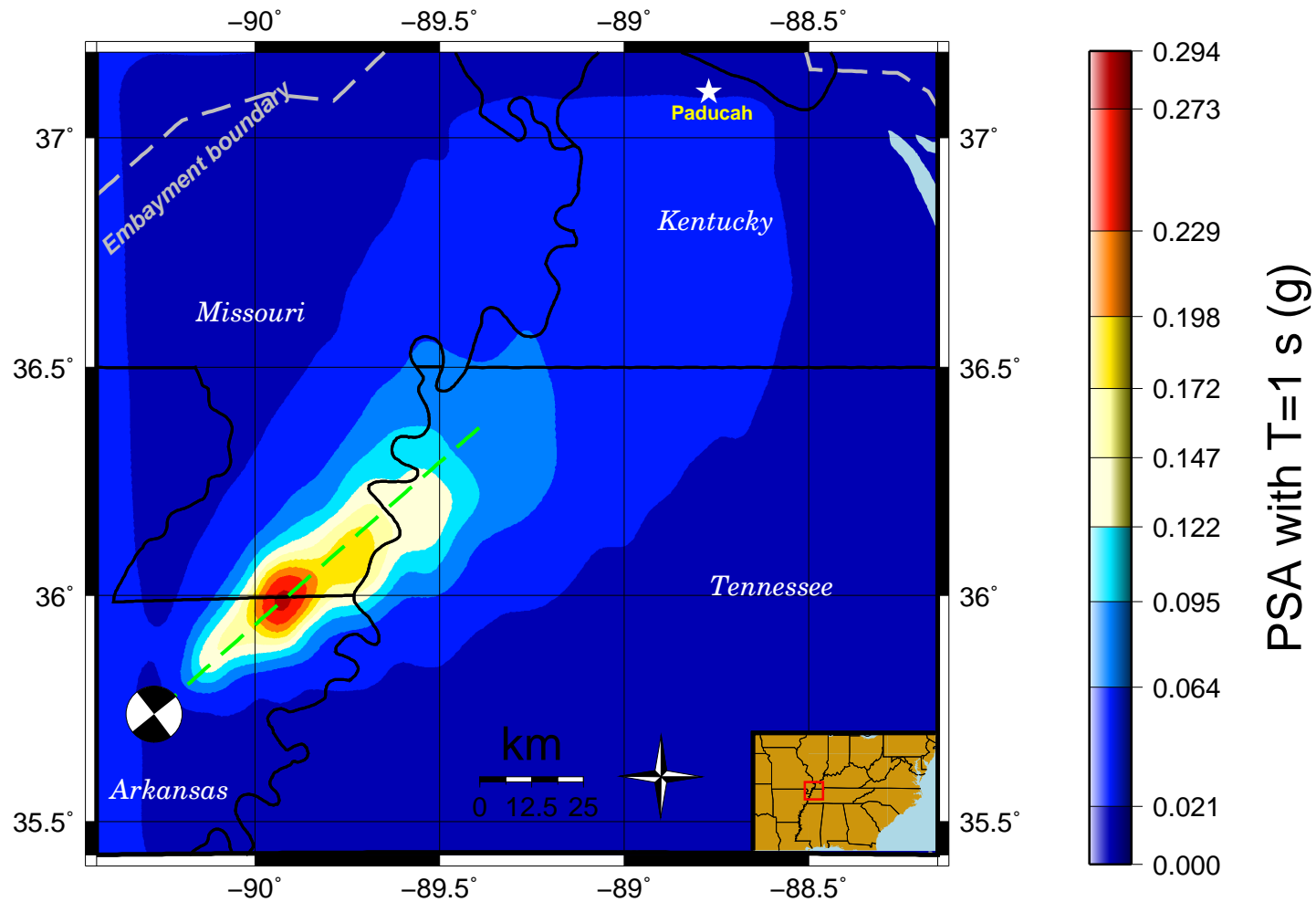


Figure 4.3: Pseudospectral acceleration with 1 second period from rupture on the strike-slip Cottonwood Grove Fault. Focal mechanism is shown at the hypocenter.

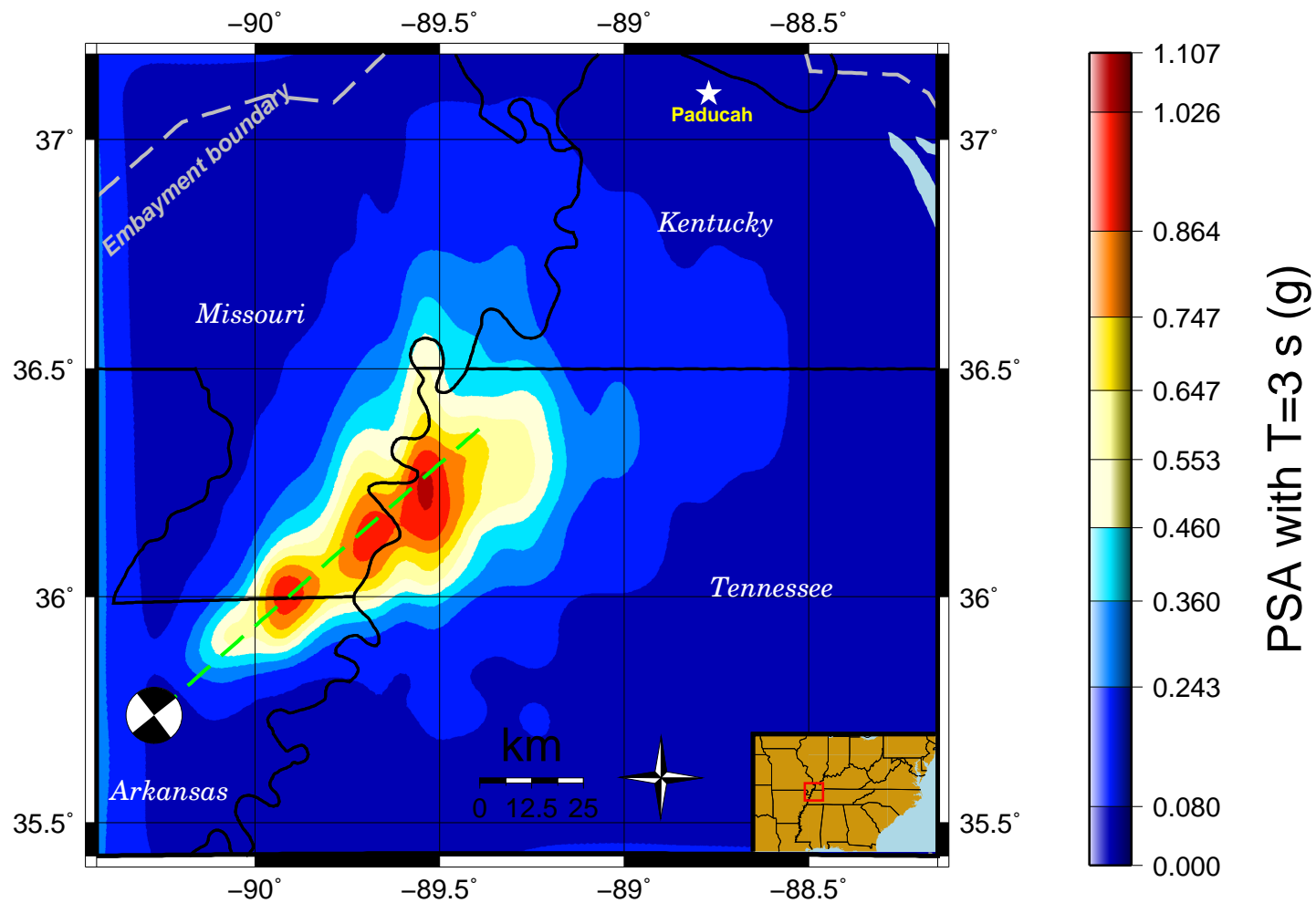


Figure 4.4: Pseudospectral acceleration with 3 second period from rupture on the strike-slip Cottonwood Grove Fault. Focal mechanism is shown at the hypocenter.

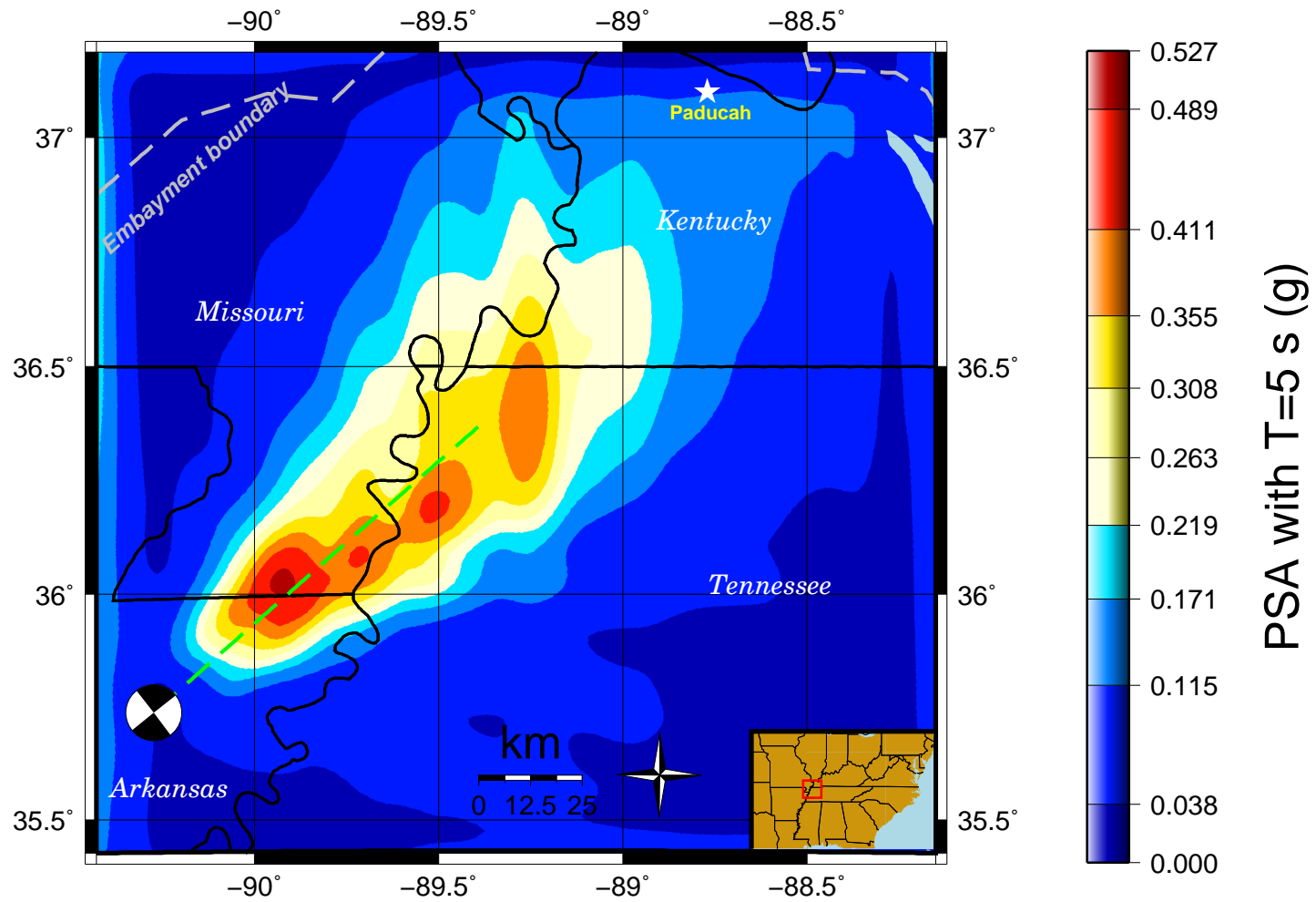


Figure 4.5: Pseudospectral acceleration with 5 second period from rupture on the strike-slip Cottonwood Grove Fault. Focal mechanism is shown at the hypocenter.

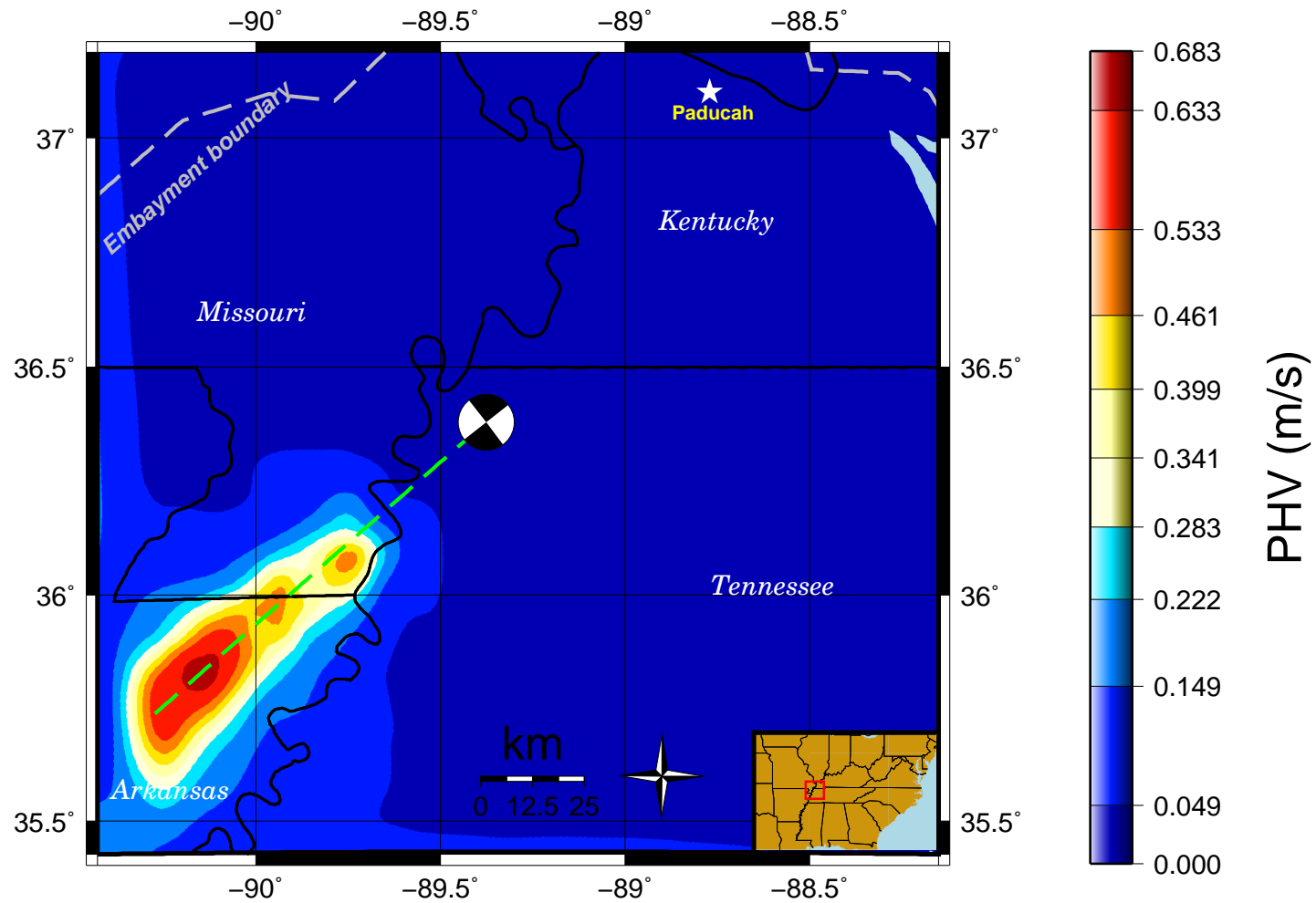


Figure 4.6: PHV from rupture on the strike-slip Cottonwood Grove Fault. Focal mechanism is shown at the hypocenter.

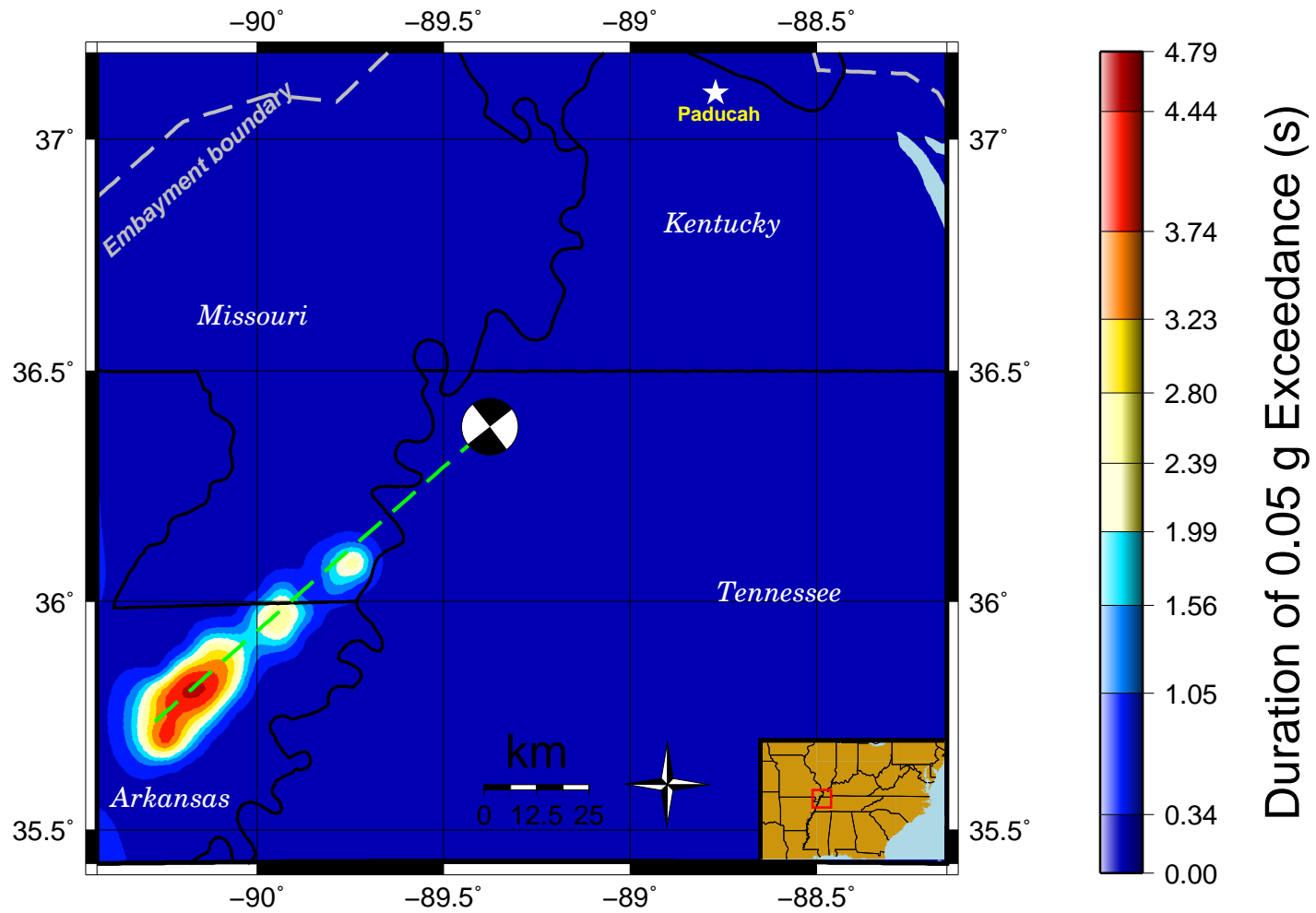


Figure 4.7: Bracketed Duration from rupture on the strike-slip Cottonwood Grove Fault. Focal mechanism is shown at the hypocenter.

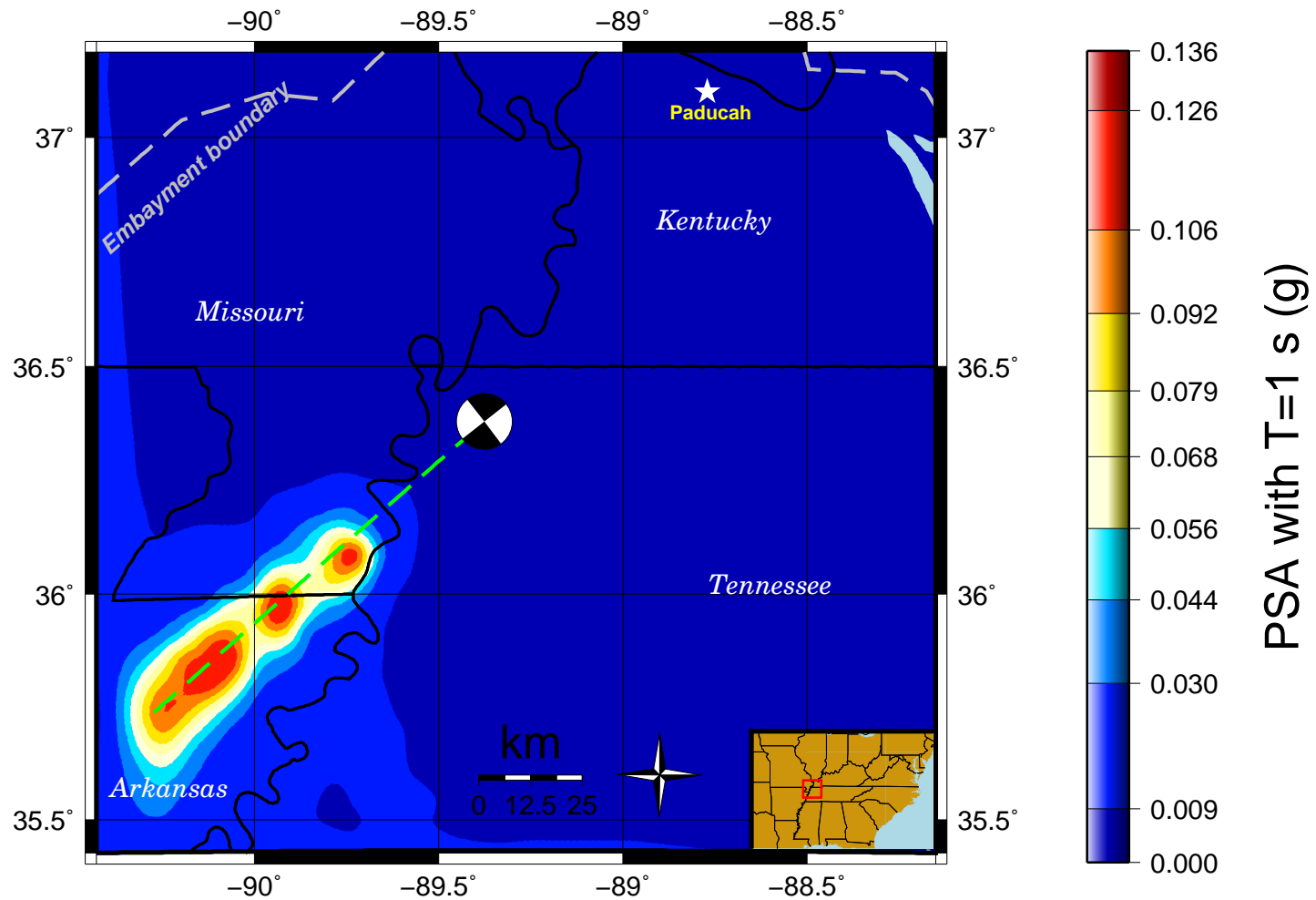


Figure 4.8: Pseudospectral acceleration with 1 second period from rupture on the strike-slip Cottonwood Grove Fault. Focal mechanism is shown at the hypocenter.

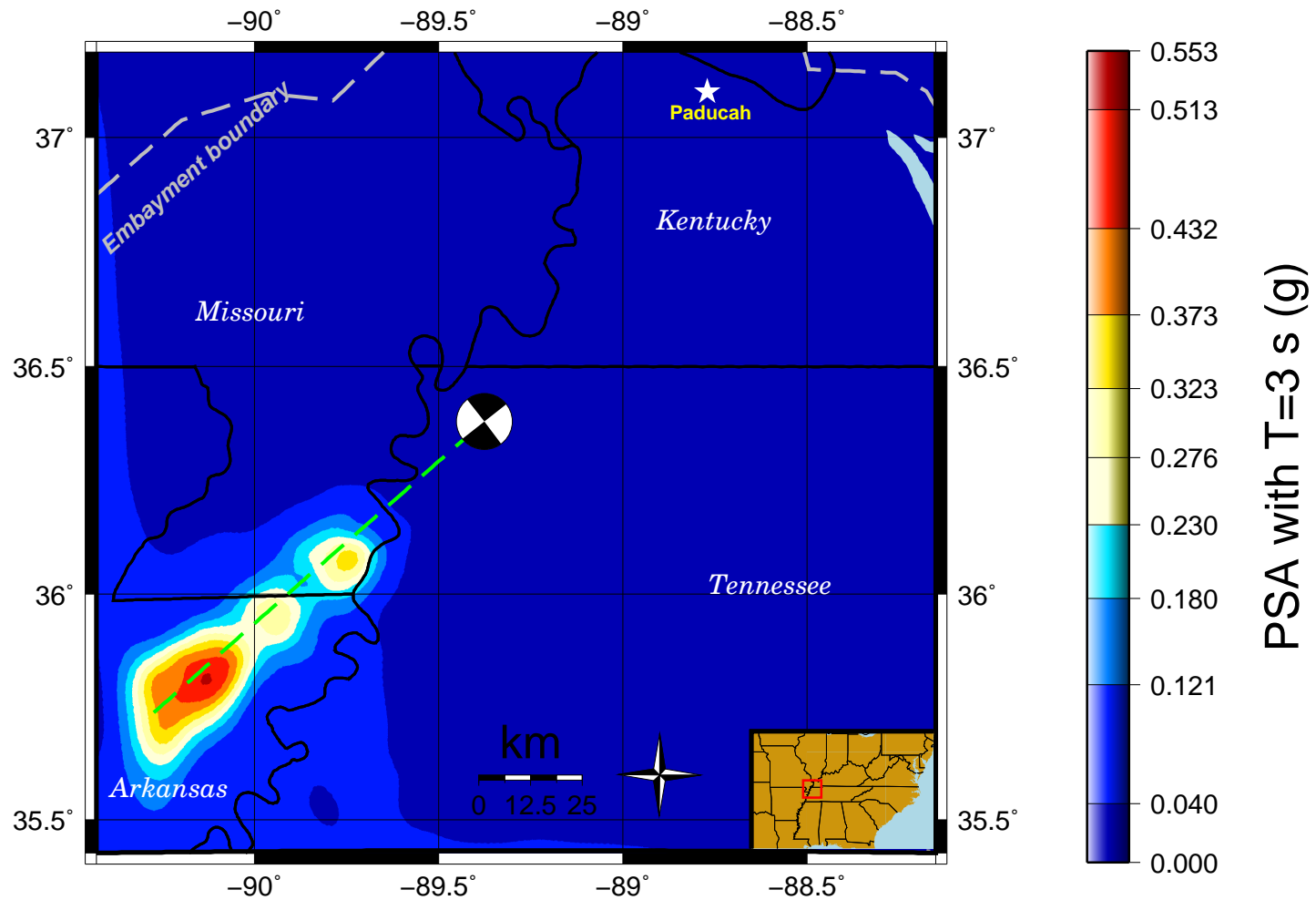


Figure 4.9: Pseudospectral acceleration with 3 second period from rupture on the strike-slip Cottonwood Grove Fault. Focal mechanism is shown at the hypocenter.

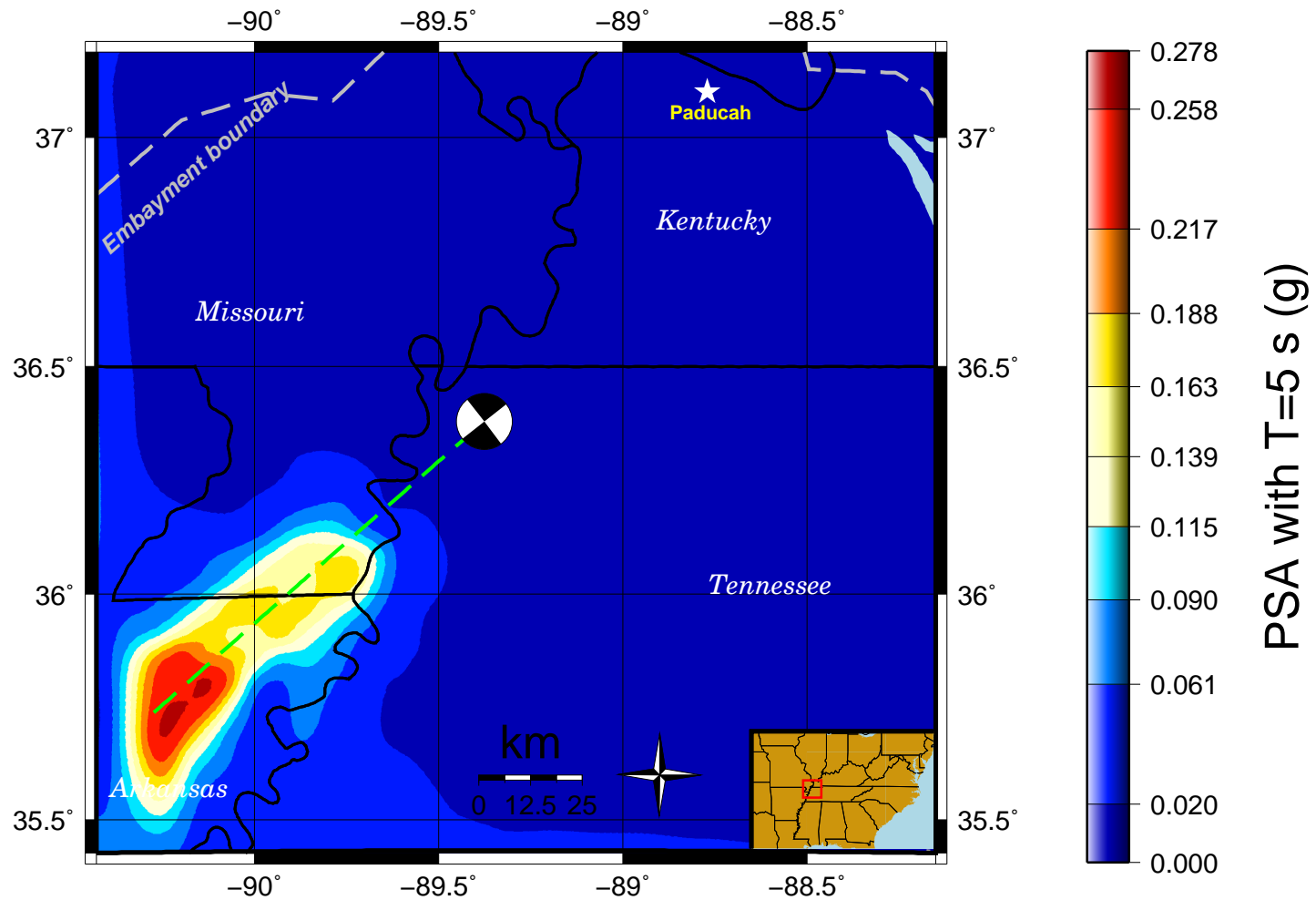


Figure 4.10: Pseudospectral acceleration with 5 second period from rupture on the strike-slip Cottonwood Grove Fault. Focal mechanism is shown at the hypocenter.

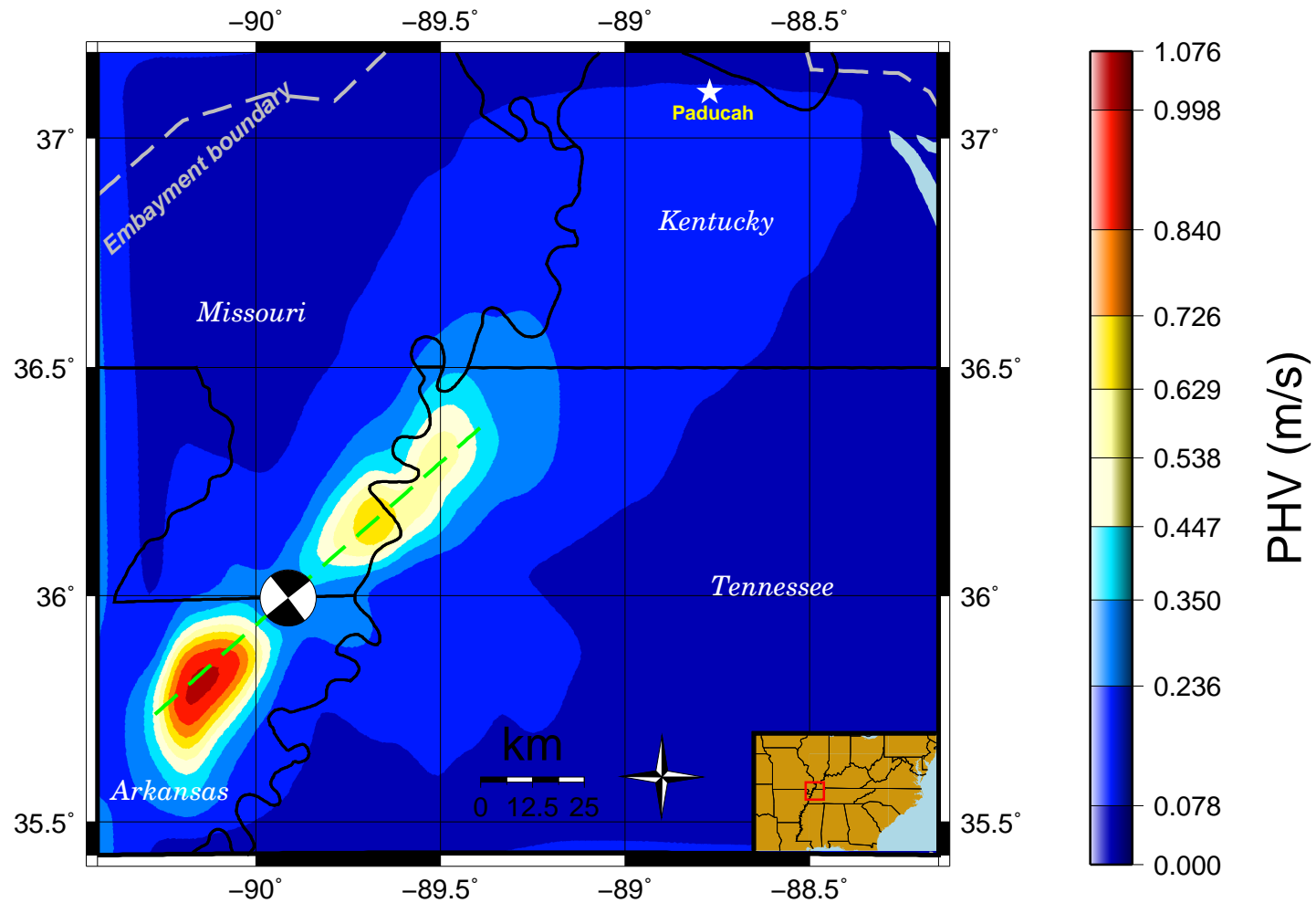


Figure 4.11: PHV from rupture on the strike-slip Cottonwood Grove Fault. Focal mechanism is shown at the hypocenter.

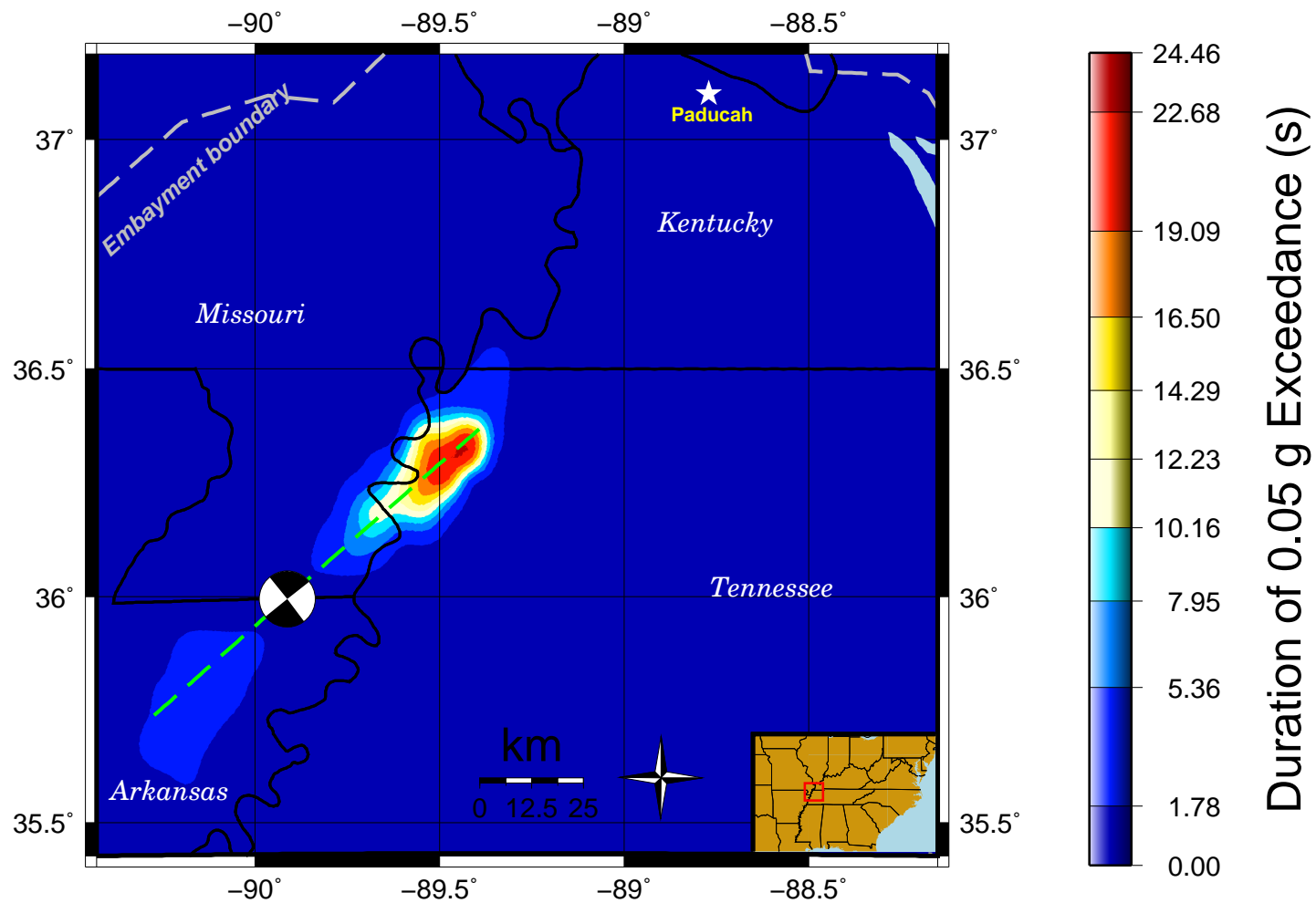


Figure 4.12: Bracketed Duration from rupture on the strike-slip Cottonwood Grove Fault. Focal mechanism is shown at the hypocenter.

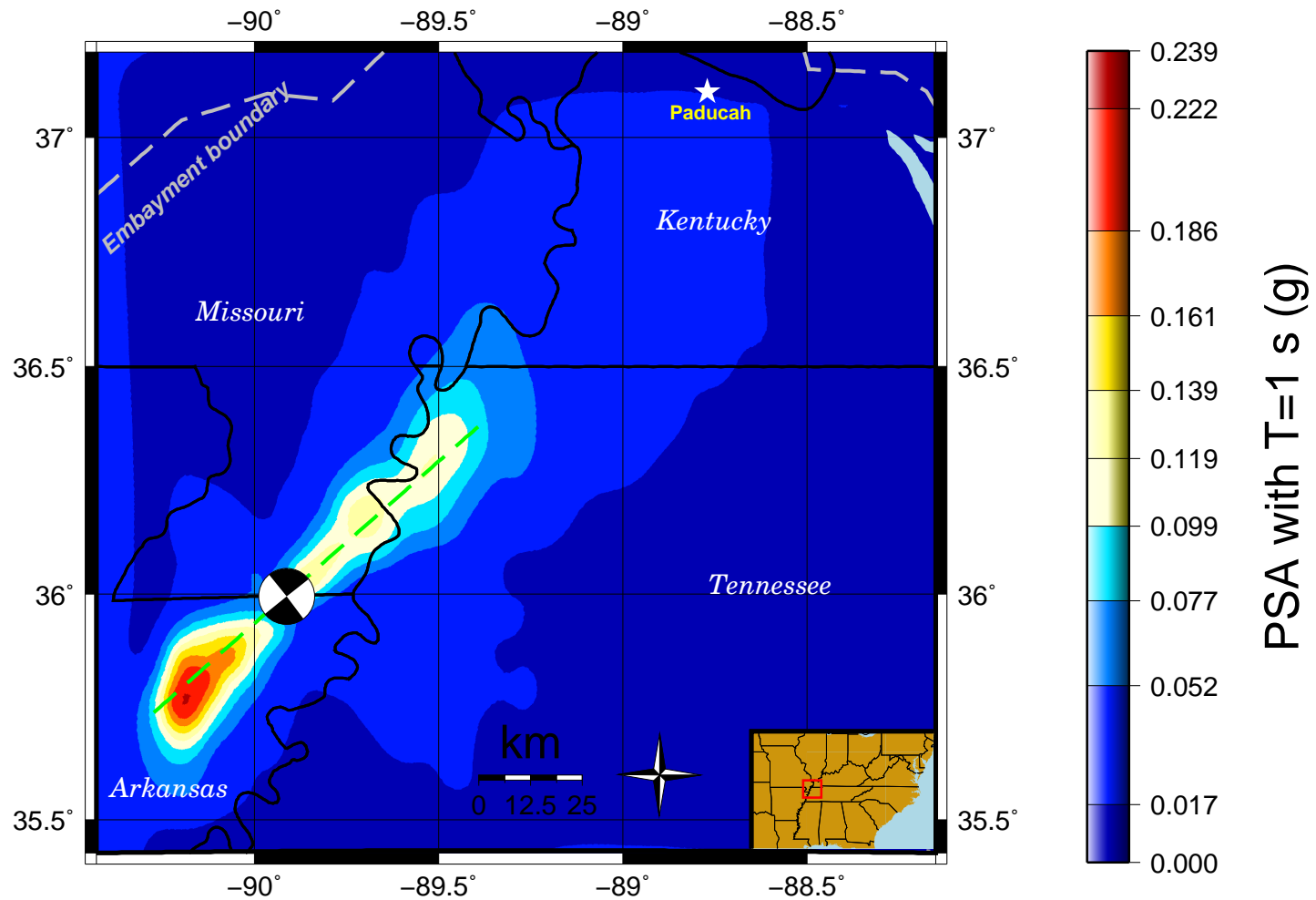


Figure 4.13: Pseudospectral acceleration with 1 second period from rupture on the strike-slip Cottonwood Grove Fault. Focal mechanism is shown at the hypocenter.

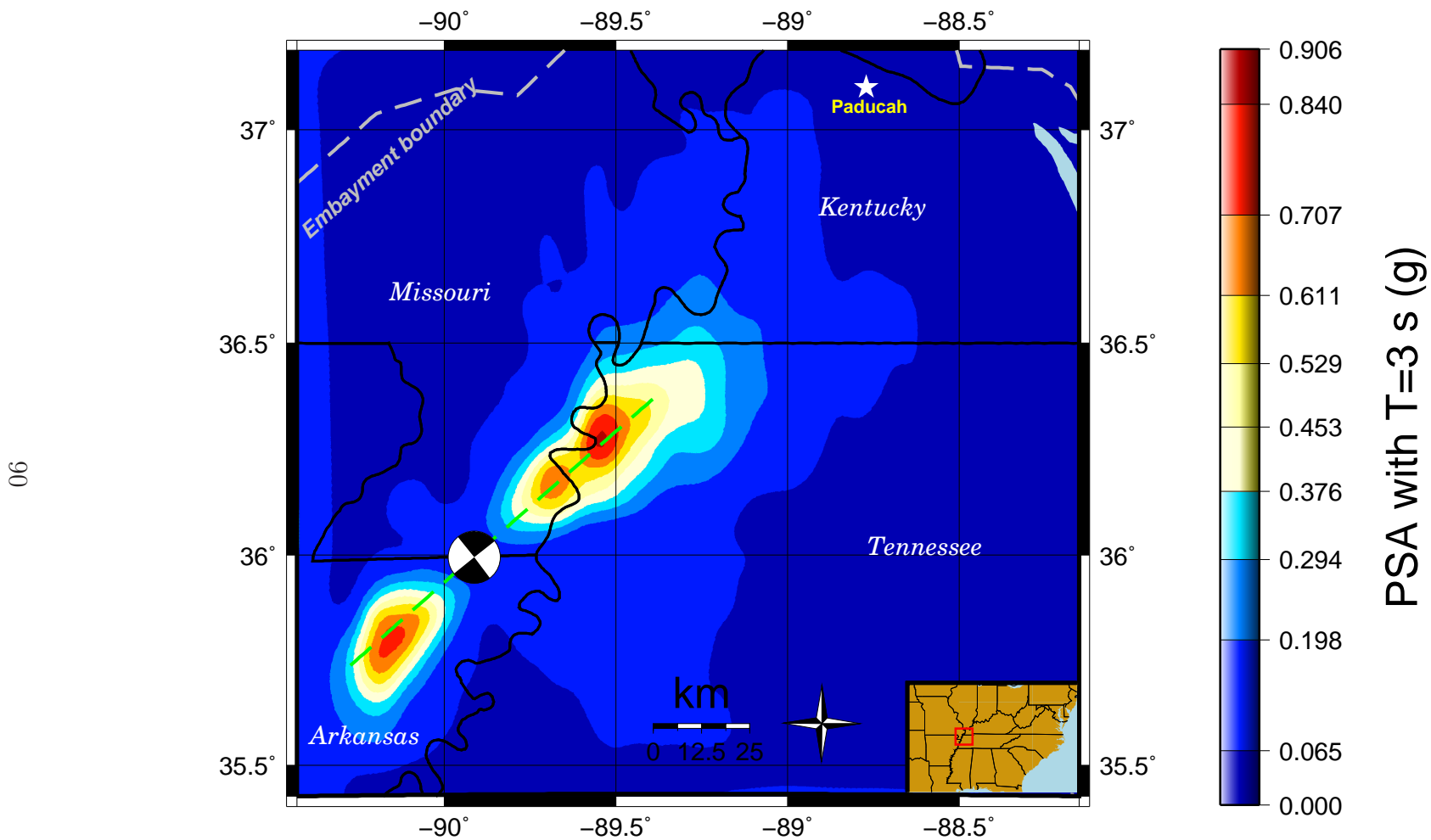


Figure 4.14: Pseudospectral acceleration with 3 second period from rupture on the strike-slip Cottonwood Grove Fault. Focal mechanism is shown at the hypocenter.

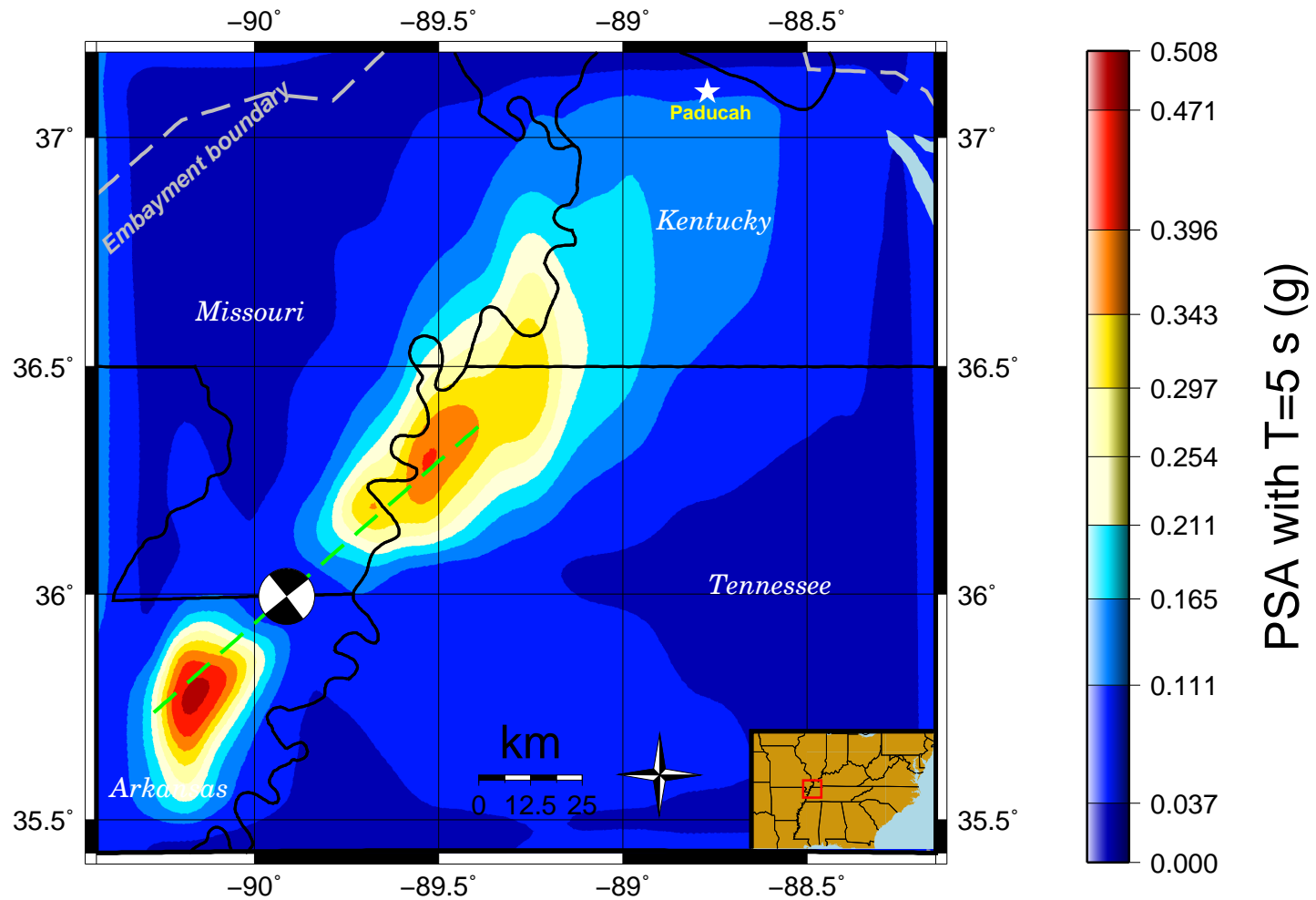


Figure 4.15: Pseudospectral acceleration with 5 second period from rupture on the strike-slip Cottonwood Grove Fault. Focal mechanism is shown at the hypocenter.

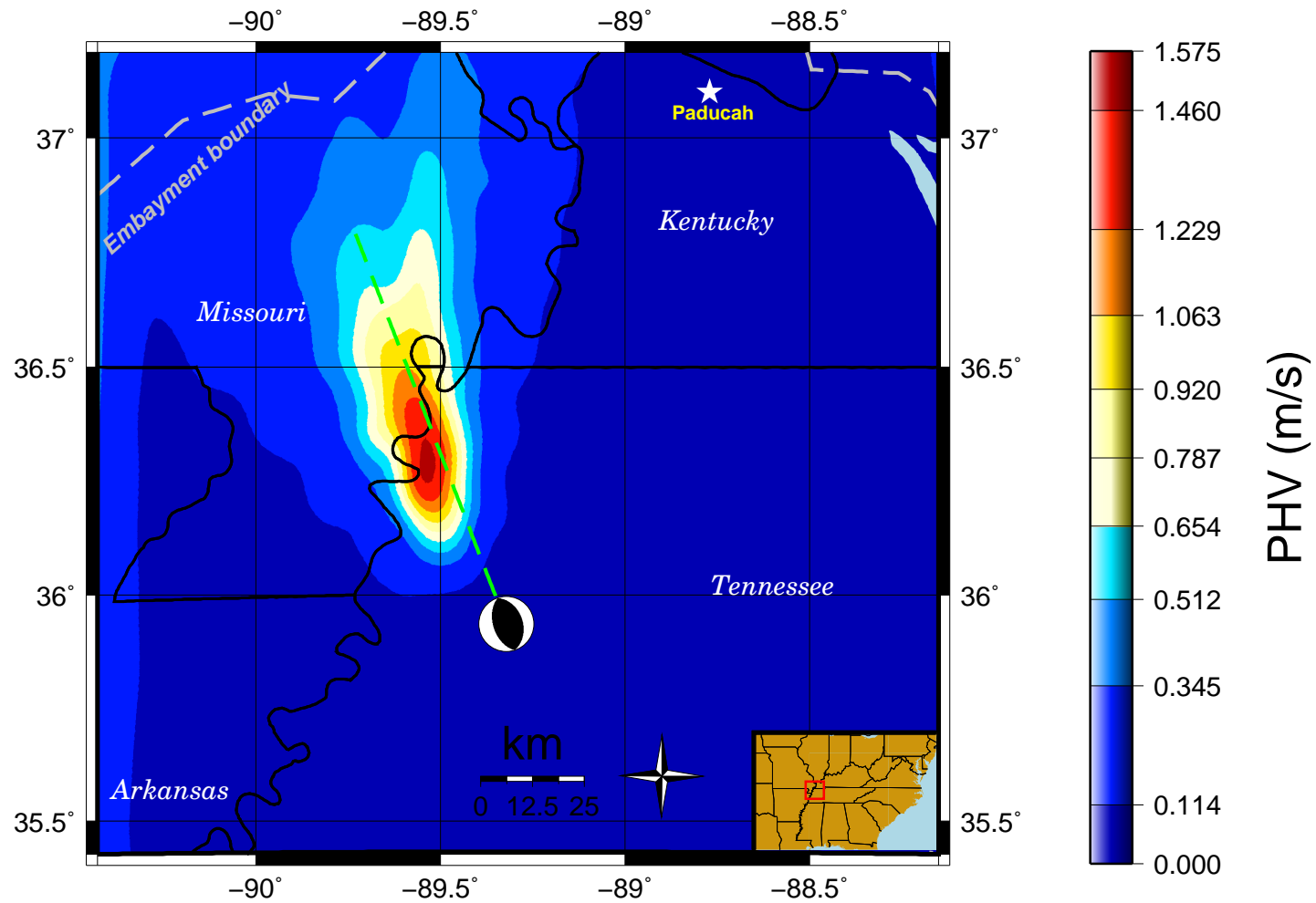


Figure 4.16: PHV from rupture on the Reelfoot thrust fault. Focal mechanism is shown at the hypocenter.

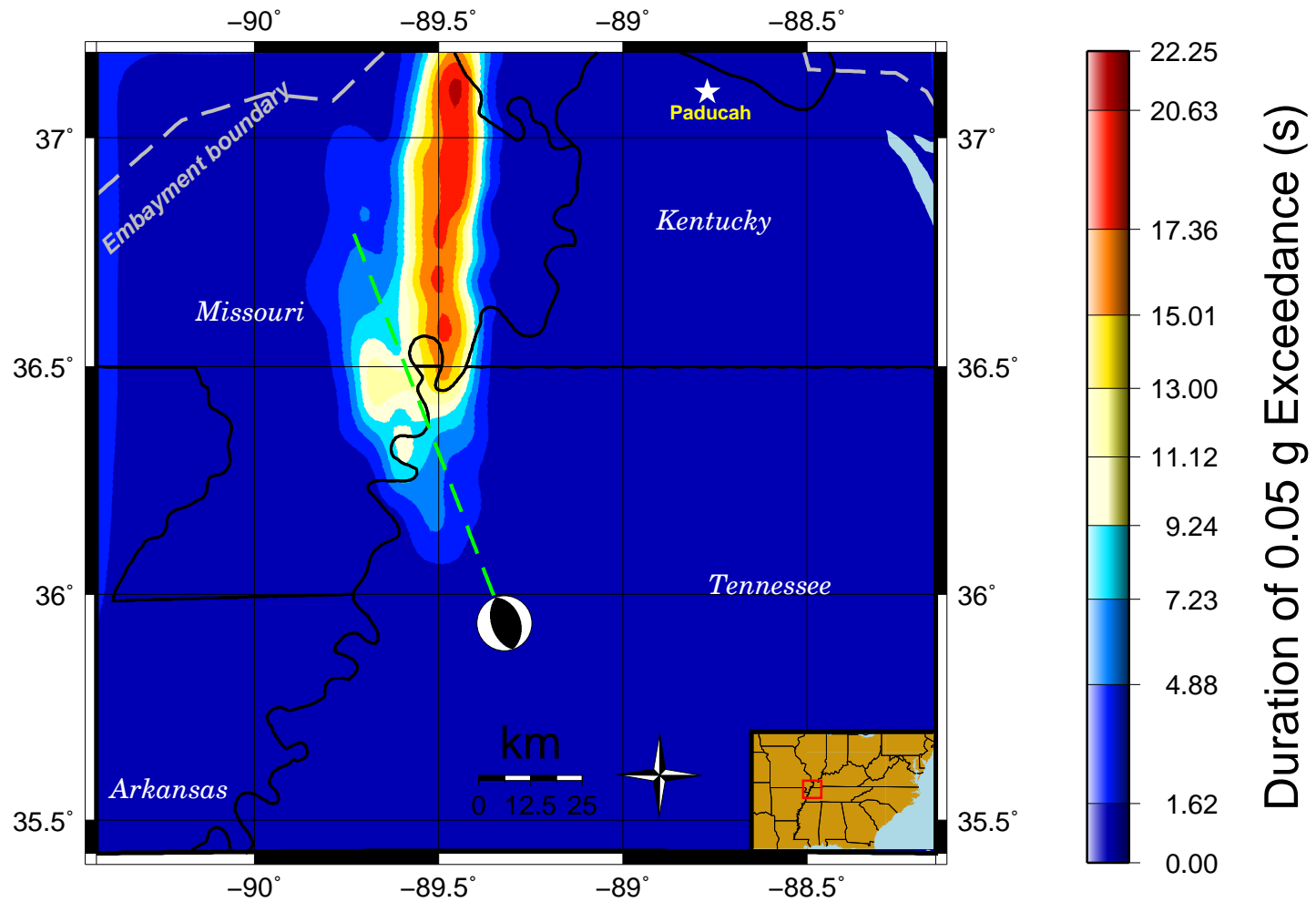


Figure 4.17: Bracketed Duration from rupture on the Reelfoot thrust fault. Focal mechanism is shown at the hypocenter.

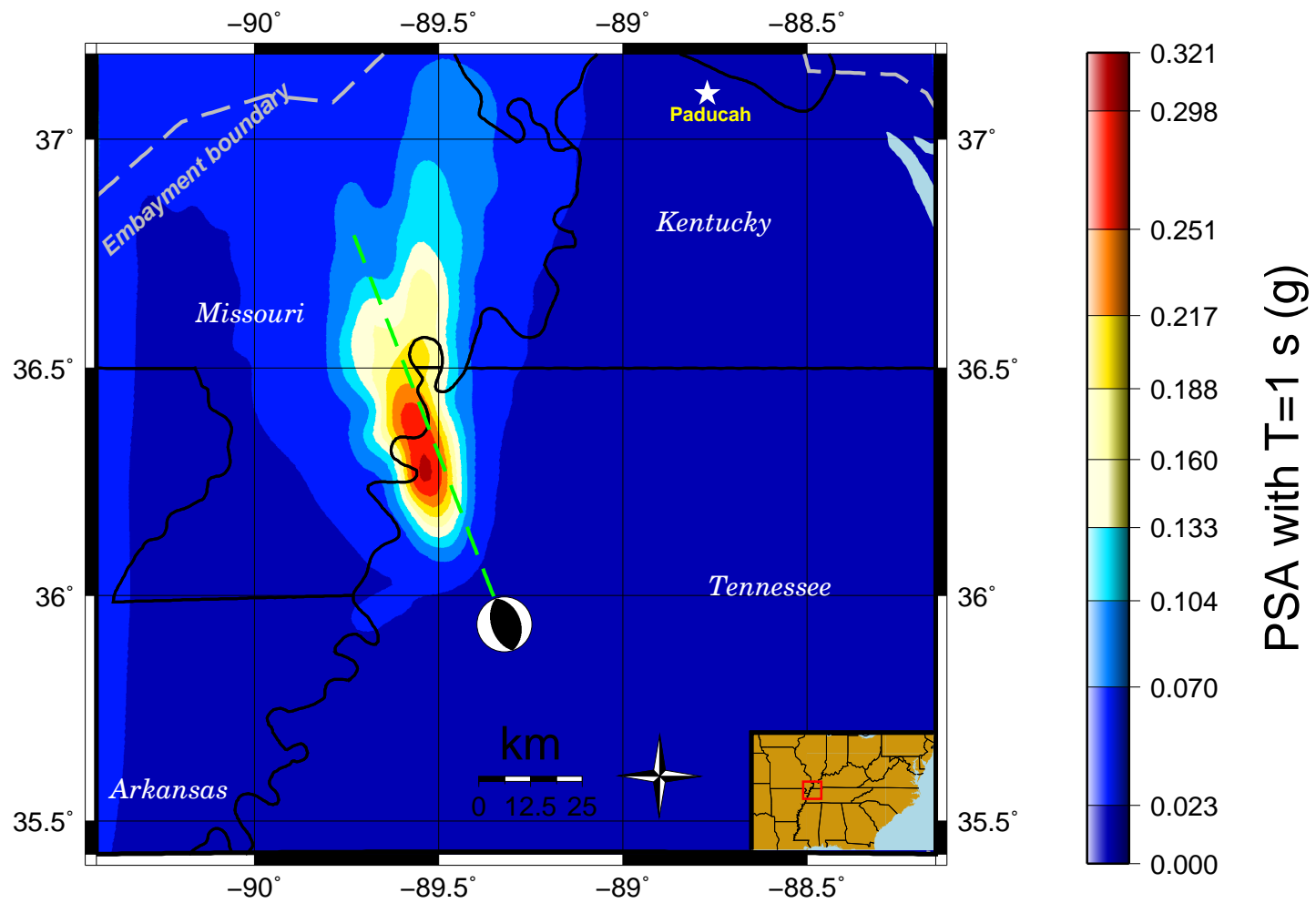


Figure 4.18: Pseudospectral acceleration with 1 second period from rupture on the Reelfoot thrust fault. Focal mechanism is shown at the hypocenter.

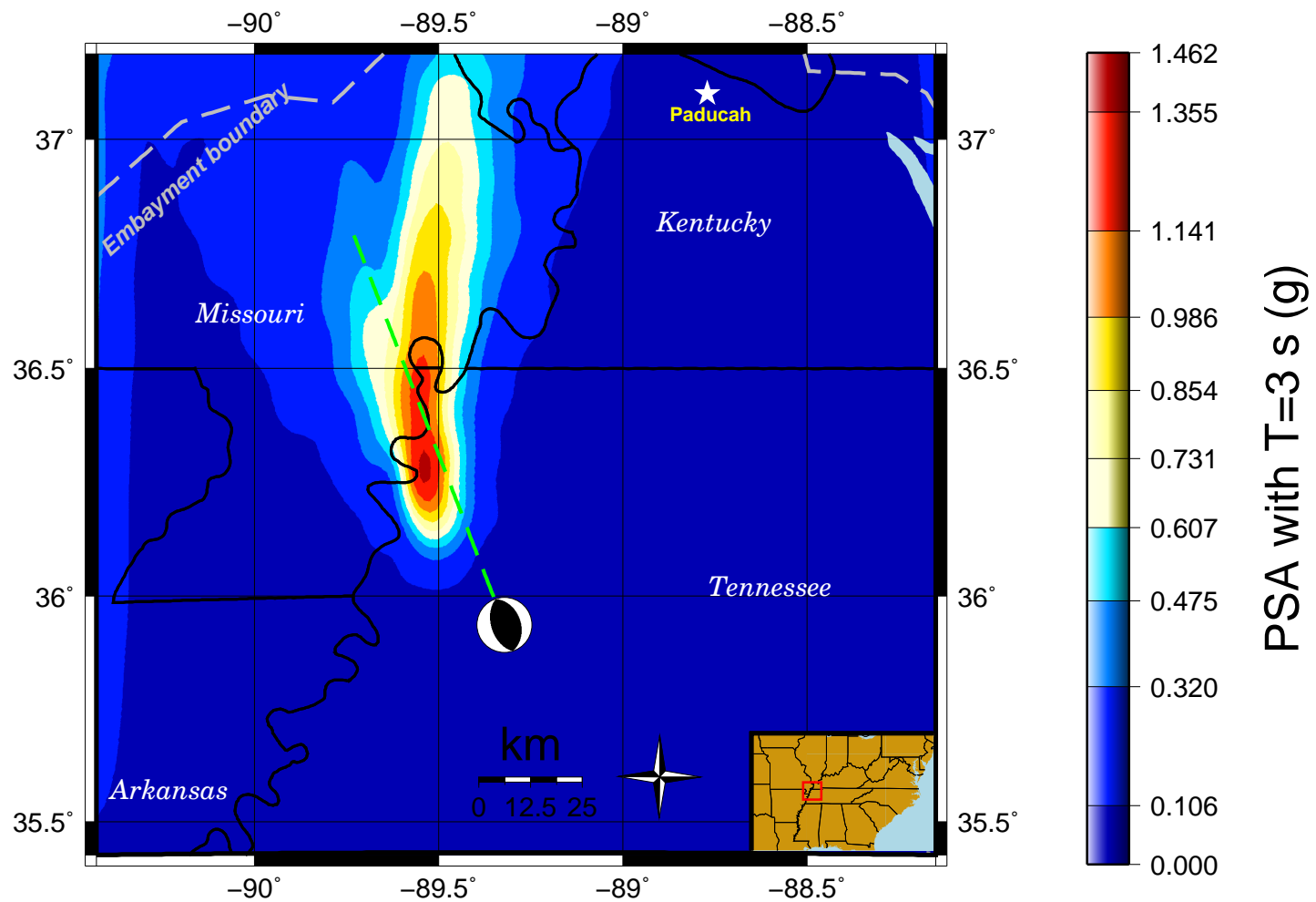


Figure 4.19: Pseudospectral acceleration with 3 second period from rupture on the Reelfoot thrust fault. Focal mechanism is shown at the hypocenter.

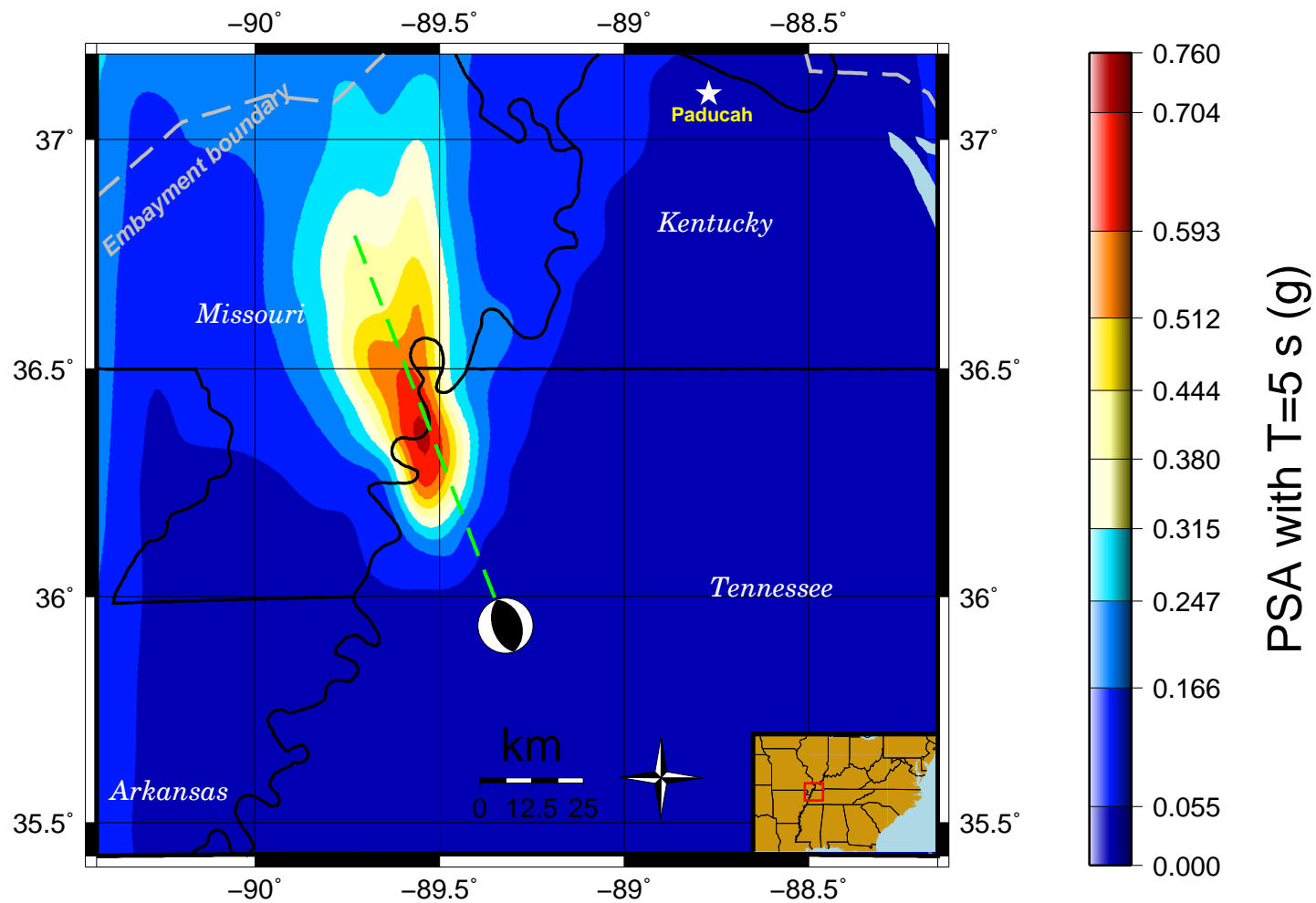


Figure 4.20: Pseudospectral acceleration with 5 second period from rupture on the Reelfoot thrust fault. Focal mechanism is shown at the hypocenter.

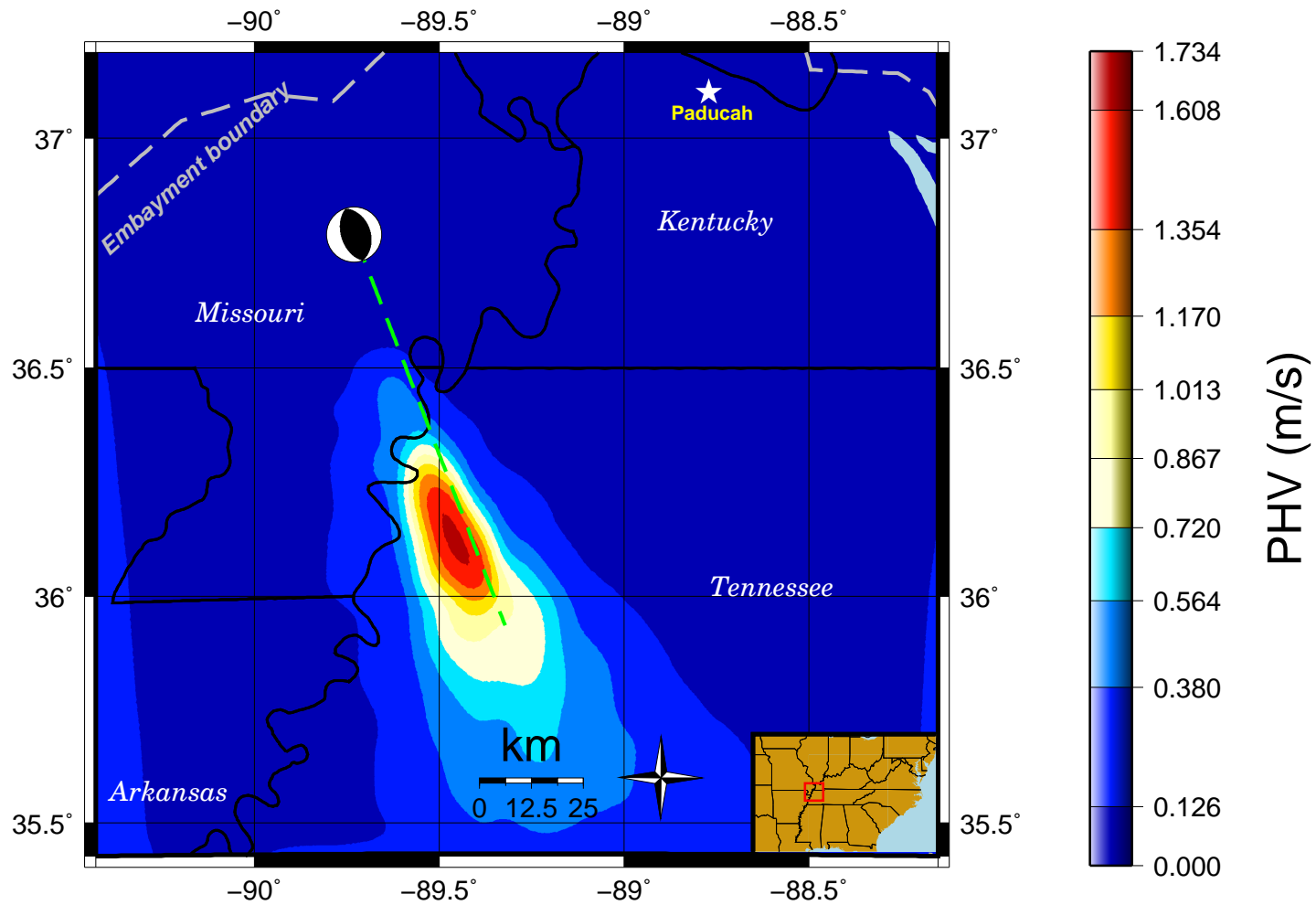


Figure 4.21: PHV from rupture on the Reelfoot thrust fault. Focal mechanism is shown at the hypocenter.

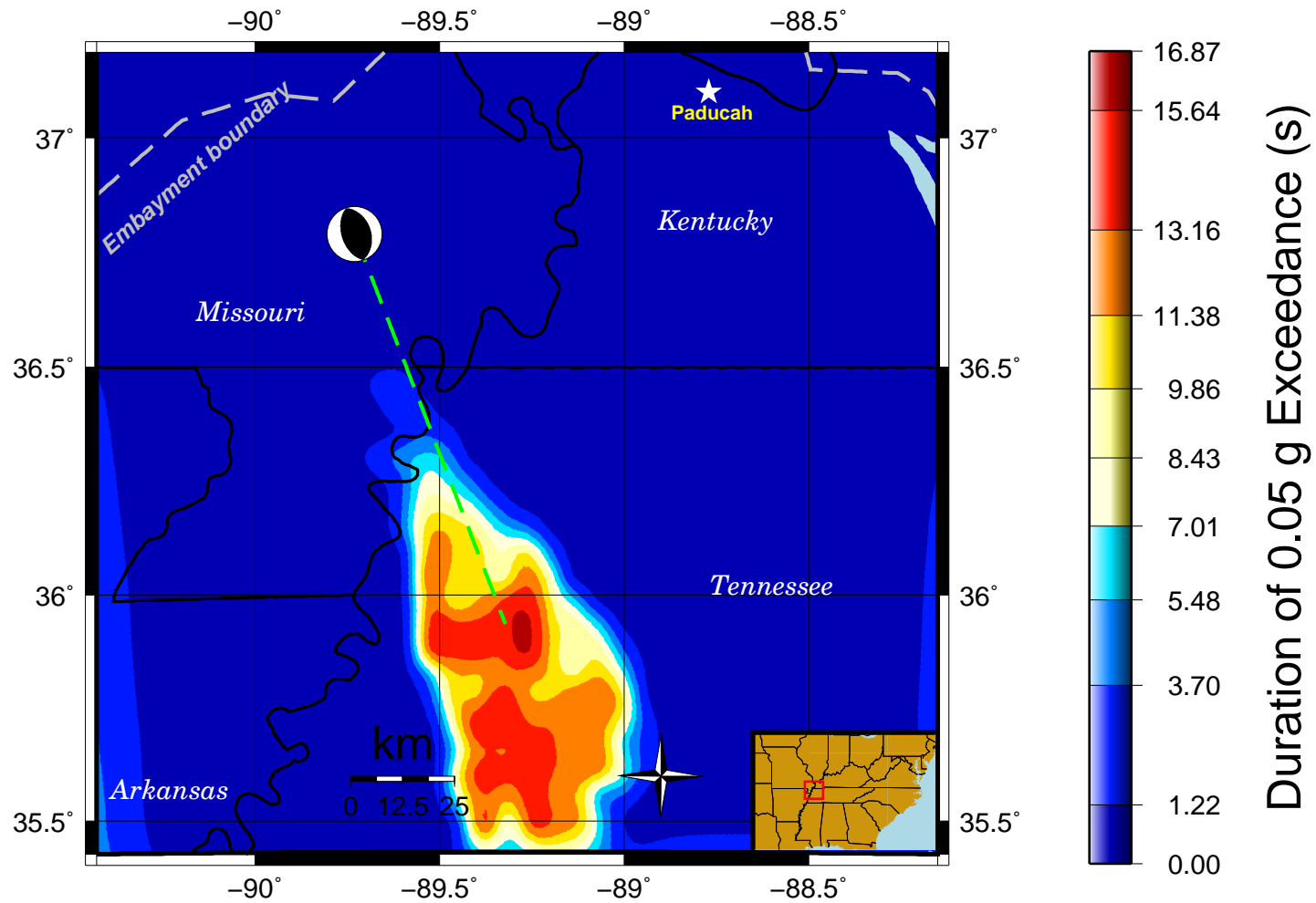


Figure 4.22: Bracketed Duration from rupture on the Reelfoot thrust fault. Focal mechanism is shown at the hypocenter.

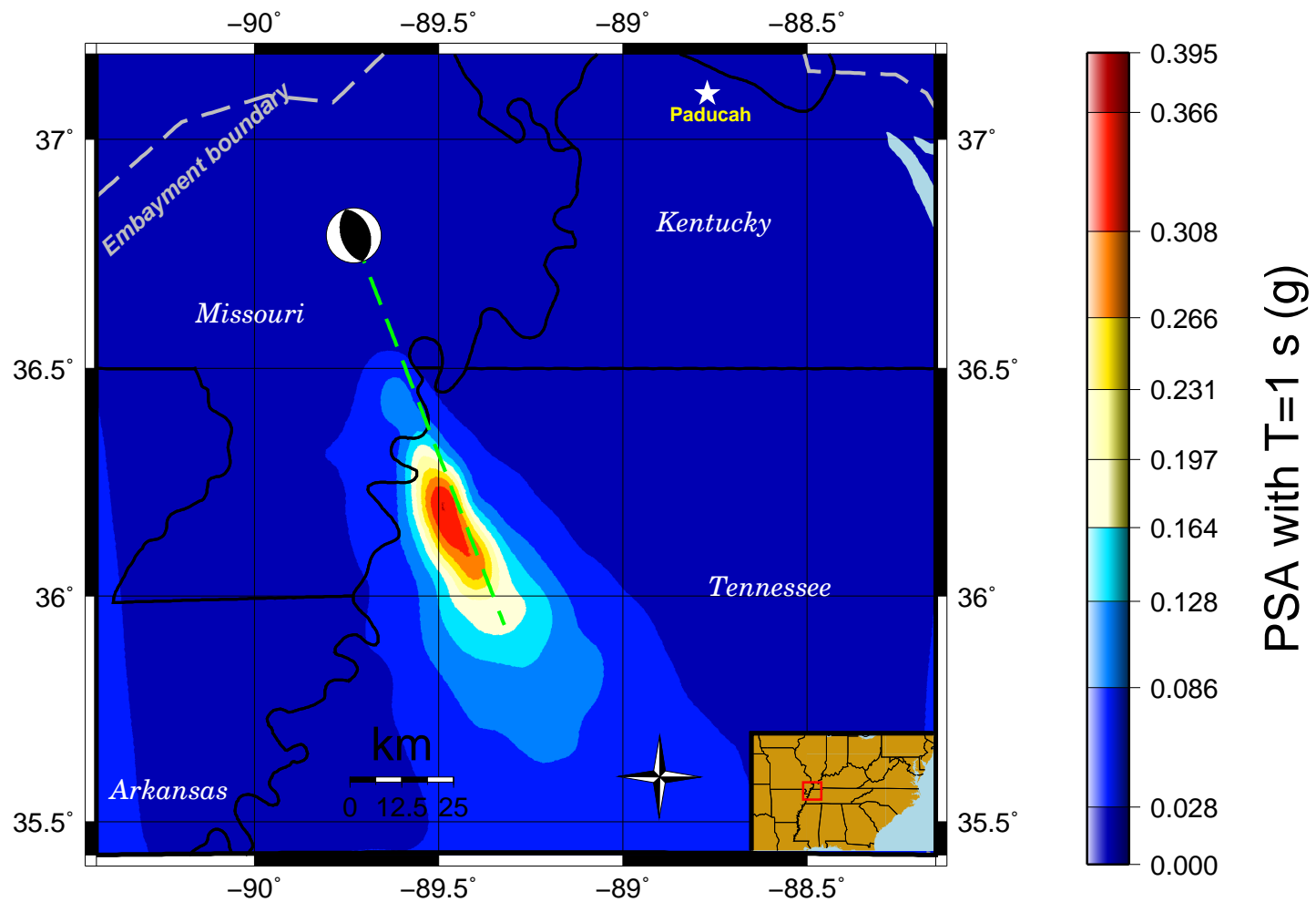


Figure 4.23: Pseudospectral acceleration with 1 second period from rupture on the Reelfoot thrust fault. Focal mechanism is shown at the hypocenter.

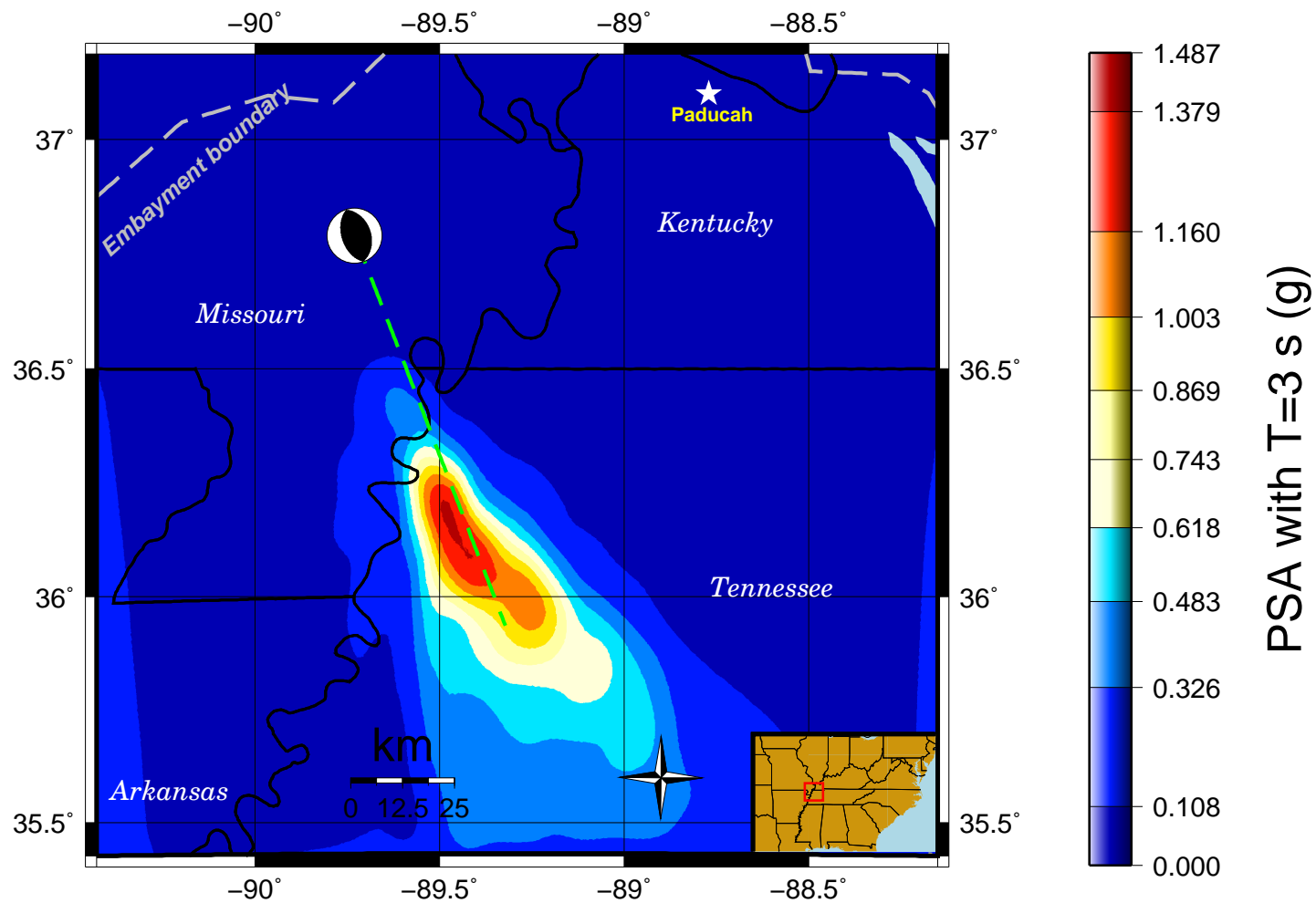


Figure 4.24: Pseudospectral acceleration with 3 second period from rupture on the Reelfoot thrust fault. Focal mechanism is shown at the hypocenter.

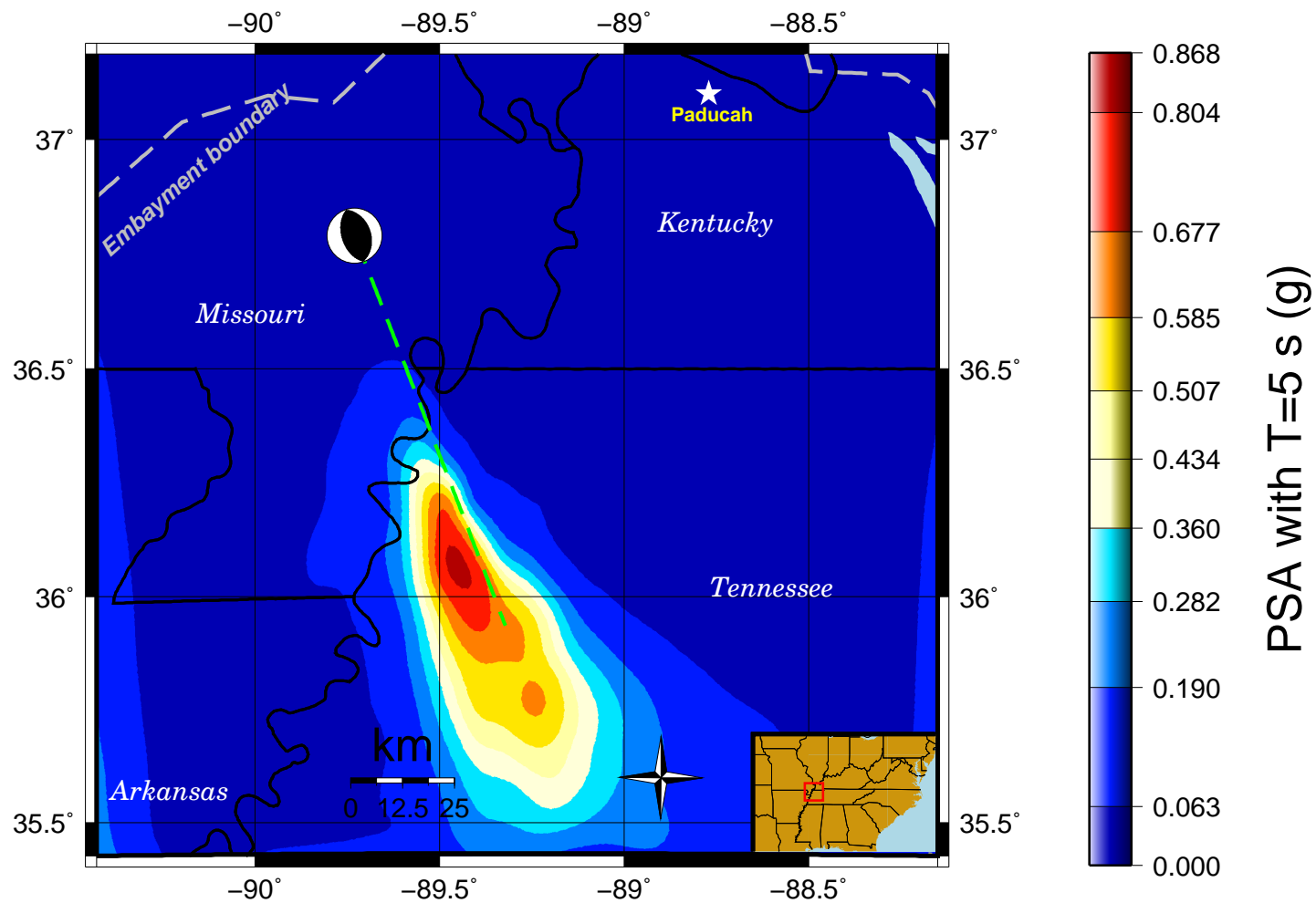


Figure 4.25: Pseudospectral acceleration with 5 second period from rupture on the Reelfoot thrust fault. Focal mechanism is shown at the hypocenter.

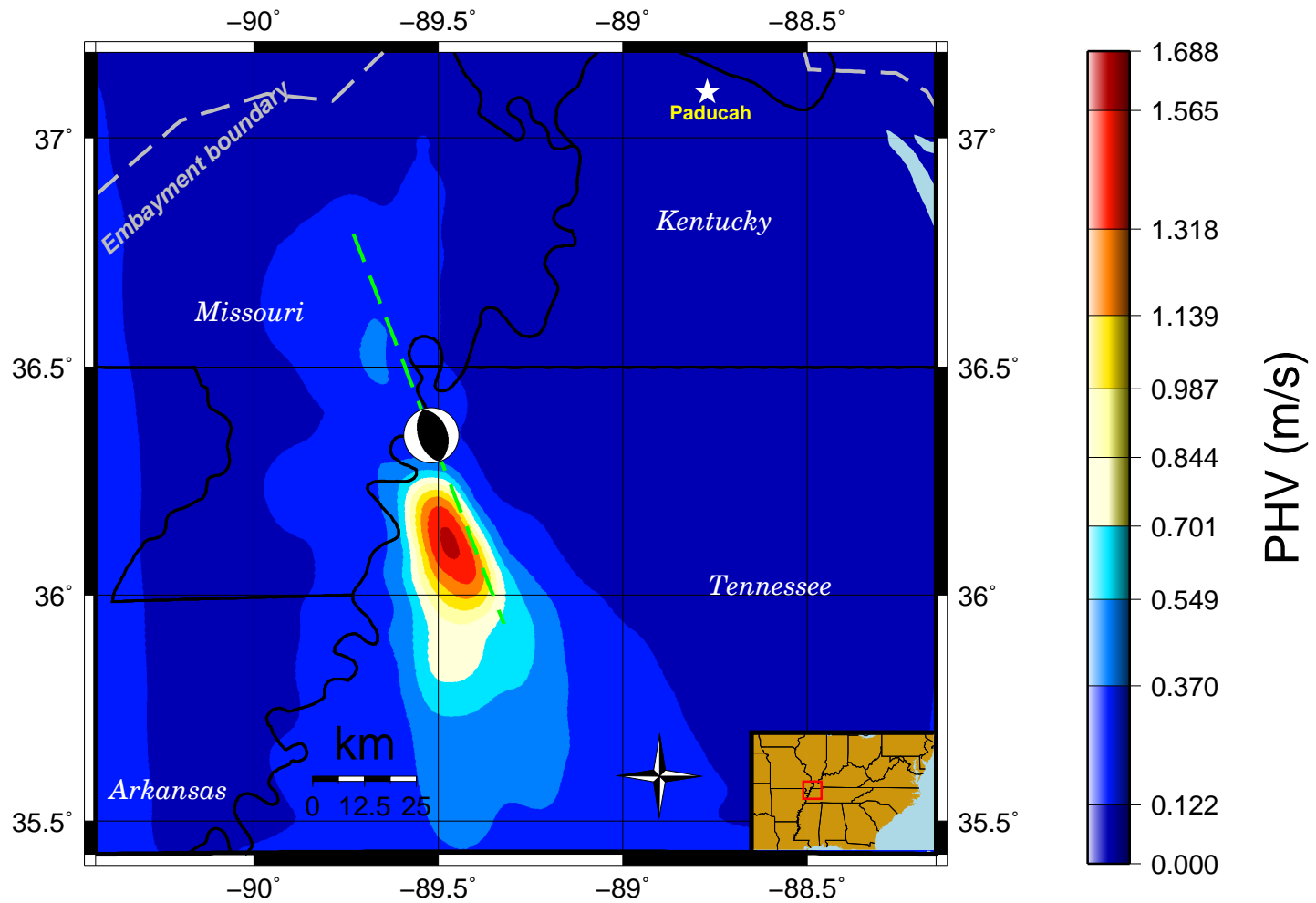


Figure 4.26: PHV from rupture on the Reelfoot thrust fault. Focal mechanism is shown at the hypocenter.

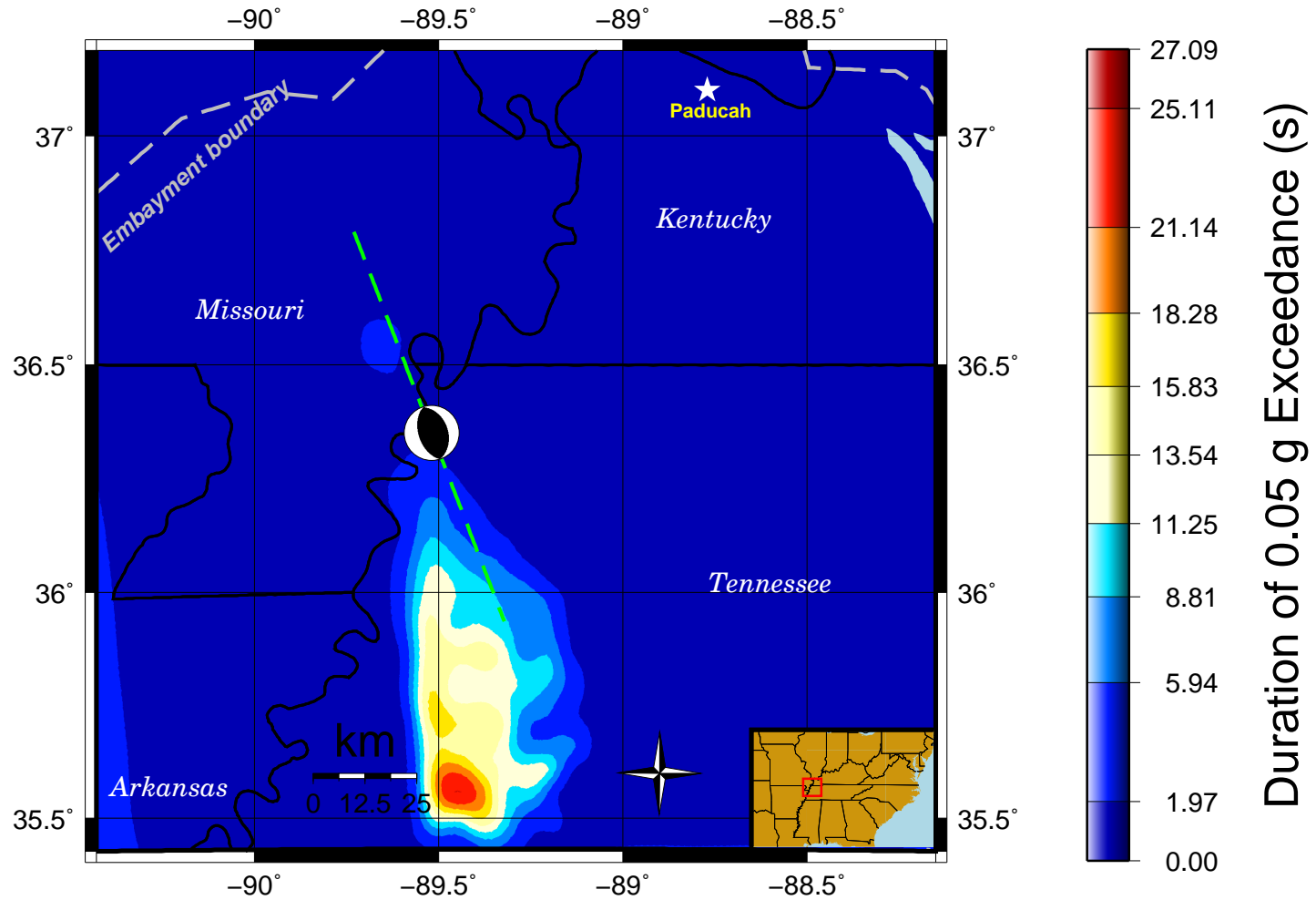


Figure 4.27: Bracketed Duration from rupture on the Reelfoot thrust fault. Focal mechanism is shown at the hypocenter.

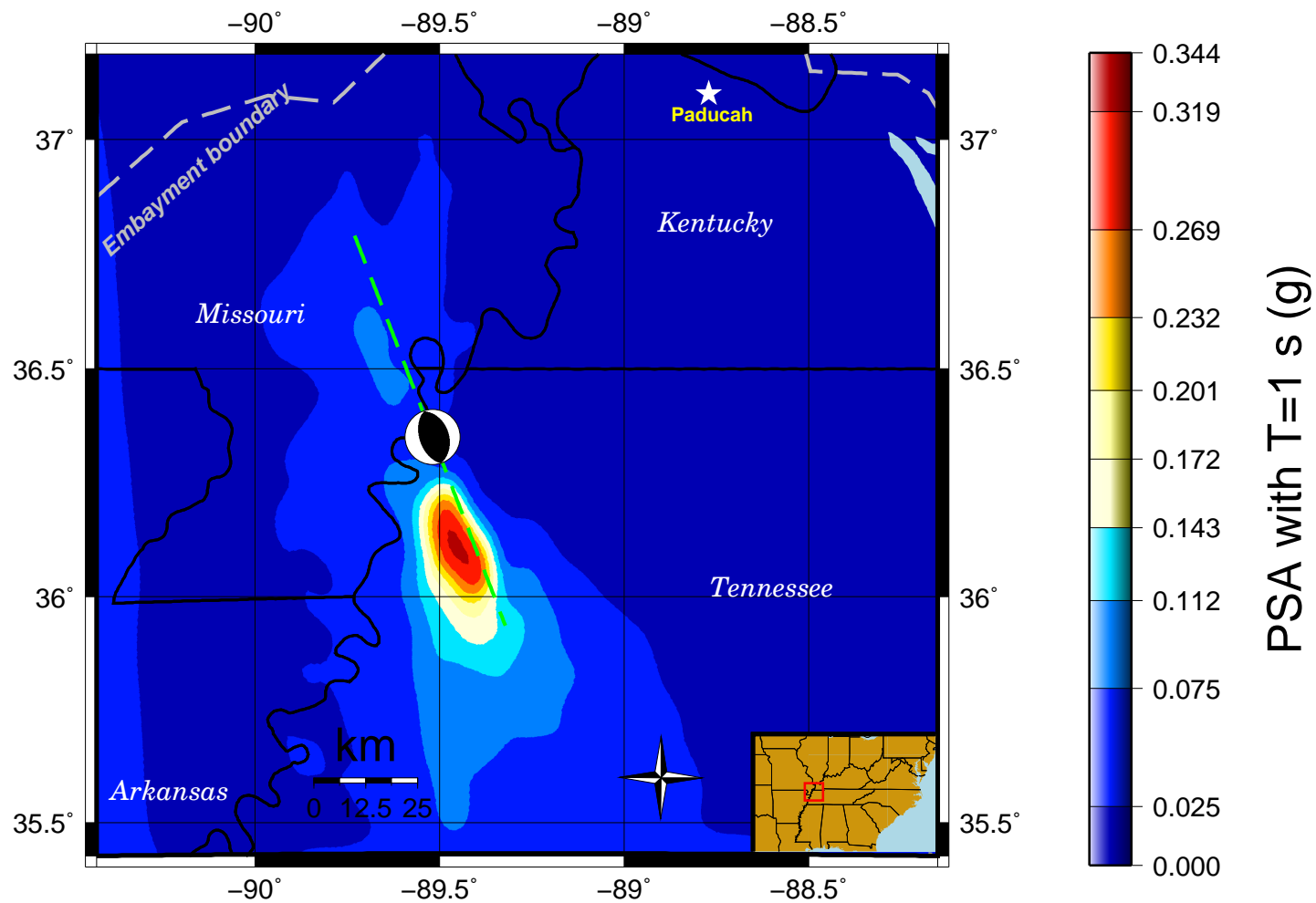


Figure 4.28: Pseudospectral acceleration with 1 second period from rupture on the Reelfoot thrust fault. Focal mechanism is shown at the hypocenter.

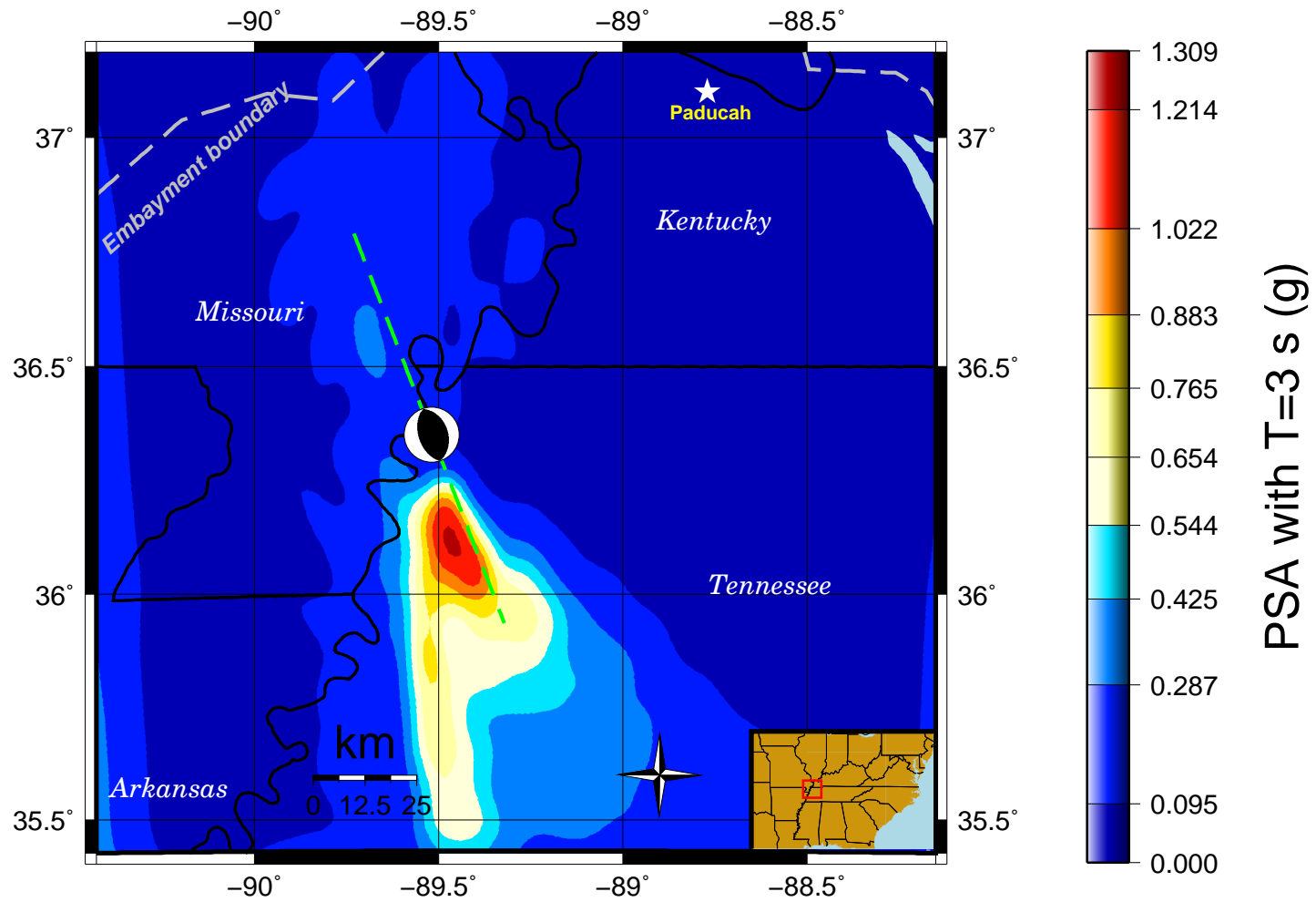


Figure 4.29: Pseudospectral acceleration with 3 second period from rupture on the Reelfoot thrust fault. Focal mechanism is shown at the hypocenter.

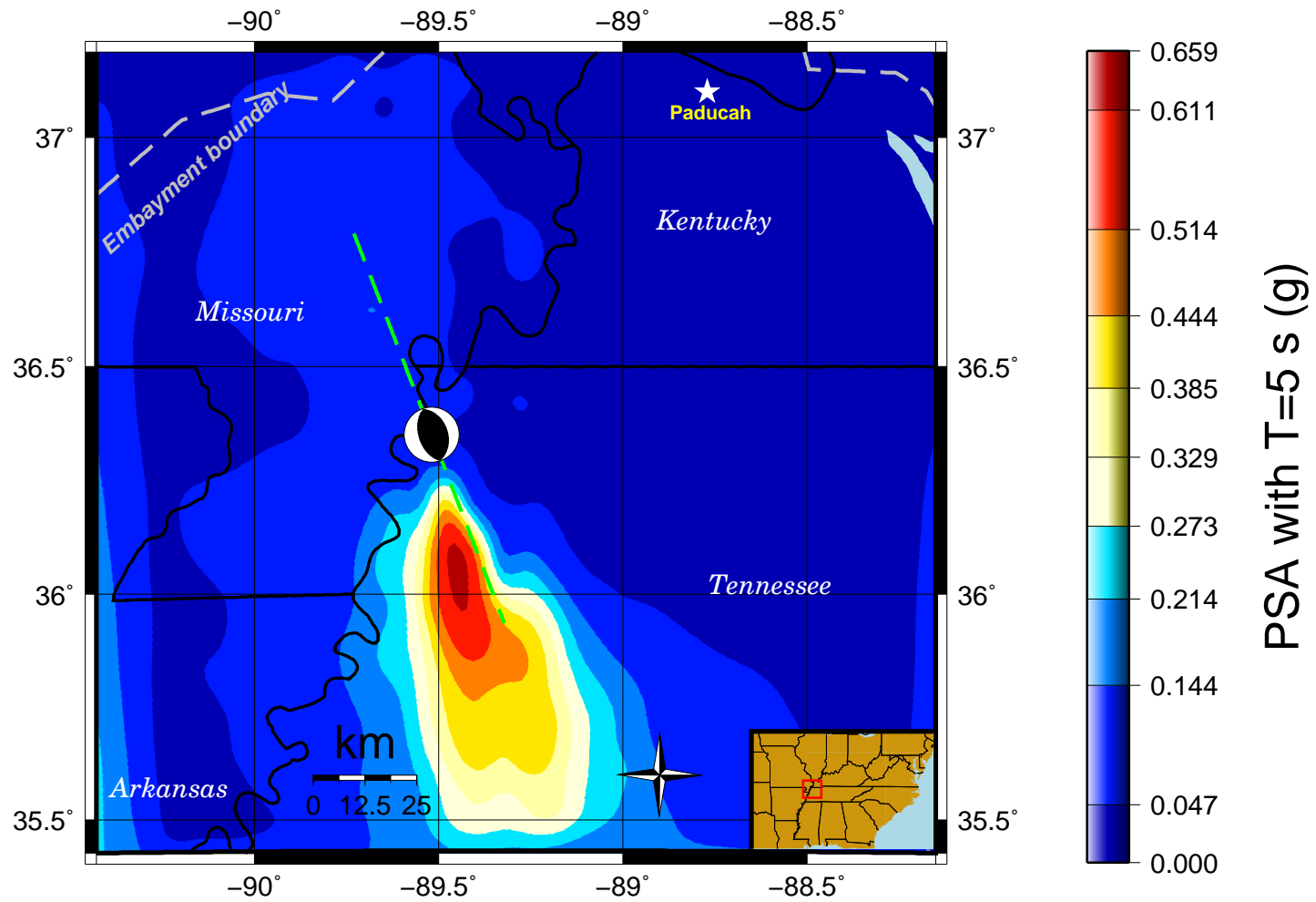


Figure 4.30: Pseudospectral acceleration with 5 second period from rupture on the Reelfoot thrust fault. Focal mechanism is shown at the hypocenter.

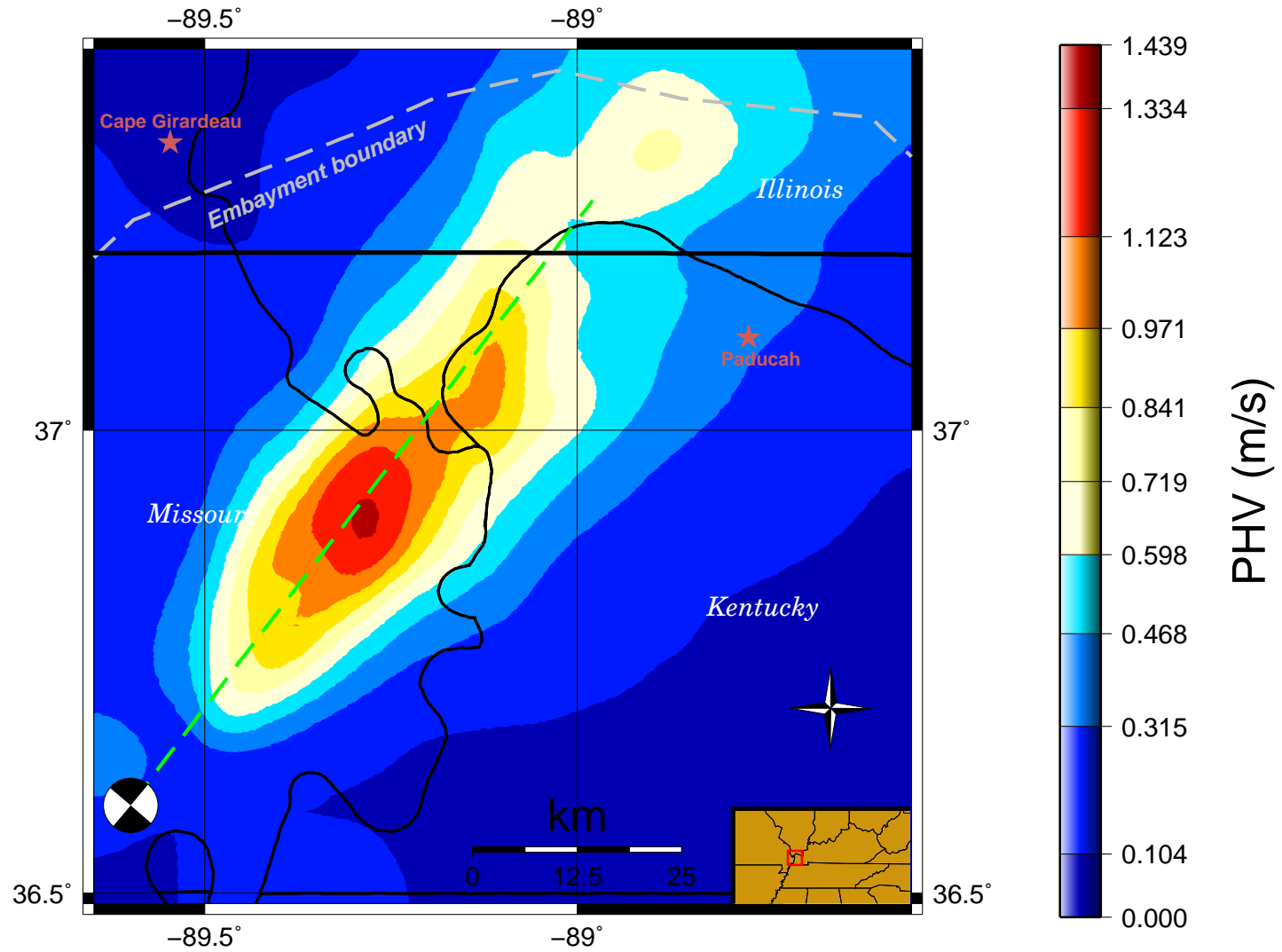


Figure 4.31: PHV from rupture on the strike-slip North fault. Focal mechanism is shown at the hypocenter.

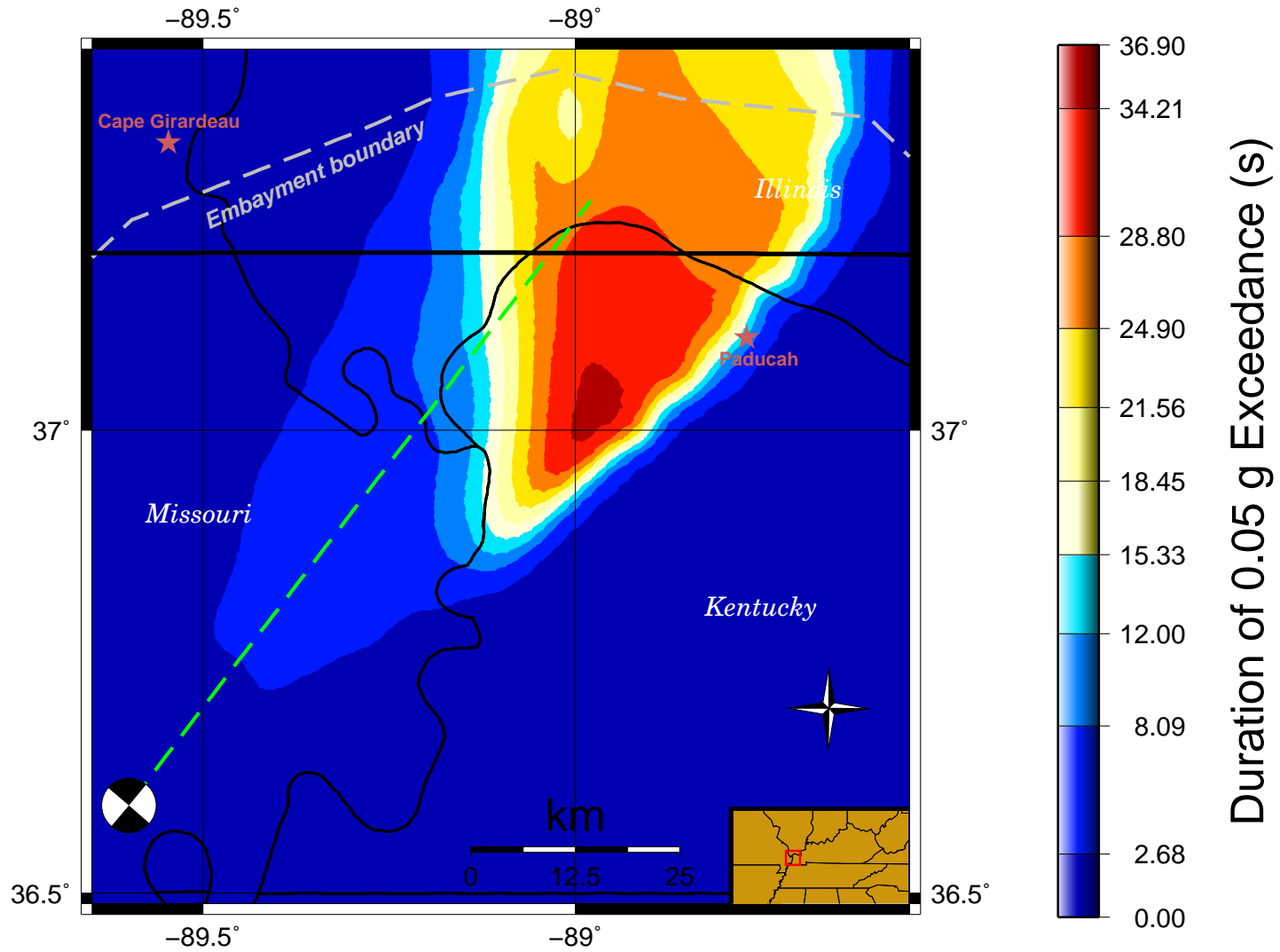


Figure 4.32: Bracketed Duration from rupture on the strike-slip North fault. Focal mechanism is shown at the hypocenter.

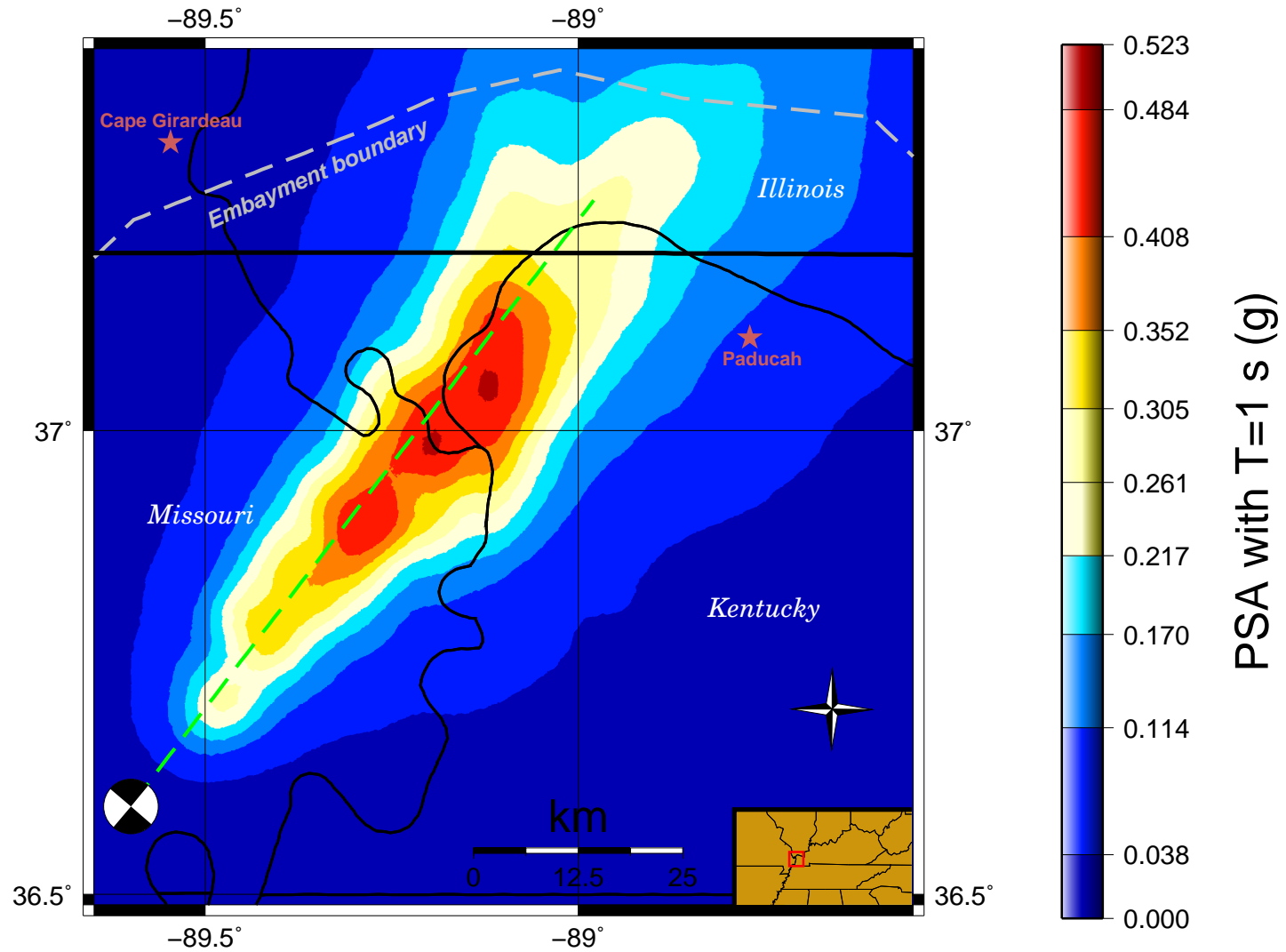


Figure 4.33: Pseudospectral acceleration with 1 second period from rupture on the strike-slip North fault. Focal mechanism is shown at the hypocenter.

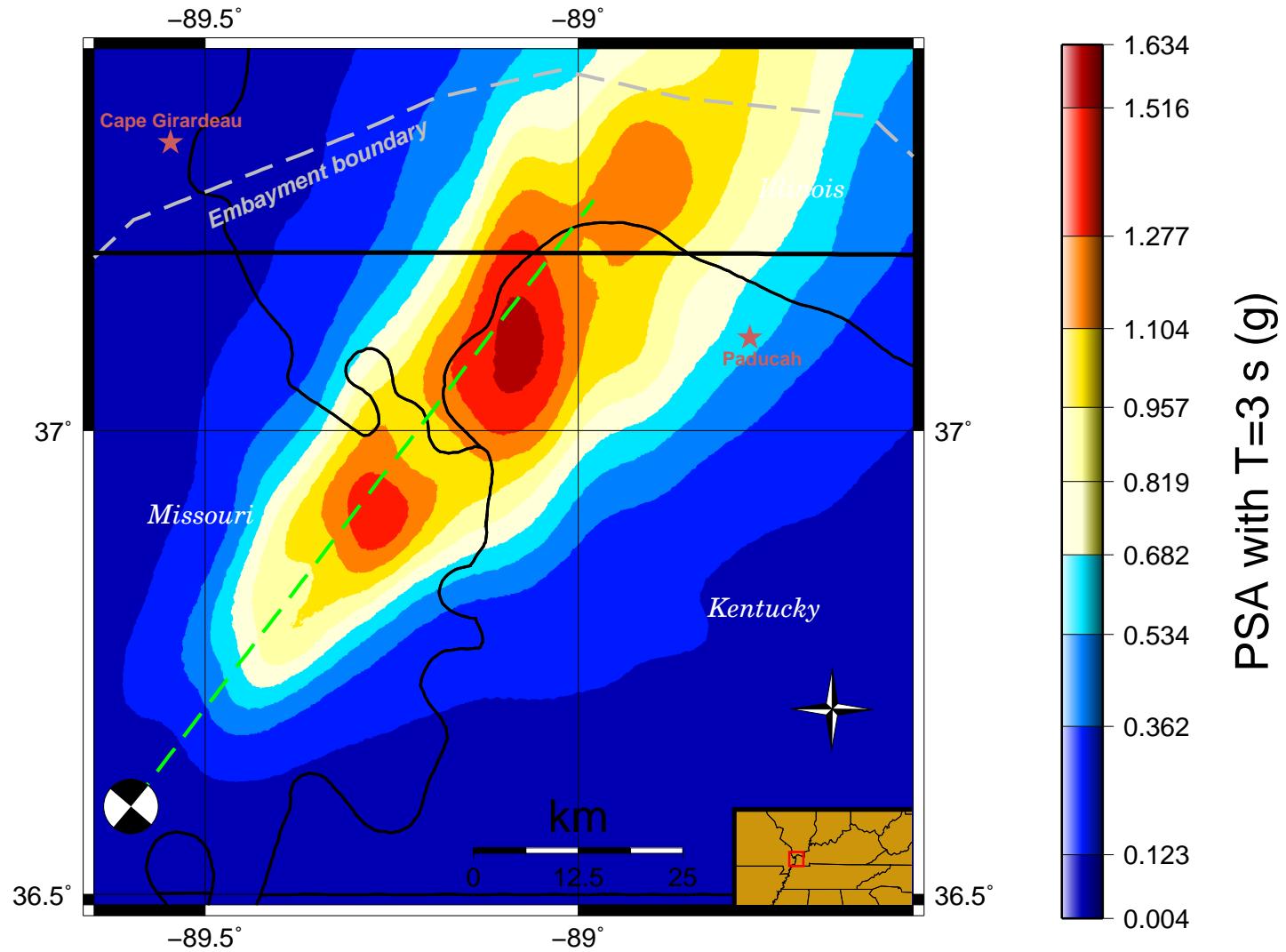


Figure 4.34: Pseudospectral acceleration with 3 second period from rupture on the strike-slip North fault. Focal mechanism is shown at the hypocenter.

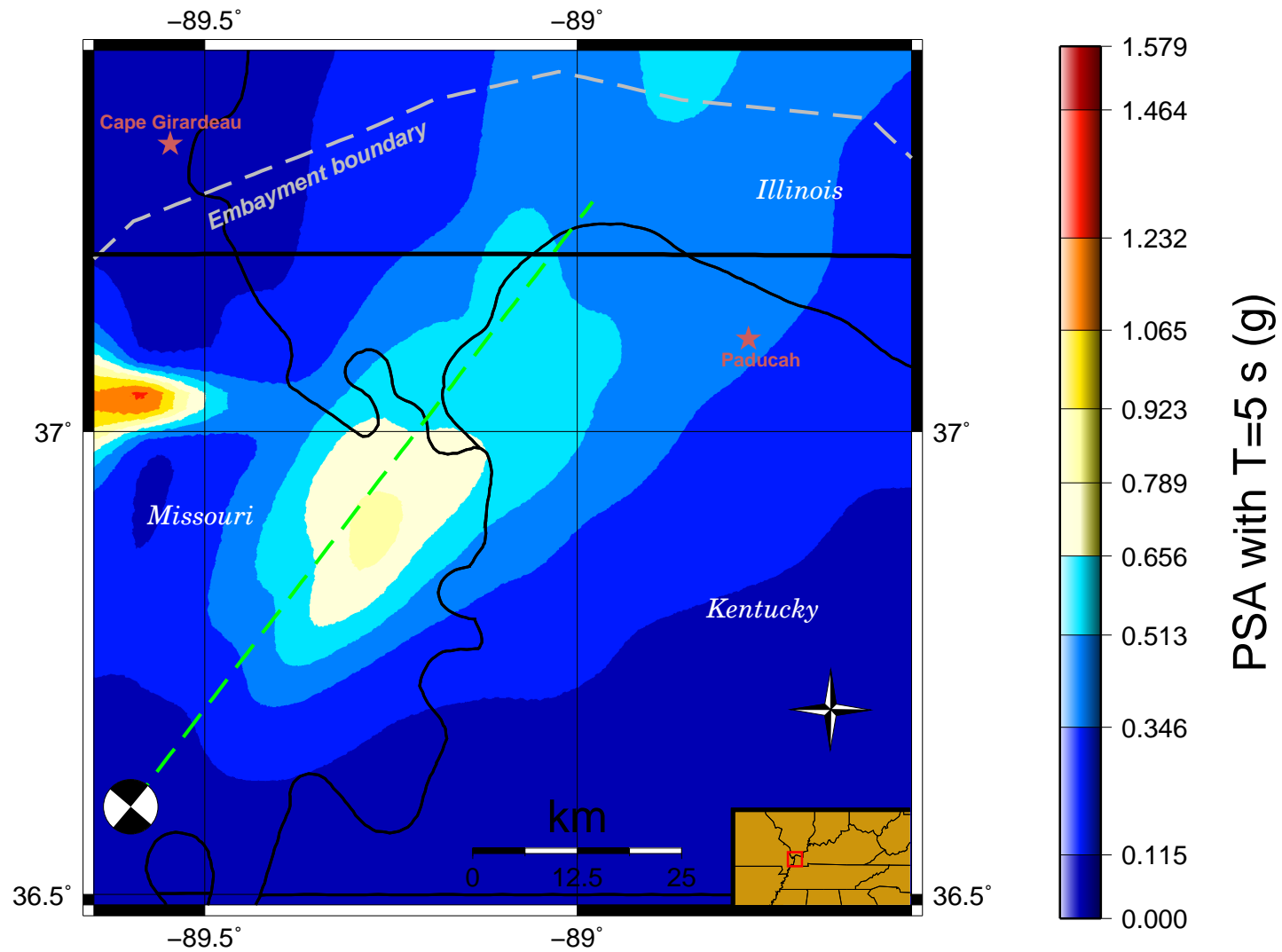


Figure 4.35: Pseudospectral acceleration with 5 second period from rupture on the strike-slip North fault. Focal mechanism is shown at the hypocenter.

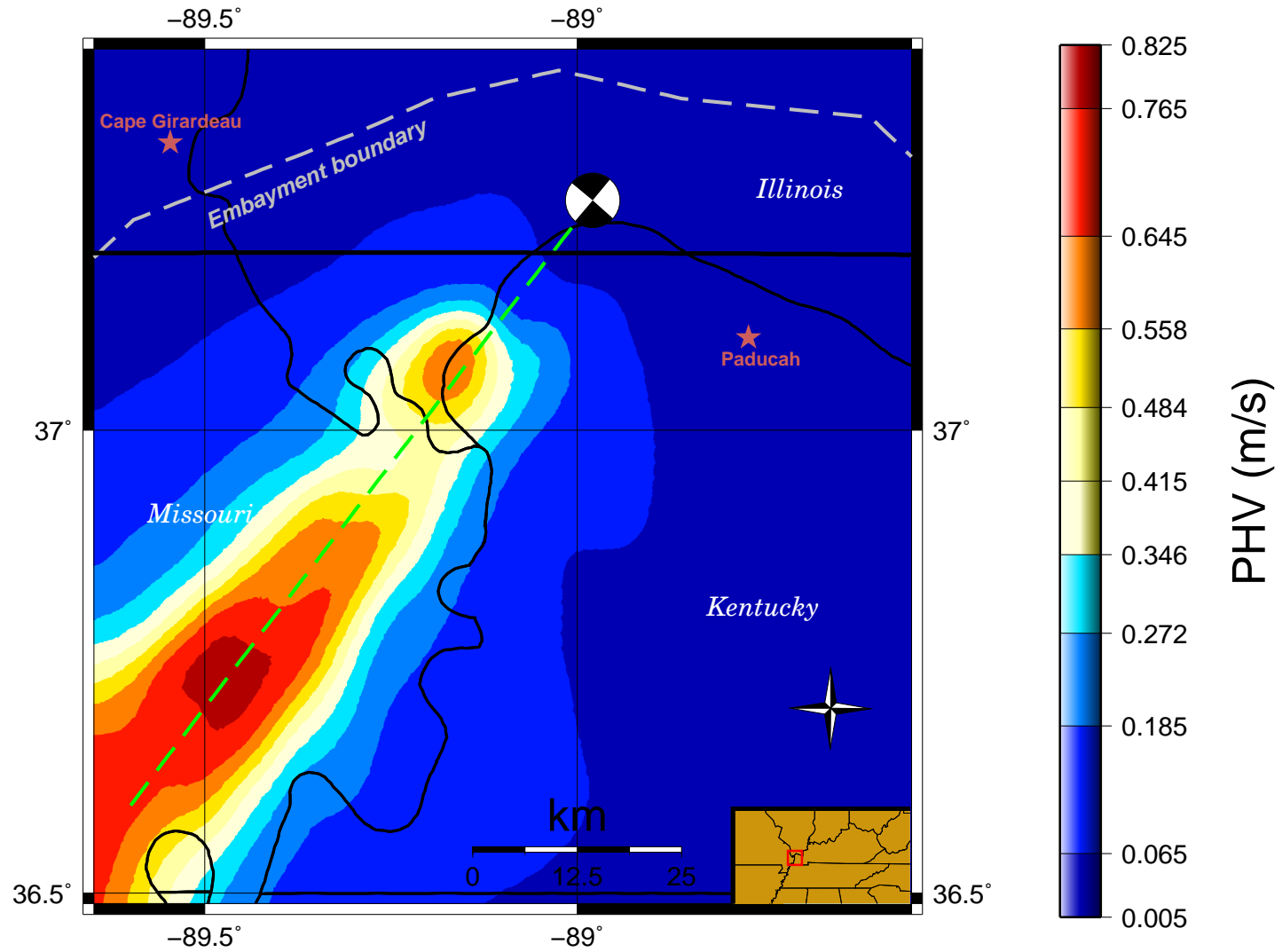


Figure 4.36: PHV from rupture on the strike-slip North fault. Focal mechanism is shown at the hypocenter.

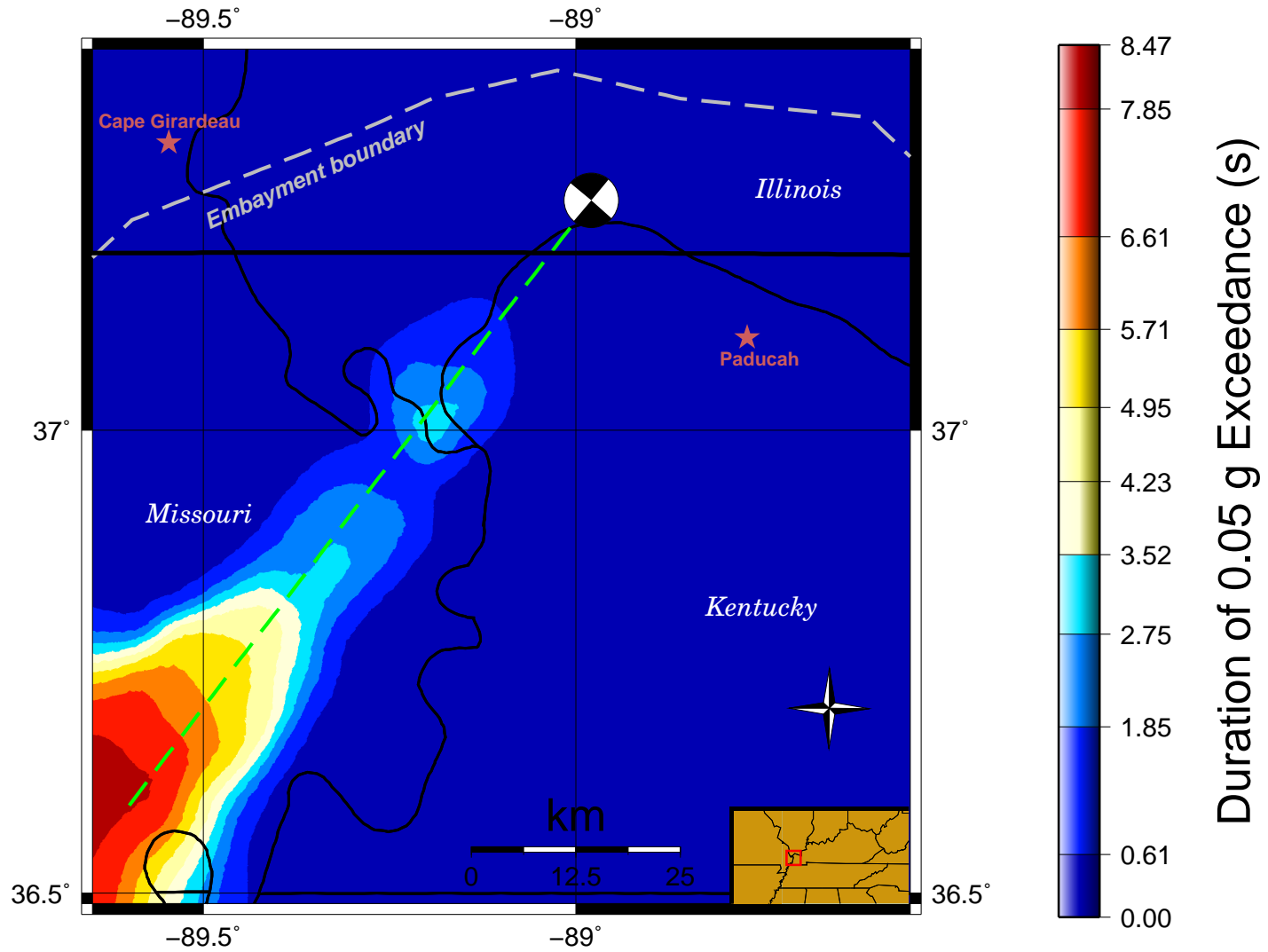


Figure 4.37: Bracketed Duration from rupture on the strike-slip North fault. Focal mechanism is shown at the hypocenter.

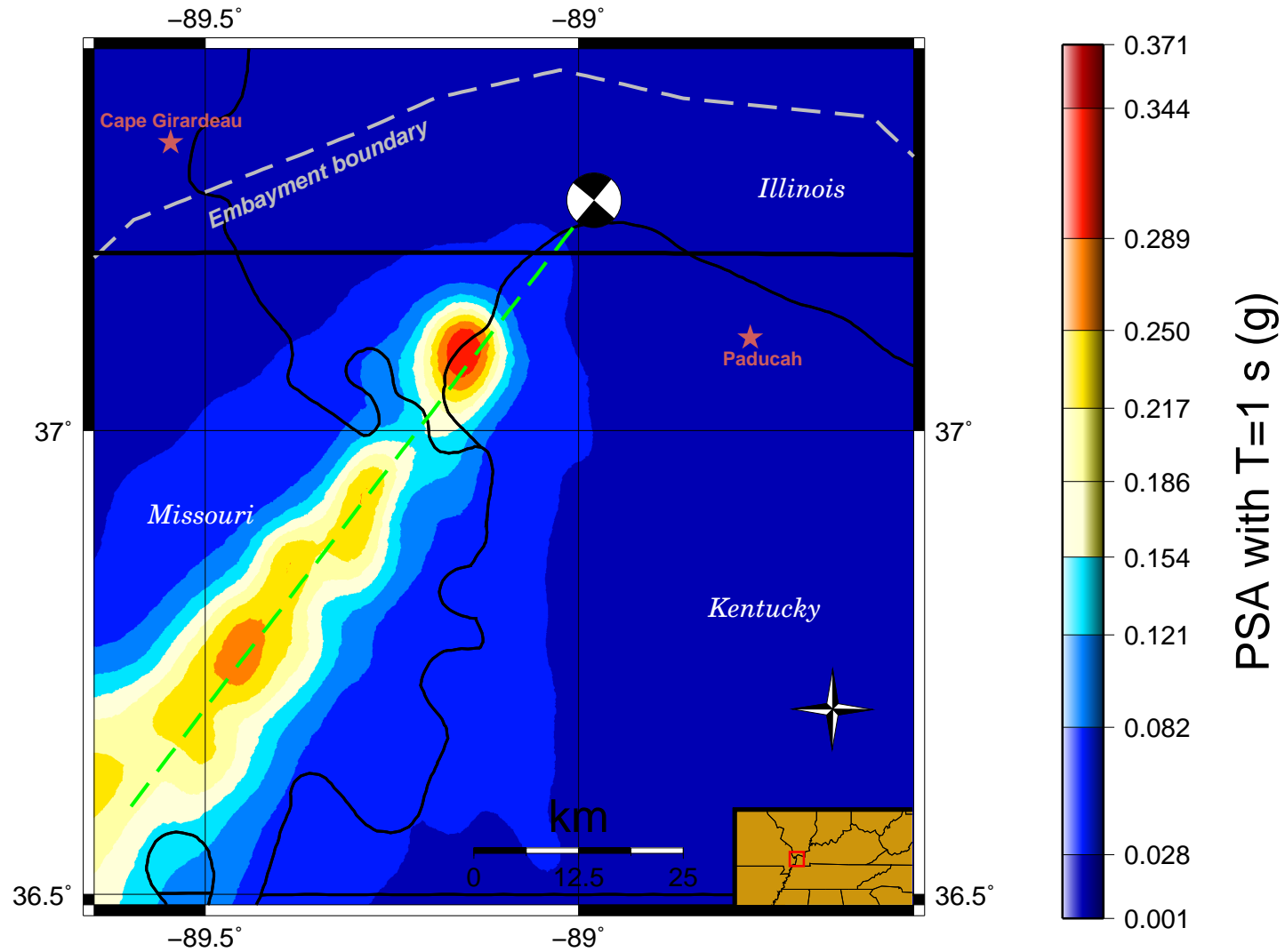


Figure 4.38: Pseudospectral acceleration with 1 second period from rupture on the strike-slip North fault. Focal mechanism is shown at the hypocenter.

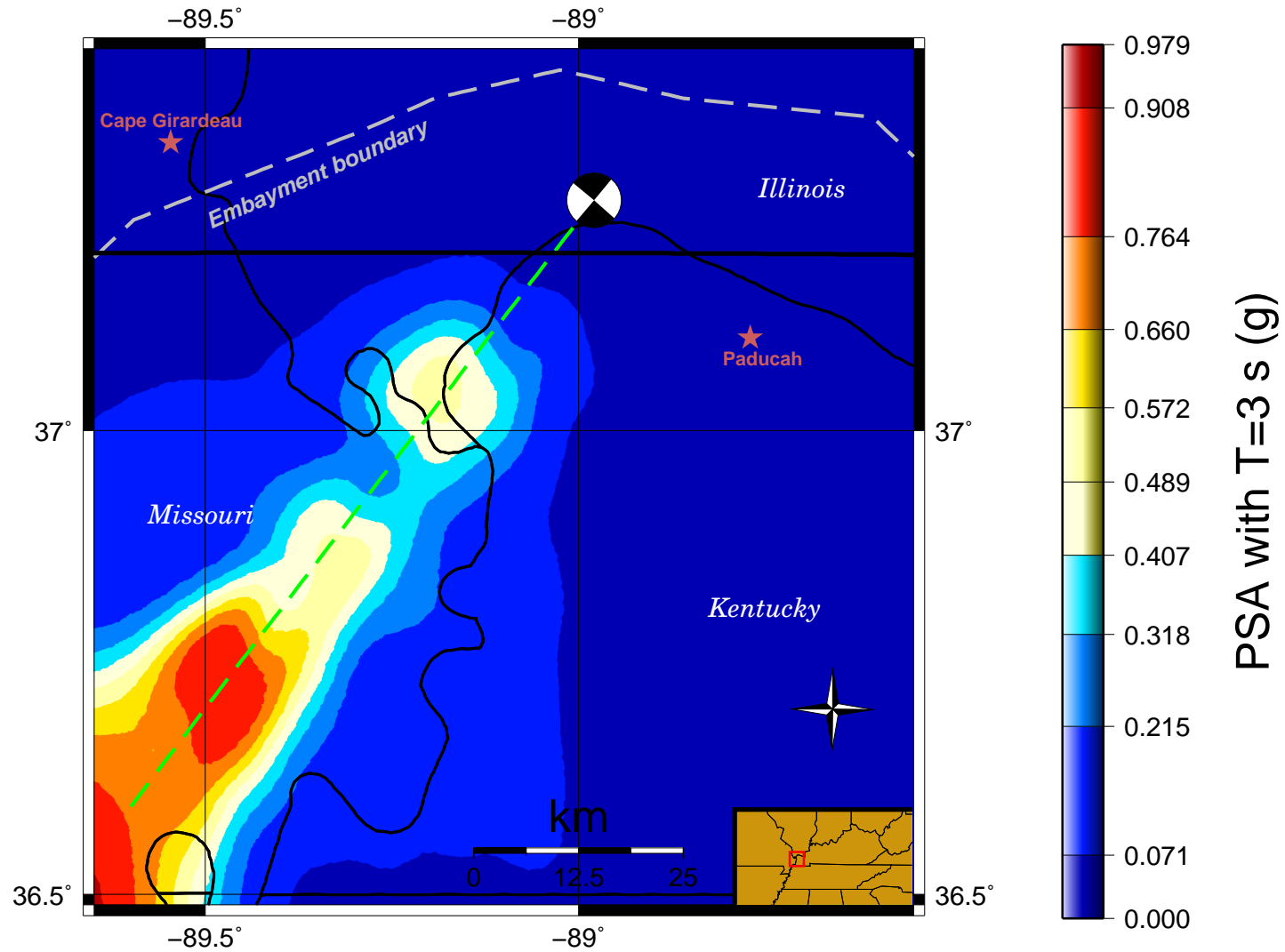


Figure 4.39: Pseudospectral acceleration with 3 second period from rupture on the strike-slip North fault. Focal mechanism is shown at the hypocenter.

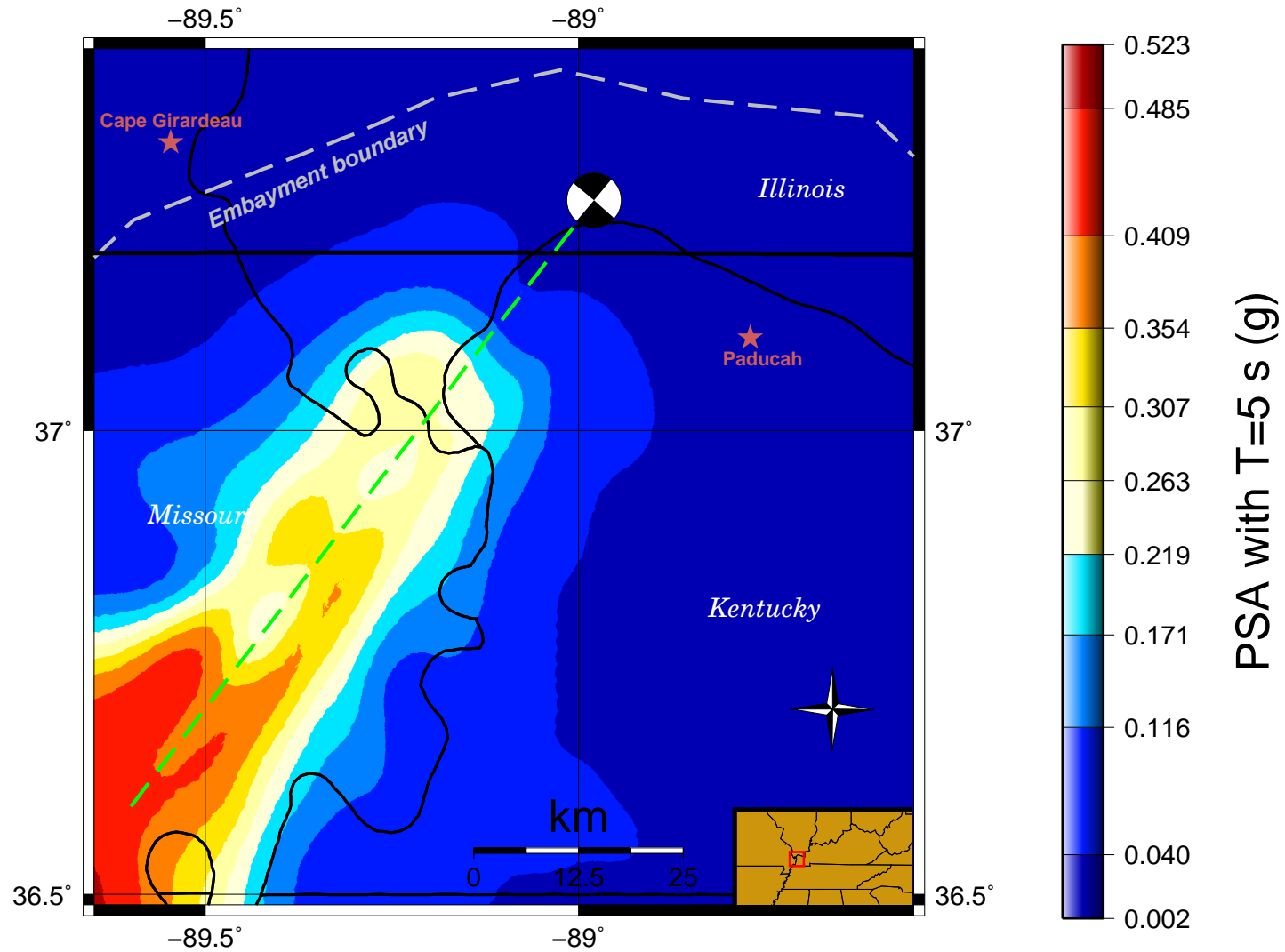


Figure 4.40: Pseudospectral acceleration with 5 second period from rupture on the strike-slip North fault. Focal mechanism is shown at the hypocenter.

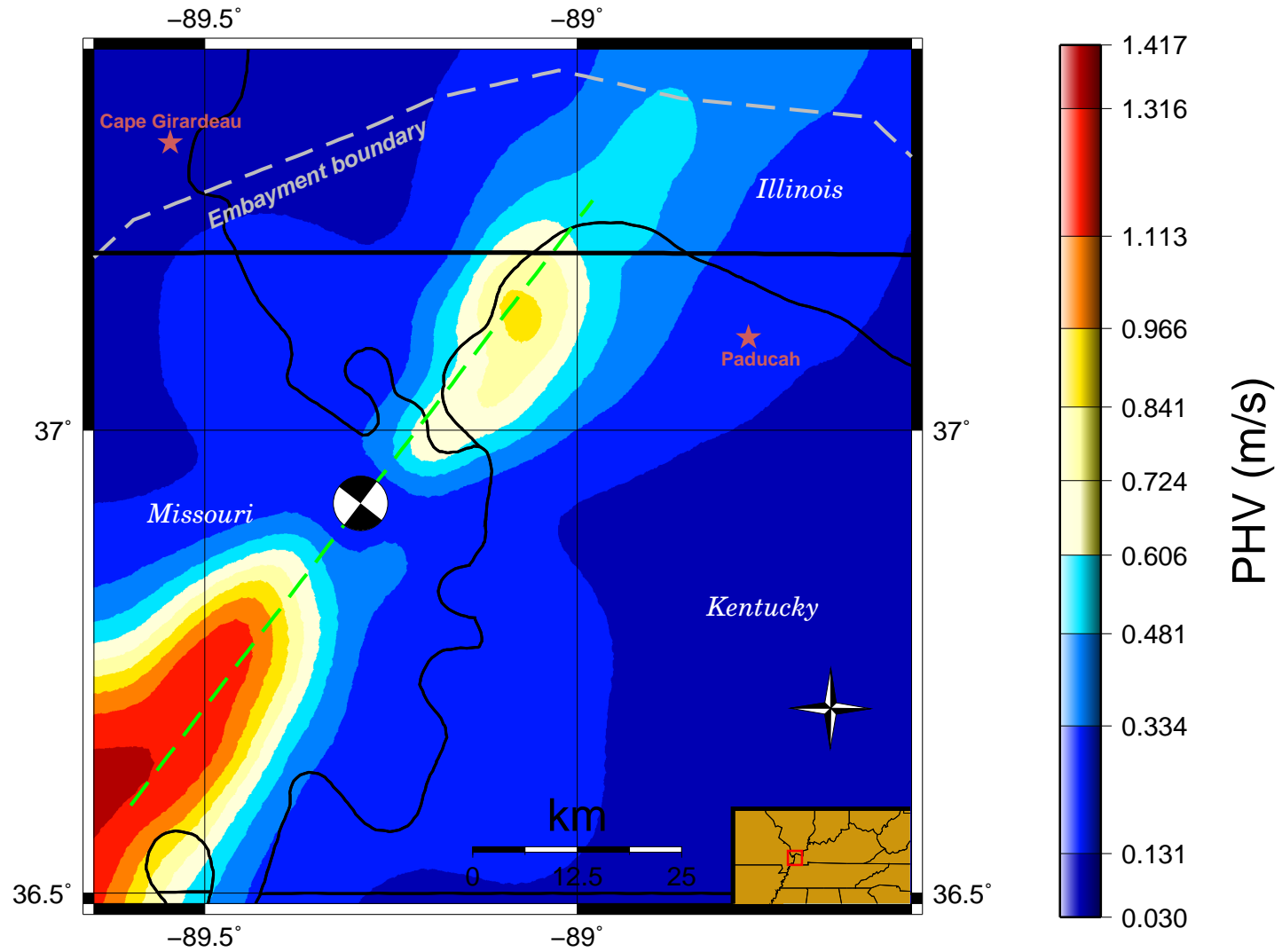


Figure 4.41: PHV from rupture on the strike-slip North fault. Focal mechanism is shown at the hypocenter.

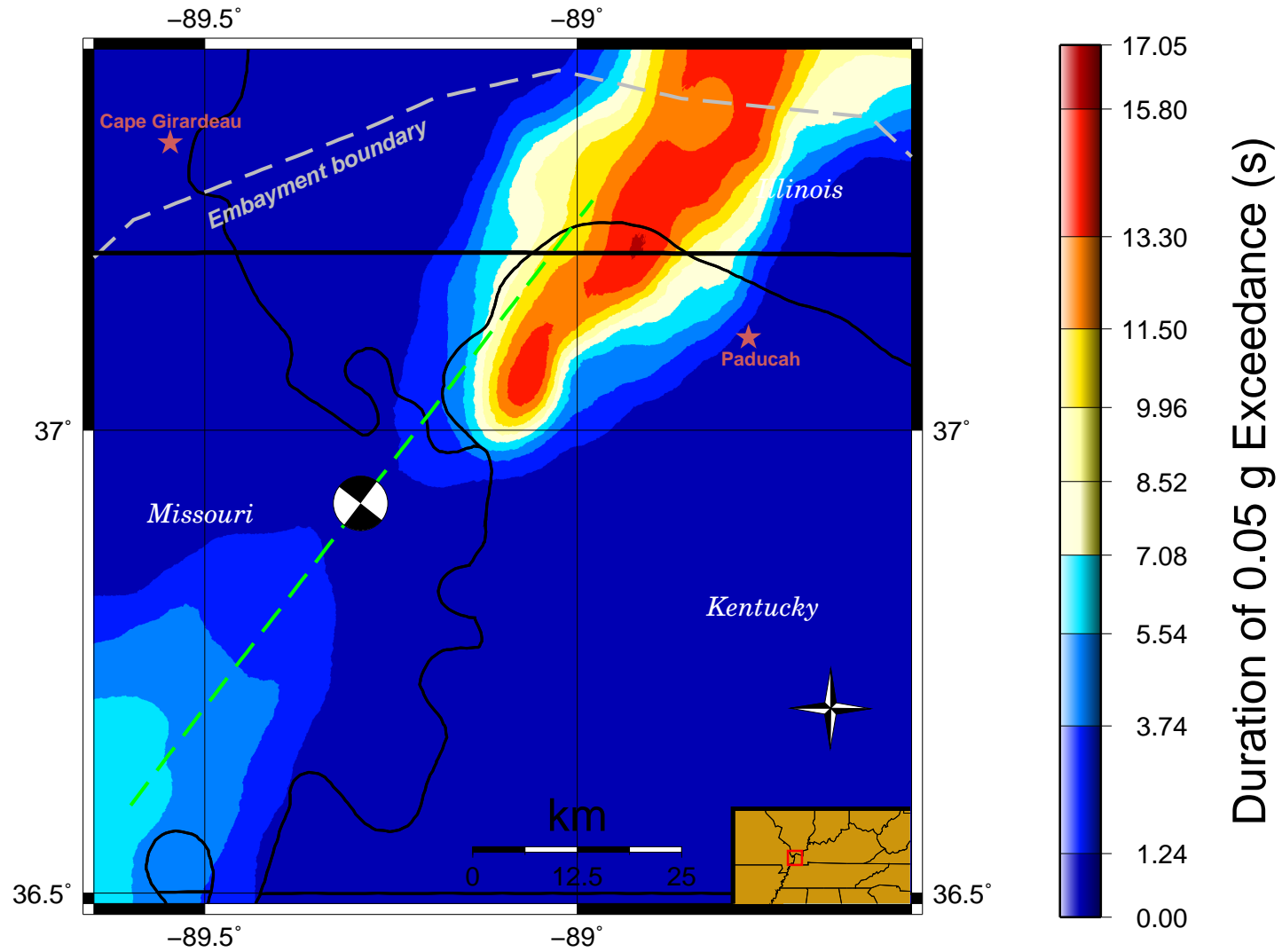


Figure 4.42: Bracketed Duration from rupture on the strike-slip North fault. Focal mechanism is shown at the hypocenter.

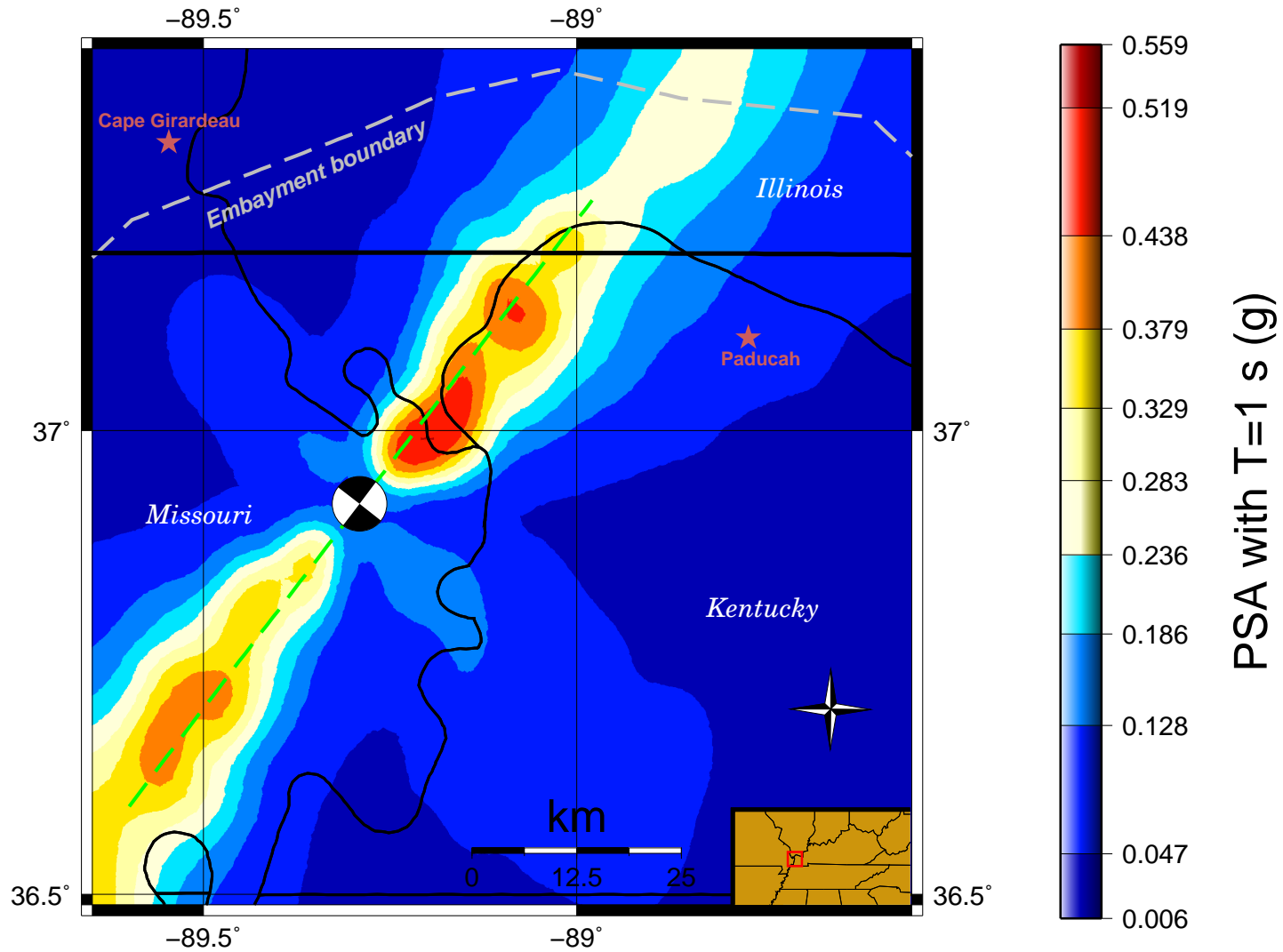


Figure 4.43: Pseudospectral acceleration with 1 second period from rupture on the strike-slip North fault. Focal mechanism is shown at the hypocenter.

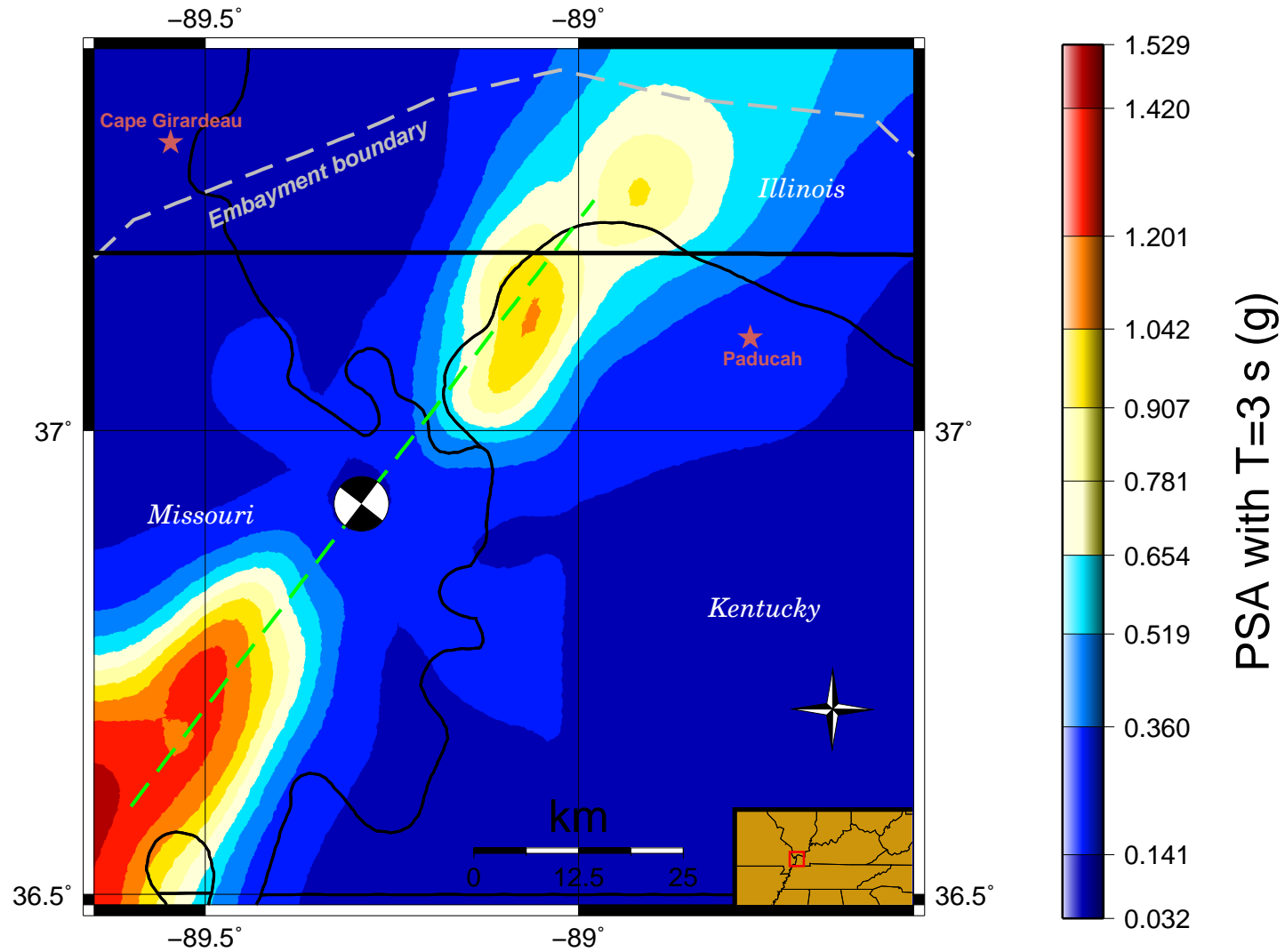


Figure 4.44: Pseudospectral acceleration with 3 second period from rupture on the strike-slip North fault. Focal mechanism is shown at the hypocenter.

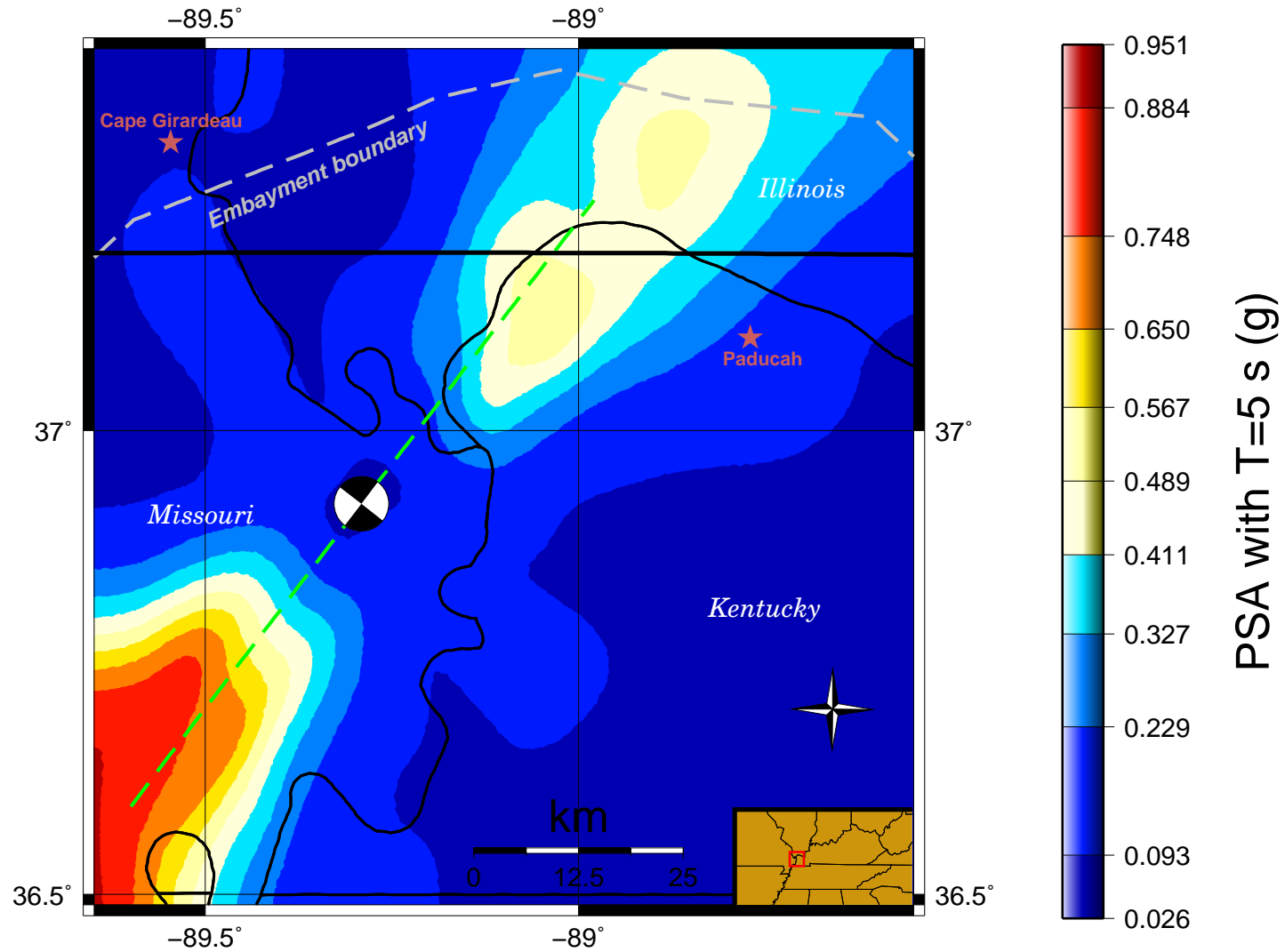


Figure 4.45: Pseudospectral acceleration with 5 second period from rupture on the strike-slip North fault. Focal mechanism is shown at the hypocenter.

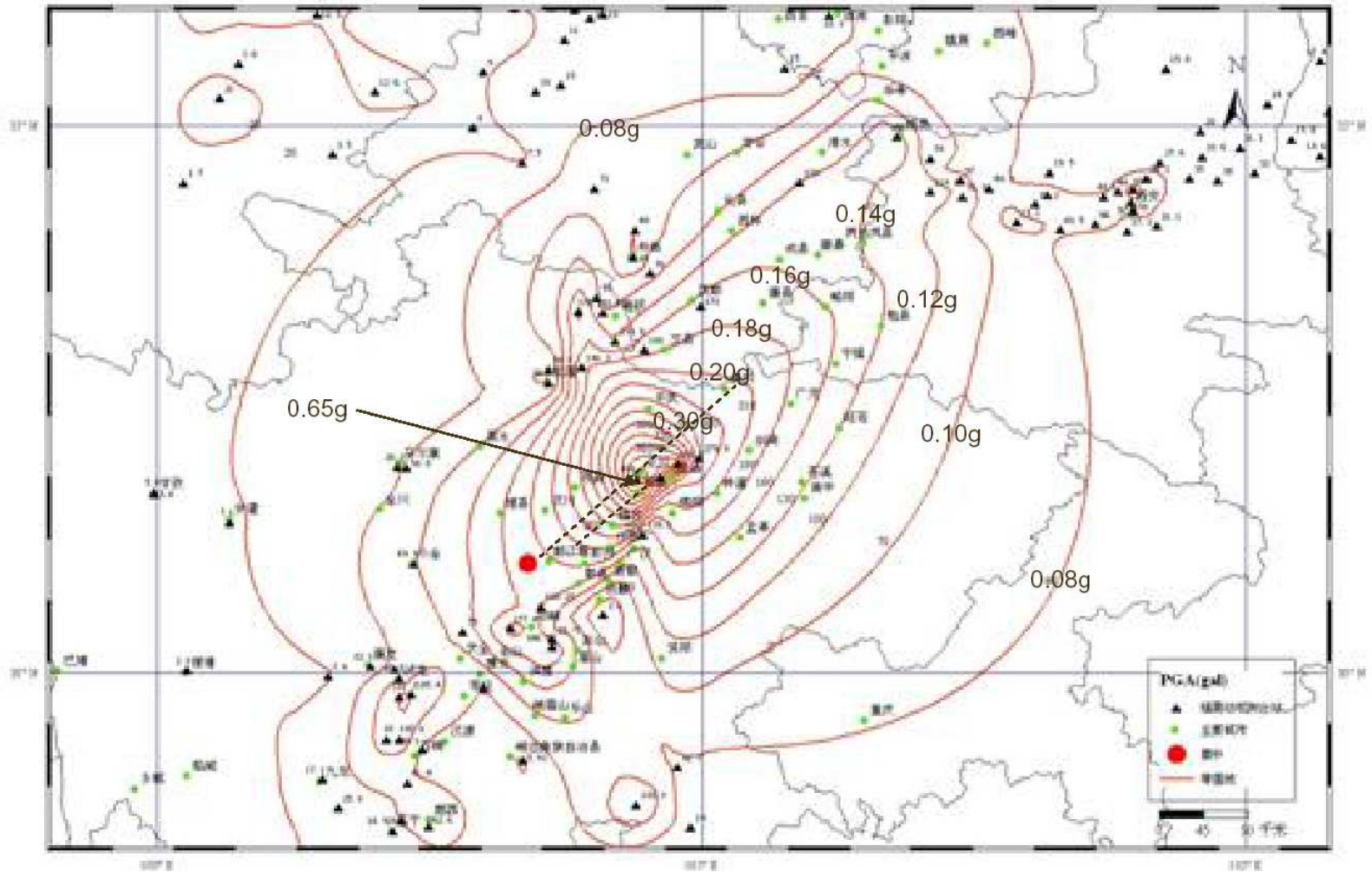


Figure 4.46: PGA from the May 12, 2008, $M_w = 7.9$ Sichuan, China earthquake.

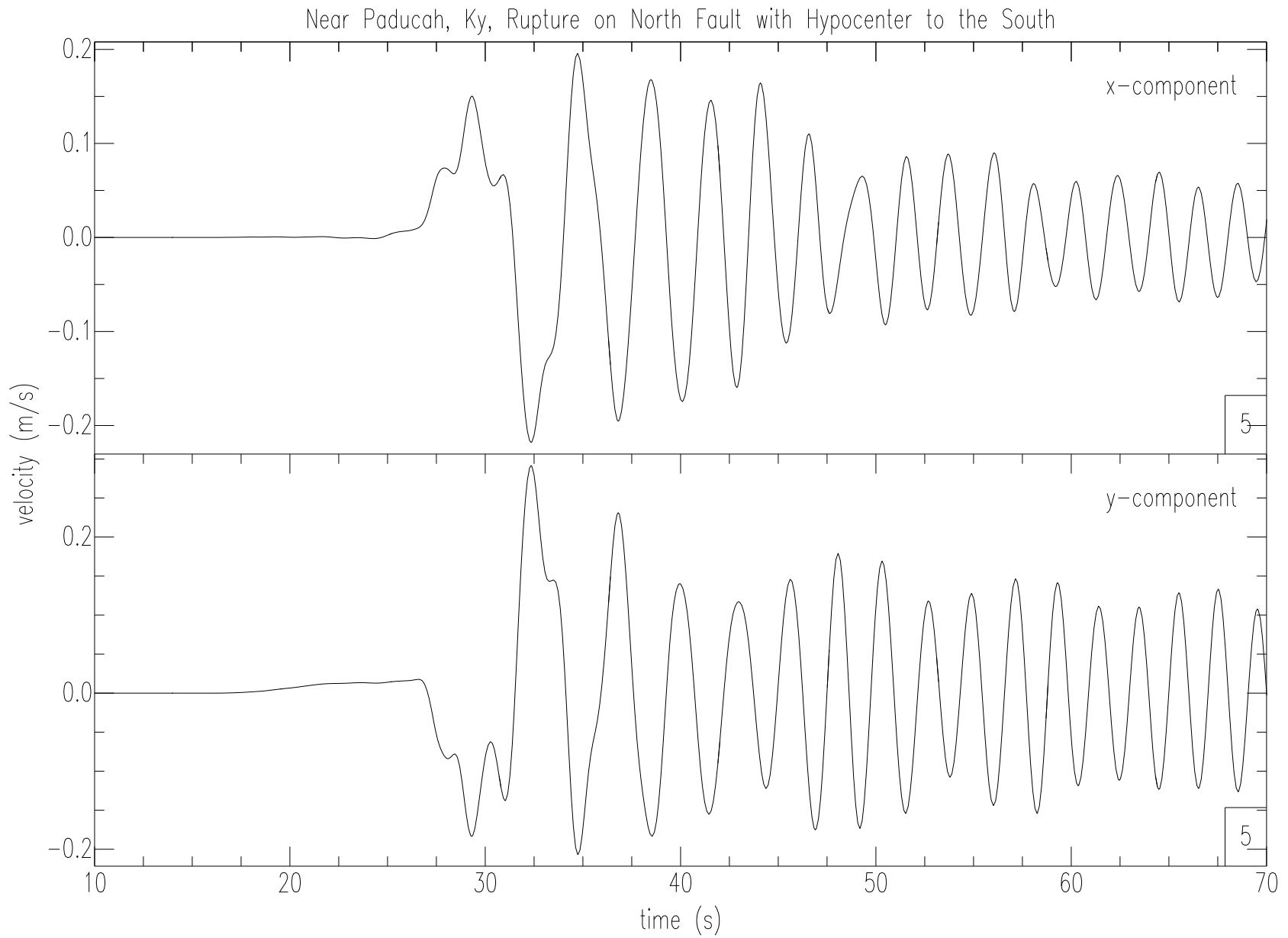


Figure 4.47: Time series at a receiver ≈ 2.28 km from Paducah, Ky in response to a rupture on the New Madrid North fault with the hypocenter to the south.

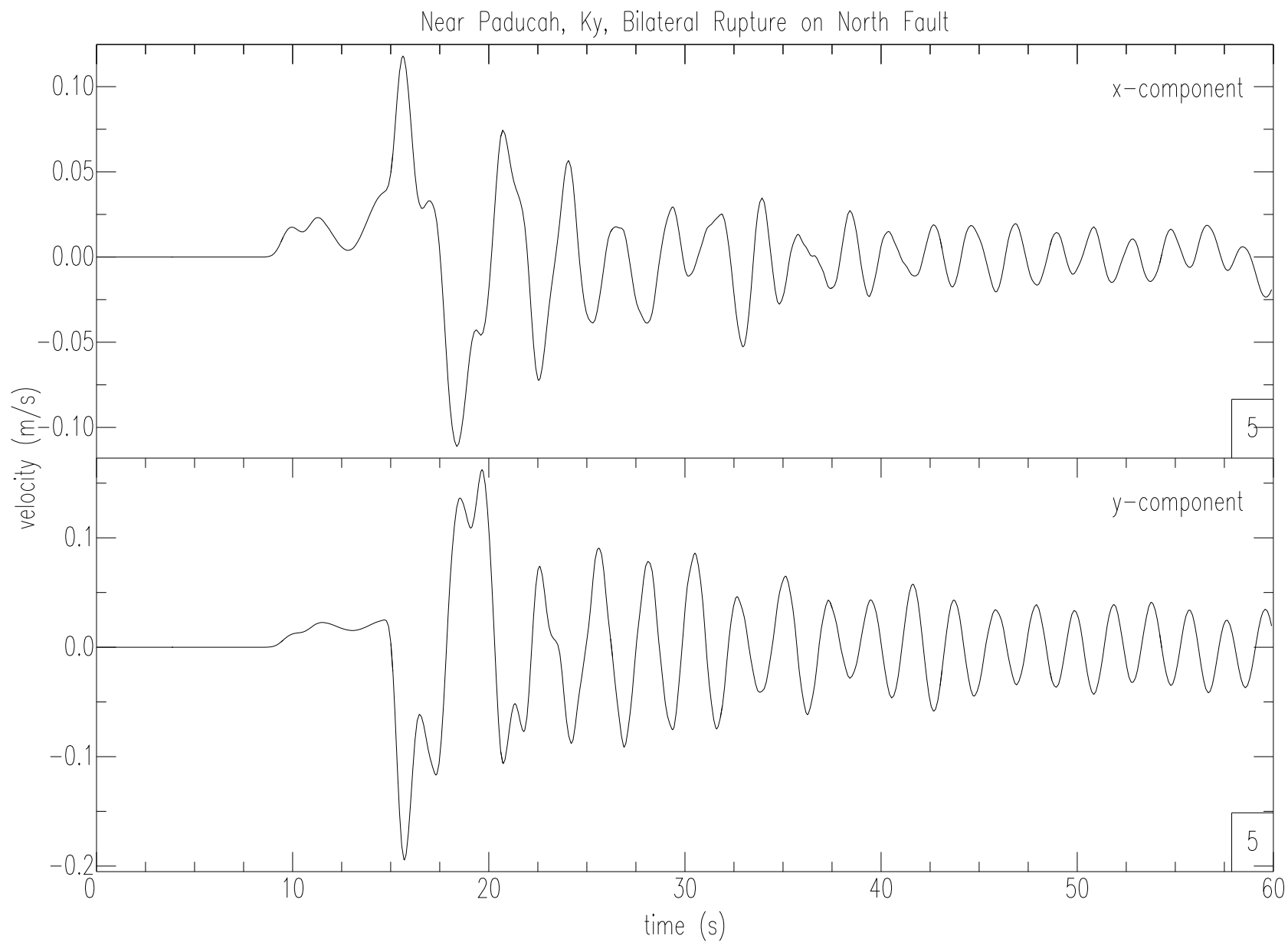


Figure 4.48: Time series at a receiver ≈ 2.28 km from Paducah, Ky in response to a bilateral rupture on the New Madrid North fault.

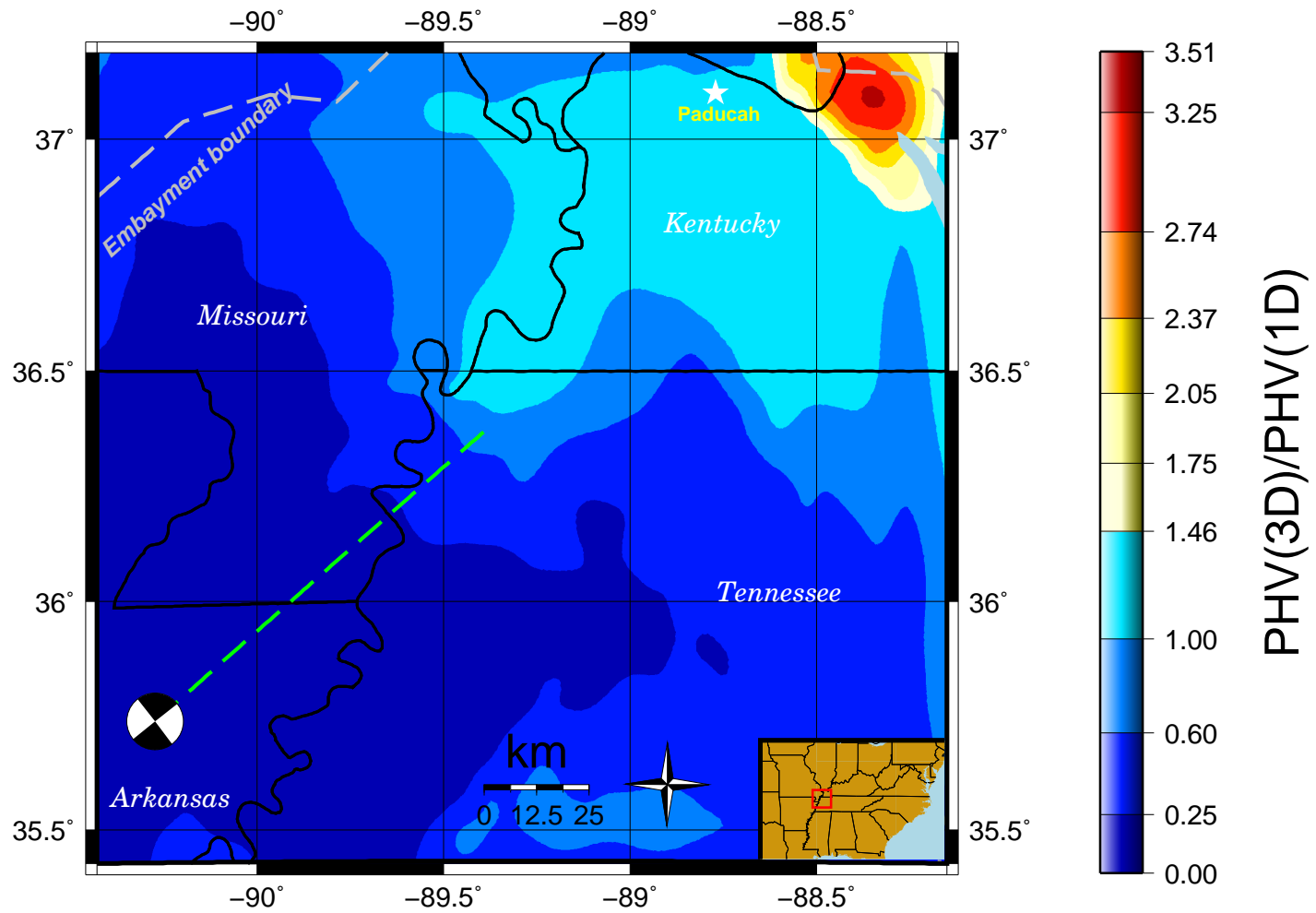


Figure 4.49: 3D/1D amplification (eqn. 3.14) map showing the effect of the 3D structure to the ground-motion response from a northward propagating rupture on the Cottonwood Grove fault. Focal mechanism is shown at the hypocenter.

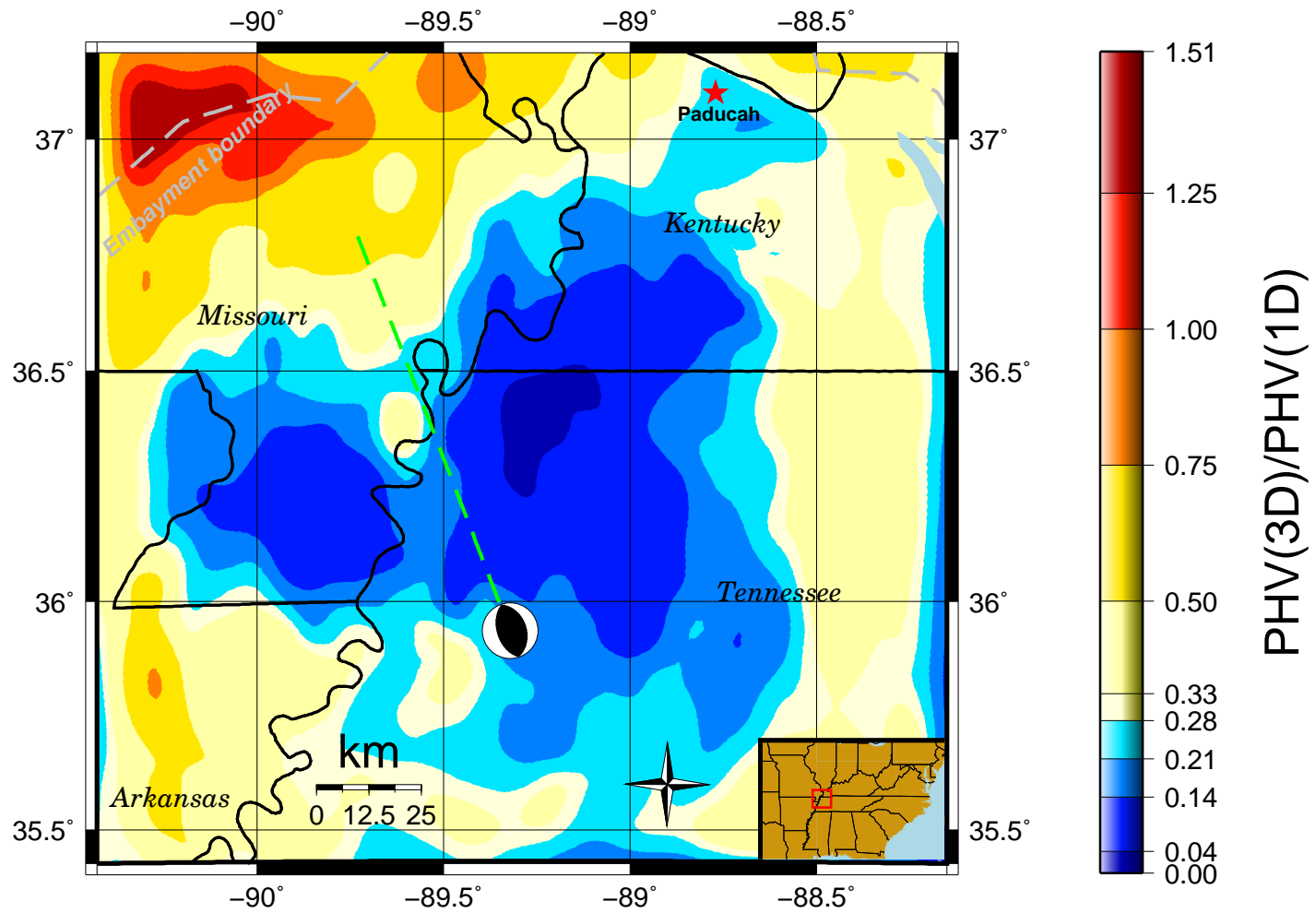


Figure 4.50: 3D/1D amplification (eqn. 3.14) map showing the effect of the 3D structure to the ground-motion response from a northward propagating rupture on the Reelfoot thrust fault. Focal mechanism is shown at the hypocenter.

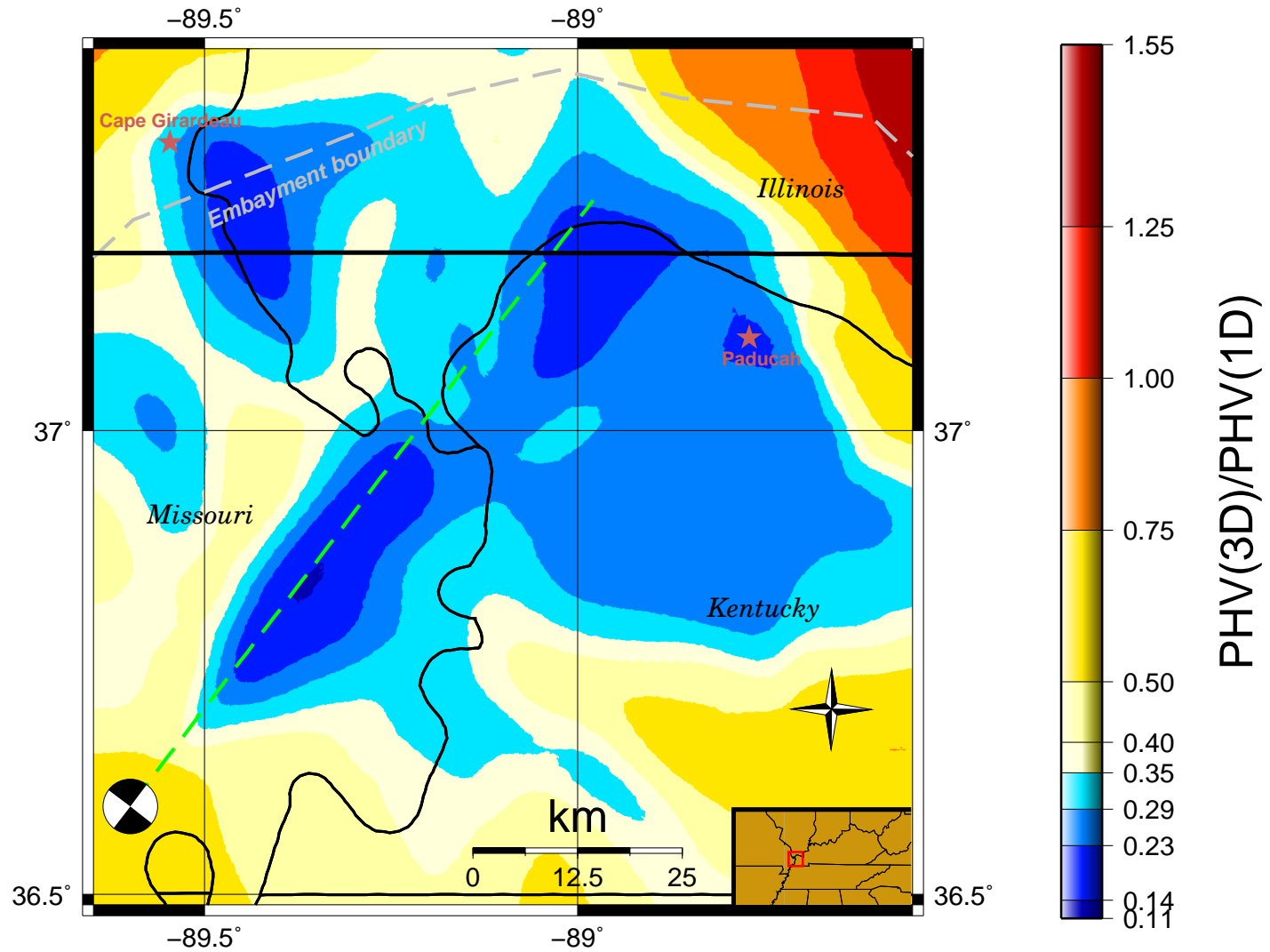


Figure 4.51: 3D/1D amplification (eqn. 3.14) map showing the effect of the 3D structure to the ground-motion response from a northward propagating rupture on the New Madrid North fault. Focal mechanism is shown at the hypocenter.

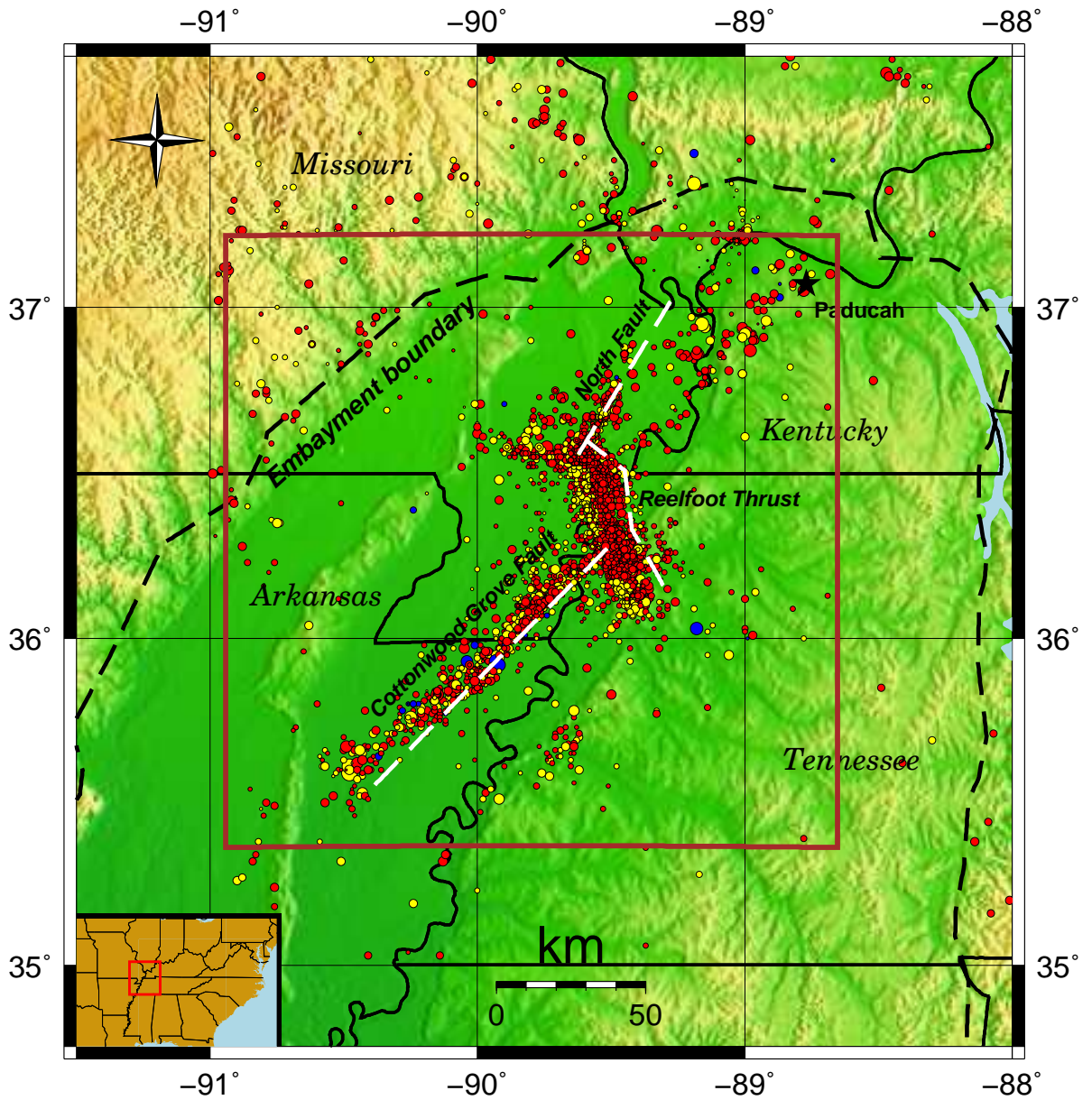


Figure 4.52: Study area showing fault traces (dashed white lines) and background seismicity since 1974. Red, yellow, and blue data points represents focal mechanisms of increasing depth.

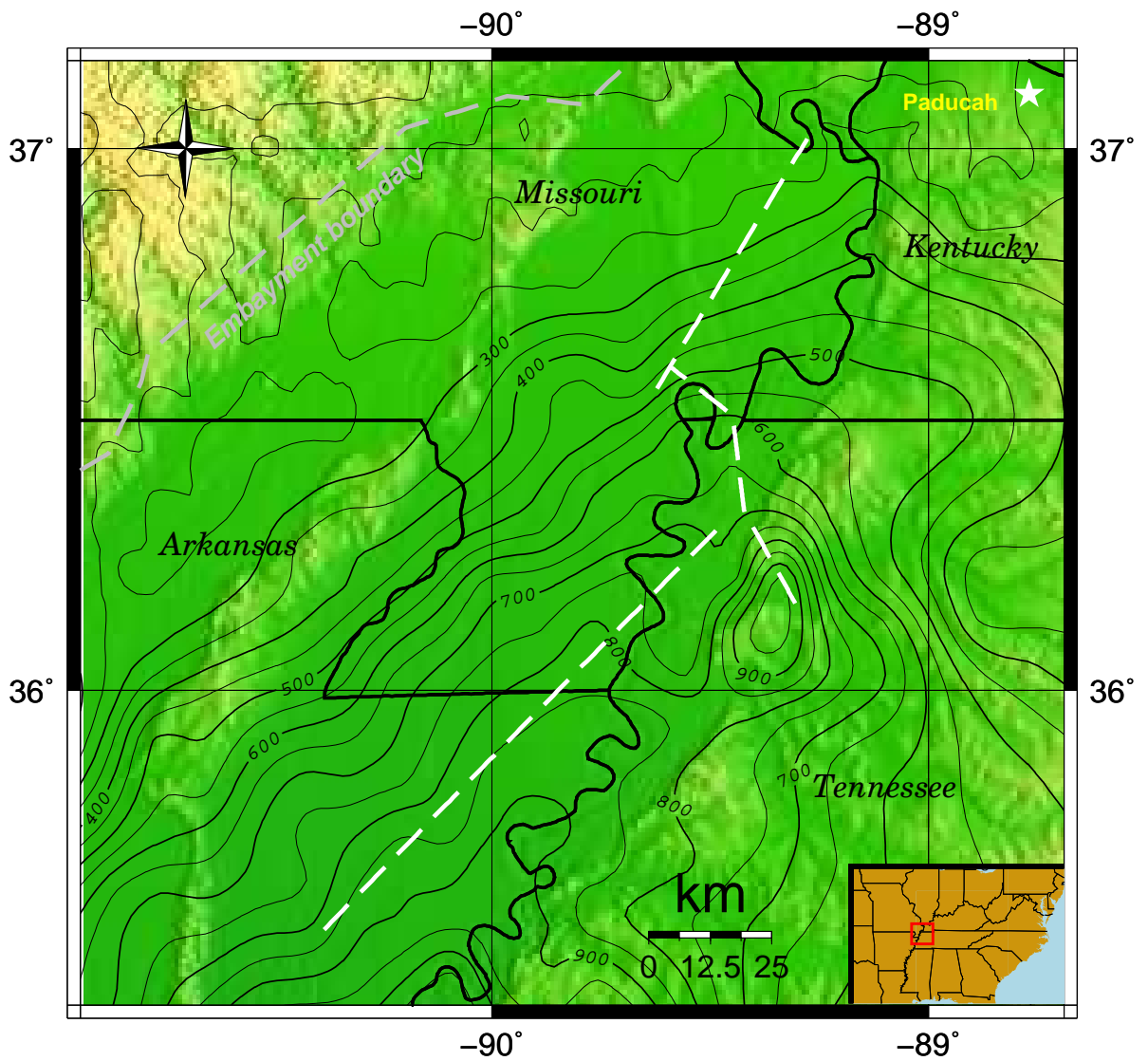


Figure 4.53: Contour map of depth to layer with a shear wave velocity of 2,000 m/s. Contour lines are in meters, with a contour interval of 50 meters.

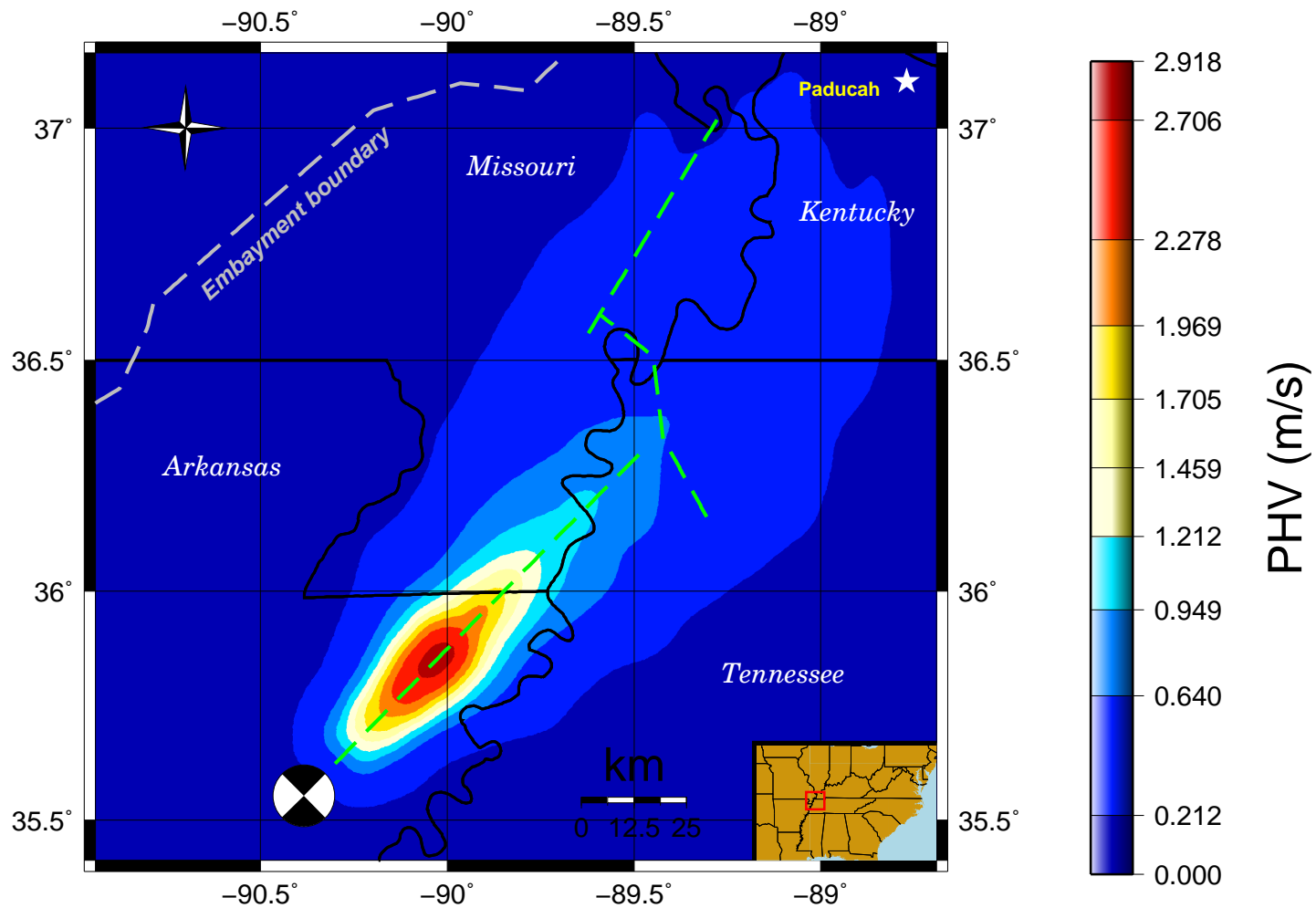


Figure 4.54: PHV from rupture on the strike-slip Cottonwood Grove fault. Focal mechanism is shown at the hypocenter.

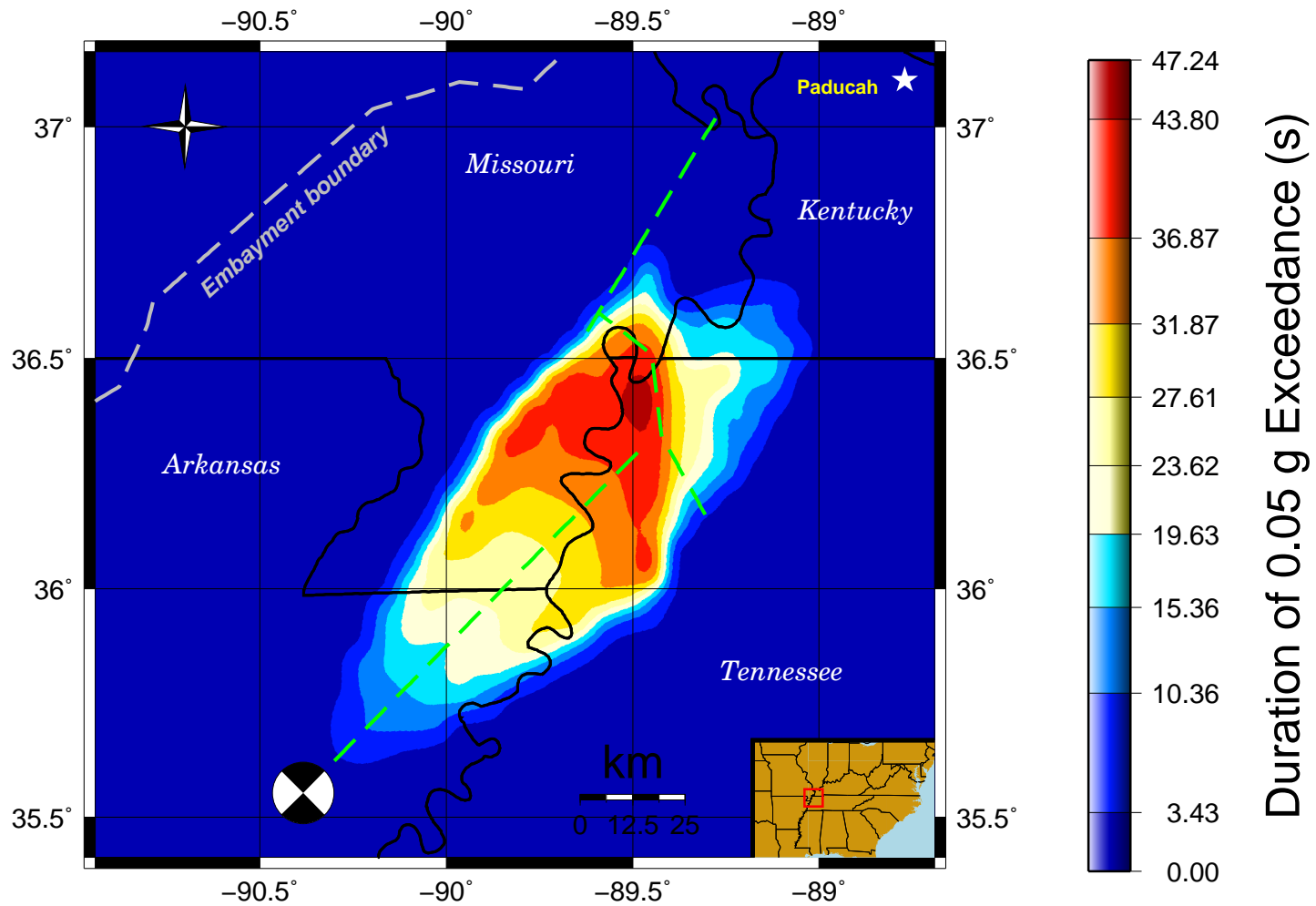


Figure 4.55: Bracketed Duration from rupture on the strike-slip Cottonwood Grove Fault. Focal mechanism is shown at the hypocenter.

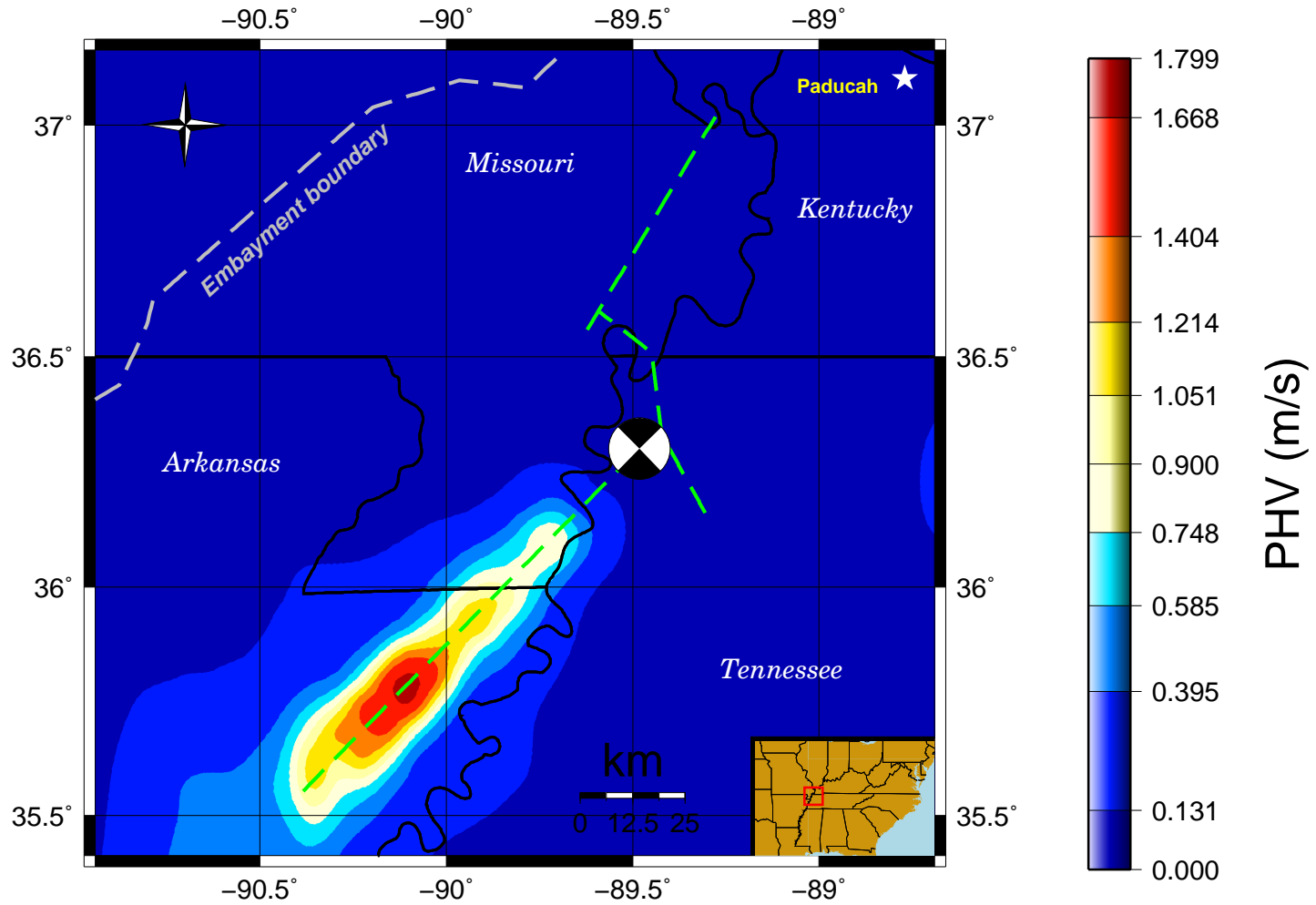


Figure 4.56: PHV from rupture on the strike-slip Cottonwood Grove Fault. Focal mechanism is shown at the hypocenter.

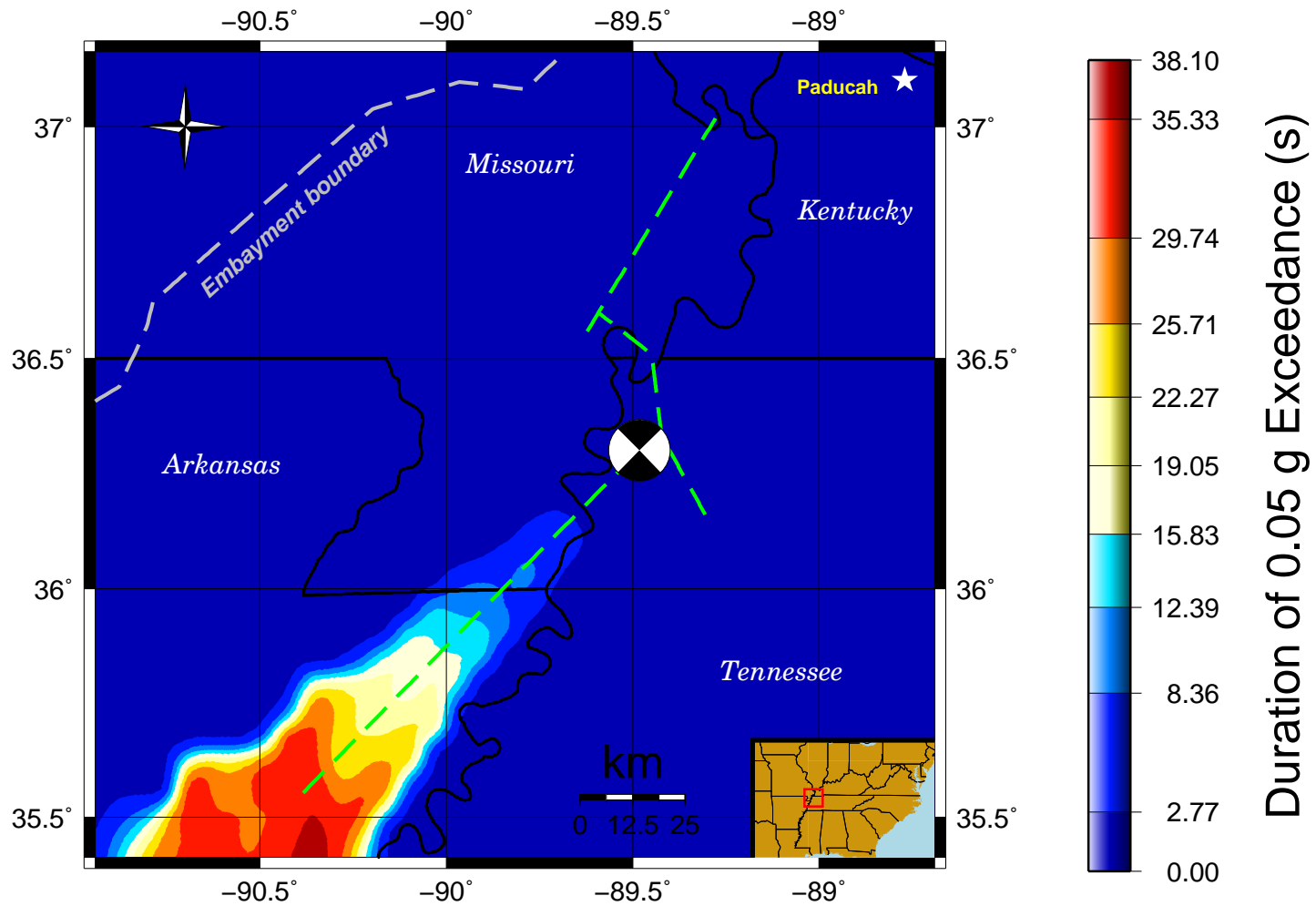


Figure 4.57: Bracketed Duration from rupture on the strike-slip Cottonwood Grove Fault. Focal mechanism is shown at the hypocenter.

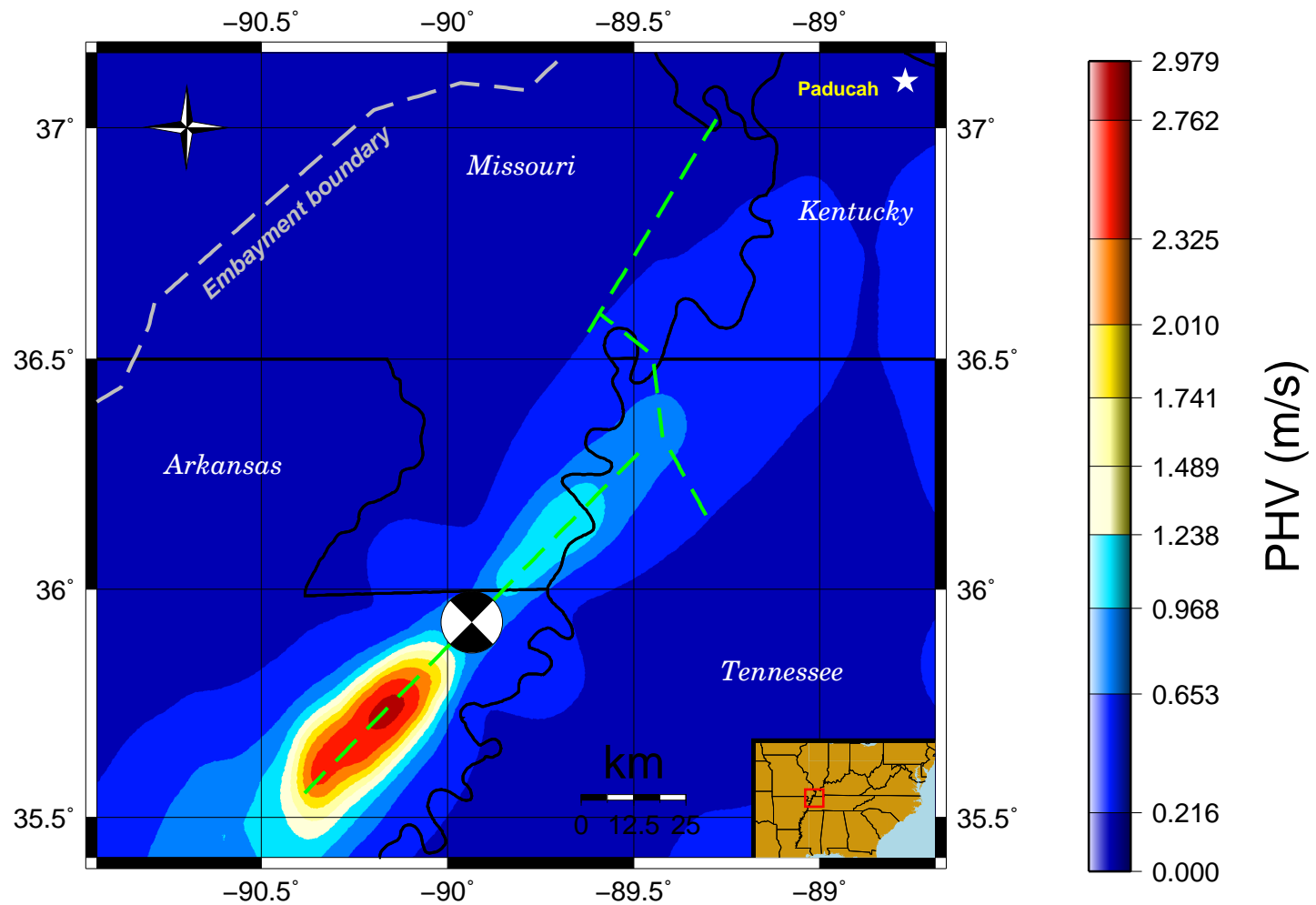


Figure 4.58: PHV from rupture on the strike-slip Cottonwood Grove Fault. Focal mechanism is shown at the hypocenter.

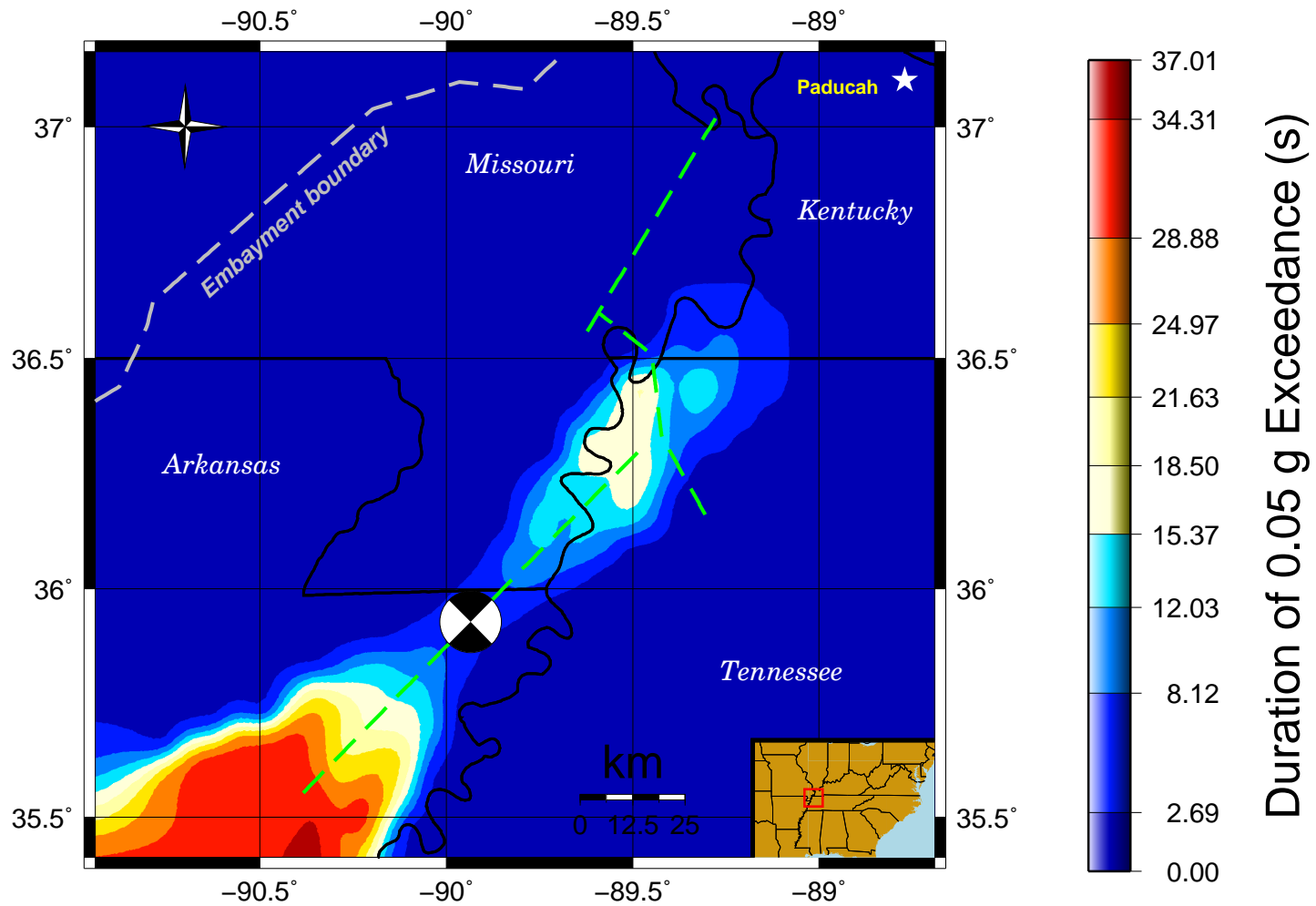


Figure 4.59: Bracketed Duration from rupture on the strike-slip Cottonwood Grove Fault. Focal mechanism is shown at the hypocenter.

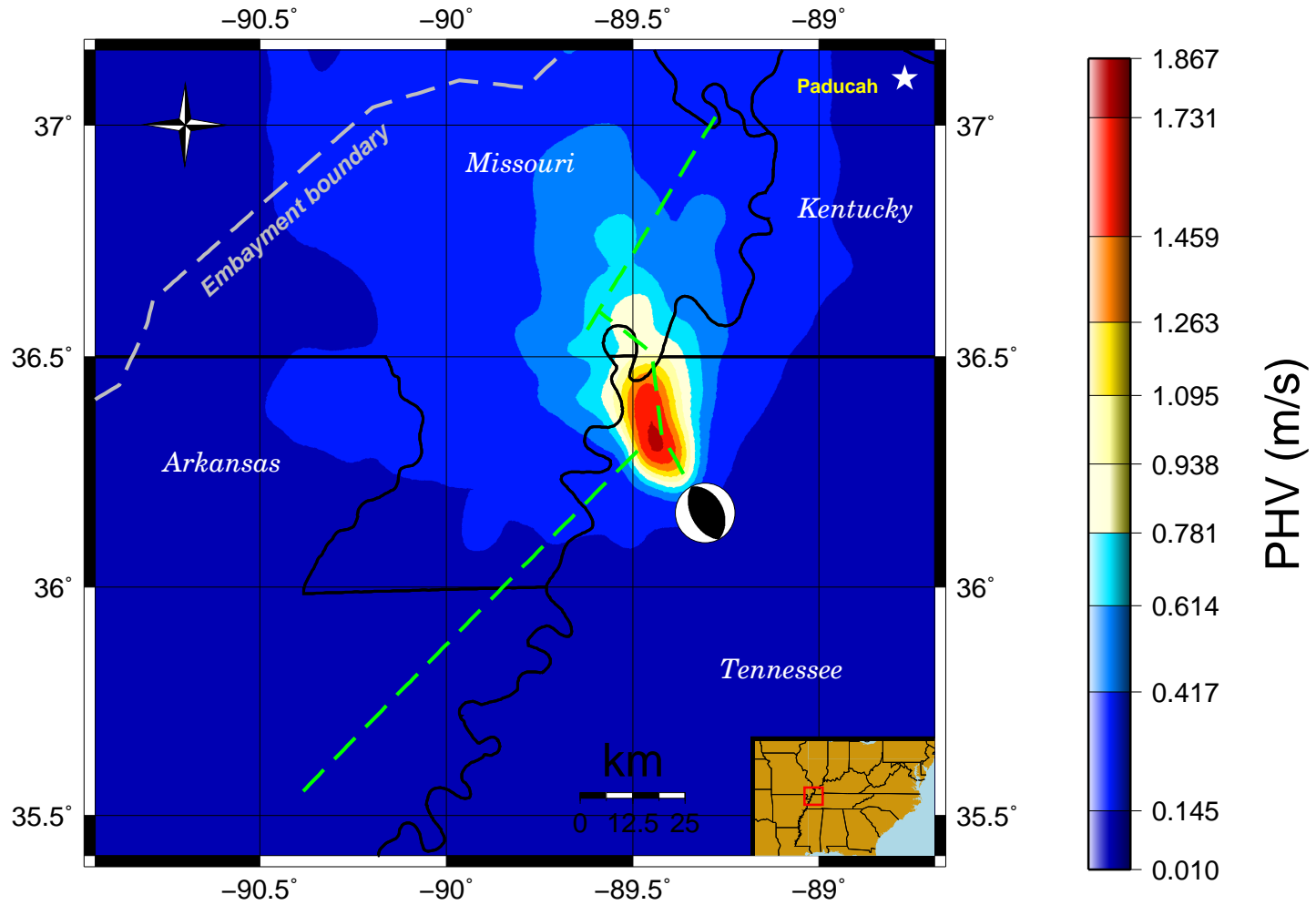


Figure 4.60: PHV from rupture on the Reelfoot thrust fault. Focal mechanism is shown at the hypocenter.

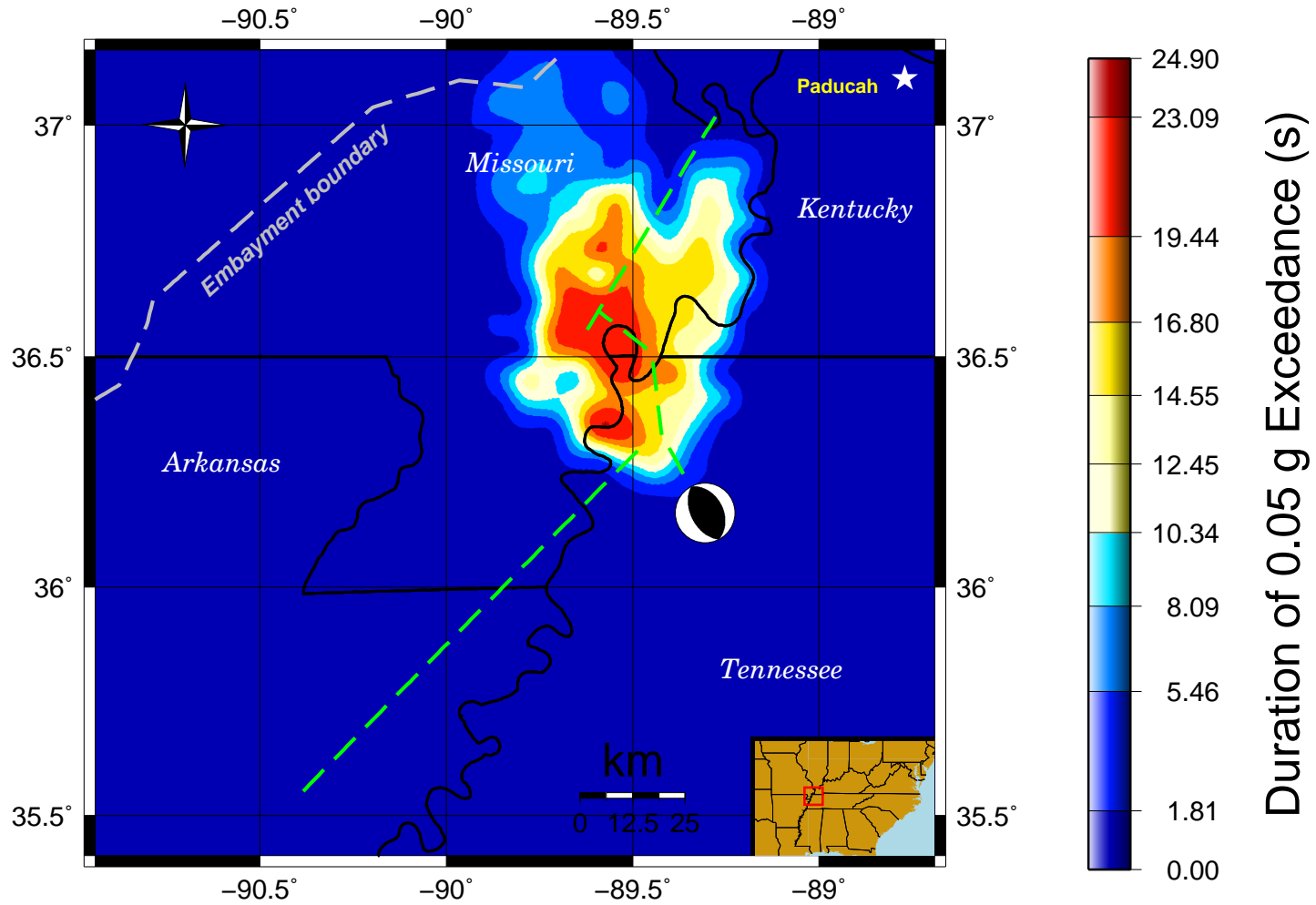


Figure 4.61: Bracketed Duration from rupture on the Reelfoot thrust fault. Focal mechanism is shown at the hypocenter.

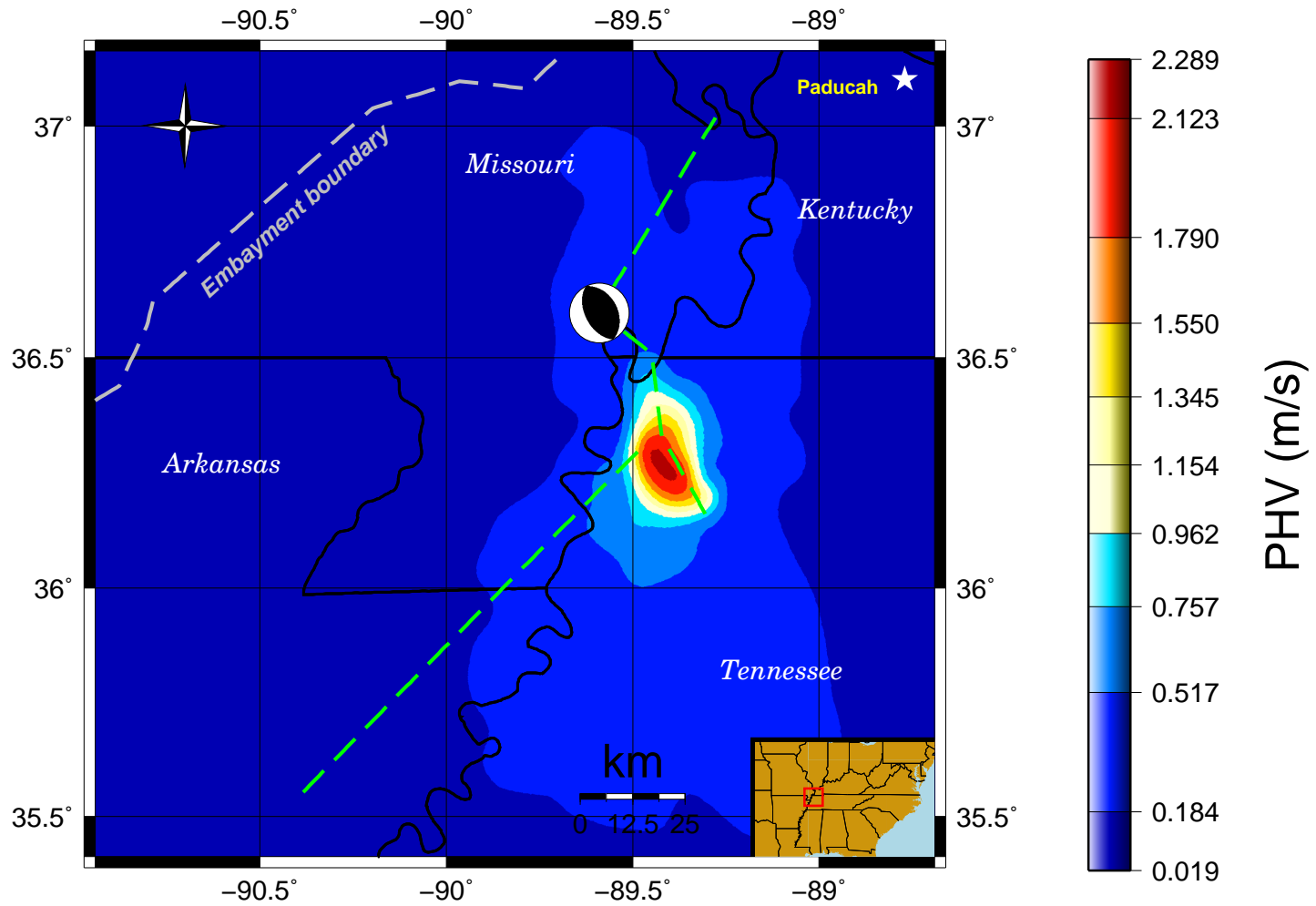


Figure 4.62: PHV from rupture on the Reelfoot thrust fault. Focal mechanism is shown at the hypocenter.

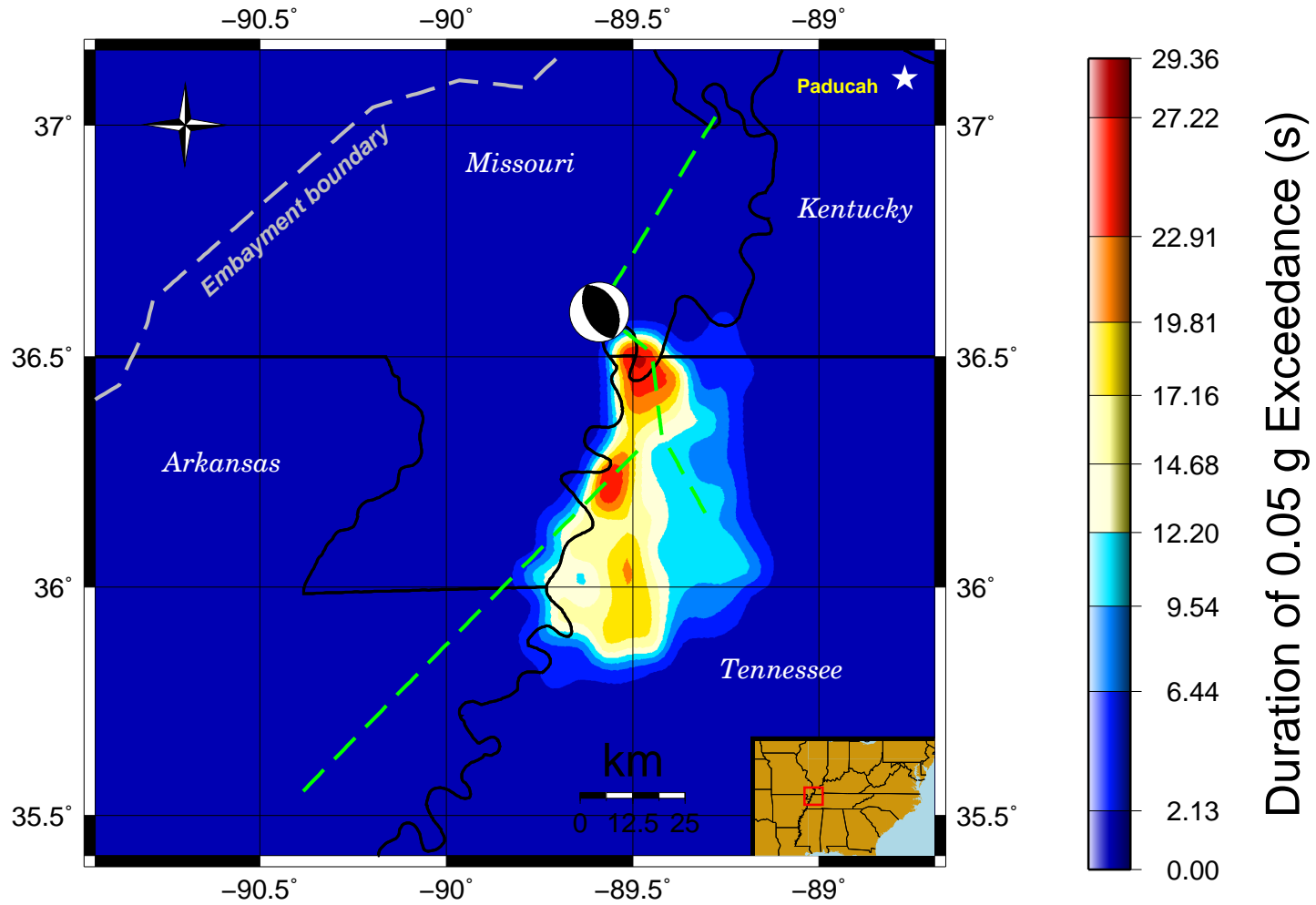


Figure 4.63: Bracketed Duration from rupture on the Reelfoot thrust fault. Focal mechanism is shown at the hypocenter.

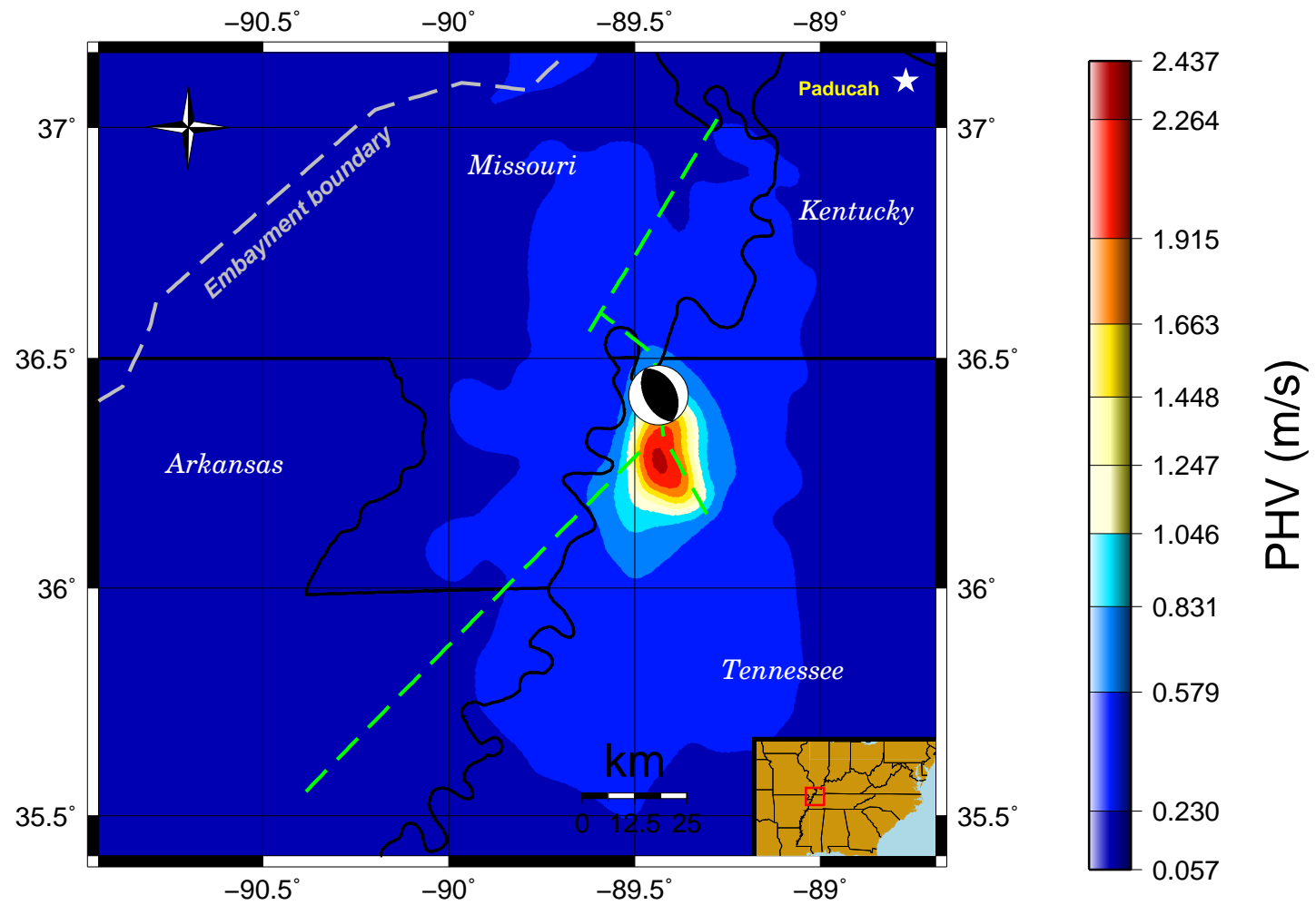


Figure 4.64: PHV from rupture on the Reelfoot thrust fault. Focal mechanism is shown at the hypocenter.

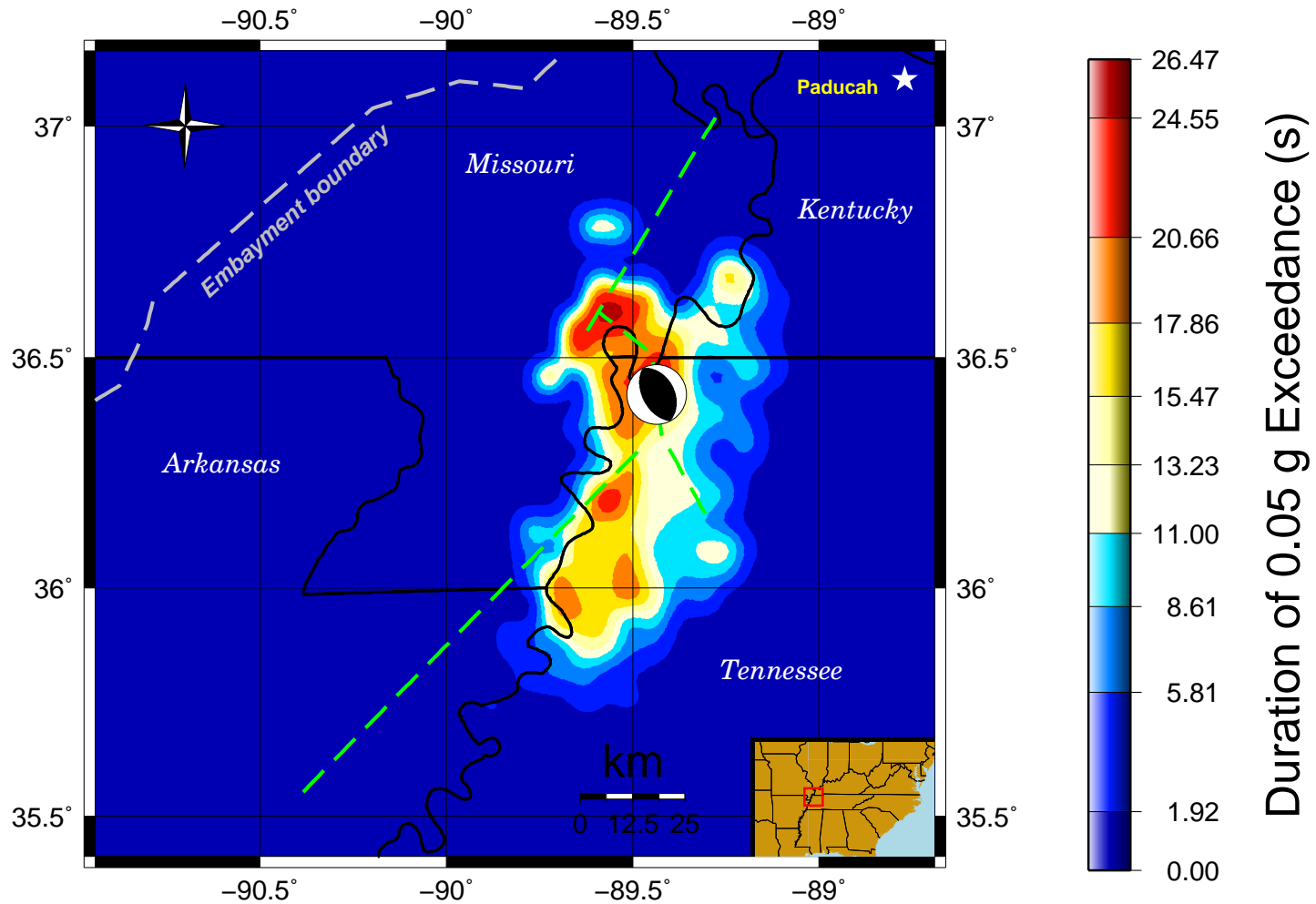


Figure 4.65: Bracketed Duration from rupture on the Reelfoot thrust fault. Focal mechanism is shown at the hypocenter.

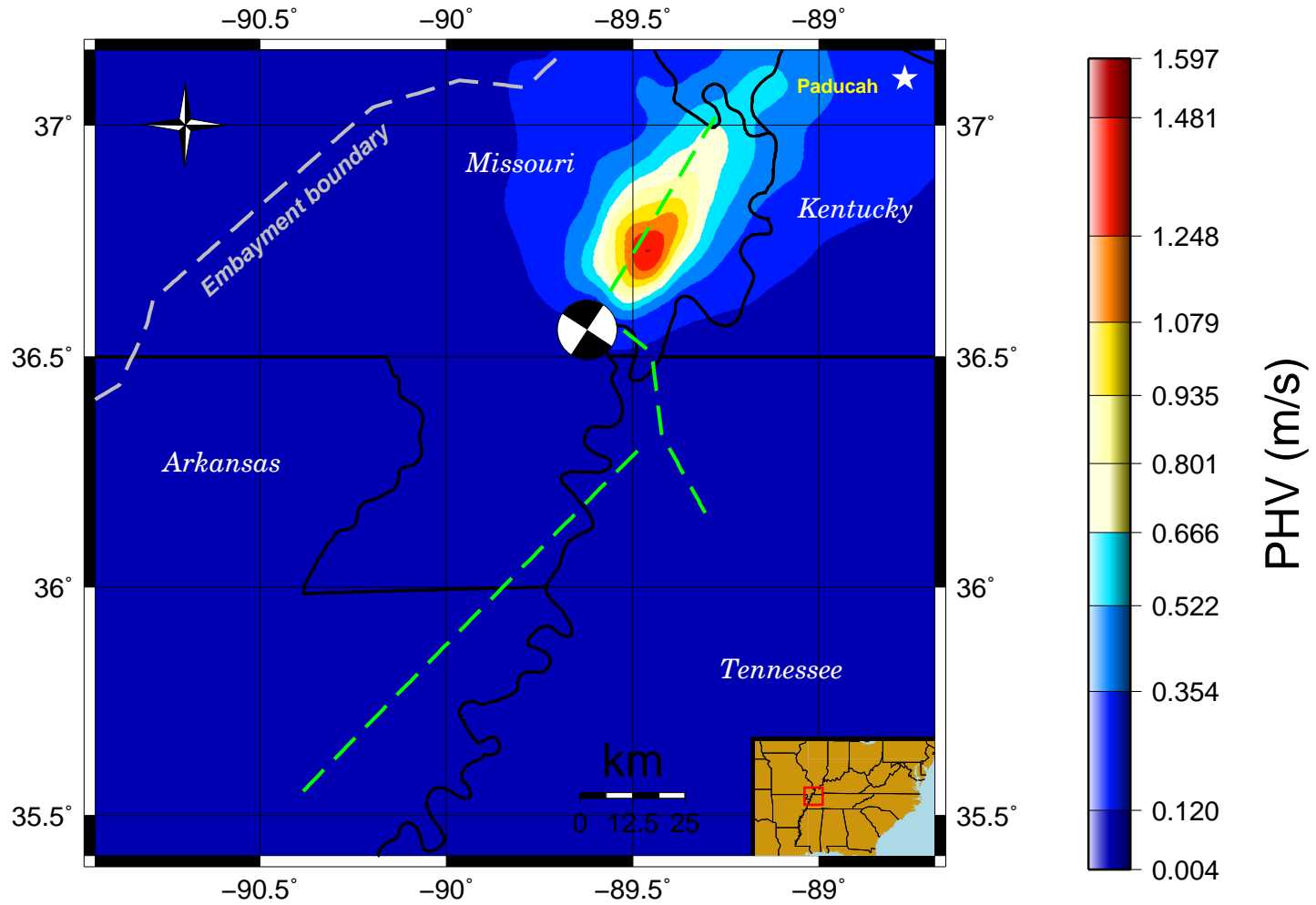


Figure 4.66: PHV from rupture on the strike-slip North fault. Focal mechanism is shown at the hypocenter.

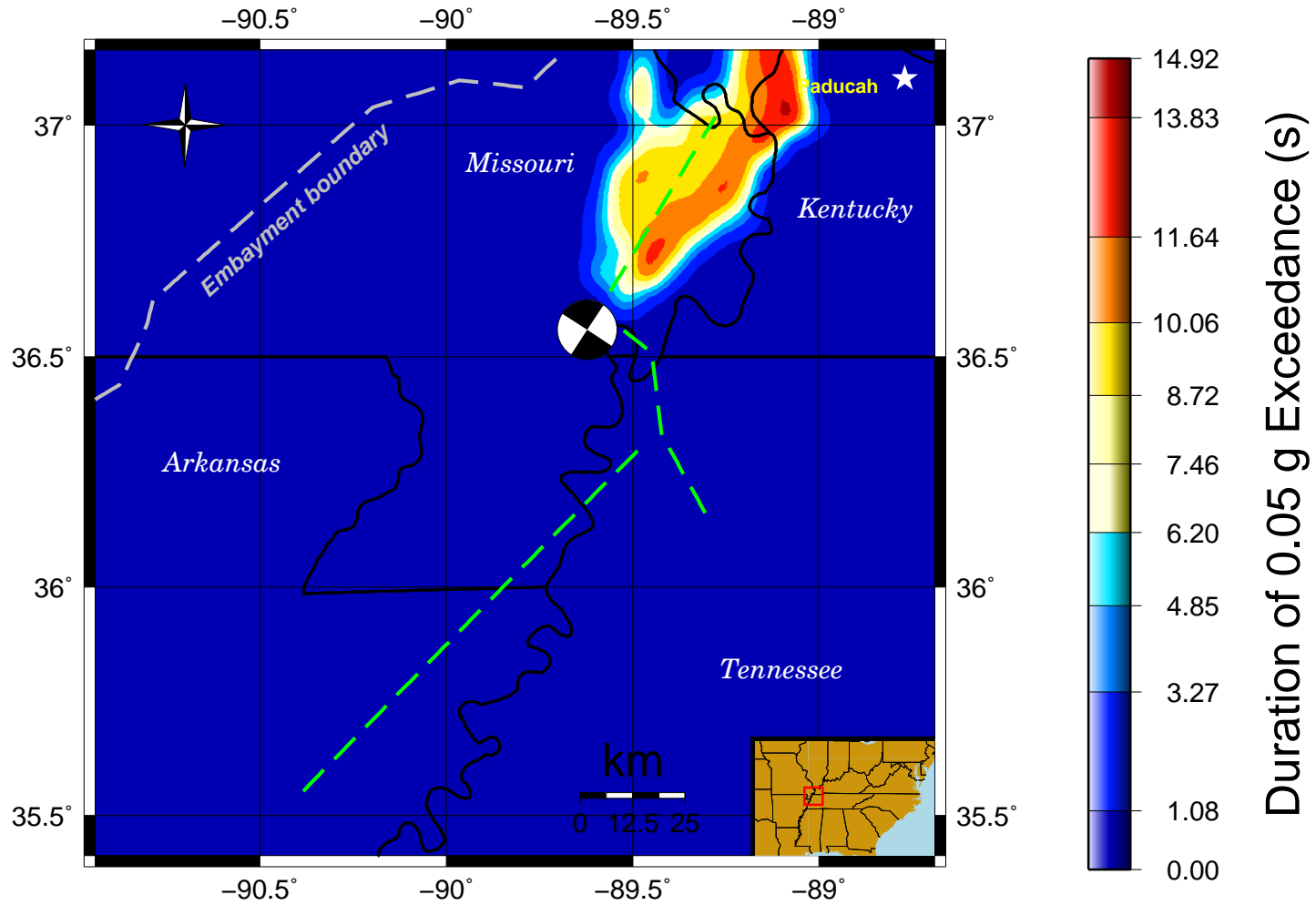


Figure 4.67: Bracketed Duration from rupture on the strike-slip North fault. Focal mechanism is shown at the hypocenter.

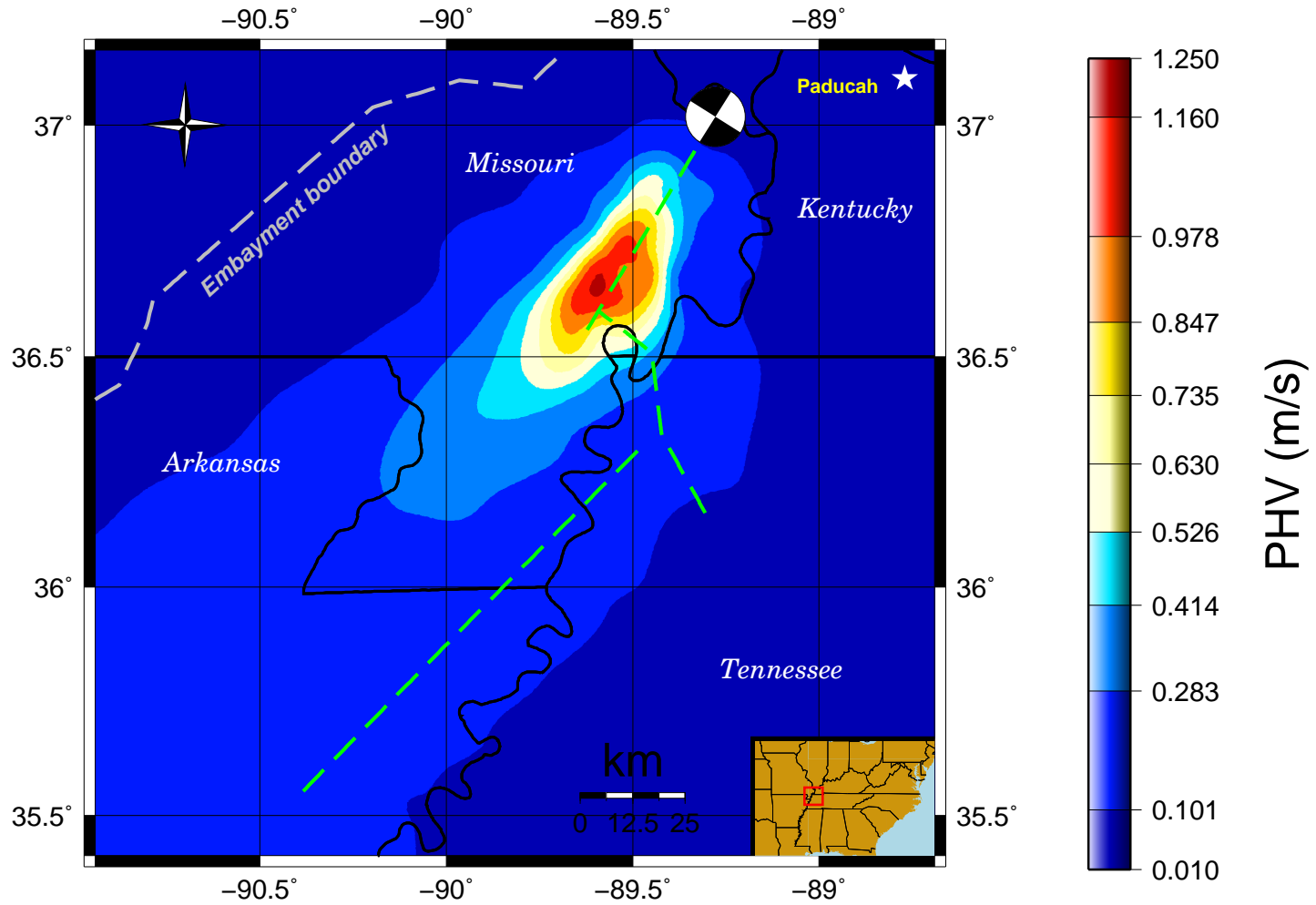


Figure 4.68: PHV from rupture on the strike-slip North fault. Focal mechanism is shown at the hypocenter.

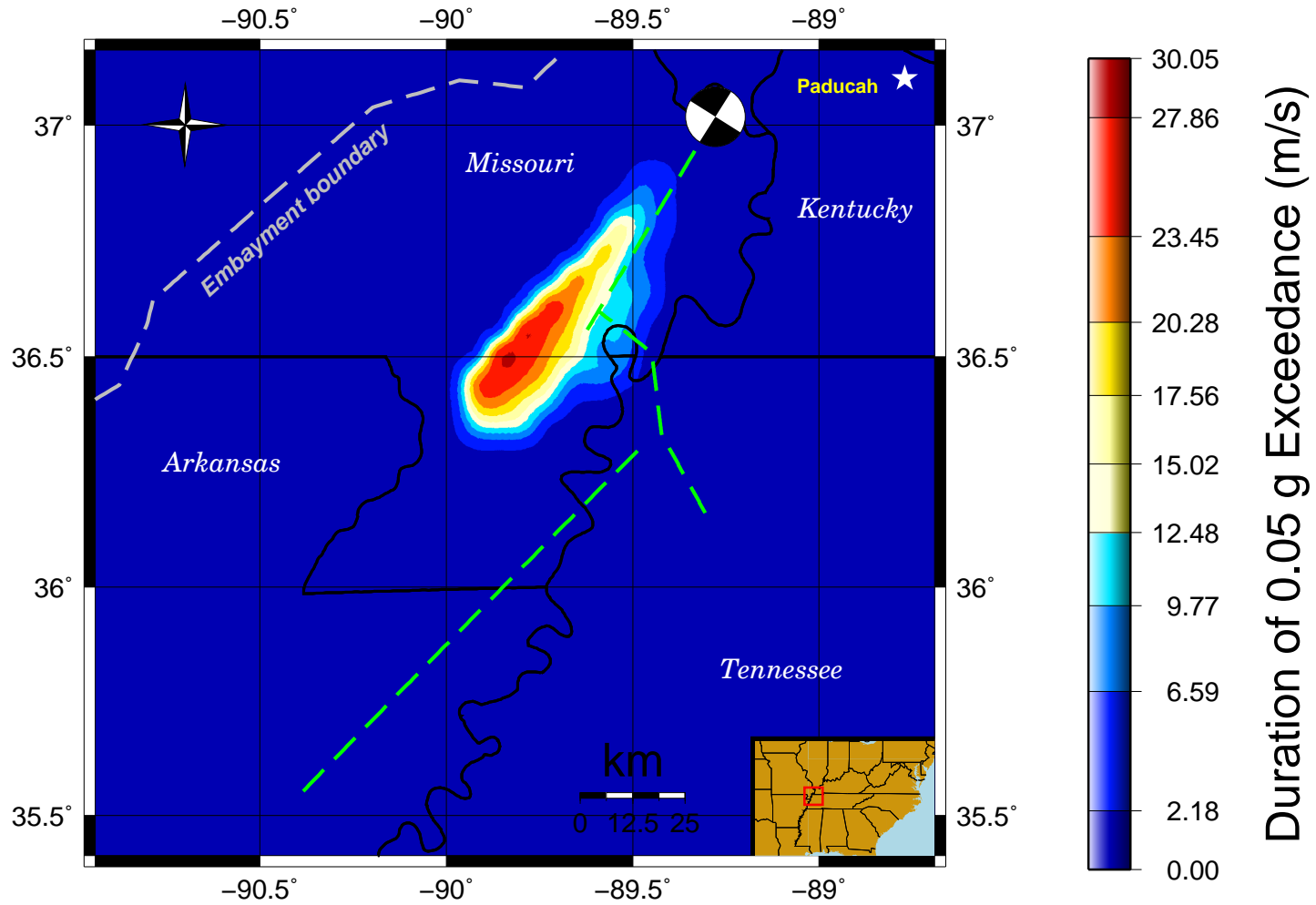


Figure 4.69: Bracketed Duration from rupture on the strike-slip North fault. Focal mechanism is shown at the hypocenter.

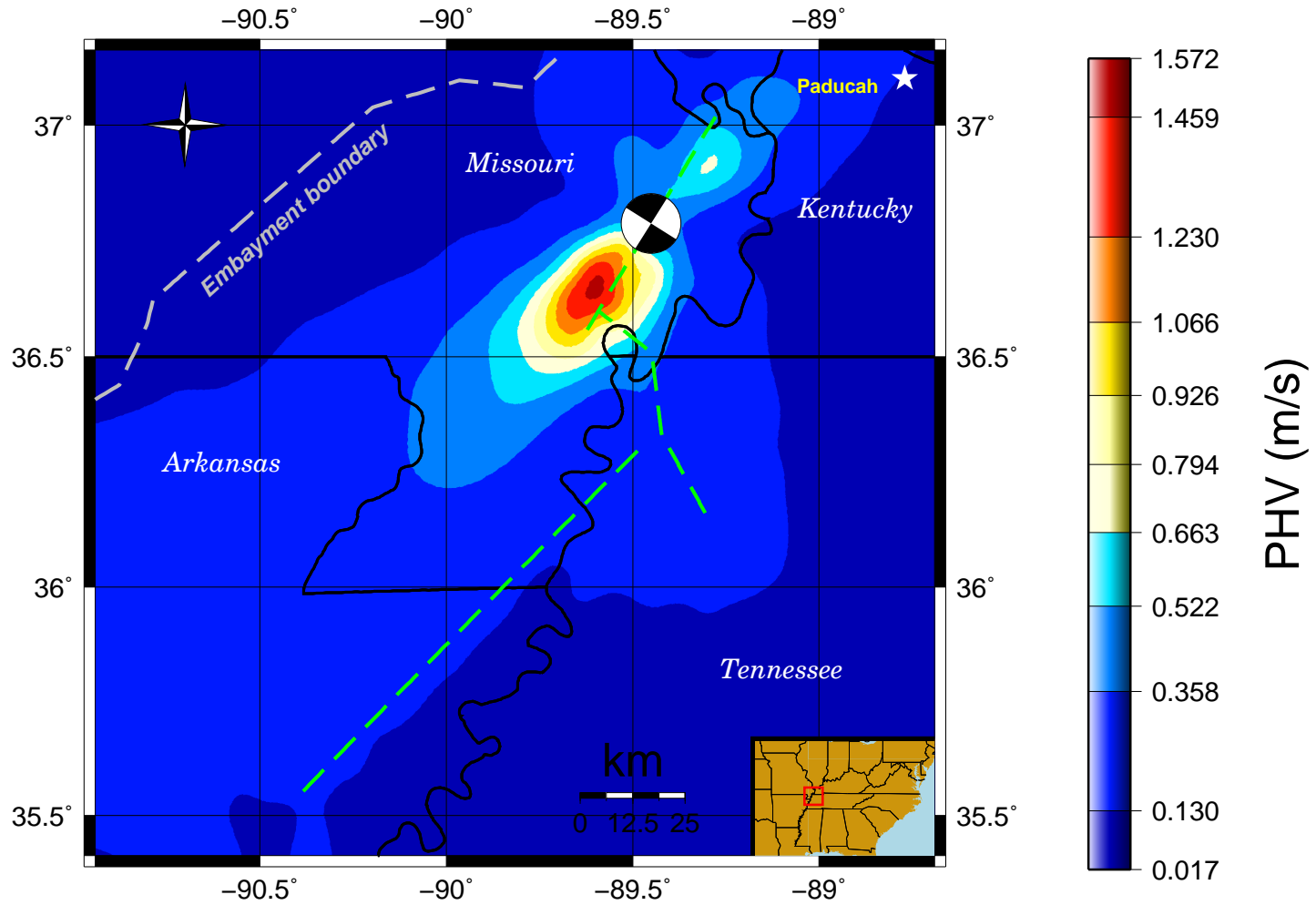


Figure 4.70: PHV from rupture on the strike-slip North fault. Focal mechanism is shown at the hypocenter.

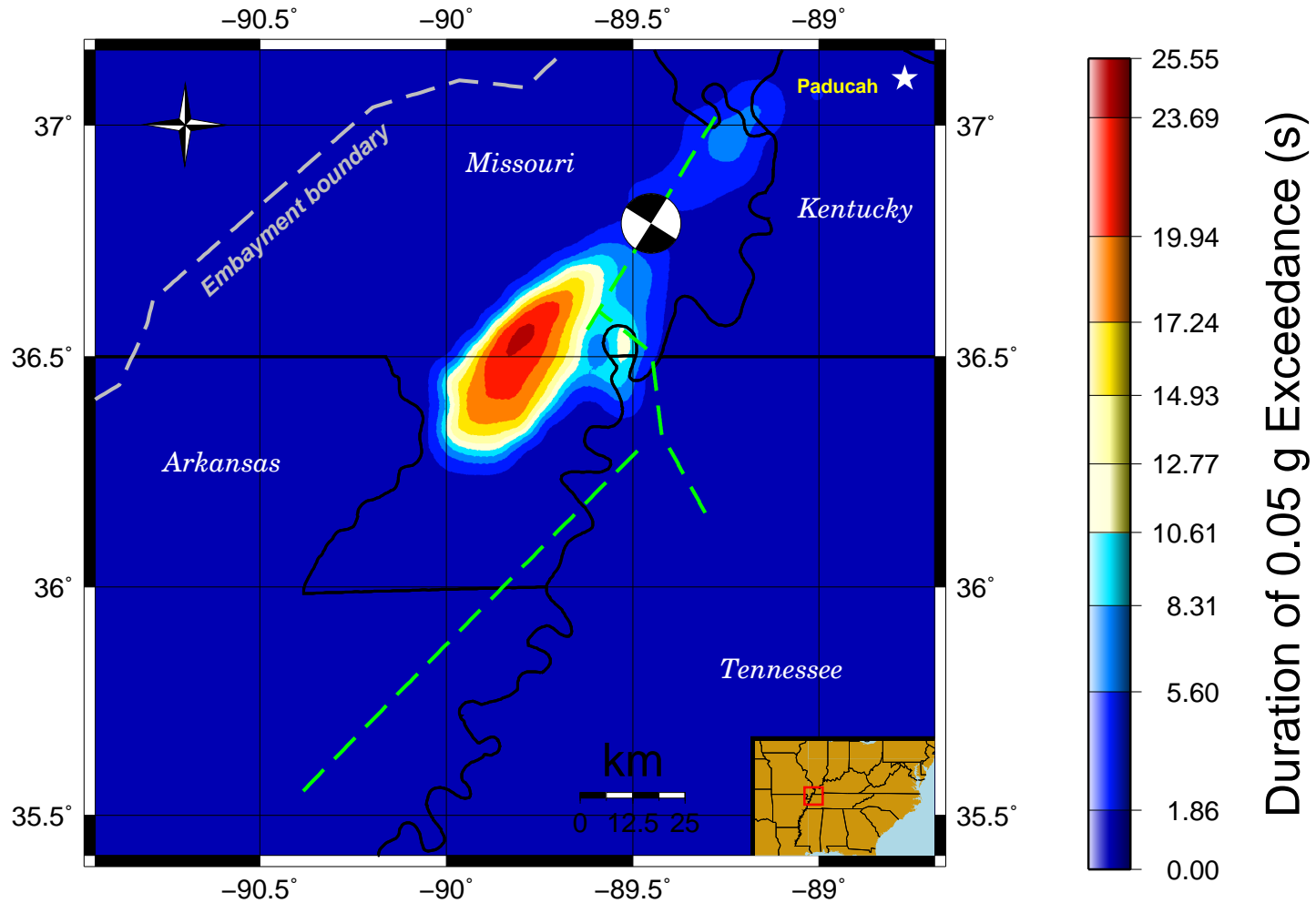


Figure 4.71: Bracketed Duration from rupture on the strike-slip North fault. Focal mechanism is shown at the hypocenter.

Computer Codes

Code for Writing Velocity Model Files

```
function Vel_Model()

% This Octave(MATLAB) function writes velocity files for
% input into vm4nufd.f. Velocities are assigned to points
% based on which two surfaces each point lies between.
% Surfaces are GRASS rasters exported as .mat files.
% The velocity model has a finer grid spacing to just below
% the Paleozoic unconformity.
% Region I, with the finer grid spacing, utilises surfaces:
% Vs30, Paleo_Unc., and PreCam
% Region II, with coarser spacing, utilises Rift_Pillow, and Moho.

%***** REGION I *****
% Set depth and vertical spacing of Region I:
% Depth of 'Shallow.txt' goes into the PreCambrian basement:
Depth=7000;
DZs=50;

% Load .mat files and assign appropriate variables:
load Paleo_Unc.mat
Paleo=map_data;

load PreCambrian.mat
PreCam=map_data;

% use of the low-velocity Vs30 data is not computationally
% feasible at this time.
%%load Vs30.mat
%%Vs30=map_data;

East=map_eastern_edge;
West=map_western_edge;
North=map_northern_edge;
South=map_southern_edge;

% determine dimensions of data:
[NYs,NXs]=size(Paleo)
NZs=round(Depth/DZs)
```

```

% determine resolution:
DYs=round((North-South)/NYs)
DXs=fix((East-West)/NXs)

% print a log file with information about this data:
fid=fopen('Data.see', 'w')
fprintf(fid,'***** REGION I *****\n')
fprintf(fid,'UNITS= meters\n')
fprintf(fid,'Coordinates= UTM Z16N\n')
fprintf(fid,'East Corner= %g\n',East)
fprintf(fid,'West Corner= %g\n',West)
fprintf(fid,'North Corner= %g\n',North)
fprintf(fid,'South Corner= %g\n',South)
fprintf(fid,'Depth= %g\n',Depth)
fprintf(fid,'NXs=%g NYs=%g NZs=%g\n', NXs, NYs, NZs)
fprintf(fid,'DXs=%g DYs=%g DZs=%g\n', DXs, DYs, DZs)
fprintf(fid,'***** REGION II *****\n')
fclose(fid)

% constant for the Faust equation (Faust, 1951)
c=56.68;
% this constant was calibrated by using the the known velocity of the
% Paleozoic limestone at 100 meters depth below station VSAP
% (Street et al, 1996).

% open file for output:
fid=fopen('Shallow.txt','w')

% initiate loop. Grid points are assigned velocities based on which
% two surfaces they fall between.
z=0;
for k=1:NZs
    y=South;
    for i=1:NYs
        x=West;
        for j=1:NXs
            if z > Paleo(i,j)
                % everything above the Paleozoic unconformity is assigned a shear
                % wave velocity based on a regression equation extracted from UKs
                % shear-wave database (Macpherson, 2008):
                Vs(i,j,k)=151.1844*(-z)^.3188;

% The minimum shear-wave velocity is set at 600 m/s because of computational
% limitations:
if Vs(i,j,k) < 600

```

```

    Vs(i,j,k)=600.0;
end

%-----
% p-wave is calculated via Brocher's regression fit (2005):
Vs(i,j,k)=Vs(i,j,k)/1000; % convert to km/s

Vp(i,j,k)=0.9409+2.0947*Vs(i,j,k)-0.8206*Vs(i,j,k)^2+ ...
    0.2683*Vs(i,j,k)^3-0.0251*Vs(i,j,k)^4;

%-----
% density calculated via Nafe-Drake curve (Brocher, 2005):
rho(i,j,k)=1.6612*Vp(i,j,k)-0.4721*Vp(i,j,k)^2+0.0671*Vp(i,j,k)^3 ...
    -0.0043*Vp(i,j,k)^4+0.000106*Vp(i,j,k)^5;

Vp(i,j,k)=Vp(i,j,k)*1000; % convert back to meters
Vs(i,j,k)=Vs(i,j,k)*1000;
rho(i,j,k)=rho(i,j,k)*1000; % convert g/cm^3 to kg/m^3
%-----

% Q is calculated via Wang (1994):
Qs(i,j,k)=0.08*Vs(i,j,k)+6.99;
Qp(i,j,k)=1.5*Qs(i,j,k);

% Name the geologic unit
unit='Post_Paleo';

    elseif (z <= Paleo(i,j)) && (z > PreCam(i,j))
        % calculate elastic parameters based on the point being in the
        % Paleozoic crust:
age=300000000;

% p-wave calculated via the Faust equation (1951):
    Vp(i,j,k)=c*(age*-z)^(1/6);

%-----
% s-wave calculated via Brocher's regression fit (2005):
Vp(i,j,k)=Vp(i,j,k)/1000; % convert to km/s

Vs(i,j,k)=0.7858-1.2344*Vp(i,j,k)+0.7949*Vp(i,j,k)^2-0.1238*Vp(i,j,k)^3 ...
    +0.0064*Vp(i,j,k)^4;
%-----

% density calculated via Nafe-Drake curve (Brocher, 2005):
rho(i,j,k)=1.6612*Vp(i,j,k)-0.4721*Vp(i,j,k)^2+0.0671*Vp(i,j,k)^3 ...

```

```

-0.0043*Vp(i,j,k)^4+0.000106*Vp(i,j,k)^5;

Vp(i,j,k)=Vp(i,j,k)*1000; % convert back to meters
Vs(i,j,k)=Vs(i,j,k)*1000;
rho(i,j,k)=rho(i,j,k)*1000; % convert g/cm^3 to kg/m^3
%-----

% for deep layers, Q is calculated from Liu (2006):
if Vs(i,j,k) <= 1000
    Qs(i,j,k)=0.06*Vs(i,j,k);
elseif 1000 < Vs(i,j,k) < 2000
    Qs(i,j,k)=0.14*Vs(i,j,k);
else
    Qs(i,j,k)=0.16*Vs(i,j,k);
end
Qp(i,j,k)=1.5*Qs(i,j,k);

% Name the geologic unit
unit='Paleozoic';

elseif (z <= PreCam(i,j))
    % calculate elastic parameters based on the point being in the
    % middle crust of the PreCambrian basement:

    % p-wave velocity calculated from non-linear regression of
    % HAMBURG data (Herrmann, 1997):
    Vp(i,j,k)=4176.0*(-z)^(.04504);

    %-----
    % s-wave calculated via Brocher's regression fit (2005):
    Vp(i,j,k)=Vp(i,j,k)/1000; % convert to km/s

    Vs(i,j,k)=0.7858-1.2344*Vp(i,j,k)+0.7949*Vp(i,j,k)^2-0.1238*Vp(i,j,k)^3 ...
    +0.0064*Vp(i,j,k)^4;
    %-----

    % density calculated via Nafe-Drake curve (Brocher, 2005):
    rho(i,j,k)=1.6612*Vp(i,j,k)-0.4721*Vp(i,j,k)^2+0.0671*Vp(i,j,k)^3 ...
    -0.0043*Vp(i,j,k)^4+0.000106*Vp(i,j,k)^5;

    Vp(i,j,k)=Vp(i,j,k)*1000; % convert back to meters
    Vs(i,j,k)=Vs(i,j,k)*1000;
    rho(i,j,k)=rho(i,j,k)*1000; % convert g/cm^3 to kg/m^3
    %-----

```



```

% for deep layers, Q is calculated from Liu (2006):
if Vs(i,j,k) <= 1000
    Qs(i,j,k)=0.06*Vs(i,j,k);
elseif 1000 < Vs(i,j,k) < 2000
    Qs(i,j,k)=0.14*Vs(i,j,k);
else
    Qs(i,j,k)=0.16*Vs(i,j,k);
end
Qp(i,j,k)=1.5*Qs(i,j,k);

% Name the geologic unit
unit='Precambrian_Basement';

    end

    % write data to external file:
    fprintf(fid,'%g %g %g %g %g %g %g %s\n', x, y,...
        -z, Vp(i,j,k), Vs(i,j,k), rho(i,j,k), Qp(i,j,k),...
        Qs(i,j,k), unit);

        x=x+DXs;
    end
    y=y+DYs;
    end
    z=z-DZs;
end

fclose(fid)

% clear memory
clear

%***** REGION II *****
% Set depth and vertical spacing of Region II:
Depth=50000;
DZ=1000;

% Load .mat files and assign appropriate variables:

load Moho.mat
Moho=map_data;

load Rift_Pillow.mat
Rift_Pillow=map_data;

```

```

East=map_eastern_edge;
West=map_western_edge;
North=map_northern_edge;
South=map_southern_edge;

% determine dimensions of data:
[NY,NX]=size(Moho)
NZ=round(Depth/DZ)

% determine resolution:
DY=round((North-South)/NY)
DX=fix((East-West)/NX)

% update log file with information about this data:
fid=fopen('Data.see', 'a')
%%fprintf(fid,'\n')
fprintf(fid,'UNITS= meters\n')
fprintf(fid,'Coordinates= UTM Z16N\n')
fprintf(fid,'East Corner= %g\n',East)
fprintf(fid,'West Corner= %g\n',West)
fprintf(fid,'North Corner= %g\n',North)
fprintf(fid,'South Corner= %g\n',South)
fprintf(fid,'Depth= %g\n',Depth)
fprintf(fid,'NX=%g NY=%g NZ=%g\n', NX, NY, NZ)
fprintf(fid,'DX=%g DY=%g DZ=%g\n', DX, DY, DZ)
fprintf(fid,'*****\n')
fclose(fid)

% constant for the Faust equation (Faust, 1951)
%%c=44.26

% open file for output:
fid3=fopen('Deep.txt', 'w')

% initiate loop. Grid points are assigned velocities based on which
% two surfaces they fall between.
z=-7000;
for k=1:NZ
    y=South;
    for i=1:NY
        x=West;
        for j=1:NX

            if z > Rift_Pillow(i,j)
                % calculate elastic parameters based on the point being in the

```

```

% middle crust of the PreCambrian basement:

% p-wave velocity calculated from non-linear regression of
% HAMBURG data (Herrmann, 1997):
Vp(i,j,k)=4176.0*(-z)^(.04504);

%-----
% s-wave calculated via Brocher's regression fit (2005):
Vp(i,j,k)=Vp(i,j,k)/1000; % convert to km/s

Vs(i,j,k)=0.7858-1.2344*Vp(i,j,k)+0.7949*Vp(i,j,k)^2-0.1238*Vp(i,j,k)^3 ...
+0.0064*Vp(i,j,k)^4;
%-----

% density calculated via Nafe-Drake curve (Brocher, 2005):
rho(i,j,k)=1.6612*Vp(i,j,k)-0.4721*Vp(i,j,k)^2+0.0671*Vp(i,j,k)^3 ...
-0.0043*Vp(i,j,k)^4+0.000106*Vp(i,j,k)^5;

Vp(i,j,k)=Vp(i,j,k)*1000; % convert back to meters
Vs(i,j,k)=Vs(i,j,k)*1000;
rho(i,j,k)=rho(i,j,k)*1000; % convert g/cm^3 to kg/m^3
%-----

% for deep layers, Q is calculated from Liu (2006):
if Vs(i,j,k) <= 1000
    Qs(i,j,k)=0.06*Vs(i,j,k);
elseif 1000 < Vs(i,j,k) < 2000
    Qs(i,j,k)=0.14*Vs(i,j,k);
else
    Qs(i,j,k)=0.16*Vs(i,j,k);
end
Qp(i,j,k)=1.5*Qs(i,j,k);

% Name the geologic unit
unit='Precambrian_Basement';

    elseif (z > Moho(i,j)) && (z<=Rift_Pillow(i,j))
        % calculate elastic parameters based on the point being in the
% fossil rift pillow:

% p-wave calculated by non-linear regression of
% HAMBURG data (Herrmann, 1997):
Vp(i,j,k)=61.0036*(-z)^(.4515);

% minimum p-wave velocity of Rift Pillow is set at 7000 m/s:

```

```

if (Vp(i,j,k) < 7000)
    Vp(i,j,k)=7000.0;
end

%-----
% s-wave calculated via Brocher's regression fit (2005):
Vp(i,j,k)=Vp(i,j,k)/1000; % convert to km/s

Vs(i,j,k)=0.7858-1.2344*Vp(i,j,k)+0.7949*Vp(i,j,k)^2-0.1238*Vp(i,j,k)^3 ...
    +0.0064*Vp(i,j,k)^4;

%-----

% density calculated via Nafe-Drake curve (Brocher, 2005):
rho(i,j,k)=1.6612*Vp(i,j,k)-0.4721*Vp(i,j,k)^2+0.0671*Vp(i,j,k)^3 ...
    -0.0043*Vp(i,j,k)^4+0.000106*Vp(i,j,k)^5;

Vp(i,j,k)=Vp(i,j,k)*1000; % convert back to meters
Vs(i,j,k)=Vs(i,j,k)*1000;
rho(i,j,k)=rho(i,j,k)*1000; % convert g/cm^3 to kg/m^3
%-----

% for deep layers, Q is calculated from Liu (2006):
if Vs(i,j,k) <= 1000
    Qs(i,j,k)=0.06*Vs(i,j,k);
elseif 1000 < Vs(i,j,k) < 2000
    Qs(i,j,k)=0.14*Vs(i,j,k);
else
    Qs(i,j,k)=0.16*Vs(i,j,k);
end
Qp(i,j,k)=1.5*Qs(i,j,k);

% Name the geologic unit
unit='Rift_Pillow';

    else
        % calculate elastic parameters based on the point being in the
% upper mantle:

% p-wave value taken from Catchings (1999):
    Vp(i,j,k)=8250.0;

%-----
% s-wave calculated via Brocher's regression fit (2005):
Vp(i,j,k)=Vp(i,j,k)/1000; % convert to km/s

```

```

Vs(i,j,k)=0.7858-1.2344*Vp(i,j,k)+0.7949*Vp(i,j,k)^2-0.1238*Vp(i,j,k)^3 ...
+0.0064*Vp(i,j,k)^4;
%-----

% density calculated via Nafe-Drake curve (Brocher, 2005):
rho(i,j,k)=1.6612*Vp(i,j,k)-0.4721*Vp(i,j,k)^2+0.0671*Vp(i,j,k)^3 ...
-0.0043*Vp(i,j,k)^4+0.000106*Vp(i,j,k)^5;

Vp(i,j,k)=Vp(i,j,k)*1000; % convert back to meters
Vs(i,j,k)=Vs(i,j,k)*1000;
rho(i,j,k)=rho(i,j,k)*1000; % convert g/cm^3 to kg/m^3
%-----

% for deep layers, Q is calculated from Liu (2006):
if Vs(i,j,k) <= 1000
    Qs(i,j,k)=0.06*Vs(i,j,k);
elseif 1000 < Vs(i,j,k) < 2000
    Qs(i,j,k)=0.14*Vs(i,j,k);
else
    Qs(i,j,k)=0.16*Vs(i,j,k);
end
Qp(i,j,k)=1.5*Qs(i,j,k);

% Name the geologic unit
unit='Upper_Mantle';

    end

    % write data to external file:
    fprintf(fid3,'%g %g %g %g %g %g %g %g %s\n', x, y,...
        -z, Vp(i,j,k), Vs(i,j,k), rho(i,j,k), Qp(i,j,k),...
Qs(i,j,k), unit);

        x=x+DX;
    end
    y=y+DY;
    end
    z=z-DZ;
end

% close output file:
fclose(fid3)

```

Code for Writing Bardwell Source File

```
function Rand_Src(N, chc)

% This is an Octave script to produce a random distribution
% of point sources on a circular finite fault plane. The output in
% a text file (Nu_LOH.1.sou) that is suitable for input into
% disfwd4.1.f.
% N is the number of point sources.
% The value of chc allows the user to either distribute
% the total moment randomly among the subevents (chc=1)
% or otherwise distribute the moment evenly among subevents.

% Enter the bounds of the east-west interval:
West=9560.44;
East=10440.44;
Dx=East-West;
Top=1960;
Bott=2840;
Dz=Bott-Top;
r=Dx/2;

% find center of the circular fault:
x0=West+r;
z0=Top+r;

% Northing (the fault is in the x-z plane but the y value will
% be randomly perturbed within a few meters):
South=2900.54;
North=3100.54;
Dy=North-South;

% fault paramters:
M0=1.3*10^15;
start=4;
rise=.4;
stk=90;
dip=89;
rake=-165;
% envelope (degrees) within which strike, dip, and rake will vary:
env=20;
% find the range of the fault parameters:
s0=stk-env/2;
d0=dip-env/2;
```

```

r0=rake-env/2;

% place points randomly within the circular fault:
k=0;
for i=1:N
    ran=rand(3,1);
    x=Dx*ran(1)+West;
    y=Dy*ran(2)+South;
    z=Dz*ran(3)+Top;
    % Only use points that fall within the circle:
    d=sqrt((x-x0)^2+(z-z0)^2);
    if d <= r
        k=k+1;
        xyz(k,:)=[x y z];
    end
end

% Divide the seismic moment among the sub events:
M=M0/k;

% Open file for Output:
fid=fopen('Nu_LOH.1.sou', 'w')
fid2=fopen('Src.plot', 'w')

Msum=0;
for i=1:k
    ran=rand(6,1);
    stk=env*ran(1)+s0;
    dip=env*ran(2)+d0;
    rake=env*ran(3)+r0;
    st=rise*ran(4)+start;
    rt=(rise-(st-start))*ran(5);
    Tst=rt+st;
    if chc == 1
        % Divide the seismic moment randomly among the point sources:
        M=(M0-Msum)*ran(6);
        Msum=Msum+M;
    end
    % write data to file:
    fprintf(fid, '%g %g %g %g %g %g 1 %g %g %g\n', ...
        xyz(i,:), M, st, rt, stk, dip, rake)
    % write dat to file for GNUplot:
    fprintf(fid2, '%g %g %g\n', xyz(i,:))
end

```

```
fprintf(fid, '# %g\n', k)
fprintf(fid, 'Total Moment= %g\n', Msum)
```

```
% Close output file:
fclose(fid)
fclose(fid2)
```


Code for Calculating PHV

```
function PHV(N)

% This is an Octave/MATLAB script that reads SAC files written by the finite
% difference code and calculates the vector sum of the peak horizontal
% velocities. The output is a text file containing UTMS and PHV
% suitable for import into the GRASS GIS or GMT.

% ** NOTE: This program utilises an external function, rsac(). That file
%   rsac.m must be in the directory from which the script is run.

% N is the number of files to be read.

%*****
% User specified data for finding the station coordinates in UTMs:

% Name of file for output:
fileout='NF2_S_3D.dat';

% Enter the southernmost and westernmost points of the region
% in UTMs:
S0=4041428;
W0=262708;

% Enter the name of the station file to get station coordinates:
load 'station.900'

%*****

% Open file for output:
fid=fopen(fileout, 'w')

for i=1:N

    num = num2str(i, '%03.4g');
    filex=['fwdcm.SAC.xx.' num];
    filey=['fwdcm.SAC.yy.' num];

    % find the peak x-component
    Data=rsac(filex);
    T=Data(:,1);
    Amp=abs(Data(:,2));
    Px=max(Amp);
```

```

% find the peak y-component
Data=rsac(filey);
T=Data(:,1);
Amp=abs(Data(:,2));
Py=max(Amp);

% Calculate the vector sum of the x and y components of
% peak horizontal velocity:
PHV=sqrt(Px^2+Py^2);

% Find the station coordinates in UTMs:
x=station(i,1)+W0;
y=station(i,2)+S0;

% Append output:
fprintf(fid, '%g|%d|%g\n', x, y, PHV)
%%fprintf(fid, '%g|%d|%g\n', xutm(i), yutm(i), PHV)

end

fclose(fid)

```

Code for Calculating Bracketed Durations

```
function Duration(N)

% This is an Octave/MATLAB script that reads SAC files written by the
% finite difference code and calculates the duration of strong ground
% motion. The bracketed technique is used to find the duration with
% a threshold corresponding to .05 g.

% ** NOTE: Input SAC files should be acceleration with units of gs!

% The output is a text file containing UTMS and durations for each
% station suitable for import into the GRASS GIS or GMT.

% ** NOTE: This program utilises an external function, rsac(). That
% file rsac.m must be in the directory from which the script is run.

% N is the number of files to be read.

%*****
% User specified data for finding the station coordinates in UTMs:

% Name of file for output:
fileout='Duration.dat';

% Enter the southernmost and westernmost points of the region
% in UTMs:
S0=4041428;
W0=262708;

% Enter the name of the station file to get station coordinates:
load 'station.900'

% Enter acceleration tolerance:
Tol=.05;

%*****

% Open file for output:
fid=fopen(fileout, 'w')

% Get Length of vector and time values:
A=rsac('fwdcm.SAC.xx.001');
L=length(A);
```

```

Data(:,1)=A(:,1);

for i=1:N

    num = num2str(i, '%03.4g');
    filex=['fwdcm.SAC.xx.' num];
    filey=['fwdcm.SAC.yy.' num];

    % read the x-component
    Datax=rsac(filex);

    % read the y-component
    Datay=rsac(filey);

    T=0; % reset time vector
    c=1; % a counter
    for j=1:L
        % Calculate the vector sum of the x and y components of
        % horizontal velocity:
        Data(j,2)= sqrt(Datax(j,2)^2+Datay(j,2)^2);
        % Test for exceedance:
        if Data(j,2) >= Tol
            T(c)=Data(j,1);
            c=c+1;
        end
    end
end

% Calculate duration:
if c==1
    dur=0;
else
    dur=max(T)-min(T);
    %%dur=exc(1,1)-exc((c-1),1);
end

% Find the station coordinates in UTM:
x=station(i,1)+W0;
y=station(i,2)+S0;

% Append output:
fprintf(fid, '%g|%d|%g\n', x, y, dur)

end

fclose(fid)

```

Code for Calculating PSA

```
function PSA2(N, T, Beta)

% This is an Octave/MATLAB script that reads SAC files writtent from
% the finite difference code and calculates the spectral acceleration
% from the ground motion record.  The psuedo-analytical technique
% described by Nigam and Jennings (1969) is used.

% The output is text files containing UTMS and the spectral
% acceleration (SA) and pseudospectral acceleration (PSA) for each
% station and is suitable for import into the GRASS GIS or GMT.

% ** NOTE: This program utilises an external function, rsac().  That
% file rsac.m must be in the directory from which the script is run.

% N is the number of files to be read.
% T is the period of the SDOF system.
% Beta is the percent of critical damping.  Usually 5% (.05).

% Compute Natural Frequency of the SDOF system:
Omega=(2*pi)/T;

%*****
% User specified paramters:

% Name of file for output:
fileout1='SA.dat';
fileout2='PSA.dat';

% Enter the southernmost and westernmost points of the region
% in UTMs:
S0=3920975;
W0=195603;

% Enter the name of the station file to get station coordinates:
load 'station.961'

%*****
% Get time increment:
Rec=rsac('fwdcm.SAC.xx.001');
```

```

% Find the time interval:
dt=Rec(2,1)-Rec(1,1)

% Find length of record
L=length(Rec)

%*****
% Calculate matrix coefficients:
sqrbsqrt(1-Beta^2);
Osqrb=Omega*sqrbsqrt;
Bsqrbsqrt/Beta/sqrbsqrt;
Oosqrbsqrt=Omega/sqrbsqrt;
exb=exp(-Beta*Omega*dt);
arg=Oosqrbsqrt*dt;
sn=sin(arg);
cs=cos(arg);

a11=exb*(Bsqrbsqrt*sn+cs);

a12=(exb/Oosqrbsqrt)*sn;

a21=-Oosqrbsqrt*exb*sn;

a22=exb*(cs-Bsqrbsqrt*sn);

rat1=(2*Beta^2-1)/(dt*Omega^2);
rat2=Beta/Omega;
rat3=(2*Beta)/(dt*Omega^3);
rat4=1/(Omega^2);
rat5=1/(dt*Omega^2);
sum1=rat1+rat2;
sum2=rat3+rat4;

b11=exb*(sum1*(sn/Oosqrbsqrt)+sum2*cs)-rat3;

b12=-exb*(rat1*(sn/Oosqrbsqrt)+rat3*cs)-rat4+rat3;

b21=exb*(sum1*(cs-Bsqrbsqrt*sn)-sum2*(Oosqrbsqrt*sn+Beta*Omega*cs))+rat5;

b22=-exb*(sum1*(cs-Bsqrbsqrt*sn)-rat3*(Oosqrbsqrt*sn+Beta*Omega*cs))-rat5;
%*****

% Open files for output:

```

```

fid1=fopen(fileout1, 'w');
fid2=fopen(fileout2, 'w')

% Loop over all stations:
for i=1:N

    % Initialize:
    xx=0;
    vx=0;
    accx=0;
    xy=0;
    vy=0;
    accy=0;

    % Open SAC files:
    num = num2str(i, '%03.4g');
    filex=['fwdcm.SAC.xx.' num];
    filey=['fwdcm.SAC.yy.' num];

    % read the x-component
    Datax=rsac(filex);

    % read the y-component
    Datay=rsac(filey);

    % Read the x and y components of horizontal velocity:
    accx= Datax(:,2);
    accy= Datay(:,2);

    % Integrate over acceleration record:
    for j=2:L
        % x component:
        xx(j)=a11*xx(j-1)+a12*vx(j-1)+b11*accx(j-1)+b12*accx(j);
        vx(j)=a21*xx(j-1)+a22*vx(j-1)+b21*accx(j-1)+b22*accx(j);

        % y component:
        xy(j)=a11*xy(j-1)+a12*vy(j-1)+b11*accy(j-1)+b12*accy(j);
        vy(j)=a21*xy(j-1)+a22*vy(j-1)+b21*accy(j-1)+b22*accy(j);

        % Compute absolute acceleration:
        zx(j)=- (2*Beta*Omega*vx(j)+Omega^2*xx(j));
        zy(j)=- (2*Beta*Omega*vy(j)+Omega^2*xy(j));
    end

    % Find the spectral acceleration:

```

```

SAx=max(zx);
SAy=max(zy);

% Find the Pseudo-spectral acceleration:
PSAx=(Omega^2)*max(xx);
PSAy=(Omega^2)*max(xy);

% Find the geometric means:
SA=sqrt(SAx*SAy);
PSA=sqrt(PSAx*PSAy);

% Find the station coordinates in UTMs:
xutm=station(i,1)+W0;
yutm=station(i,2)+S0;

% Append output:
fprintf(fid1, '%g|%d|%g\n', xutm, yutm, SA)
fprintf(fid2, '%g|%d|%g\n', xutm, yutm, PSA)

end

fclose(fid1)
fclose(fid2)

```


Code for Writing Snapshot Files

```
function Snap(N,tm)

format long g

% This is an Octave/MATLAB script that reads SAC files written by the
% finite difference code and finds the vector sum of horizontal
% velocities and discreet points in time (snapshots). The output is a
% text file containing UTMS and PHV and the correct times suitable
% for import into the GRASS GIS or GMT.

% ** NOTE: This program utilises an external function, rsac(). That
% file rsac.m must be in the directory from which the script is run.

% N is the number of files to be read.
% tm is the time in seconds for which the snapshot is desired.

%*****
% User specified data for finding the station coordinates in UTMs:

% Name of file for output:
fileout='Snap.';

% Enter the southernmost and westernmost points of the region
% in UTMs:
S0=4041428;;
W0=262708;

% Enter the beginning values for x and y:
x0=7000;
y0=7000;

% Enter the grid spacing:
Dxy=3000;

% Enter the number of x-nodes and y-nodes:
Nx=30;
Ny=30;

%*****

c=1;
% Find the UTMs for each station:
y=y0;
```

```

for j=1:Ny
    x=x0;
    for i=1:Nx
        xutm(c)=x;
        yutm(c)=y;
        x=x+Dxy;
        c=c+1;
    end
    y=y+Dxy;
end

% Open file for output:
label = num2str(tm, '%03.4g');
fileout=[fileout, label]
fid=fopen(fileout, 'w');

for i=1:N

    x=(xutm(i)+W0);
    y=(yutm(i)+S0);

    num = num2str(i, '%03.4g');
    filex=['fwcm.SAC.xx.' num];
    filey=['fwcm.SAC.yy.' num];

    % read x-component data:
    Data=rsac(filex);
    T=Data(:,1);
    Ampx=Data(:,2);

    % read y-component data:
    Data=rsac(filey);
    T=Data(:,1);
    Ampy=Data(:,2);

    % find the entry corresponding to the correct time:
    L=length(T);
    dt=Data(2,1)-Data(1,1);
    if (tm==0)
        ent=1;
    else
        ent=round(tm/dt);
    end

    Vel=sqrt(Ampx(ent)^2+Ampy(ent)^2);

```

```
fprintf(fid, '%g %d %g\n', x, y, Vel)
end
fclose(fid)
```

SAC Macro for Preprocessing

```
* This is a SAC macro to read in the files from
* readfwd.out, lowpass filter the data, and
* then re-write the SAC files.
```

```
* run command as SAC> macro LP 'integer1', 'integer2', 'real',
* where 'integer*' are the starting and ending file numbers
* and 'real' is the corner frequency.
```

```
ECHO ON
```

```
do i from $1 to $2
```

```
* Uncomment to trim data:
** cut 0 100
```

```
if $i LT 10
  READ fwdcm.SAC.xx.00$i fwdcm.SAC.yy.00$i
elseif $i LT 100
  READ fwdcm.SAC.xx.0$i fwdcm.SAC.yy.0$i
else
  READ fwdcm.SAC.xx.$i fwdcm.SAC.yy.$i
endif
```

```
* filter:
LOWPASS CORNER $3
```

```
* Uncomment the following to convert to gs:
** DIF
** MUL 0.101971621
```

```
* Uncomment the following to convert to displacement:
** INT
```

```
if $i LT 10
  WRITE fwdcm.SAC.xx.00$i fwdcm.SAC.yy.00$i
elseif $i LT 100
  WRITE fwdcm.SAC.xx.0$i fwdcm.SAC.yy.0$i
else
  WRITE fwdcm.SAC.xx.$i fwdcm.SAC.yy.$i
endif
```

```
enddo
```

Code for Writing Source Files

```
function Source(chc)

% This is an Octave script to discretize the finite fault plane
% and assign the various fault paramters.  A regularly spaced
% grid of several thousand points is used.

% The hybrid -k^2 spectral slip model (Gallovic, 2004).
% The slip file must be present in the working directory
% and must have the extension *.ksquare.
% The rupture time of each subevent is calculated as a
% function of distance from hypocenter and a simplified
% 1D velocity model.

% The fault trace is a linear segment, the strike of which is
% determined by the user-defined end points.

% The Output is a text file (*.sou) that is suitable
% for input into disfwd4.1.f.
% Data files for plotting the rupture front arrival time and
% the slip distribution are also written.

% chc chooses between a strike slip fault or a dipping fault.
% for strike-slip, enter 'chc=1', for dipping, enter 'chc=2'.

% The code produces a log file, *.see, that provides information
% about the fault paramters.

% ** NOTE ** There is a lot of paramters to enter.  Make sure you
% get it all!

% ** ALSO ** The script is inefficient as it uses several loops that
% could probably be combined.  However, it seems to be fast enough
% for jobs on the order of 16000 points.

% ***** USER SPECIFIED DATA *****

% Enter the name of this event, e.g., 'CG_mid':
name='NF_mid';

% Enter the UTM coordinates of the southernmost corner of the fault:
```

```

%%%Sx=203967.4; % CG
%%%Sy=3959785.7; % CG
%%%Sx=287124.25; % RF old
%%%Sy=3989079.42; % RF old
%%%Sx=286885.9; % RF
%%%Sy=3990218.67; % RF
Sx=267418; % NF
Sy=4053098.96; % NF

% Enter the northernmost corner of the fault plane:
%%%Nx=270884.5; % CG
%%%Ny=4014675.5; % CG
%%%Nx=258040.03; % RF old
%%%Ny=4070624.1; % RF old
%%%Nx=261056.01; % RF
%%%Ny=4061302.49; % RF
Nx=324433.2; % NF
Ny=4124131.12; % NF

% Enter the southern boundary of the region (UTMs):
%%%S0=3920975; % Large region
S0=4041428; % Small region

% Enter the western boundary of the region (UTMs):
%%%W0=195603; % Large region
W0=262708; % Small region

% Enter the top and bottom of the fault plane (depth, m):
Top=2000;
Bott=17000;
W=Bott-Top;

% Enter the fault parameters:
%%Mw=7.5; % Moment magnitude
start=0; % s
dip=90; % deg
dp=dip;
rake=180; % deg
re=rake;

% Enter the coordinates of the hypocenter (UTMs):
xhyp=(Nx+Sx)/2;
%yhyp=(Sy+Ny)/2;
zhyp=9000;

```

```

% Enter the envelope within which strike, dip, and rake will vary (deg):
env=5;

% Enter the over all rupture start time (s):
t=0;

% ***** END USER SPECIFIED DATA *****

format long g

% Convert from UTMs to FD coordinate system:
Sx=Sx-W0;
Sy=Sy-S0;
Nx=Nx-W0;
Ny=Ny-S0;
xhyp=xhyp-W0;
%%yhyp=yhyp-S0;

% calculate length of fault (m):
L=sqrt((Nx-Sx)^2+(Ny-Sy)^2);

% Calculate the fault area (km^2):
A=(L*W)/(1000^2);

% Calculate the moment magnitude as a function of area (Wells and
% Coppersmith,1994):
if chc==2
    Mw=4.33+.9*log10(A);
else
    Mw=3.98+1.02*log10(A);
end

% Compute the seismic moment (N-m):
M0=10^((3/2)*Mw+9.1);

% Find 'slope' and 'int' of fault trace:
m=(Ny-Sy)/(Nx-Sx);
b=Ny-m*Nx;

yhyp=m*xhyp+b; % find y-component of hypocenter

% convert slope to azimuth:
if m < 0
    stk=270-((180/pi)*atan(m));
else

```

```

    stk=90-((180/pi)*atan(m));
end

% find the range of the fault parameters within specified envelope:
s0=stk-env/2;
d0=dip-env/2;
r0=rake-env/2;

% Open files for Output:
outfl=[name '.sou'];
momfl=[name '.mom.dat'];
rtfl=[name '.rt.dat'];
rupfl=[name '.rup.dat'];
grsfl=[name '.grass'];
logfl=[name '.see'];
fid1=fopen(outfl, 'w') % for disfwd4.1.f
fid2=fopen(momfl, 'w') % for GMT
fid3=fopen(rupfl, 'w') % for GMT
fid4=fopen(grsfl, 'w') % for GRASS
fid5=fopen(logfl, 'w') % log file
fid6=fopen(rtfl, 'w') % for GMT

%*****
% DISCRETIZE THE FAULT PLANE:

% Discretization of fault plane should match that of the slip model:
slpfl=[name(1:2) '.ksquare'];
slip=load(slpfl); % load the file containing the slip data.
nnx=sqrt(length(slip));
nnz=nnx;

% determine the spacing in x and z directions:
dx=L/nnx;
dz=W/nnz;
N=nnx*nnz; % total number of subevents

% NOTE: dx is grid spacing along strike
% find the x-component of grid spacing:
dstk=dx/sqrt(m^2+1);

if Nx < Sx
    dstk=-dstk;
end

```



```

% loop to determine the coordinates of each subevent:
z=Top;
c=0;
for j=1:nnz
    x=Sx;
    for i=1:nnx
        c=c+1;
        y=m*x+b;
        cord(c,1)=x;
        cord(c,2)=y;
        cord(c,3)=z;
        x=x+dstk;
    end
    z=z+dz;
end

% Let's use vectors:
x=cord(:,1);
y=cord(:,2);
z=cord(:,3);

% If the fault plane is non-vertical, then modify coordinates accordingly:
if chc==2
    slp=tan((dp*pi)/180);

    for i=1:N

        x(i)=x(i)+(.8/slp)*(-z(i)+Top);
        y(i)=y(i)+(.8/slp)*(-z(i)+Top);

    end

end

%*****
% Assign Seismic Moment Based on the Hybrid k^-2 Slip Distribution
% (Frantisek Gallovic, 2002)

slipamp=slip(:,3); % vector of slip amplitudes

% Find the maximum slip and average slip:
maxslip=max(slipamp);
avgslip=sum(slipamp)/length(slipamp);

% Find the subevent area:

```

```

Asub=(A*1000000)/N; % square meters

% Loop to calculate moment:
c=0; % count the number of subevents with non-zero slip
for i=1:N
    Vs(i)=2242*z(i)^.05576; % compute 1D S-wave velocity 3051
    rho(i)=1155.6767*z(i)^.1023103; % compute 1D density 2045.6767
    RM(i)=rho(i)*(Vs(i)^2)*slipamp(i)*Asub; % calculate the moment
    if slipamp(i) > 0
        c=c+1;
    end
end

% Find the difference between derived moment and target moment:
diff=M0-sum(RM);
% Accuracy with no adjustment:
acc=sum(RM)/M0;

% amount that each non-zero subevent must be adjusted by to reach
% the target moment:
adj=diff/c;
% Loop to make-up target moment:
for i=1:N
    if RM(i) > 0
        RM(i)=RM(i)+adj;
    end
end

% Verify that the sum of subevents equals the target moment:
tm=sum(RM);

%*****

% Find the maximum sub event moment:
Mmax=max(RM);

% spread parameter for rise time calculation E[.8,1]:
del=.9;

% Find the shortest assumed rise time based on M0 (s):
if (Mw < 7)
    rt0=.9;
else
    rt0=2;
end

```

```

% Print Nu_LOH.1.sou first line header:
fprintf(fid1, '1 %g 1\n', N)

%*****

% Loop over all subevents yet again to compute fault parameters and write
% the source file:
for i=1:N

    % generate random matrix in order to perturb strike, dip, and rake within
    % the specified envelope.
    ran=rand(3,1);
    stk=env*ran(1)+s0;
    dip=env*ran(2)+d0;
    rake=env*ran(3)+r0;

    % calculate the rise time of each sub event (Harmsen, 2008):
    rt1=rt0+((RM(i))/(Mmax))*del;
    if (z >= 2000) % 5000 in Harmsen
        rt=rt1;
    else
        rt2=rt0+del*((5000-z(i))/5000);
        rt=max(rt1,rt2);
    end

    %*****
    % Calculate the rupture-front arrival time based on a 1D velocity
    % model:
    dist=sqrt((x(i)-Sx)^2+(y(i)-Sy)^2); % find distance along strike
    % find horizontal hypocentral distance:
    %hypdist=sqrt((x(i)-xhyp)^2+(y(i)-yhyp)^2+(z(i)-zhyp)^2);
    hypdist=sqrt((x(i)-xhyp)^2+(y(i)-yhyp)^2);
    % find approximate velocity at depth of point:
    Vs=2207*z(i)^.05576;
    % find the rupture front arrival time:
    st=hypdist/(.8*Vs);
    %*****

    % write data to file for finite difference code:
    fprintf(fid1, '%g %g %g %g %g %g 1 %g %g %g\n', ...
        x(i), y(i), z(i), RM(i), st, rt, stk, dip, rake)

    % write files for plotting in GMT:
    fprintf(fid2, '%g %g %g\n', dist, -z(i), slipamp(i))

```

```

fprintf(fid6, '%g %g %g\n', dist, -z(i), rt)
fprintf(fid3, '%g %g %g\n', hypdist, -z(i), st)

% write files for plotting in GRASS:
xutm=x(i)+W0;
yutm=y(i)+S0; % convert to UTM's
fprintf(fid4, '%g %d %g\n', xutm, yutm, -z(i))

end

xhyp=xhyp+W0; % convert to UTM's
yhyp=yhyp+S0;

% Print a log file with information about this source:
fprintf(fid5, '***** SOURCE PARAMETERS *****\n')
fprintf(fid5, 'Northern most point= %g, %g\n', Nx, Ny)
fprintf(fid5, 'Southern most point= %g, %g\n', Sx, Sy)
fprintf(fid5, 'Hypocenter (x,y,z)= %g, %g, %g\n', xhyp, yhyp, zhyp)
fprintf(fid5, 'Length of the main fault (m) = %g\n', L)
fprintf(fid5, 'Width of main fault (m)=%g\n', W)
fprintf(fid5, 'Area of Main fault (km^2)= %g\n', A)
fprintf(fid5, 'Total number of subevents= %g\n', N)
fprintf(fid5, 'Number of points along the length of the fault= %g\n', nnx)
fprintf(fid5, 'Number of points along the width of the fault= %g\n', nnz)
fprintf(fid5, 'Moment Magnitude = %g\n', Mw)
fprintf(fid5, 'Maximum Slip (m) = %g\n', maxslip)
fprintf(fid5, 'Average Slip = %g\n', avgslip)
fprintf(fid5, 'Sum of subevent moments (N-m)=%g\n', tm)
fprintf(fid5, 'Target Moment (N-m)= %g\n', M0)
fprintf(fid5, 'Accuracy before adj.= %g\n', acc)
fprintf(fid5, 'Strike (deg)=%g\n', stk)
fprintf(fid5, 'Dip (deg)=%g\n', dp)
fprintf(fid5, 'Rake (deg)=%g\n', re)
fprintf(fid5, 'Envelope in which parameters vary (deg)=%g\n', env)
fprintf(fid5, 'Start Time (s)=%g\n', start)
fprintf(fid5, '*****\n')

% Close output files:
fclose(fid1)
fclose(fid2)
fclose(fid3)
fclose(fid4)
fclose(fid5)
fclose(fid6)

```

Code for Writing Reelfoot Fault Source Files

```
function SourceRF4()

% This is an Octave script to discretize the Reelfoot finite fault
% plane and assign the various fault paramters.  A regularly spaced
% grid of several thousand points is used.

% The hybrid  $-k^2$  spectral slip model (Gallovic, 2004).
% The rupture time of each subevent is calculated as a
% function of distance from hypocenter and a simplified
% 1D velocity model.

% The fault trace is composed of linear segments, the strike of which
% is determined by the user-defined end points.

% The Output is a text file (*.sou) that is suitable
% for input into disfwd4.1.f.
% Data files for plotting the rupture front arrival time and
% the slip distribution are also written.

% The code produces a log file, *.see, that provides information
% about the fault paramters.

% ** NOTE ** There is a lot of paramters to enter.  Make sure you
% get it all!

% ** ALSO ** The script is inefficient as it uses several loops that
% could probably be combined.  However, it seems to be fast enough
% for jobs on the order of 16000 points.

% ***** END USER SPECIFIED DATA *****
% Enter the name of this event, e.g., 'CG_mid':
name='RF_mid';

% Enter the UTM coordinates of the end points of the 3 segments:
x1=292626.3; %
y1=4004266.3; %
x2=282551.5;
y2=4023433.1;
x3=280683.9;
y3=4043189.6;
x4=267995.9;
y4=4053636.7;
```

```

% Enter the southern boundary of the region (UTMs):
S0=3920000; % Large region
%%S0=4041428; % Small region

% Enter the western boundary of the region (UTMs):
W0=150000; % Large region
%%W0=262708; % Small region

% Enter the top and bottom of the fault plane (depth, m):
Top=1000;
Bott=20000;
zrange=Bott-Top;

% Enter the fault parameters:
%%Mw=7.5; % Moment magnitude
start=0; % s
dip=39.5; % deg
dp=dip;
rake=90; % deg
re=rake;

% Enter the coordinates of the hypocenter (UTMs):
xhyp=(x2+x3)/2; % hypocenter at southern end

%yhyp=(Sy+Ny)/2;
zhyp=9000;

% Enter the envelope within which strike, dip, and rake will vary (deg):
env=5;

% Enter the over all rupture start time (s):
t=0;

% ***** END USER SPECIFIED DATA *****

format long g

% Convert from UTMs to FD coordinate system:
x1=x1-W0;
y1=y1-S0;
x2=x2-W0;
y2=y2-S0;
x3=x3-W0;
y3=y3-S0;

```

```

x4=x4-W0;
y4=y4-S0;
xhyp=xhyp-W0;

% calculate length of fault (m):
L1=sqrt((x1-x2)^2+(y1-y2)^2);
L2=sqrt((x2-x3)^2+(y2-y3)^2);
L3=sqrt((x3-x4)^2+(y3-y4)^2);
L=L1+L2+L3;

% Find 'slope' and 'int' of 3 segments of the fault trace:
m1=(y2-y1)/(x2-x1);
m2=(y3-y2)/(x3-x2);
m3=(y4-y3)/(x4-x3);
b1=y1-m1*x1;
b2=y2-m2*x2;
b3=y3-m3*x3;

% find y-component of hypocenter
if xhyp > x2
    m=m1;
    b=b1;
elseif xhyp > x3
    m=m2;
    b=b2;
else
    m=m3;
    b=b3;
end
yhyp=m*xhyp+b;

% find the general strike:
stk=(y4-y1)/(x4-x1);
% convert slope to azimuth:
if stk < 0
    stk=270-((180/pi)*atan(stk));
else
    stk=90-((180/pi)*atan(stk));
end

% find the range of the fault parameters within specified envelope:
s0=stk-env/2;
d0=dip-env/2;
r0=rake-env/2;

```

```

% Open files for Output:
outfl=[name '.sou'];
momfl=[name '.mom.dat'];
rtfl=[name '.rt.dat'];
rupfl=[name '.rup.dat'];
grsfl=[name '.grass'];
logfl=[name '.see'];
fid1=fopen(outfl, 'w') % for disfwd4.1.f
fid2=fopen(momfl, 'w') % for GMT
fid3=fopen(rupfl, 'w') % for GMT
fid4=fopen(grsfl, 'w') % for GRASS
fid5=fopen(logfl, 'w') % log file
fid6=fopen(rtfl, 'w') % for GMT

%*****
% DISCRETIZE THE FAULT PLANE:

% Discretization of fault plane should match that of the slip model:
slpfl=[name(1:2) '.ksquare'];
slip=load(slpfl); % load the file containing the slip data.
nnx=sqrt(length(slip));
nnz=nnx;

% determine the spacing in x and z directions:
dx=L/nnx;
dz=zrange/nnz;
N=nnx*nnz; % total number of subevents

% loop to determine the coordinates of each subevent:
z=Top;
c=0;
for j=1:nnz
    x=x1;
    for i=1:nnx
        c=c+1;
        % use a piecewise function for fault strike:
        if x > x2
            m=m1;
            b=b1;
        elseif x > x3
            m=m2;
            b=b2;
        else
            m=m3;
            b=b3;
        end
    end
end

```



```

end
% because the plane is dipping, there is a new 'b' for each z value:
tlt=(z-Top)*tan(dip*(pi/180));

%*****
% shift x values:
if z > Top && i==1
    mp=-1/m; % find the line perpendicular to strike
    y2=m*x+b;
    bp=y2-mp*x;
    xp=(bp-b+tlt)/(m+1/m);
    xshift=x-xp;
    x=x-xshift;
end
%*****

y=m*x+b-tlt;
cord(c,1)=x;
cord(c,2)=y;
cord(c,3)=z;
% NOTE: dx is grid spacing along strike
% find the x-component of grid spacing:
dstk=-dx/sqrt(m^2+1);
x=x+dstk;
end
z=z+dz;
end

% Let's use vectors:
x=cord(:,1);
y=cord(:,2);
z=cord(:,3);

%*****

% Find the true width of the fault:
W=sqrt((x(N)-x(nnx))^2+(y(N)-y(nnx))^2+(z(N)-z(nnx))^2);

% Calculate the fault area (km^2):
A=(L*W)/(1000^2);

% Calculate the moment magnitude as a function of area (Wells and
% Coppersmith,1994):
Mw=4.33+.9*log10(A);

```

```

% Compute the seismic moment (N-m):
M0=10^((3/2)*Mw+9.1);

%*****
% Assign Seismic Moment Based on the Hybrid k^-2 Slip Distribution
% (Frantisek Gallovic, 2002)

slipamp=slip(:,3); % vector of slip amplitudes

% Find the maximum slip and average slip:
maxslip=max(slipamp);
avgslip=sum(slipamp)/length(slipamp);

% Find the subevent area:
Asub=(A*1000000)/N; % square meters

% Loop to calculate moment:
c=0; % count the number of subevents with non-zero slip
for i=1:N
    Vs(i)=2242*z(i)^.05576; % compute 1D S-wave velocity 3051
    rho(i)=1155.6767*z(i)^.1023103; % compute 1D density 2045.6767
    RM(i)=rho(i)*(Vs(i)^2)*slipamp(i)*Asub; % calculate the seismic moment
    if slipamp(i) > 0
        c=c+1;
    end
end

% Find the difference between derived moment and target moment:
diff=M0-sum(RM);
% Accuracy with no adjustment:
acc=sum(RM)/M0;

% amount that each non-zero subevent must be adjusted by to reach
% the target moment:
adj=diff/c;
% Loop to make-up target moment:
for i=1:N
    if RM(i) > 0
        RM(i)=RM(i)+adj;
    end
end

% Verify that the sum of subevents equals the target moment:
tm=sum(RM);

```

```

%*****

% Find the maximum sub event moment:
Mmax=max(RM);

% spread parameter for rise time calculation E[.8,1]:
del=.9;

% Find the shortest assumed rise time based on M0 (s):
if (Mw < 7)
    rt0=.9;
else
    rt0=2;
end

% Print Nu_LOH.1.sou first line header:
fprintf(fid1, '1 %g 1\n', N)

%*****

% Loop over all subevents yet again to compute fault parameters and
% write the source file:
for i=1:N

    % generate random matrix in order to perturb strike, dip, and rake within
    % the specified envelope.
    ran=rand(3,1);
    stk=env*ran(1)+s0;
    dip=env*ran(2)+d0;
    rake=env*ran(3)+r0;

    % calculate the rise time of each sub event (Harmsen, 2008):
    rt1=rt0+((RM(i))/(Mmax))*del;
    if (z >= 2000) % 5000 in Harmsen
        rt=rt1;
    else
        rt2=rt0+del*((5000-z(i))/5000);
        rt=max(rt1,rt2);
    end

%*****
% Calculate the rupture-front arrival time based on a 1D velocity
% model:

% find distance along strike

```

```

if x(i) > x2
    dist=sqrt((x(i)-x1)^2+(y(i)-y1)^2);
elseif x(i) > x3
    dist=sqrt((x(i)-x2)^2+(y(i)-y2)^2)+L1;
else
    dist=sqrt((x(i)-x3)^2+(y(i)-y3)^2)+L1+L2;
end

% find horizontal hypocentral distance:
if xhyp == x4 % south propagating rupture
    if x(i) > x2
        hypdist=sqrt((x(i)-x2)^2+(y(i)-y2)^2)+L2+L3;
    elseif x(i) > x3
        hypdist=sqrt((x(i)-x3)^2+(y(i)-y3)^2)+L3;
    else
        hypdist=sqrt((x(i)-x4)^2+(y(i)-y4)^2);
    end
elseif xhyp == x1 % north propagating rupture
    if x(i) > x2
        hypdist=sqrt((x(i)-xhyp)^2+(y(i)-yhyp)^2);
    elseif x(i) > x3
        hypdist=sqrt((x(i)-x2)^2+(y(i)-y2)^2)+L1;
    else
        hypdist=sqrt((x(i)-x3)^2+(y(i)-y3)^2)+L1+L2;
    end
else % bilateral rupture
    if x(i) > x2
        hypdist=sqrt((x(i)-x2)^2+(y(i)-y2)^2)+(L2/2);
    elseif x(i) > x3
        hypdist=sqrt((x(i)-xhyp)^2+(y(i)-yhyp)^2);
    else
        hypdist=sqrt((x(i)-x3)^2+(y(i)-y3)^2)+(L2/2);
    end
end

% find approximate velocity at depth of point:
Vs=2207*z(i)^.05576;
% find the rupture front arrival time:
st=hypdist/(.8*Vs);
%%st=.2*rand+st-.1; % allow arrival time to fluctuate
%*****

% write data to file for finite difference code:
fprintf(fid1, '%g %g %g %g %g %g 1 %g %g %g\n', ...
    x(i), y(i), z(i), RM(i), st, rt, stk, dip, rake)

```

```

% write files for plotting in GMT:
fprintf(fid2, '%g %g %g\n', dist, -z(i), slipamp(i))
fprintf(fid6, '%g %g %g\n', dist, -z(i), rt)
fprintf(fid3, '%g %g %g\n', dist, -z(i), st)

% write files for plotting in GRASS:
xutm=x(i)+W0;
yutm=y(i)+S0; % convert to UTMs
fprintf(fid4, '%g %d %g\n', xutm, yutm, -z(i))

end

xhyp=xhyp+W0; % convert to UTMs
yhyp=yhyp+S0;

% Print a log file with information about this source:
fprintf(fid5, '***** SOURCE PARAMETERS *****\n')
fprintf(fid5, 'Northern most point= %g, %g\n', x4, y4)
fprintf(fid5, 'Southern most point= %g, %g\n', x1, y1)
fprintf(fid5, 'Hypocenter (x,y,z)= %g, %g, %g\n', xhyp, yhyp, zhyp)
fprintf(fid5, 'Length of the main fault (m) = %g\n', L)
fprintf(fid5, 'Width of main fault (m)=%g\n', W)
fprintf(fid5, 'Area of Main fault (km^2)= %g\n', A)
fprintf(fid5, 'Total number of subevents= %g\n', N)
fprintf(fid5, 'Number of points along the length of the fault= %g\n', nnx)
fprintf(fid5, 'Number of points along the width of the fault= %g\n', nnz)
fprintf(fid5, 'Moment Magnitude = %g\n', Mw)
fprintf(fid5, 'Maximum Slip (m) = %g\n', maxslip)
fprintf(fid5, 'Average Slip = %g\n', avgslip)
fprintf(fid5, 'Sum of subevent moments (N-m)=%g\n', tm)
fprintf(fid5, 'Target Moment (N-m)= %g\n', M0)
fprintf(fid5, 'Accuracy before adj.= %g\n', acc)
fprintf(fid5, 'Strike (deg)=%g\n', stk)
fprintf(fid5, 'Dip (deg)=%g\n', dp)
fprintf(fid5, 'Rake (deg)=%g\n', re)
fprintf(fid5, 'Envelope in which parameters vary (deg)=%g\n', env)
fprintf(fid5, 'Start Time (s)=%g\n', start)
fprintf(fid5, '*****\n')

% Close output files:
fclose(fid1)
fclose(fid2)
fclose(fid3)
fclose(fid4)

```

```
fclose(fid5)
fclose(fid6)
```

Animations

Below are listed links to movie files that display animations for all of the earthquake scenarios discussed in the text. The first nine files are animations of the scenarios discussed in section 4.1 while the following nine, marked “S1”, are ruptures along faults digitized from [Johnston and Schweig \(1996\)](#) as discussed in section 4.3. Click on an *.mpg file to view an animation.

LIST OF FILES

File Name	Size (MB)	Description
CG_up.mpg	20.1	South–north rupture, Cottonwood Grove fault
CG_down.mpg	11.4	North–south rupture, Cottonwood Grove fault
CG_mid.mpg	19.8	Bilateral rupture, Cottonwood Grove fault
RF_up.mpg	19.7	South–north rupture, Reelfoot fault
RF_down.mpg	19.3	North–south rupture, Reelfoot fault
RF_mid.mpg	13.6	Bilateral rupture, Reelfoot fault
NF_up.mpg	12.8	South–north rupture, North fault
NF_down.mpg	10.1	North–south rupture, North fault
NF_mid.mpg	10.6	Bilateral rupture, North fault
CG_upS1.mpg	21.2	South–north rupture, Cottonwood Grove fault
CG_downS1.mpg	20.9	North–south rupture, Cottonwood Grove fault
CG_midS1.mpg	14.5	Bilateral rupture, Cottonwood Grove fault
RF_upS1.mpg	16.6	South–north rupture, Reelfoot fault
RF_downS1.mpg	16.5	North–south rupture, Reelfoot fault
RF_midS1.mpg	14.5	Bilateral rupture, Reelfoot fault
NF_upS1.mpg	12.6	South–north rupture, North fault
NF_downS1.mpg	21.3	North–south rupture, North fault
NF_midS1.mpg	21.2	Bilateral rupture, North fault

References

- Alterman, Z., Karal, F., 1968. Propagation of elastic waves in layered media by finite difference methods. *Bulletin of the Seismological Society of America* 58, 367–398.
- Antolik, M., Dreger, D. S., 2003. Rupture Process of the 26 January 2001 Mw 7.6 Bhuj, India, Earthquake from Teleseismic Broadband Data. *Bulletin of the Seismological Society of America* 93, 1235–1248.
- Bakun, W., Hopper, M., 2004. Magnitudes and Locations of the 1811-1812 New Madrid, Missouri, and the 1886 Charleston, South Carolina, Earthquakes. *Bulletin of the Seismological Society of America* 94, 64–75.
- Bard, P., Bouchon, M., 1985. The two-dimensional resonance of sediment-filled valleys. *Bulletin of the Seismological Society of America* 75, 519–541.
- Bouchon, M., Coutant, O., 1994. Calculation of synthetic seismograms in a laterally varying medium by the boundary element-discrete wavenumber method. *Bulletin of the Seismological Society of America* 84, 1869–1881.
- Brocher, T. M., 2005. Empirical Relations between Elastic Wavespeeds and Density in the Earth's Crust. *Bulletin of the Seismological Society of America* 95, 2081–2092.
- Catchings, R., 1999. Regional V_p , V_s , V_p/V_s , and Poisson's ratios across earthquake source zones from Memphis, Tennessee, to St. Louis, Missouri. *Bulletin of the Seismological Society of America* 89, 1591–1605.
- Chen, K.-C., Chiu, J.-M., Yang, Y.-T., 1996. Shear-wave velocity of the sedimentary basin in the upper Mississippi embayment using S-to-P converted waves. *Bulletin of the Seismological Society of America* 86, 848–856.
- Chiu, J., Johnston, A., Yang, Y., 1992. Imaging the active faults of the central New Madrid seismic zone using PANDA array data. *Seismological Research Letters* 63, 375–393.
- Cramer, C. H., 2001. A seismic hazard uncertainty analysis for the New Madrid seismic zone. *Engineering Geology* 62, 251 – 266.
- Csontos, R., 2007. Three dimensional modeling of the Reelfoot rift and New Madrid seismic zone. Ph.D. thesis, University of Memphis, Memphis, TN.
- Dart, R., Swolfs, H., 1998. Contour mapping of relic structures in the Precambrian basement of the Reelfoot rift, North American midcontinent. *Tectonics* 17, 235–249.
- Ervin, C., McGinnis, L., 1975. Reelfoot rift; reactivated precursor to the Mississippi embayment. *Bulletin of the Seismological Society of America* 86, 1287–1295.

- Faust, L. Y., 1951. Seismic velocity as a function of depth and geologic time. *Geophysics* 16, 192–206.
- Frankel, A., Stephenson, W., 2000. Three-dimensional simulations of ground motions in the Seattle region for earthquakes in the Seattle fault zone. *Bulletin of the Seismological Society of America* 90, 1251–1267.
- Gallovic, F., Brokesova, J., April 2004. On strong ground motion synthesis with k^{-2} slip distributions. *Journal of Seismology* 8, 211–224.
- Graves, R., 1996. Simulating seismic wave propagation in 3D elastic media using staggered-grid finite differences. *Bulletin of the Seismological Society of America* 86, 1091–1106.
- Grollimund, B., Zoback, M., 2001. Did deglaciation trigger intraplate seismicity in the New Madrid seismic zone? *Geology* 29, 175–178.
- Harmsen, S., Hartzell, S., Liu, P., 2008. Simulated ground motion in Santa Clara valley, California, and vicinity from $M \geq 6.7$ scenario earthquakes. *Bulletin of the Seismological Society of America* 98, 1243–1271.
- Hartzell, S., Guatteri, M., Mai, P. M., Liu, P.-C., Fisk, M., 2005. Calculation of Broadband Time Histories of Ground Motion, Part II: Kinematic and Dynamic Modeling Using Theoretical Green's Functions and Comparison with the 1994 Northridge Earthquake. *Bulletin of the Seismological Society of America* 95, 614–645.
- Herrero, A., Bernard, P., 1994. A kinematic self-similar rupture process for earthquakes. *Bulletin of the Seismological Society of America* 84, 1216–1228.
- Herrmann, R., Ammon, C., 1997. Faulting parameters of earthquakes in the New Madrid, Missouri, region. *Engineering Geology* 46, 299–311.
- Hildenbrand, T., 1985. Rift structure of the northern Mississippi embayment from the analysis of gravity and magnetic data. *Journal of Geophysical Research* 90, 12607–12622.
- Horton, S. P., Kim, W.-Y., Withers, M., 2005. The 6 June 2003 Bardwell, Kentucky, Earthquake Sequence: Evidence for a Locally Perturbed Stress Field in the Mississippi Embayment. *Bulletin of the Seismological Society of America* 95, 431–445.
- Johnston, A. C., Schweig, E. S., 1996. The enigma of the New Madrid earthquakes of 1811–1812. *Annual Review of Earth and Planetary Sciences* 24, 339–384.
- Kagawa, T., Zhao, B., Miyakoshi, K., Irikura, K., 2004. Modeling of 3D basin structures for seismic wave simulations based on available information on the target area: case study of the Osaka basin, Japan. *Bulletin of the Seismological Society of America* 94, 1353–1368.

- Kawase, H., 1996. Cause of the damage belt in Kobe: “The basin-edge effect”, constructive interference of the direct *S*-Wave with the basin-induced diffracted Rayleigh waves. *Seismological Research Letters* 67, 5–25 – 5–34.
- Kawase, H., Aki, K., 1989. A study on the response of a soft basin for incident *S*, *P*, and Rayleigh waves with special reference to the long duration observed in Mexico City. *Bulletin of the Seismological Society of America* 79, 1361–1382.
- Kelly, K., Ward, R., Treitel, S., Alford, R., 1976. Synthetic seismograms: A finite-difference approach. *Geophysics* 41, 2–27.
- Komatitsch, D., Vilotte, J.-P., 1998. The spectral element method: An efficient tool to simulate the seismic response of 2D and 3D geological structures. *Bulletin of the Seismological Society of America* 88, 368–392.
- Kramer, Steven, L., 1996. *Geotechnical Earthquake Engineering*. Prentice Hall, Upper Saddle River, NJ.
- Levander, A. R., 1988. Fourth-order finite-difference *P-SV* seismograms. *Geophysics* 53, 1425–1436.
- Liu, P., Archuleta, R., 2006. Efficient modeling of *Q* for 3D numerical simulation of wave propagation. *Bulletin of the Seismological Society of America* 96, 1352–1358.
- Liu, P., Archuleta, R. J., 2002. The effect of a low-velocity surface layer on simulated ground motion. *Seismological Research Letters* 73, 267.
- Ma, S., Archuleta, R. J., Liu, P., 2004. Hybrid Modeling of Elastic *P-SV* Wave Motion: A Combined Finite-Element and Staggered-Grid Finite-Difference Approach. *Bulletin of the Seismological Society of America* 94, 1557–1563.
- Magistrale, H., Day, S., Clayton, R. W., Graves, R., 2000. The SCEC Southern California Reference Three-Dimensional Seismic Velocity Model Version 2. *Bulletin of the Seismological Society of America* 90, S65–76.
- Magistrale, H., McLaughlin, K., Day, S., 1996. A geology-based 3D velocity model of the Los Angeles basin sediments. *Bulletin of the Seismological Society of America* 86, 1161–1166.
- McBride, J., Pugin, A., Nelson, W., Larson, T., Sargent, S., Devera, J., Denny, F., Woolery, E., June 2003. Variable post-Paleozoic deformation detected by seismic reflection profiling across the northwestern “prong” of New Madrid seismic zone. *Tectonophysics* 369, 171–191(21).
- McKeown, F., Pakiser, L. e., January 1982. Overview and Discussion. In F.A. McKeown and L.C. Pakiser (eds.), *Investigations of the New Madrid Missouri, Earthquake Region*. U.S. Geological Survey Professional Paper 1236-A. Geological Survey, Denver, CO (USA), Technical Report USGS-PP-1236, Denver, CO.

- Minkoff, S. E., 2002. Spatial parallelism of a 3D finite difference velocity-stress elastic wave propagation code. *SIAM Journal on Scientific Computing* 24, 1–19.
- Moczo, P., Kristek, J., Halada, L., 2004. *The Finite-difference Method for Seismologists: An Introduction*. Comenius University, Bratislava, Slovakia.
- Nigam, N., Jennings, P., 1969. Calculation of response spectra from strong-motion earthquake records. *Bulletin of the Seismological Society of America* 59, 909–922.
- Nuttl, O., January 1982. Damaging earthquakes of the central Mississippi valley. In F.A. McKeown and L.C. Pakiser (eds.), *Investigations of the New Madrid Missouri, Earthquake Region*. U.S. Geological Survey Professional Paper 1236-B. Geological Survey, Denver, CO (USA), Technical Report USGS-PP-1236, Denver, CO.
- Olsen, K., 2000. Site amplification in the Los Angeles basin from three-dimensional modeling of ground motion. *Bulletin of the Seismological Society of America* 90, S77–94.
- Pitarka, A., 1999. 3D Elastic finite-difference modeling of seismic motion using staggered grids with nonuniform spacing. *Bulletin of the Seismological Society of America* 89, 54–68.
- Pollitz, F., Kellogg, L., Burgmann, R., 2001. Sinking mafic body in a reactivated lower crust: a mechanism for stress concentration at the New Madrid seismic zone. *Bulletin of the Seismological Society of America* 91, 1882–1897.
- Saikia, C. K., Pitarka, A., Ichinose, G. A., 2006. Effects of irregular structure of the Mississippi embayment on ground-motion amplification. *Bulletin of the Seismological Society of America* 96, 1448–1473.
- Saikia, C. K., Somerville, P., 1997. Simulated hard-rock motions in Saint Louis, Missouri, from large New Madrid earthquakes ($M_w \geq 6.5$). *Bulletin of the Seismological Society of America* 87, 123–139.
- Shearer, P. M., 1999. *Introduction to Seismology*, 1st Edition. Cambridge University Press, Cambridge, New York.
- Shumway, A. M., 2008. Focal mechanisms in the northeast New Madrid seismic zone. *Seismological Research Letters* 79, 469–477.
- Smalley Jr, R., Ellis, M., Paul, J., Van Arsdale, R., June 2005. Space geodetic evidence for rapid strain rates in the New Madrid seismic zone of central USA. *Nature* 435, 1088–1090.
- Somerville, P., Irikura, K., Graves, R., Sawada, S., Wald, D., Abrahamson, N., Iwasaki, Y., Kagawa, T., Smith, N., Kowada, A., 1999. Characterizing crustal earthquake slip models for the prediction of strong ground motion. *Seismological Research Letters* 70, 59–80.

- Stein, S., Wysession, M., 2005. An introduction to Seismology, Earthquakes, and Earth Structure. Blackwell Publishing, Malden, MA.
- Street, R., Wang, Z., Woolery, E., Hunt, J., Harris, J., 1997. Site effects at a vertical accelerometer array near Paducah, Kentucky. *Engineering Geology* 46, 349–367, neotectonics and Earthquakes in the Central Mississippi Valley.
- Street, R., Woolery, E., Chiu, J., 2004. Shear-wave velocities of the post-Paleozoic sediments across the upper Mississippi embayment. *Seismological Research Letters* 75, 390–405.
- Street, R., Woolery, E., Wang, Z., Harris, J., 1995. A Short Note on Shear-wave velocities and other site conditions at selected strong-motion stations in the New Madrid seismic zone. *Seismological Research Letters* 66, 56–63.
- Street, R., Woolery, E. W., Wang, Z., Harris, J. B., 2001. NEHRP soil classifications for estimating site-dependent seismic coefficients in the Upper Mississippi Embayment. *Engineering Geology* 62, 123 – 135.
- Top500, November 2008. Top 500 Supercomputer List. Website.
URL <http://www.top500.org>
- Toshinawa, T., Ohmachi, T., 1992. Love-wave propagation in a three-dimensional sedimentary basin. *Bulletin of the Seismological Society of America* 82, 1661–1677.
- Tuttle, M. P., Schweig, E. S., Sims, J. D., Lafferty, R. H., Wolf, L. W., Haynes, M. L., 2002. The earthquake potential of the New Madrid seismic zone. *Bulletin of the Seismological Society of America* 92, 2080–2089.
- USGS, 2008. USGS website on the May 12, 2008 Sichuan earthquake.
URL <http://earthquake.usgs.gov/eqcenter/eqinthenews/2008/us2008ryan>
- Van Arsdale, R. B., TenBrink, R. K., 2000. Late Cretaceous and Cenozoic geology of the New Madrid seismic zone. *Bulletin of the Seismological Society of America* 90, 345–356.
- Vance, D., 2006. Shear-wave velocities and derivative mapping for the upper Mississippi embayment. Master’s thesis, University of Kentucky, Lexington, KY.
- Virieux, J., 1984. *SH*-wave propagation in heterogeneous media: Velocity-stress finite-difference method. *Geophysics* 49, 1933–1942.
- Virieux, J., 1986. *P-SV*-wave propagation in heterogeneous media: Velocity-stress finite-difference method. *Geophysics* 51, 889–901.
- Wald, D. J., Allen, T. I., 2007. Topographic slope as a proxy for seismic site conditions and amplification. *Bulletin of the Seismological Society of America* 97, 1379–1395.
- Wang, Z., 1998. Two-dimensional ground-motion simulation in the upper Mississippi embayment. Ph.D. thesis, University of Kentucky, Lexington, KY.

- Wang, Z., Street, R., Woolery, E., Harris, J., 1994. Q_s estimation for unconsolidated sediments using first-arrival SH -wave critical refractions. *Journal of Geophysical Research* 99, 13,543–13,551.
- Wang, Z., Woolery, E. W., 2006. Recordings from the deepest borehole in the New Madrid seismic zone. *Seismological Research Letters* 77, 148–153.
- Wells, D., Coppersmith, K., 1994. New empirical relationships among magnitude, rupture length, rupture width, rupture area, and surface displacement. *Bulletin of the Seismological Society of America* 84, 974–1002.
- Wessel, P., Smith, W., 1998. New version of the Generic Mapping Tools released. *EOS, Transactions, American Geophysical Union* 79, 579.
- Xiaojun, L., Zhenghua, Z., Moh, H., Ruizhi, W., Haiyin, Y., Dawei, L., Yongnian, Z., Jianwen, C., 2008. Preliminary Analysis of Strong-Motion Recordings from the Magnitude 8.0 Wenchuan, China, Earthquake of 12 May 2008. *Seismological Research Letters* 79, 844–854.
- Zeng, Y., Anderson, J., Yu, G., 1994. A composite source model for computing realistic synthetic strong ground motions. *Geophysical Research Letters* 21, 725–728.

Vita

Kenneth Armstrong Macpherson,

- Born Lanark, Scotland, U.K., 1970
- Immigrated to the United States in 1974
- Naturalized U.S. citizen in 2007

Education

University of Kentucky

Lexington, KY

Degree Program: Ph.D.

Area of Concentration: Geophysics

Murray State University

Murray, KY

Degree: Master of Science

Major: Mathematics

Degree: Bachelor of Science

Dual Major: Geology, Mathematics

Appointments

February 2009 - June 2009: Geoscience Intern, Pioneer Natural Resources
August 2008-February 2009: Research Assistant, University of Kentucky
August 2007 - August 2008: Graduate School Fellow, University of Kentucky
August 2006 - August 2007: Algebra³ Fellow, UK/Bath County High School
August 2005 - August 2006: Teaching Assistant, University of Kentucky
August 2004 - May 2005: Lecturer, Murray State University
January 2001 - May 2004: Teaching Assistant, Murray State University

Awards

- First place in the student poster competition at the Eastern Section of the Seismological Society of America annual meeting in October, 2008, for *Strong Ground Motion in the Upper Mississippi Embayment from Finite-Fault, Finite-Difference Simulations*.
- Second place in the Society for Industrial and Applied Mathematics “Math Matters, Apply It!” 2009 student contest for “The Math behind Earthquake Simulations”.